Damage Tolerance Behaviour of Integral Aircraft Structures Obtained by Stationary Shoulder Friction Stir Welding

Vom Promotionsausschuss der
Technischen Universität Hamburg
zur Erlangung des akademischen Grades
Doktor-Ingenieur (Dr.-Ing.)

genehmigte Dissertation

von
Alessandro Barbini

aus
Pisa (Italien)

2021

1. Gutachter: Prof. Dr.-Ing. Norbert Huber
2. Gutachter: Prof. Dr.-Ing Xiang Zhang
Vorsitzende: Prof. Dr. Erica Lilleodden

Mündliche Prüfung: 3. Juli 2020

Abstract

Research focusing on new ways to achieve weight reduction without sacrificing the safety performances of an aircraft is the subject of a constant push in the aeronautical industry. The use of riveting to join skin and stringer is highly optimised but in order to reduce structural weight, aside from the continuous development of new materials, it is important to use the already available materials in an efficient way. For this reason, friction stir welding (FSW) was looked at for many years as a suitable replacement alternative for riveting but the focus of the research was mostly driven with a material science point of view. Therefore, the development of a new solid-state welding technology ensuring good material properties and, at the same time, being investigated as a structural joint is still a necessity.

The present-study addresses the development of a new procedure for joining skin and stringers made of dissimilar aluminium alloys by stationary shoulder friction stir welding (SSFSW), which is to be applied in primary aircraft structures. Three different joint configurations were developed, and their performances were compared. At first, a fundamental analysis of the correlation between the two main process parameters, welding speed and rotational speed on heat development and joint formation, was conducted. The correlation between the generated microstructure and the mechanical properties of the three configurations was investigated on coupon-size specimens. In the following step, the fatigue behaviour in sub-component scale was studied in terms of fatigue life and crack initiation for two of the joint configurations. In the last phase of the work, 5-stringer panels were realised by SSFSW using the joint configuration, which showed the best properties in the performed analysis. These panels were investigated in the context of a damage-tolerant environment to understand fatigue crack growth and residual strength behaviour in comparison to conventional joining technologies.

At the coupon level, the three joint configurations showed higher mechanical performances for different loading conditions with respect to a conventionally riveted skin and stringer. The interface between the skin and the stringer’s alloys proved to play the largest influence on the strength of the joints. The two welding parameters control the geometry of this by influencing the material flow and heat generation. The notch-skin double pass (NS-DP) configuration proved to have limitations in terms of process development and were excluded from the study for up-scaled components. The sub-components realised by SSFSW with the two remaining joint variants showed higher fatigue performances in hoop-directions with respect to riveted structures. The SSFSW technology leads to half the stress concentration of a riveted T-joint and an increase of 50% in the fatigue limit. In spite of a similar fatigue life, in the NS-SP joints, crack turning and unwanted delamination of the stringer was observed. In the longitudinal load direction, a higher fatigue life was recorded for the 3-Part joints in the high-cycle area with respect to the NS-SP variant. From the fatigue crack growth (FCG) tests of the 5-stringer panels, the optimum load redistribution between skin and stringers joined by the SSFSW led to a reduction of the FCG rate for short cracks away from the stringers. This structural behaviour improves the FCG with respect to riveted and adhesive bonded structures. An increase in lifespan over 62% for a crack length that reaches the two-bay width has been shown. The residual strength of the SSFSW panels was measured for a two-bay crack showing a significant improvement over conventional joining techniques and confirming the superior quality of structures realised by SSFSW in a damage-tolerant environment.

Zusammenfassung

Die Forschung, die sich auf neue Wege konzentriert, um eine Gewichtsreduzierung zu erreichen, ohne die Sicherheitsleistung eines Flugzeugs zu beeinträchtigen, ist in der Luftfahrtindustrie ein ständiges Thema. Die Verwendung von Nieten zum Verbinden von Haut und Stringer ist in hohem Maße optimiert. Um jedoch das strukturelle Gewicht zu verringern, ist es wichtig, neben der kontinuierlichen Entwicklung neuer Materialien die bereits verfügbaren Materialien auf effiziente Weise zu verwenden. Aus diesem Grund wurde das Reibrührschweißen (FSW) seit vielen Jahren als geeignete Ersatzalternative für das Nieten angesehen, der Schwerpunkt der Forschung lag jedoch hauptsächlich auf materialwissenschaftlichen Gesichtspunkten. Daher ist die Entwicklung einer neuen Festkörperschweißtechnologie, die gute Materialeigenschaften gewährleistet und gleichzeitig als strukturelle Verbindung untersucht wird, weiterhin eine Notwendigkeit.

Die vorliegende Studie befasst sich mit der Entwicklung eines neuen Verfahrens zum Verbinden von Haut und Stringern aus unterschiedlichen Aluminiumlegierungen durch stationäres Schulterreibungsrührschweißen (SSFSW), das in primären Flugzeugstrukturen angewendet werden soll. Drei verschiedene Verbindungskonfigurationen wurden entwickelt und ihre Leistungsfähigkeit verglichen. Zunächst wurde eine grundlegende Analyse der Korrelation zwischen den beiden Hauptprozessparametern Schweißgeschwindigkeit und Drehzahl bei Wärmeentwicklung und Ausbildung der Schweßnaht durchgeführt. Die Korrelation zwischen der erzeugten Mikrostruktur und den mechanischen Eigenschaften der drei Konfigurationen wurde an Probekörpern mit Coupongröße untersucht. Im folgenden Schritt wurde das Ermüdungsverhalten im Teilkomponentenmaßstab in Bezug auf die Ermüdungslebensdauer und die Rissentstehung für zwei der Verbindungskonfigurationen untersucht. In der letzten Phase der Arbeit wurden von SSFSW 5-Stringer-Paneele unter Verwendung der Fugenkonfiguration realisiert, die die besten Eigenschaften in der durchgeführten Analyse zeigten. Diese Platten wurden hinsichtlich der Schadenstoleranzeigenschaften untersucht, um das Ermüdungsrisswachstum und das Verhalten der Restfestigkeit im Vergleich zu herkömmlichen Verbindungstechnologien zu verstehen.

Auf Couponebene zeigten die drei Verbindungskonfigurationen höhere mechanische Belastbarkeit für unterschiedliche Belastungsbedingungen in Bezug auf eine herkömmlich genietete Haut/Stringer-Verbindungen. Es zeigte sich, dass die Grenzfläche zwischen der Haut und den Stringerlegierungen den größten Einfluss auf die Festigkeit der Gelenke hat. Die beiden Schweißparameter steuern deren Geometrie durch Beeinflussung des Materialflusses und der Wärmeerzeugung. Die Notch-Skin-Double-Pass-Konfiguration (NS-DP) zeigte Einschränkungen hinsichtlich der Prozessentwicklung und wurde für hochskalierte Komponenten aus der Studie ausgeschlossen. Die von SSFSW mit den beiden verbleibenden Gelenkvarianten realisierten Unterkomponenten zeigten höhere Ermüdungsleistungen in Hoop-Richtungen in Bezug auf genietete Strukturen. Die SSFSW-Technologie führt zu einer Halbierung der Spannungskonzentration eines genieteten T-Stücks und einer Erhöhung der Ermüdungsgrenze um 50%. Trotz einer ähnlichen Ermüdungslebensdauer wurde in den NS-SP-Verbindungen eine Rissbildung und eine unerwünschte Delamination des Stringers beobachtet. In Längsrichtung der Belastung wurde für die 3-teiligen Verbindungen im Hochzyklusbereich eine höhere Lebensdauer gegenüber der NS-SP-Variante verzeichnet. Aus den Ermüdungsrisswachstumstests (FCG-Tests) der 5-Stringer-Paneele ergab sich, dass die optimale Lastumverteilung zwischen Haut und Stringern, die durch das SSFSW verbunden wurden, zu einer Verringerung der FCG-Rate für kurze

Risse von den Stringern weg führte. Dieses strukturelle Verhalten verbessert das Ermüdungsrisswachstum in Bezug auf genietete und geklebte Strukturen. Bei einer Risslänge, die die Breite von zwei Feldern erreicht, wurde eine Verlängerung der Lebensdauer um mehr als 62% festgestellt. Die Restfestigkeit der SSFSW-Platten wurde für einen Zwei-Feld-Riss gemessen, der eine signifikante Verbesserung gegenüber herkömmlichen Verbindungstechniken zeigte und die überlegene Qualität der von SSFSW in einer schaden toleranten Systemmumgebung bestätigte.

Contents

Symbols and Abbreviations

a	Half crack length
a, b	Constants of Basquin's power function
AA	Aluminium Alloys
AS	Advancing Side
ASTM	American Society for Testing and Materials
b	Distance between stringers
C	Parameter of the Paris' equation
CDF	Cumulative Density Function
COD	Crack-Opening Displacement
CTOD	Crack Tip-Opening Displacement
CV	Coefficient of Variance
DIC	Digital Image Correlation
DP	Double Pass
E	Young's modulus
EDM	Electrical Discharge Machining
EPFM	Elasto-Plastic Fracture Mechanics
FAA	Federal Aviation Administration
FAR	Federal Aviation Requirements
FCG	Fatigue Crack Growth
FCGR	Fatigue Crack Growth Rate
FEM	Finite Element Method
FSW	Friction Stir Welding
FTA	Fault Tree Analysis
F_x	Force in welding direction
GAG	Ground-Air-Ground
GP	Guinier-Preston
GPB	Guinier-Preston Bagaryatskii
HAZ	Heat Affected Zone
HV	Vickers Hardness
ISO	International Organisation for Standardization

K_c	Plane strain Fracture Toughness
K_I, K_{II}	Stress Intensity Factor for mode I and mode II crack opening
K_R	Fracture resistance
$\mathrm{K_t}$	Stress concentration
LDC	Large Damage Capability
LEFM	Linear Elastic Fracture Mechanics
LISA	Light Integrate Structure for future generation Aircraft
M	Torque applied by the tool
MR	Median Rank
MTTF	Mean Time To Failure
N	Cycles to failure
n	Exponent of the Paris's equation
NS	Notch-Skin
PDF	Probability Density Function
Q	Welding power
R	Stress ration
RPM	Rotations Per Minute
RS	Retreating Side
S	Stress
S, S'	Phases in the precipitation of AA 2024
SD	Standard Deviation
SEM	Scanning Electron Microscope
SIF	Stress Intensity Factor
$\mathrm{S_{max}}$	Maximum stress in cyclic loading
$\mathrm{S_{min}}$	Minimum stress in cyclic loading
SP	Single Pass
SSFSW	Stationary Shoulder Friction Stir Welding
SSSS	Supersaturated Solid Solution
SZ	Stir Zone
TMAZ	Thermo-Mechanically Affected Zone
TWI	The Welding Institute
UTS	Ultimate Tensile Strength

v	Welding Speed
WS	Welding Speed
α, β	Scale and the shape parameters in Weibull distribution
β-angle	Angle formed by the interface
β-factor	Non-dimensional factor for the calculation of the SIF
δ	Crack tip opening displacement according to Wells
δ_5	Modified CTOD according to Schwalbe
ΔS	Stress amplitude
ε	Engineering normal strain
ε_T	True normal strain
η, η'	Phases in the precipitation of AA 7050
σ	Engineering normal stress
σ_T	True normal stress
σ_y	Yield stress
τ	Shear stress
φ	Slip/Stick ratio coefficient
ω	Angular velocity

1. Introduction

1.1. Motivation

The increase in air traffic, which is expected in the future, and the necessity to produce a large amount of new aircrafts have brought up the problem of sustainability in an industrial sector that is becoming increasingly dependent on production volumes [1]. This increment in production, considered alongside the increased number of aircrafts cruising through the skies every day, risks clashing against the general trend of society to reduce CO_2 emissions, and achieving a more sustainable future for new generations. In order to solve this dilemma, the new manufacturing concepts will have to be more environmentally friendly by the efficient use of energy and the reduction in thermal and gas emissions. Not only is the new green manufacturing technique needed but the new produced aircraft will also have to aim for a reduction in gas emissions. This goal, for the aircraft industry, is a golden opportunity since the reduction of the weight of airplanes without sacrificing safety performance has always been the main drive behind the development of new technologies. A lighter structure leads to reduced fuel consumption and the consequent environmental footprint that is left by each aircraft.

In order to reduce structural weight, aside from the continuous development of new materials, it is important for the materials already available to be used in an efficient way. This means that the right materials have to be used in the right locations in aircrafts according to design requirements and they have to be joined in an efficient and cost-effective way, which increases safety while reducing the number of manufacturing processes and the parts reject rate.

Friction Stir Welding (FSW) has been considered by many experts as *the* solution for a wide range of applications. The aerospace industry, in particular, has been looking with interest to FSW since decades due to the possibility of welding precipitation-hardened aluminium alloys as well as other materials that are considered difficult to join with other welding technologies. In spite of these premises, FSW has not been applied on a large scale yet in the aerospace industry owing to several reasons—with two of them of particular interest for the research approach in this work:

- The conservative approach in the aerospace field
- Focus of scientific research

Conservatism in the aerospace industry is what ensures the current level of safety, which is the most valuable and protected element in this field. The negative aspect of a conservative approach consists of difficulty in the introduction of new technologies in service. These technologies have to compete with well-established methods that have already matured operational experience and for which large amounts of test data are available. In order to qualify new technologies, the economic impact is very significant as large testing campaigns and evaluations have to be carried on. For example, it can be seen that the building-block approach that is used, among others, for the qualification of new structures realized in composite materials (Figure 1.1). For these reasons, new aircrafts are mostly based on older proven technologies, such as riveting, and only a few virgin technologies are introduced.

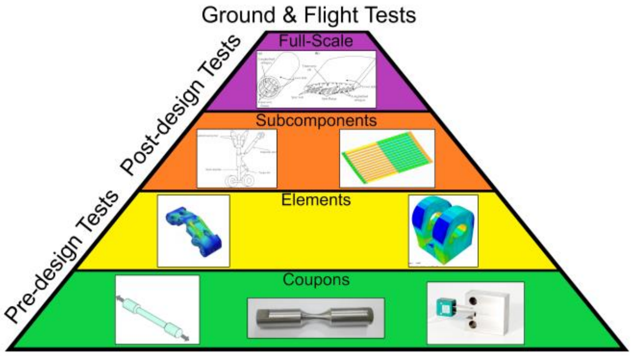

Figure 1.1. Building-block approach for the characterization of new technologies [2, 3]

If we compare FSW with the conventional riveted-joining method, it is clear that riveting is many steps ahead. The amount of research completed for riveted connections made of these a highly sophisticated joining technology with a well-known behaviour. However, the possibility of FSW as a joining technique is great, both in terms of weight reduction and productivity.

The second reason that caused a delay in the application of FSW to aeronautical structures is related to the type of research that has been performed with regard to the FSW process. Initially, the research was focused on the process' development and the understanding of material flow as well as joint formation. This deep understanding contributed greatly to the development of the technology and the expansion of the range of materials and parameters in which FSW could be applied. On top of this, many new variants from the original process have been developed such as a bobbin tool FSW [4] and Stationary Shoulder FSW (SSFSW), which is the joining technique that has been employed in this research. The other focus of the scientific research was driven from a purely material science point of view by analysing the influence of FSW on the microstructural transformations that the different materials undergo and relating them with the mechanical properties of the realised joints. However, such research lacks a deep understanding of the joints from structural points of view, which are important for final application in aircrafts. Some attempts in the past were focused of FSW structural research on butt joints since this was considered to be the best "business case" for FSW. The only efforts in FSW skin/stringer joints was conducted by EMBRAER and by Airbus (as part of the EU Project Tango). However, in both cases overlap joints were used. While considering Figure 1.1, it is clear that great efforts have been made to build the base of the pyramid but very little has been investigated with respect to the higher level of complexity in the joints. It is important to remember that FSW or SSFSW are not just contributing to materials modification but are also technologies that need to be investigated as a structural joint as well.

The author believes that this lack of knowledge can be filled by combining a deep understanding of the SSFSW process from a material science point of view as well as investigating the joints as a structure that has to fulfil a certain design criterion which is necessary in a damage-tolerant aircraft structure.

1.2. Objectives

The need for a credible alternative to riveted joints in primary aircraft structures realized in aluminium alloys is evident as presented in the motivation for this work. SSFSW is a new technology that shows high potential to be employed for such an application. In spite of a few studies that were performed with regard to SSFSW, the problems introduced by the tool limited its application and analysis in an aeronautical environment with larger structures and more complex geometries. Hence, the objectives of this study are as follows:

- Development of a robust tool system, which allows the extension of the parameter window for the SSFSW application
- Application of SSFSW to skin–stringer joints and the development of different welding configurations for local analysis
- Analysis of the interaction of the process parameters with the thermal cycle, joint formation, and microstructural evolution leading to the resulting mechanical properties of the joints
- Analysis of the interaction between the joint configurations and the critical point for fatigue initiation in the sub-components.
- Determination of fatigue life curves for different joint configurations and comparison with riveted joints
- Investigation of the influence of the SSFSW process on the fatigue crack growth (FCG) and the residual strength behaviour of multi-stringer structures

1.3. Scientific Approach

The scientific approach of the thesis to reach the target objectives is depicted in the form of a schematic in Figure 1.2. At the beginning of the work, a systematic study of the tool used for SSFSW is performed. A new tool is developed in order to solve the problems of robustness inherent in the process and the window of the parameters for optimisation is expanded.

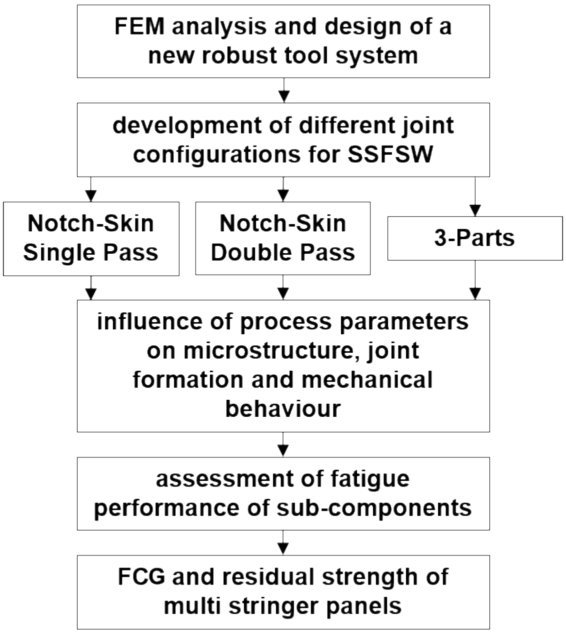

Figure 1.2. Schematic diagram of the scientific approach to the present thesis

Subsequently, different weld configurations were identified as possible candidates for the application of SSFSW to skin–stringer aircraft structures. For each welding configuration, a parameter window that leads to defect-free joints was defined. Each developed configuration was investigated within the limits of the parameters window to first understand the influence of the process parameters on the generated microstructure and on the joint-formation mechanism. In the second phase, the mechanical performances of the joints were analysed and correlated with both the process parameters and the microstructure.

In the following step, the set of parameters that provided the highest mechanical strength in different load directions was used for the two joint configurations to realize the sub-components to be analysed in terms of fatigue life and crack initiation. Through the knowledge acquired, it was possible to select the best joint configuration and realize multi-stringer panels. In the end, an understanding of the FCG properties and the residual strength of large components allow the assessment of the damage tolerability of the integral panel realized by SSFSW in order to be used directly in the aeronautical industry.

1.4. Structure

This study, in agreement with the scientific approach presented in Figure 1.2, is structured as follows:

In Chapter 1, the motivations behind the current work are introduced and the objectives of the study are delineated.

Chapter 2 provides a concise overview of FSW and stationary shoulder FSW, with some highlights regarding material flow and precipitate phenomena, which are useful for the understanding of the work. The state-of-the-art current skin–stringer connection, with the typical analysis methods in terms of damage tolerance, are additionally provided.

The experimental setup and procedure for joining skin and stringers by SSFSW is described in Chapter 3. Furthermore, base materials are introduced, and analytical techniques for material and structural characterization are presented.

In Chapter 4, the causes for the failure of SSFSW tools are determined through an FEM analysis. The design procedure for a new probe and the surrounding system with the benefit produced for the robustness of the process are presented.

In Chapter 5, the notch-skin single pass (NS-SP) configuration is analysed in detail and the correlation between the process parameters, microstructure features, and mechanical properties are highlighted and explained. At first, the process is analysed in terms of force and torque generated for the different welding parameters, thus showing the influences on the material flow around the probe and on the thermal cycles. Subsequently, the joint formation and the microstructural properties of the joints are discussed with a particular emphasis on some of the most important generated features. In the end, the mechanical properties of the coupons are comprehensively analysed for different load configurations, thus emphasizing on the microstructural influences on them.

In Chapter 6, the three joint configurations are compared in terms of joint formation, microstructure, and mechanical properties for the same set of welding parameters. The key differences between these joint configurations are presented in detail. The final part of this chapter is dedicated to the strain analysis of the joint under different load conditions, thereby showing how the strain redistribution is strongly influenced by the configuration of the joints.

Chapter 7 presents the results of the fatigue analysis of the sub-components for two-joint configurations that showed higher mechanical performances in the previous chapter. After describing the probabilistic model used to treat the results from the tests, the S-N curves obtained for each load condition are analysed and compared with the base materials and a similar riveted configuration. Furthermore, the critical areas for fatigue initiation are identified and the crack surfaces are investigated.

In Chapter 8, the damage tolerance analysis of multi-stringer panels realized with the 3-Parts joint configuration is performed. In order to do so, the fatigue crack growth behaviour of the structure is analysed and compared with similar components that are realized by riveting and adhesive bonding. The strain field around the crack for different damage levels is characterized by the use of digital image correlation (DIC) to have a deeper understanding of the factors influencing the crack driving force. At last, the residual strength in the case of panels that undergo severe two-bay crack damage is measured to investigate the possibility of fuselage structures realized with such technology to withstand the limit loads.

Finally, Chapter 9 summarizes the main conclusions that are drawn in this study.

2. State-of-the-art

Initially, a concise overview of friction stir welding and stationary shoulder FSW is given in this chapter, with some highlights about microstructural transformation in the two aluminium alloys of interest. The last part of this chapter is dedicated to the current level of development in fuselage structures and the type of analysis performed to characterize them.

2.1. Conventional Friction Stir Welding

The nature of FSW as a solid-state joining technique, in contrast with other welding technologies that rely on the melting of the materials, enables joining a wider variety of alloys that were considered traditionally impossible to be welded. Since its invention at The Welding Institute (TWI) in 1991 [5], FSW has been considered a joining solution that is particularly suitable for the fuselage structure [6] due to the possibility of joining high-strength aluminium alloys.

The FSW process can be divided into four main phases; each of them is characterized by a specific movement of the tool and a change in the applied forces. Initially, the non-consumable tool starts to rotate and penetrates the materials. At the end of the plunging phase, a vertical force is applied by the tool, thereby increasing the pressure between the tool and the work piece and leading to an increase in friction that favours the plasticization of the materials. In the next step, the rotation of the tool is kept constant and by moving it along the abutting edges of the two plates, and the material is stirred and mixed. Material transportation is the key feature of creating the joint between the two parts. At the end of the weld, the tool is extracted from the work piece while sustaining the rotation. This last phase is the cause for the typical end hole that is present in all the FSW processes.

The typical tool that is used in FSW is formed by two main components: a shoulder, which is the area in direct contact with the crown surface of the workpiece and a probe, which is the penetrating part in the materials (Figure 2.1). The shape and the dimensions of these two components can greatly vary depending on the materials that are to be joined and the configuration of the joint itself [7, 8]. The three parameters that are initially set on the tool according to the thickness of the materials to be joined are the probe length, the plunge depth, and the tilt angle. This last aspect ensures that the shoulder holds the material stirred by the probe, thereby improving the surface finishing. An incorrect probe length or plunge depth can independently disrupt the joint quality from the welding parameters chosen, thus leading to, for example, an insufficient penetration, which is detrimental for the mechanical properties [9-11].

During the welding process itself, the two parameters that are most influential in the joint performance are the rotational speed and the welding speed (WS), which are shown in Figure 2.1. In specific cases, the vertical force applied by the tool on the work piece can be controlled as well during the process, thereby reducing the possibility of the defects caused by the uneven surfaces of the joining parts. The combination between all the parameters influences the energy transferred in the weld, the consequent temperature distribution, and the material flow around the tool [12-16].

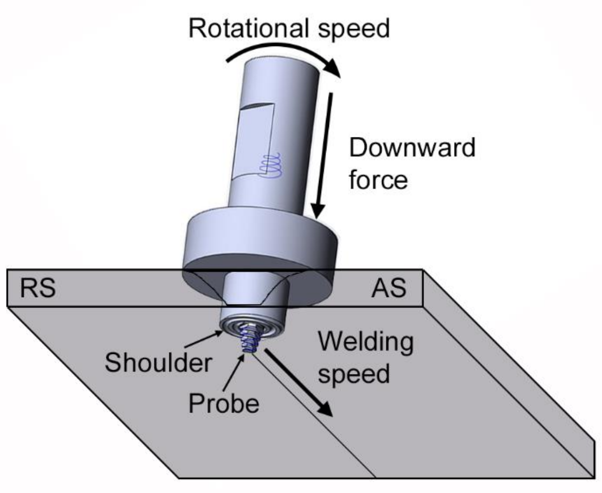

Figure 2.1. Schematic drawing of the FSW process

Owing to the rotation of the tool, the material flow induced by the process is asymmetric, leading to different velocities between the two sides of the weld [17, 18]. The higher material's speed is observed in the part of the weld in which the welding speed and the vector tangent to the rotational speed have the same direction and is called the Advancing Side (AS). The opposite part, where the speed is the lowest, is named the Retreating Side (RS). The variation in the flow between these two parts leads to differences in the material transportation around the tool and, consequently, in the strain rate and the strain accumulated during each rotation. All the physical aspects, such as the friction between tool and the surrounding material as well as the strain that this part undergoes contributes to the heat generation and material flow [19-22]. For this reason, the joint formation and the resulting microstructure need to be analysed carefully in order to understand its relationship with the welding parameters.

The typical microstructure generated during FSW can be divided into three main zones, according to the different mechanical and thermodynamic histories that the materials experience (Figure 2.2). The material in direct contact with the tool, which is undergoing strong plastic deformation and high temperature exposure, forms the stir zone (SZ) in the centre of the weld. Aside from the SZ, there is the presence of a Thermo-Mechanical Affected Zone (TMAZ), which experiences elevated temperature and deformation owing to the transmission of shear forces. The last zone that is influenced by the process is called the Heat Affected Zone (HAZ), where there is no mechanical influence from the tool and only the heat transferred from the weld centre influences the microstructure. The boundary of this area is not visible by microscopy since no changes in grain size and orientation can be observed with respect to the base material—only the precipitations are affected.

Figure 2.2. Example of an FSW cross-section with different weld zones

The SZ microstructure is characterized by a dynamically recrystallized fine-grained structure formed by high strain rate and frictional heating developed in the area [23-25]. The grain size changes through the thickness due to different temperature and velocity gradients that the material experiences during the weld. Another typical microstructural feature is represented by concentric circles, usually referred as ‘onion rings’, which are created by two different material flows around the probe [26-28]. The grains size in the SZ decreases, moving from the crown to the root side of the weld owing to the temperature and the speed gradient through the thickness [29].

In the TMAZ, the base material’s grain structure is deformed in an upward flowing pattern around the SZ. Although the TMAZ experiences plastic deformation, recrystallization does not occur due to the insufficient strain rate. The asymmetry in material transportation is observable in the transition zones between the SZ and the TMAZ, which usually differ in size and grain-orientation while moving towards the AS or RS.

The relationship between static mechanical properties and welding parameters for aluminium alloys were investigated in several studies, including the influence of the residual stresses generated [30-33]. The possibility of joining different alloys without any filler material and maintenance of good performance of the welds is of particular importance [34, 35]. In these cases, the location of the alloys between AS and RS is critical. Owing to the asymmetric welding behaviour, it was proved that it is beneficial to position a higher-strength aluminium alloy in the RS of the joint [36-38].

The fatigue properties of FS-welded joints can be compared with the base material performance. The fatigue results are approaching the base material in the high-fatigue cycles range for many of the most common aluminium alloys [39]. In the case of AA 2024-T3, the fatigue crack growth (FCG) behaviour was investigated and showed a dependence on the location of the initial notch [40]. Inside the SZ, the FCG rate is mainly influenced by microstructural transformations. However, when the crack enters into the weld, the residual stress field introduced by the process plays a key role [40]. When the crack location is directly in the weld and propagating alongside it, the FCG rate is at the same level—if not higher—than the base material owing to the refined microstructure in the SZ that compensate for the loss in strength [41].

2.1.1. Precipitation Evolution in FSW of AA 2024-T3 and AA 7050-T7651

The strengthening mechanism for the two alloys of interest in this study, AA 2024-T3 and AA 7050-T7651, are based on precipitation-hardening. In order to improve the mechanical properties, precipitates are formed at the nanometric scale, which contributes to the strength of alloys by obstructing the movement of the dislocations. Precipitation processes are caused by the decrease of the solid solubility of certain alloying elements with decreasing temperature. After FSW, the precipitates’ morphology and distribution among the different welding areas is affected. These variations in the precipitates are the main cause for the changes in the hardness of the joints since the strengthening effect of grain size variation is small in these two aluminium alloys [42]. Owing to the intrinsic relationship between the evolution of precipitates and the hardness profile, these variations can be used to track the microstructural transformation that the weld areas experience as well as for the joining process used in this study.

It is generally accepted that the precipitation sequence in 7XXX alloys is as follow [43-45]:

$$Supersaturated\ solid\ solution\ (SSSS) \rightarrow GP\ zones \rightarrow \eta'(MgZn_2) \rightarrow \eta(MgZn_2)$$

In the case of AA 7050-T7651, η’, in particular, are the main strengthening precipitates. According to the previous studies [46-48], the HAZ is characterized by the coarsening of the η’ and an increase in the volume of η precipitates and vacancy-reach clusters, GP(II) zones. This transformation, which is caused by the temperature reached during the process in the HAZ—around 250ºC [49]—causes a drastic reduction in hardness. In the SZ, owing to temperatures above 500 ºC, the dissolution of strengthening precipitates can be observed, followed by heterogeneous re-precipitation and natural aging. After stabilizing, the main precipitates are η’ and solute-reach clusters as well as GP(I) zones, which contribute to a large recovery of the hardness. In the TMAZ, a continuous evolution of precipitates are observed, which is supported by an increasing hardness profile in the area up to the levels of the SZ.

In the case of AA 2024, the precipitation sequence is given as [50, 51] follows:

$$SSSS \rightarrow GPB\ zone \rightarrow S'(Al_2CuMg) \rightarrow S$$

With Guinier Preston Bagaryatskii (GPB) zones, the solute of Cu and Mg atoms are formed as the main hardening precipitation mechanism in the T3 state. Previous studies provided a good description of the precipitate evolution in the different FSW areas [52-54]. In the SZ, due to high temperatures, most of the precipitates are dissolved, thus allowing the nucleation of new GPB zones. Consequently, the hardness values in the area increased, recovering to almost the same level as the base material after natural aging. In the TMAZ, the temperature is not high enough to dissolve the precipitates, but it leads to an increase in the fraction of the coarse S and S’ precipitates. These, combined with the minimal GPB zones fractions, lead to hardness reduction to minimum levels. The precipitation state in the HAZ depends on the temperature decrease, moving away from the weld centre. Moving away from the base material towards the TMAZ, the GPB zones gradually dissolve and are replaced by fine S’ and S precipitates. These particles, once formed, tend to become coarse with growing temperature. For this reason, the hardness continuously evolves from the base material value, with an initial decrease, followed by a peak in the centre of the HAZ, and a drop near the boundary between HAZ and TMAZ.

2.2. Stationary Shoulder FSW

The welding technology used in the current study is a variant of the previously described FSW. In conventional FSW, the rotating shoulder, beside partially contributing to the material flow in the upper part of the joint and maintaining the material in a position during welding, provides the majority of the frictional heat, especially for thin plates [55, 56]. This property of the process is undesirable in welding materials with low thermal conductivity or thin sheets, where a lower and homogeneously distributed heat is necessary for the realization of sound welds. In order to overcome the aforementioned issues, the Stationary Shoulder FSW (SSFSW) was invented by simply uncoupling the rotations of the probe and the shoulder [57].

For these reasons, a part of the research interest was focused on titanium alloys, which, despite being joinable by conventional FSW, allowed an extremely narrow range of parameters and caused a drastic reduction of the tool life owing to chemical wearing at high temperatures [57-60]. In Ti-alloys, the heat generated by the FSW remains concentrated in the area around the tool and by using SSFSW, it is possible to extend the range of welding parameters and to reduce the tool wearing. The results achieved in the case of titanium raised interest around the process for other low-thermal conductivity materials as well, such as acrylonitrile butadiene styrene (ABS) and other polymers [61-63].

From a process point of view, the absence of a rotating shoulder leads to a reduction of the energy transferred into the weld. The probe becomes the only part of the tool that produces heat by friction with the surrounding material as well as strain energy. The shoulder only has the function of keeping the plasticized material in the surroundings of the probe and it provides only a small contribution (below 2%) to the total heat produced by ironing the top surface of the work-piece. The torque developed during the process is drastically reduced as the surface over which the shear forces are applied during each rotation is formed by the only probe surface. However, a careful design is required for the tool when welding materials with high thermal conductivity, owing to the forces that the probe has to withstand, as it will be seen in Chapter 4.

In aluminium alloys, the microstructural zones formed after the process are the same as previously presented in the case of conventional FSW (Figure 2.3). In spite of the fact that the same areas are formed, at first, the differences can be noticed in the SZ, with the absence of the enlargement on the crown side of the weld. The lack of shoulder rotation and respective heat generation leads to a homogeneous distribution of the microstructure through the SZ thickness in terms of both the grain size and the crystallographic orientation [64].

Figure 2.3 Example of SSFSW cross-section with different weld zones

TMAZ and HAZ have a smaller sizes in comparison to the FSW owing to the reduced thermal field and power dissipation [65]. In case of the overlap joints, the reduced vertical material transportation experienced in SSFSW is beneficial to create smaller hook-angles and lengths [66]. In case of dissimilar welds, the lower heat reduces the diffusion in the SZ between the two alloys [67]. The hardness distribution is similar through the thickness of both high- and low-strength aluminium alloys, showing that the precipitates' distribution is homogenized [68-70].

One of the most interesting features of SSFSW is the extremely smooth surface on the crown side of the weld. The absence of the rotational marks on the surface leads to much smaller roughness measurements with respect to the FSW and, in the same order of magnitude, as the base materials. Not only is the roughness reduced but the sliding shoulder also simplifies the control of the undercut- and thickness-reduction of the joints. The mechanical properties of the joints obtained by

SSFSW show a general trend of improvement in both the yield strength and the UTS owing to the reduced size of the HAZ as well as a better strain distribution [67, 71]. The more concentrated thermal field in SSFSW causes both a reduction of tensile residual stresses in the SZ and a narrowing of the area subjected to these stresses [72, 73].

2.3. Design of the Fuselage Skin–stringer Structures

In order to guarantee the lowest weight configurations with adequate strength to support all the operational loads with high reliability, the aircraft structures are deeply optimized. The main components of aircraft structures are the fuselage, wings, and landing gears. These can be divided into different groups according to their repercussions on aircraft safety, usually as primary, secondary, and tertiary structures. Although the definition of each division is performed by each aircraft manufacturer, the FAA Advisory Circular 25.1529-1A defines the primary structures as a ‘structure that significantly contributes to the carrying of flight, ground, or pressure loads’ [74].

The largest structure in an aircraft is the fuselage which is mainly formed by primary parts and, as such, it is a structure which has the most demanding design requirements. On a simplified model, the fuselage can be seen as a beam pinned over the wings and subjected to different load conditions, depending on the different phases of a mission (i.e., taxiing, climb, flight, etc.). During flight, the loads mainly cause tension stress in the upper parts of the fuselage, shear stress at the sides, and compression stress at the bottom. These stress conditions are promoted by cabin pressurization and by the fuselage bending. During aircraft taxiing, the top and bottom stresses are inverted—but with lower amplitude due to the absence of pressurization. In modern aircrafts, the fuselage is usually defined as a semi-monocoque construction, which is formed mainly by an external skin as well as longitudinal and circumferential stiffeners [75-77].

The circumferential elements are divided into frames and bulkheads depending on whether they carry or do not carry concentrated forces. Frames are lighter structures that are needed to maintain the fuselage shape and prevent the instability of stringers. Bulkheads are positioned in areas where highly concentrated loads are applied, such as wings, rudders, stabilizers, and landing gears, and they help to redistribute these loads on the skin. The longitudinal elements are called longerons and stringers, with the main function of carrying the bending moment applied to the fuselage and stabilizing the external skin. Owing to the bending moments, these elements are mostly subjected to axial loading. Finally, the fuselage skin involves working as a membrane and carries loads that are brought about by cabin pressurization and external torsional or transverse forces. In this study, the focus is on the skin–stringer structural detail of the fuselage, as shown in Figure 2.4.

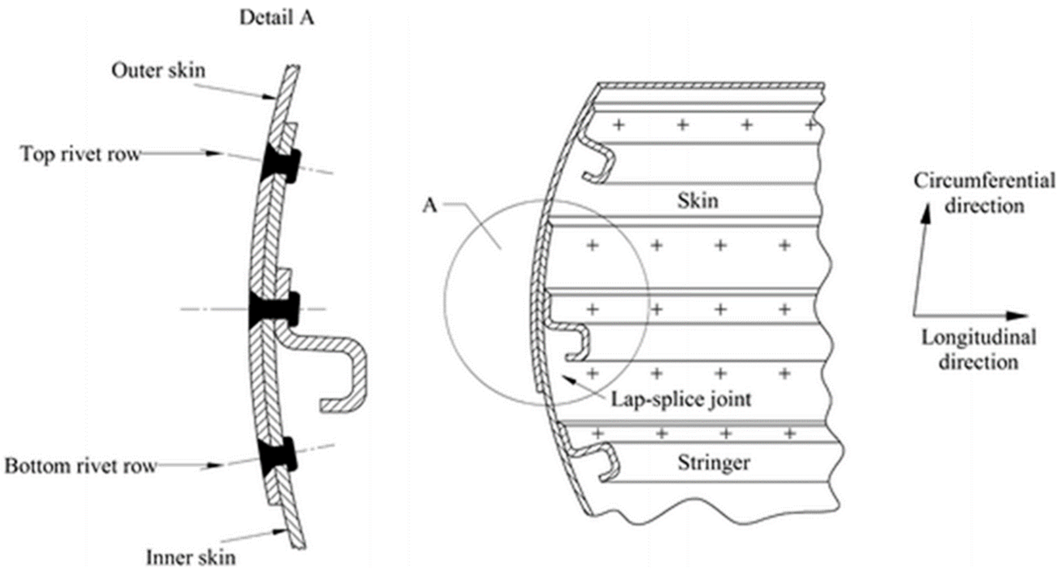

Figure 2.4. Example of riveted skin–stringer configuration [78]

The skin–stringer panels are designed based on the function of their position in the aircraft, according to the different load conditions. In order to optimize the structure, different materials with dissimilar strength, cross–sections, and stringers spacing are tailored to specific requirements.

2.3.1. Damage-tolerance Design Approach

Historically, there are three different approaches for ensuring the safety of primary aircraft structures [79]. These can be briefly be summarized as follows:

- **Safe-life Design**: This design was the first used in the aeronautical field and is still applied to the military environment, where the calculation of the costs is different from the case of civil industries. The components designed with this approach are replaced after a certain amount of time, calculated in terms of ground-air-ground (GAG) cycles or flight hours. The safe-life is obtained from fatigue tests that simulate the operational condition of the component. These parts are designed in a conservative way with particularly high safety factors. Once a component has reached the limit of its safe-life, it is replaced without checking for the presence of cracks. In this approach, the presence of defects owing to the manufacturing or the assembly processes of the components that could lead to a drastic reduction of their operative life are not considered.
- **Fail-safe Design**: In this philosophy, a structure can sustain a certain amount of damage without the risk of catastrophic failure. The two main approaches are based on adding redundant load-path elements or crack stoppers which increase the residual strength of the structure and stop or delay the propagation of a crack before critical crack size is reached. The risk of substituting parts that are still operative is reduced and the aircraft remains airworthy until the damage is detected and repaired. It is important to define proper inspection intervals in order to detect any particular defect in the structure. These intervals are established by considering the service experience of the structure and not the period of initiation and growth of the cracks.

- **Damage-tolerance Design**: In this approach, it is assumed that the presence of initial flaws or defects in the structure will grow and propagate under operative loads. The key point involves detecting the cracks in the structure before they start the phase of unstable propagation, which could bring it to the failure. Fracture mechanics is the instrument that the damage tolerance approach is using for the evaluation of crack growth and the residual strength characteristic of the structure for the definition of inspection intervals. The investigation of crack propagation is performed in order to establish the time necessary for the crack to reach the critical size, which depends on the residual strength of the different structural elements (Figure 2.5).

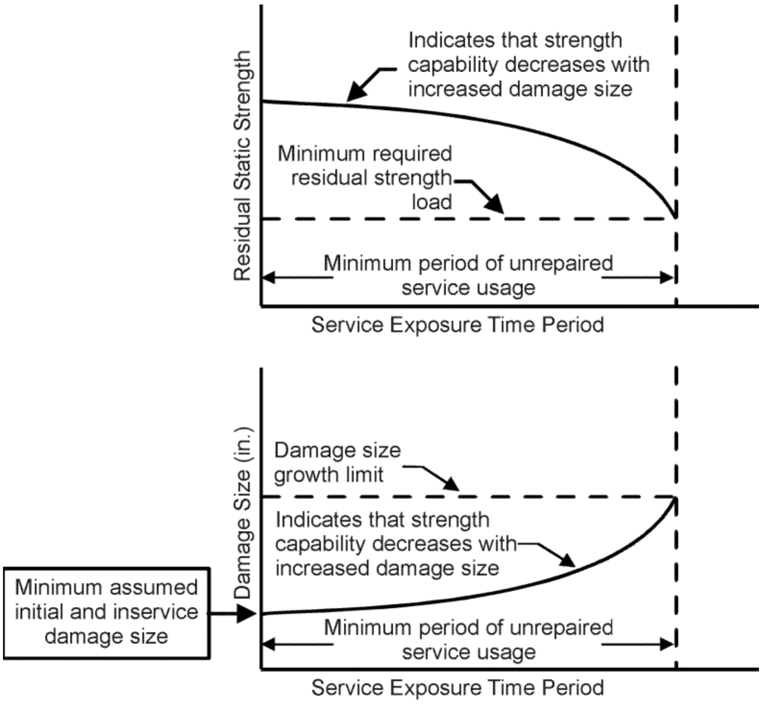

Figure 2.5. Schematic of the damage-tolerance guidelines [80]

From this overview, it is clear that the three pillars on which the damage-tolerance design is based are slow-crack growth, residual strength, and inspection intervals. This last pillar is of industrial interest and depends on the damage location and the accessibility of the area. The first two pillars are investigated in the current research and fracture mechanics is the tool used to analyse them.

2.3.1.1. Basic Concepts of Fracture Mechanics

Many books, such as Broek and Anderson [81, 82], present fracture-mechanics theories in a very detailed way, describing the two main fields of investigation, the linear–elastic fracture mechanics (LEFM), and the elasto–plastic fracture mechanics (EPFM). The EPFM theory is used when the plastic zone at the crack tip is sufficiently large in comparison to the crack length or the geometrical dimension of the structure. Therefore, the stress-intensity factor (SIF) cannot be used to characterize the stress field at the crack-tip [83, 84]. In this study, the main focus is on the LEFM and so a few basic concepts are introduced.

The two general approaches to the linear elastic fracture mechanics (LEFM) are based on the energy balance and on the singular nature of stress distribution at the crack tip. Sharp discontinuities in the materials cause an amplification of the stress field at their tip. In 1957, Irwin [85], using the equations developed by Westergaard [86], settled a series of linear elastic stress field solutions for the problem of a crack present in a wide plate. The three different modes of opening for a crack and the components of the stress field at its tip are shown in Figure 2.6.

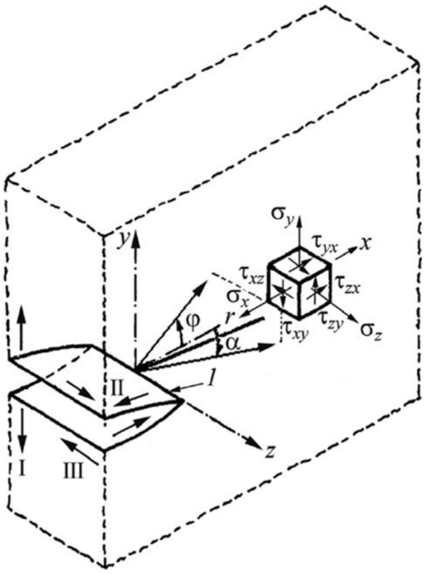

Figure 2.6. Crack opening modes and stress field components [87]

The recurring parameter in Irwin's stress field equation, necessary to describe the intensity of stress singularity at the crack tip, is the SIF, which, in the case of the Mode I opening, is defined as follows:

$$K_I = \beta\sigma\sqrt{\pi a}, \tag{2.1}$$

where σ is the uniform stress applied at the infinite and normal to the crack plane, a is the half length of the through thickness crack, and β is a non-dimensional factor that can be a function of the crack length itself as well as other geometrical features. For linear elastic materials, Irwin was able to correlate the SIF with the elastic energy release rate (G_I) [88] by using the elastic crack-tip solution and the energy theory of Griffith [89].

The importance of the SIF for structural analysis is determined by its unique capability to describe the stress field in the crack-tip region once the influence of external variables, such as loading conditions and the geometry of the cracked body, are known. In contrast with stress that depends on coordinate variables, the SIF remains the same for different types of cracks and shaped bodies. For these reasons, the SIF can be used to determine the strength of the cracked structures that are subjected to both the monotonic and fatigue loads.

2.3.1.2. Slow-crack Growth under Fatigue Loads

Crack growth is a result of cyclic stress owing mission loads, such as gusts and manoeuvres as well as fuselage pressurization. The most common crack growth mechanism is fatigue crack growth and although it is difficult to prevent, it can be controlled. The life of a structure subjected to fatigue loads can usually be divided into two main phases: crack initiation and the FCG. For conventional riveted skin–stringer joints, the initial damage develops from riveted holes. Depending on the analysis performed, the crack can initiate only on the skin or on both members at the same rivet location [80]. Since in the damage-tolerance design initial crack is assumed to exist in a critical location, the analysis of the FCG behaviour becomes fundamental.

In order to predict the crack growth behaviour of a structure, the SIF has to be described as a function of the crack size. In a skin–stringer panel, the initial crack (2a) can be positioned either under a severed stringer or at the centre of a bay, in between two intact stringers [90]. The simplest way to represent the FCG data is by plotting the crack size as a function of the number of cycles. Under constant-amplitude fatigue loading, the stress history can be converted into an SIF history, with the stress history changing cycle-by-cycle with the increasing crack length. Once the SIF as a function of the half-crack length (a) and the (a) vs. N curve are known, it is possible to describe the fatigue crack-growth rate (FCGR) as a function of the SIF variations (Eq. (2.2)).

$$\frac{da}{dN} = f(\Delta K, R) \tag{2.2}$$

In this equation, $\Delta K = K_{max} - K_{min}$, $R = K_{min}/K_{max}$, and K is defined as in Eq. (2.1) at the maximum and minimum stresses, respectively.

For metallic materials, the Eq. (2.2) shows a sigmoidal shape when plotted on a double-logarithmic scale, as shown in Figure 2.7. Three distinguished regions can be observed depending on the values of the SIF range. For a low ΔK (threshold region), the curve tends to converge on a vertical asymptote, indicating that there is no crack propagation when $\Delta K < \Delta K_{th}$. On the opposite side, the stable-tearing crack growth region can be identified, where the FCGR is high. The vertical asymptote in this area is represented by the fracture toughness of the specimen. When $K_{max} > K_c$, the crack propagation becomes unstable, thus leading to the final failure.

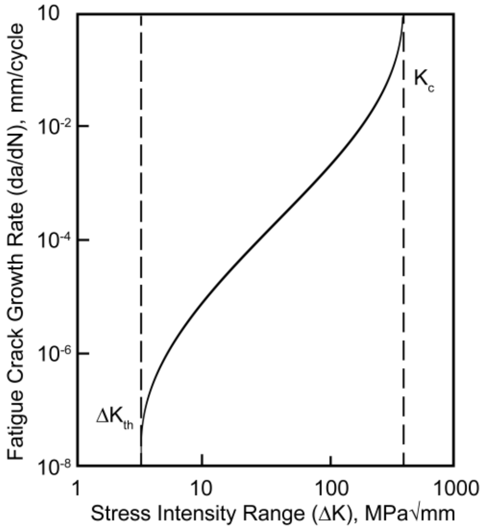

Figure 2.7. Example of FCGR behaviour in metals [80]

The central part of the graph corresponds to stable macroscopic crack growth, which covers a significant portion of fatigue life, particularly for thin-sheet materials with stress concentrators, such as rivet holes. This region is where the most of the structural research was focused and many equations were developed to describe the FCGR [91].

The correlation between the SIF range and the FCGR was further developed by Elber [92]. He observed that the plastic deformations occurring at the crack tip remain as the crack propagates; so, that the crack surfaces open and closes at non-zero load levels. Therefore, when a specimen is cyclically loaded, the crack surfaces are in contact for a value of SIF, which is higher than the one corresponding to the minimum load. The portion of the cycle below this value (K_{op}) does not contribute to crack propagation, leading to the definition of the effective SIF range as $\Delta K_{eff} = K_{max} - K_{op}$. This crack closure phenomenon explains the influence of the stress ratio on the FCGR and it is particularly interesting in the case of variable-amplitude loading in order to account for the effects of overloads on crack propagation.

2.3.1.3. Residual Strength of Cracked Panels

In a damage-tolerant design context, once the crack propagation behaviour is established and the inspection intervals are defined, the last part of the analysis has to be focused on the residual strength of the structure. The residual strength of a cracked structure is defined as its load-carrying capacity, and it is depending on the crack configuration and the fracture-toughness of materials [80].

For thin-metal sheets, where the crack extends by the tearing mode of the fracture, the estimation of the residual strength capability is based on the crack-resistance curve. In this case, unstable failure occurs when the applied SIF (K), the crack driving force, reaches or exceeds the material's fracture resistance (K_R) and $\partial K/\partial a \geq \partial K_R/\partial a$. According to these descriptions of the plane stress fracture toughness (K_c) are represented by the tangency point between the two curves $K(a)$ and $K_R(a)$ [81].

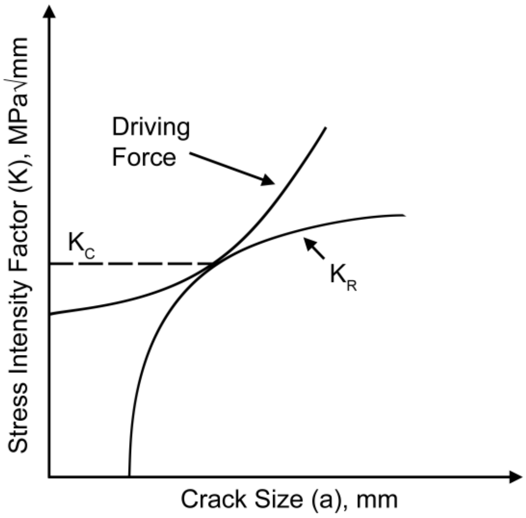

Figure 2.8. Schematic K-R curve; K_c occurs at the point of tangency between the driving force and the R-curve

In built-up structures, such as stiffened skin–stringer panels, strength analysis can become complicated due to the complex geometrical construction of the components. In general, prediction techniques are based on the critical value of the stress-intensity factor for a given geometry and loading. This means that the residual strength of single elements, i.e., just skin, has to be calculated and then the interaction between them have to be considered. For example, if you considered a two-stringer panel with a central crack, the geometric factor (β) varies once the skin crack approaches the stringer and the load redistribution has to be evaluated to determine the residual strength.

Owing to complexity behind the development of reliable residual strength models for the complex structure, it is a common practice in the aerospace industry to evaluate the behaviour of stiffened panels under a monotonic load once the fatigue crack reaches a length of two bays. In fact, the Federal Aviation Administration (FAA), through The Federal Aviation Requirements (FAR 25.571), established that the fuselage structure should be able to withstand sufficient static loads with a crack extended over the two stringer bays in order to fulfil the Large Damage Capability (LDC).

3. Experimental Procedure and Materials

In this chapter, after introducing the materials used in this work, a concise overview of the welding procedure, including the equipment and clamping used for the production of the specimens and components, is given. In the last part, the characterization methods, used to investigate the different properties of the joints, are described.

3.1. Base Materials

The base materials used in this study are two typical aluminium alloys that are employed in the fuselage structure of a modern aircraft and were proposed by EMBRAER as part of a partnership in the LISA project (Light Integrate Structure for future generation Aircraft). The two materials are representative for the skin and the stringers of an airplane, with the distinctive properties necessary to guarantee its structural integrity and damage tolerance.

3.1.1. Skin material: AA2024-T3

The material chosen to represent the skin of an aircraft are Al-Cu AA 2024-T3 sheets with 2-mm thickness. This material combines moderate yield strength with excellent fatigue crack growth-resistance and good fracture-toughness [93]. The sheets of this alloy were obtained by rolling and the temper used was T3, i.e., solution heat-treated, cold-worked, and naturally-aged to a substantially stable condition. The mechanical properties and chemical composition of this material are listed in the Table 3.1 and Table 3.2.

Table 3.1. Mechanical properties of AA 2024-T3 used in this study

Hardness (HV0.2)	Yield Strength (MPa)	Tensile Strength (MPa)	Elongation (%)
134	313,8 ± 1.3	465.4 ± 2.2	21.3 ± 0.3

Table 3.2. Chemical composition of the AA 2024 used in this study in weight % – obtained by optical emission spectrometry

Cu	Zn	Mg	Mn	Fe	Si	Cr	Zr	Ti	Al
4.4	-	1.5	0.6	≤0.5	≤0.5	0.1	-	0.15	Remainder

3.1.2. Stringer Material: AA7050-T7651

The material used for the stringers in this study was suggested to be the Al-Zn alloy AA7050-T7651. The Z-shape stringers used to produce the welds were realised as extrusion profiles of 3.6 meters from Alcoa. In order to achieve the T7651 temper, the stringer was solution heat-treated, stress-relieved by stretching up to a controlled amount, and then artificially over aged in order to achieve good exfoliation corrosion resistance. The cross-section of stringers with the respective nomenclature and all the dimensions are shown in Figure 3.1. The foot of the stringer was removed by milling before welding since there was no necessity of it due to the absence of the riveting overlap joint.

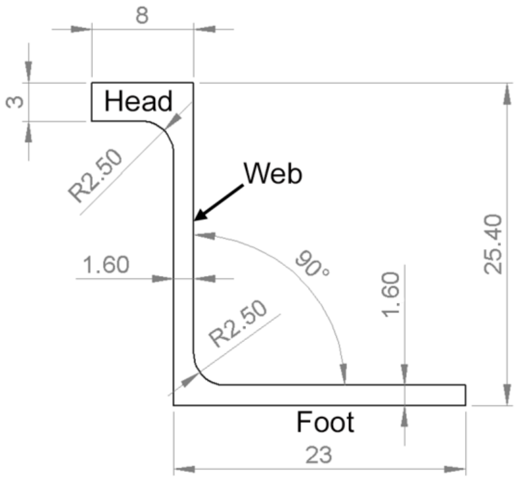

Figure 3.1. Schematic drawing of the extruded Z-stringer

This material is normally chosen in the aircraft industry due to its high strength, combined with a good level of toughness. The mechanical properties and the chemical composition of the stringers used in this study are reported in Table 3.3 and Table 3.4.

Table 3.3. Mechanical properties of AA 7050-T7651 used in this study

Hardness (HV0.2)	Yield Strength (MPa)	Tensile Strength (MPa)	Elongation (%)
158	488,8 ± 2.4	532.9 ± 2.0	8.6 ± 1.2

Table 3.4. Chemical composition of the AA 7050 used in this study in weight percent—obtained by optical emission spectrometry

Cu	Zn	Mg	Mn	Fe	Si	Cr	Zr	Ti	Al
2.3	6.2	2.25	-	≤0.15	≤0.12	-	0.1	-	Remainder

3.2. Welding Procedure

3.2.1. Joint Configurations

While the same welding process was used for the entirety of this work, two different joint configurations were investigated (Figure 3.2).

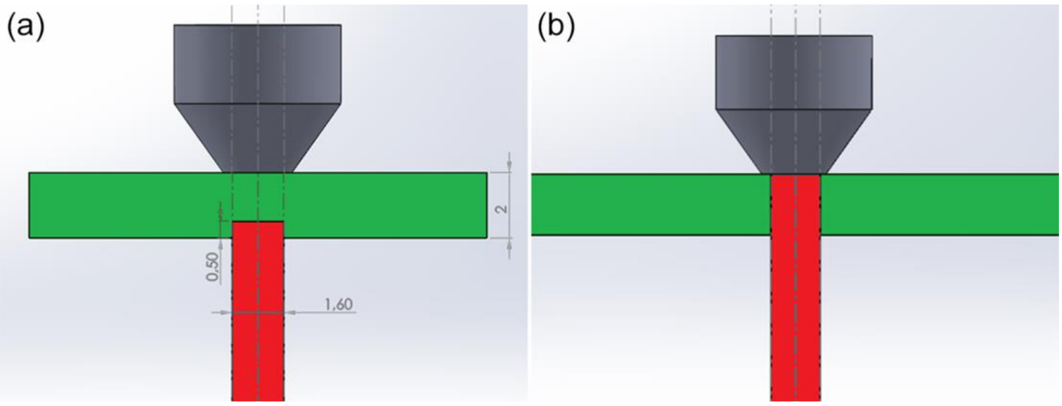

Figure 3.2. Schematic representation of the two joint configurations: (a) Notch Skin and (b) 3-Parts

The configuration shown in Figure 3.2a, which will be called notch-skin from now on, was realized by milling a groove in the skin sheet of width and depth equal to 1.6 and 0.5 mm, respectively, where the stringer could be accommodated. Two different variants of this configuration were analysed, namely single pass (SP) and double pass (DP). The difference between the two consists of the number of welds realized on the single skin–stringer joint. In the SP variant, the connection between the two components was realized in a single run, with the probe centred in the centreline of the stringer web. On the other hand, the DP variant was realized by two consecutive runs—each of them was displaced by 0.8 mm from the centreline of the stringer web.

The second configuration analysed, Figure 3.2b, was realized by joining two sheets of the skin-material and the milled stringer in one single step. This welding variant will be called the 3-Parts joint in this study since three different components are joined together in one single run.

3.2.2. Welding Equipment

In this study, a procedure was developed to join the primary structures of the aircraft fuselages by SSFSW. Skins and stringers, produced by different aluminium alloys and technologies, were welded in T-joint configurations in different scales from a specimen size up to real components. The skin–stringer welds by SSFSW were realized in the Tricept T9000 robot built on a gantry system by Loxin, Pamplona, Spain (Figure 3.3). The T9000 is controlled by a Siemens 840D controller and includes an option that confers extra accuracy and stiffness to the module.

Figure 3.3. Gantry Tricept T9000 welding machine for FSW

The main component of the T9000, as shown in Figure 3.3, consists of moveable gantry (1), the working table (6), the Siemens 840D controller (7), which included the Direct Measuring System (DMS) and the moveable tricept module (in red). The tricept main components are the three linear actuators (2), the sliding tube (3), and the wrist (4), and it has 5 degrees of freedom with a repeatability of less than 10 µm and an accuracy of 50 µm. While this robot concept is generally in use for machining big parts in the railway and aircraft vehicle industry, the spindle (5) mounted on the T9000 was custom-built by Mühlbauer, Roding, Germany, in order to satisfy the increasingly requested performances necessary for the FSW-based processes. In this study, all the welds were performed in position control and process parameters like torque, axial force, and radial force were recorded.

The probes used to realize the welds by SSFSW were made of MP159, a Nickel–Cobalt-based multiphase alloy. The probe tip was conical with three flat surfaces, with an inclination of 36º (Triflat) to facilitate the stirring of material by creating a speed gradient and no threads. The diameter tapered from 5 mm to 2.8 mm over a length of 2.2 mm (30º of the taper angle). The shoulder material was Uddeholm Unimax (Uddeholm), a chromium-molybdenum-vanadium alloyed tool steel. The shoulder hole was nominally 5.1 mm and had a flat area of 8 mm in diameter around the hole. The lower surface of the shoulder was coated with the commercially available ASOT 3031 (Albrecht–Schumacher) in order to reduce the friction coefficient and guarantee a better surface finish of the weld. A schematic view of the two main tool components is shown in Figure 3.4.

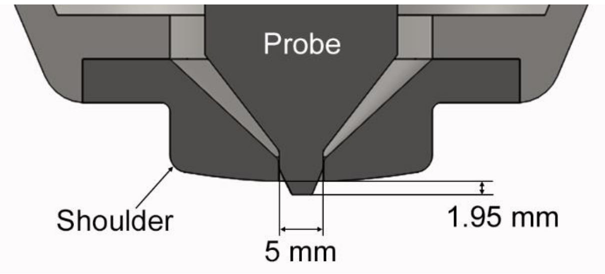

Figure 3.4. Schematic view of the used tool

A detailed description of the design procedure of the new tool and the improvement of the process' robustness connected with it is presented in Chapter 4.

On the working table, a specifically designed clamping system was fixed, aligning it with the welding longitudinal axis of the machine's gantry. The clamping system was produced in collaboration with Witte (Witte Barskamp KG) and allows the clamping of the stringer between the two vacuum tables that generates the forces for the vertical fixing of the skin. The horizontal movement of half of the clamping table is performed by using a pneumatic actuator to facilitate the positioning of the stringer. In case of the 3-Parts joints, extra clamping forces are necessary on the lateral side of the skin-sheets in order to avoid the opening of the joint during the welding procedure.

3.2.3. Welding Parameters

In this study, the influence of the two main welding parameters, the welding speed and the rotational speed, were investigated for the three joint configurations. The parameters used in this work are summarized in Table 3.5. All the welds were realized in position control with a fixed probe length of 1.95 mm and a tilt angle of 2º. The welding head automatically found the vertical position of the work pieces when a force in the Z-direction, equal to 300 N, was measured. At this point, the probe started to rotate and plunged into the joints until it reached a depth of 2.1 mm. The limits of the parameter window were defined on blind welds that were 2 mm-thick AA 2024-T3 in order to avoid the formation of defects in the weld and, at the same time, to prevent tool failure. At a rotation speed equal to 1500 RPM, all the attempted welds presented tunnel defects in the AS owing to a reduction in the friction coefficient and the impossibility of transporting the material completely around the probe. A similar defect occurred when the welding speed was increased over 600 mm/min—in this case, it was a result of low temperature and reduced plasticization of the material.

Table 3.5. Overview of the welding parameters used in this study

Process Parameter Window					
Welding Speed (mm/min)			**Rotational Speed (RPM)**		
180	300	420	800	1000	1200

In order to have a correct centring of the SZ with respect to the stringer, the preliminary welds were conducted at the beginning and the end of the clamping system, and a correction was applied to the welding program in order to account for misalignments. In general, a 0.15mm correction towards the RS of the joint was necessary owing to the asymmetric material flow around the probe that causes a displacement of the SZ centre in the opposite direction.

In order to correlate the process parameters with the microstructure, joint formation, and mechanical properties of the joints, a full factorial design study was used for both the variants of the notch-skin configuration. Two levels were chosen for the welding speed (300 and 420 mm/min) and three levels were chosen for the rotational speed (800–1200 RPM), with three replicates for each combination. An extra combination of parameters, WS=180 mm/min and RS=1200 RPM, was used as a baseline as it was proved in a previous study to guarantee the highest mechanical properties when the same two alloys were welded in a butt-joint configuration [67]. For the 3-Parts joint configuration, a reduced study was applied and some values over the parameter window were chosen to cover different welding conditions. The combinations of WS/RPM are as follows: 300/800, 420/1000, 180/1200, and 420/1200.

3.3. Thermal Cycle Analysis

To correlate the process parameters and the measured forces with the temperature reached during welding and microstructural properties, the thermal cycle was monitored at different characteristic positions. For this, K-type thermocouples were embedded in the skin, both in the AS and RS at mid-thickness and at distances of 15 mm from the centre of the weld.

3.4. Metallographic Analysis

The samples used for microstructural analysis was extracted from the same welds produced for mechanical testing and an example of the cutting plan for these welds is shown in Figure 3.5. To obtain cross-sections for metallographic analysis, the samples were cut by diamond-abrasive wheels and embedded in a cold-mounting resin. The embedded samples were prepared by standard metallographic specimen preparation procedures by using flat grinding and finish polishing. For microstructural analysis using polarized light microscopy, the samples were anodized using a 3 volume-percent solution of HBF4, known as BARKER solution, at 24 V for 3 minutes. The grain size was measured following the ASTM standard E112-13.

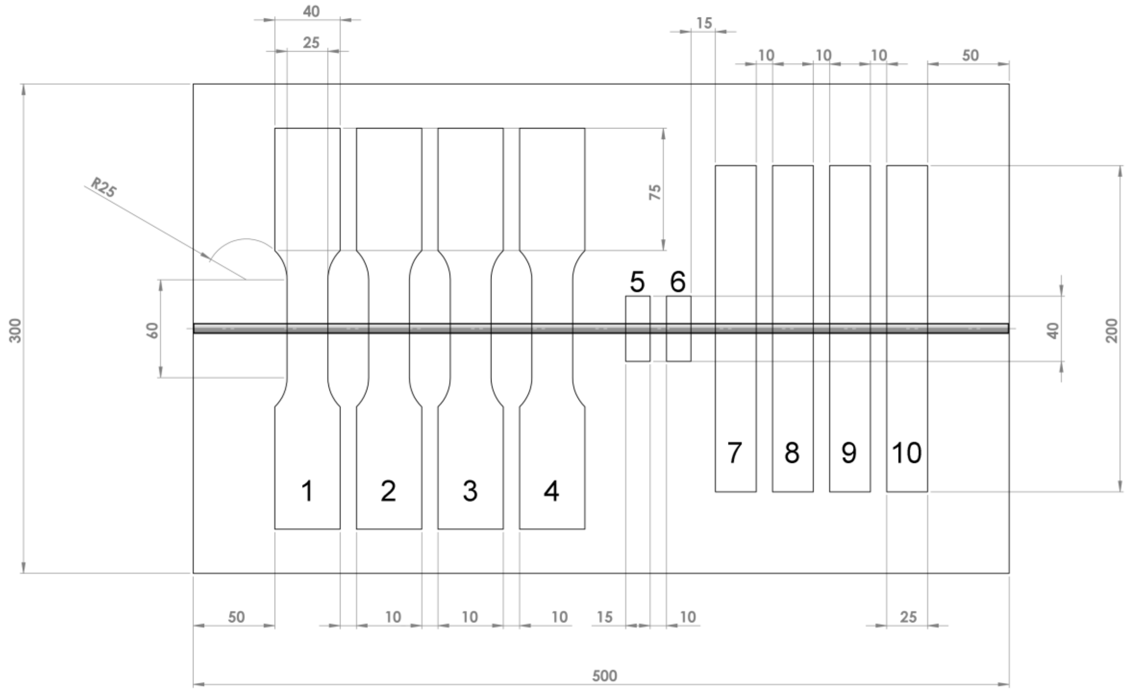

Figure 3.5. Example of cutting plan for the produced welds; specimen 1-4: hoop tests; 5-6: metallography and hardness; 7-10: pull-out

Optical microscopy observations were conducted using a Leica DM IRM optical light microscope (Leica Microsystems GmbH). To characterize the various features of welded microstructures and to analyse the fracture surfaces, a SEM (QuantaTM 650 FEG, FEI Company) was used. Samples for SEM analysis were not etched or mounted in resin.

3.5. Mechanical Testing at Coupon Level

In this work, initial mechanical testing was performed on specimens at the coupon level in terms of microhardness and tensile tests in different directions for all the process parameters and configurations. The size of the welded plates and the position of the different samples can be observed in Figure 3.5. A distance of 50 mm was left from the edges of the plates in order to guarantee that the process is in a steady state according to the standard ISO 25239. The welded coupons were tested after a post-weld natural aging process of at least 30 days with no further heat or surface treatment [47, 94].

3.5.1. Microhardness Test

Vickers hardness was measured on the samples to investigate the local mechanical properties. The analysis was performed according to the standard ASTM E384-10 by using Zwick Roell Indentec ZHV 2 hardness-testing equipment. Indentation lines were positioned horizontally and vertically at half of the skin and stringer thickness, respectively. A distance of 400 µm was kept between the indentations and a load of 0.2 kgf and a dwell time of 10 seconds were applied.

3.5.2. Pull-out and Hoop-strength Tests

The dimensions of the pull-out specimens and the test set-up were decided in agreement with EMBRAER. A schematic representation of the test arrangement is shown in Figure 3.6.

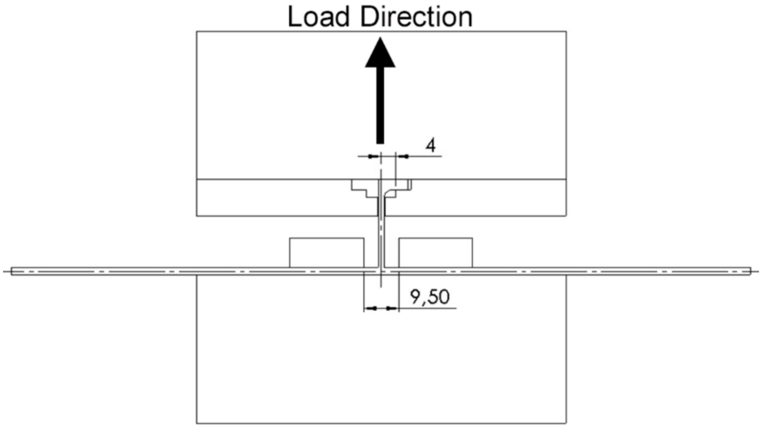

Figure 3.6. Schematic representation of the pull-out test setup

The hoop-strength specimens were machined by EDM in a way that the skin would have a dog-bone shape, with a 60-mm gauge length and a width of 25 mm according to the standard ASTM E8-09. The displacement was measured with an MTS extensometer of initial length equal to 50 mm. Both of these tests were performed using a universal testing machine (Zwick/Roell type 1478) in the displacement control at a speed of 1 mm/min. The technical drawings of the specimens can be seen in Appendix A.

3.5.3. Strain Analysis by Digital Image Correlation

Strain analysis was performed by measuring the displacement and strain via optical metrology during hoop and pull-out testing. A DIC system (ARAMIS 4M V6.3, by GOM), consisting of a 2 CCD cameras with 50 mm of focal length, was used for the 3D analysis of the specimen surface in different loading states. The surfaces of the welded coupons were spray painted in two different stages. A white layer of paint was deposited to avoid reflection, followed by a stochastic black pattern, to create a random grey intensity distribution. A mesh of facets is applied on the surface and each facet, with a specific grey value, could be recognised during the test while the specimen’s surface deforms. The DIC system records the deformation of the facets during test computing the changes in the shape and the motion of each centre point by comparing the images in different states. A sensor connected with the computer is used as a control unit for the system and as an analogue to the digital converter to obtain the load level at each stage acquisition directly from the testing machine. In this study, each facet had a size of 15 × 15 pixels and a distance between the facets of 13 pixels. The cameras were positioned at a distance of 150mm from each other, with an angle (counter clockwise) of 25º in respect to the longitudinal axis of the lenses. The distance between the two cameras and the measured object was equal to 320mm. These computational and hardware setups lead to a point resolution for strain measurements of 450µm.

3.6. Fatigue Tests of Sub-components

The fatigue analysis at sub-component scale was performed for the set of parameters and joint configurations that lead to the highest mechanical properties. Two different load cases were applied to the specimens, hoop and longitudinal direction, simulating the two stress directions brought about by cabin pressurization.

The sub-components were designed according to [95], where the specimens used by AIRBUS to test the fatigue life of the laser welded skin-stringer connections were presented. All the tests were performed on a Schenck servo-hydraulic fatigue machine with a 63-kN load cell. Three specimens for each of the six load levels were tested at a stress ration R = 0.1 after applying a sinusoidal wave form, with a frequency of 20 Hz. All the specimens were tested in an as-welded condition in order to account for the surface-finish produced by the SSFSW process.

In hoop-direction tests, four specimens were extracted by a milling procedure out of a 1-m long weld for each joint configuration analysed. In order to guarantee the results of the tests were independent from the quality of a single welding procedure, whenever possible, not more than one specimen for each weld has been tested at the same load level. A schematic view of the sub-component and the assembly procedure is shown in Figure 3.7.

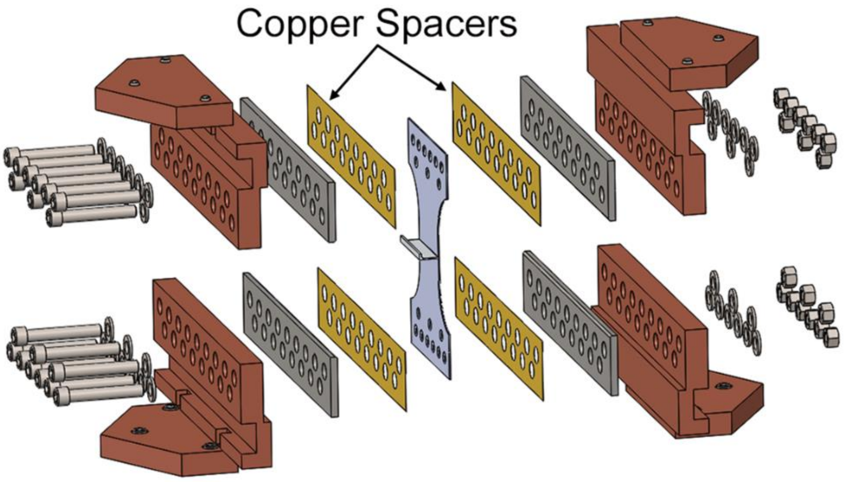

Figure 3.7. Test setup for fatigue tests in the hoop direction

Copper spacers and a reduced torque of 100 Nm for each M14 (12.9) screw were used to avoid the indentations of the specimens in the grip area that would cause premature failure.

In the longitudinal direction tests, each specimen was extracted by milling from a 600-mm long weld. A special clamping system was designed to transfer the load not only in the skin but also in the stringer as well. Pure aluminium spacers were inserted between the clamping device and the stringer in order to avoid scratches and indentations on it. The section of the stringer was reduced with a large radius (250mm) to drive failure away from the clamping area, which was critical due to the high-stress concentration sensitivity of the AA 7050 (see Figure 3.8).

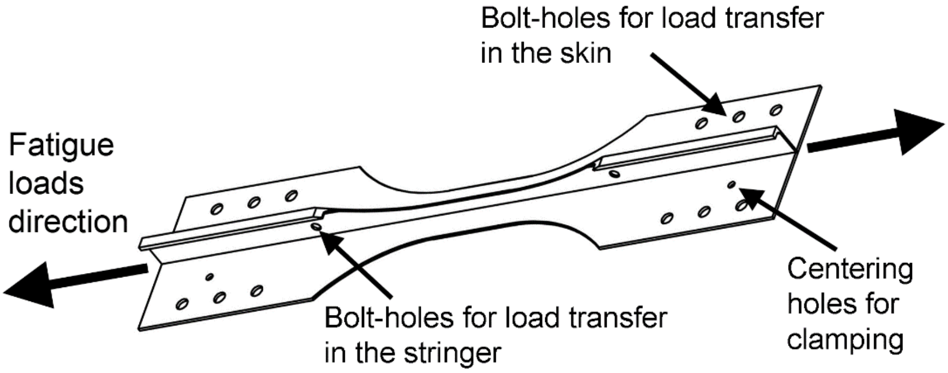

Figure 3.8. Schematic view of the longitudinal fatigue specimens with the clamping system load transfer

The detailed design of the specimens for both the test directions are reported in Appendix A. The description of the statistical analysis used in this study to characterize the fatigue life of the sub-components obtained with different joint configuration is presented in Section 7.1 prior to the results.

3.7. Fatigue Crack Propagation and Residual Strength of Panels

Five stringer panels with a pitch of 195.25mm and 2m length were welded using the joint configuration chosen according to the results of the fatigue tests (see section 3.6). The specifications and the specimen design for these tests were agreed with EMBRAER in order to have a direct comparison with a similar analysis performed by them for the riveted joints. The central stringers were severed in order to insert the initial notch with a half-crack length equal to 6 mm (both sides equal to 12 mm).

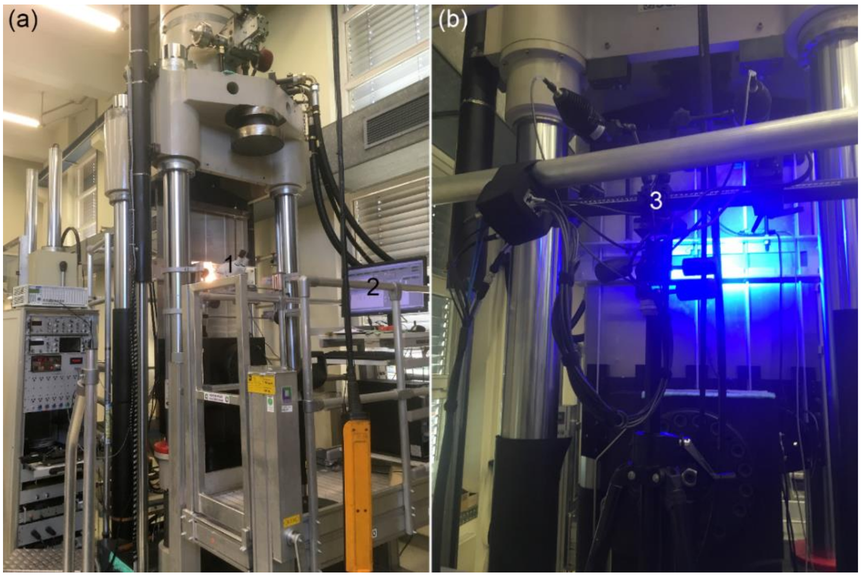

Figure 3.9. Test setup for FCG and residual strength testing with (a) front of the specimen with the measuring devices and (b) back of the specimen with the ARAMIS system.

A Schenck servo-hydraulic fatigue-testing machine with a 250-ton load cell, was used for testing at a constant load amplitude by using a 1-Hz sinusoidal wave form and an R-ratio of 0.1. Two anti-buckling devices were designed and applied to both sides of the panels in order to reduce the out-of-plane displacement. The front of the test set-up can be seen in Figure 3.9a, where the crack length was measured with a microscope moveable parallel to the specimen surface (1). The outside panel surface was polished along the width, where the crack is expected to grow, facilitating the detection and measurement of fatigue cracks. The measurements of COD, potential and crack length were recorded and stored in the computer (2) together with the respective number of cycles.

In Figure 3.9b, the back of the test set-up is shown where the DIC analysis was performed by means of the two cameras and lights (3) mounted over a scaffolding. In the residual strength tests, crack propagation was performed with the same parameters as before until the length of the two bays was reached. The panels with the two-bays crack were successively monotonically loaded until the final failure was reached.

3.7.1. Application of DIC during FCG Experiments

During the tests, the DIC system (ARAMIS 6M V8) was directly connected to the servo-hydraulic machine through an analogical input in order to automatically trigger the system once a load of 178 kN was reached. One image was acquired every 100 cycles and one extra image was taken under static conditions when the crack-length was measured at the maximum load. The two lenses had a focus length of 75 mm, which allowed the capture of a maximum surface of 135 × 110 mm at a measuring distance of 930 mm and a camera distance of 380 mm.

4. Development of a New Tool System for SSFSW

A SSFSW tool undergoes more severe operational conditions in comparison to the one used in conventional FSW. Owing to the uncoupling between the probe and the shoulder as well as the reduced heat generated during the process, the forces and moments applied to the probe are higher, as shown by Barbini et al. [67]. The beginning of the transverse movement after initial plunging, when peaks in the welding force and torque were observed during the experiments, is particularly critical for probe lifetime. The tool system, previously used (Figure 4.1), presented several failures in this initial phase and a very limited operational life. The ending part of the tool system consisted of a probe holder—the probe itself and a shoulder with a space where a supporting rotational bearing was inserted.

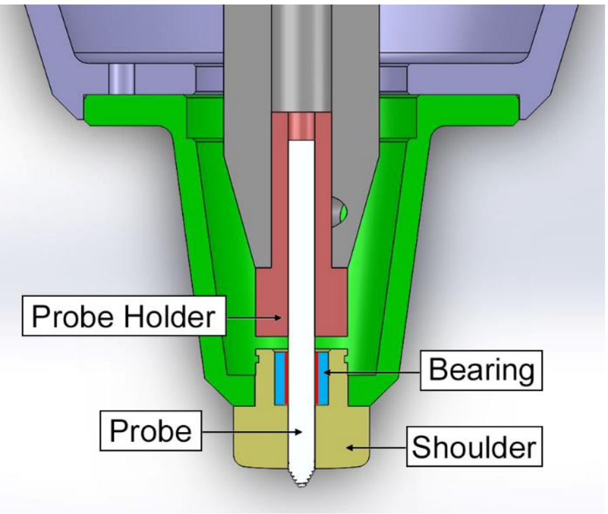

Figure 4.1. Schematic drawing of the previous SSFSW tool system

In order to understand the reason for the unreliable behaviour of the system, a systematic FEM analysis of the most critical area was performed; this encompassed the shoulder top part and the probe ending, where all the failures occurred. The material properties of the probe and the shoulder a at high temperature (500ºC), which were used for the simulation, were obtained from previous investigation conducted by Hilgert [96] and are summarized in Table 4.1.

Table 4.1. Properties of the probe and the shoulder’s materials at 500°C [96]

Material	Yield Strength (MPa)	Young Modulus (GPa)
Probe - MP159	1561 ± 0.3 %	205 ± 0.8 %
Shoulder - Hotvar	1249 ± 0.9 %	166 ± 0.1 %

All the components were modelled as perfectly elastic since the term of comparison from the base materials was the yield strength and a permanent plastic deformation in the probe or the shoulder are to be absolutely avoided. The load system applied to the tool consisted of two concentrated forces, parallel and perpendicular to the probe axis, of 3.5 kN and 2 kN, respectively, and a torque of 5 Nmm. In order to be more conservative in the calculation, all the forces and moments measured during the process were directly applied to the probe surface that plunges into the material. For a full understanding of the failure causes, three different mechanical models were developed, and the results are shown in Figure 4.2. From a preliminary analysis, it was possible to verify that the influence of the torque on the stress field generated in the probe was negligible (less than 1%) for all the conditions and was not considered in the rest of the study.

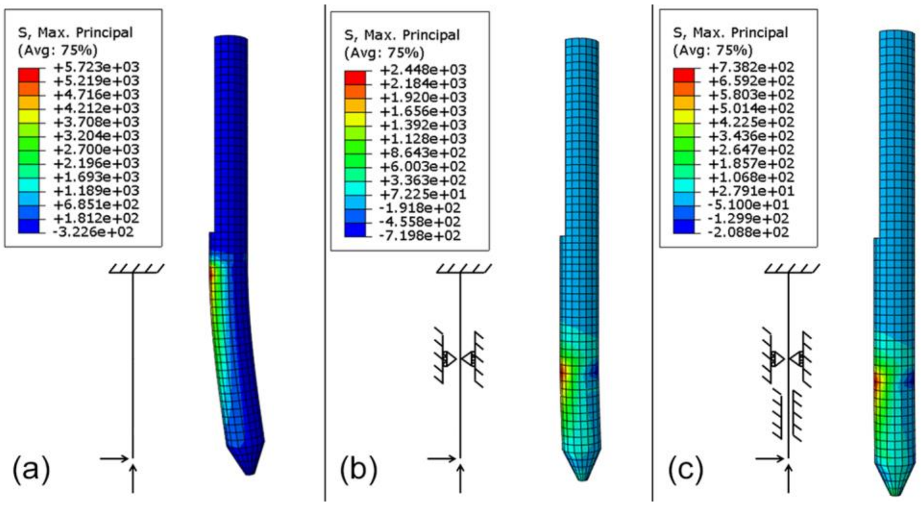

Figure 4.2. Results of FEM simulations for a 5-mm probe: (a) ‘ideal’ case with no probe support, (b) bearing support, and (c) bearing and shoulder support

In Figure 4.2a, the ‘ideal condition’ where the probe does not need any support from the bearing is represented. It is clear that with this design, the maximum principal stress is too high to be withstood by the tool and failure would directly happen at the end of the probe-holder. By adding a constraint to the simulation that represents the presence of the bearing (Figure 4.2b), the stress is reduced by more than 50% by reducing the free length on which the lateral force acts; it is, however, still higher than the yield strength of the probe. The last case analysed represents the ‘real condition’ (Figure 4.2c), where both the bearing and the shoulder are introduced in the simulated mechanical system. In this configuration the maximum stress is drastically reduced and reaches a peak of about half of the yield strength of MP159. Once it was clear that the reason for the failure was not directly connected with high stresses, the analysis of the displacement was performed, with the results shown in Figure 4.3.

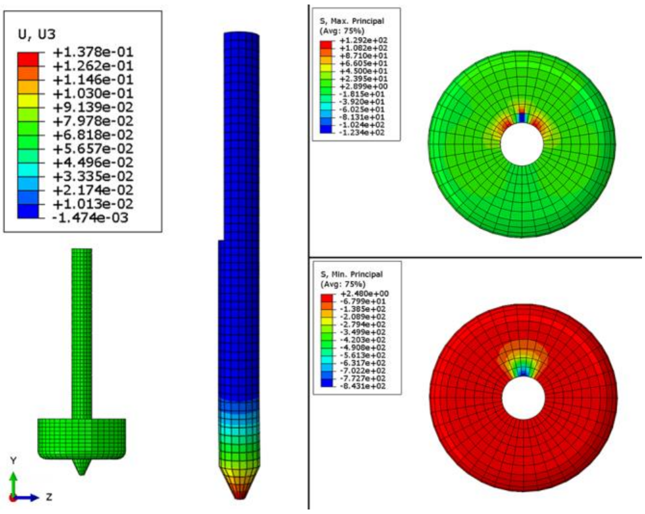

Figure 4.3. Results of the FEM simulation of a 6-mm probe and shoulder combined

The problem while considering the ‘real condition’ is that the probe displacement is too large with respect to the gap between this and the shoulder that is nominally equal to 0.05 mm. The high displacement leads to unwanted contact between the probe and the shoulder, which has a serious consequence on the life of the entire tool system. Owing to this contact, multiple events can happen that cause deterioration. The first result is a drastic increase in the temperature of the system owing to the friction between the two components. This can either lead to the failure of the bearing that will not be able to support the probe any longer or the deterioration of the material properties of the probe, i.e., the reduction of the yield strength and its subsequent failure. In case the probe and the bearing do not immediately fail, the problem is shifted to the shoulder, which will undergo severe wearing, which will increase the gap between the two elements. This larger gap brings the situation to the analysis presented in Figure 4.2b with no support from the shoulder as well as the consequent failure of the probe due to high stress.

The results of this study are summarized using fault tree analysis (FTA), which is a methodology that is commonly used in the aerospace industry [97]. It is shown in Figure 4.4.

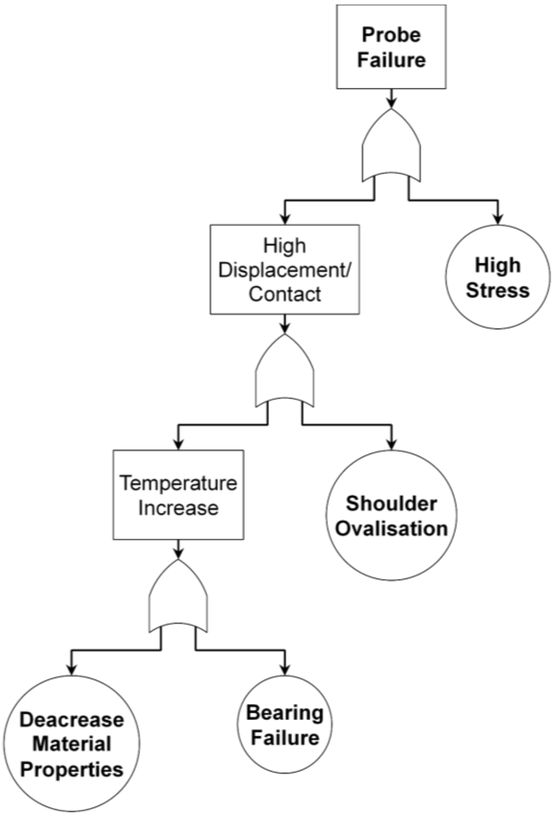

Figure 4.4. Fault tree analysis (FTA) of the previous SSFSW system

Once the reasons for the failure of the old tool system were established, it was possible to realize a knowledge-based redesign of the probe that would not only allow the reduction, if not the elimination of the failure but also simplify the assembly procedure and the regulation of the probe length. The new design, with the FEM analysis performed on it, is shown in Figure 4.5. While the terminal part of the probe in contact with the surrounding material during welding was not modified, the cross-section of all the upper part was enlarged in order to increase the stiffness and, consequently, reduce the displacements. In order to reduce the stress concentrations that could lead to fatigue issues caused by the high forces and the frequency of rotation during the process, the diameter increase was accurately tailored, and a large radius was implemented in the transitional region. The edge at the end of the diameter enlargement allows the positioning of commercially available spacer rings that simplify the regulation of the probe length and also allows a more precise calibration of it, with a tolerance of less than 0.05 mm.

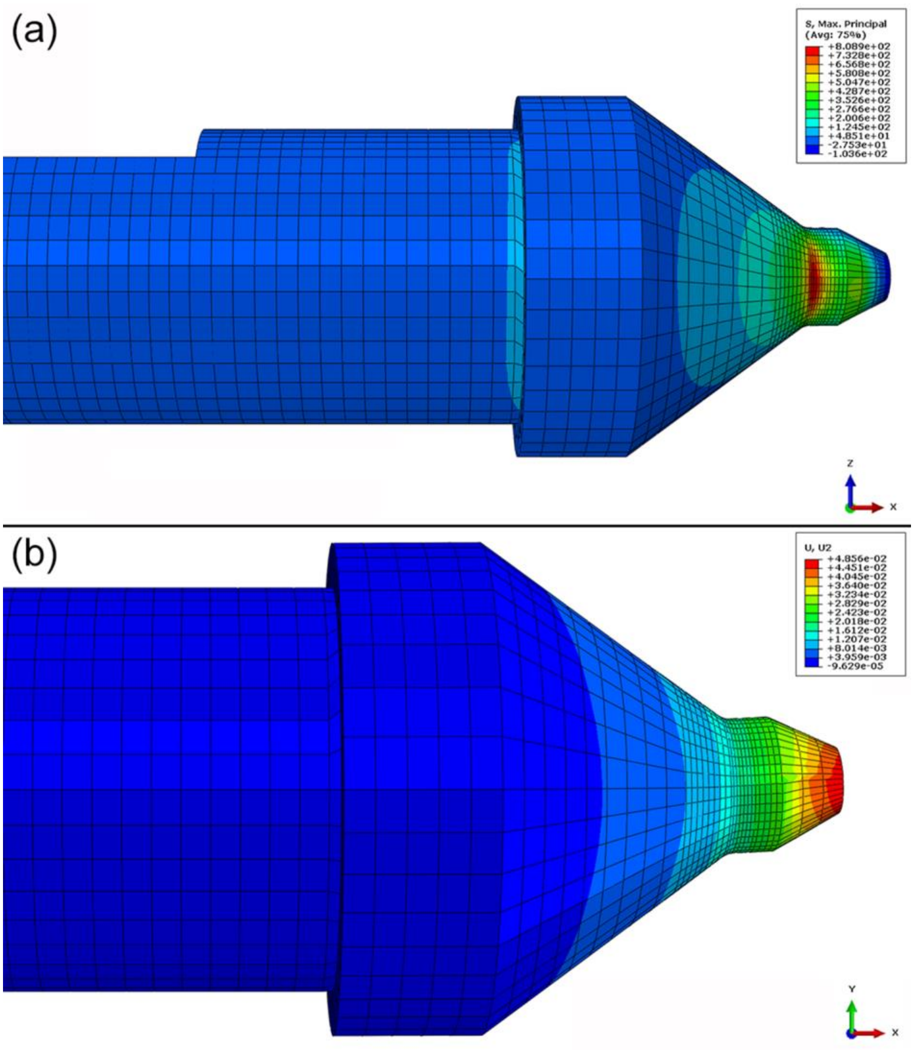

Figure 4.5. Results of the FEM simulation of the new probe in terms of (a) stress and (b) transverse displacement

The quantitative results of the FEM simulations performed for all the different cases and for the new probe design are summarized in Table 4.2.

Table 4.2. Summary of the results from the FEM simulation

	S_{max}, (MPa)	U, (mm)	ΔS_{max}	ΔU
‘Ideal condition’	5723	2.80	+237%	-
Probe with bearing	2248	0.46	+57%	-
‘Real condition’	738	0.09	−53%	+80%
New design	810	0.02	−48%	−60%

S_{max} is the maximum principal stress and U is the probe displacement in the area where the probe is within the shoulder. For the differences in stress and displacement (ΔS_{max} and ΔU), the yield strength of MP159 and the gap between probe and shoulder were used as references.

With the new probe design, the maximum stress is around 50% of the yield strength of the material and the displacement is less than 60% of the available space between the shoulder and the probe. Owing to these results, not only the robustness and the stability of the process was increased but it was also possible to significantly expand the range of parameters, i.e., welding and rotational speeds, enlarging the window available for this study and the possibilities of optimization.

In the end, starting from the redesign of the probe, the all-tool system could be improved as shown on the right in Figure 4.6.

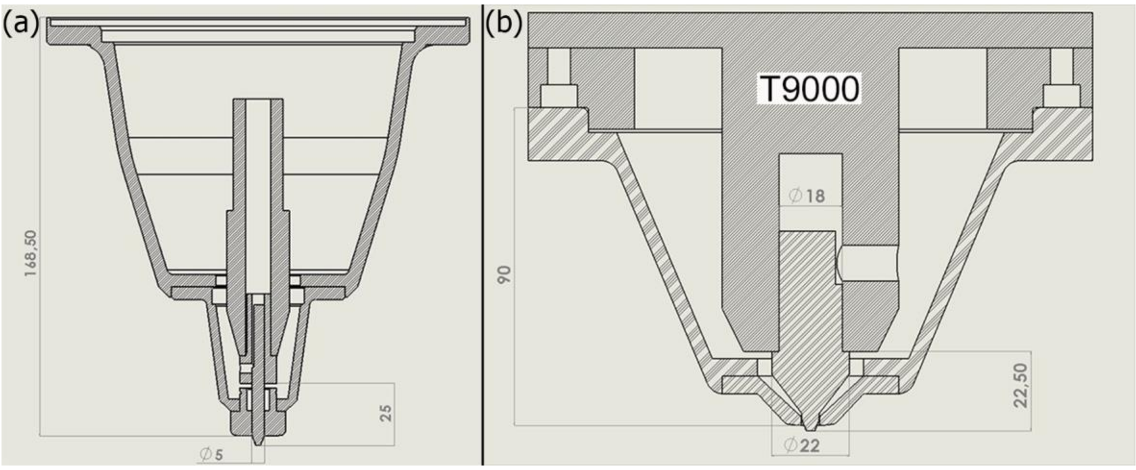

Figure 4.6. Schematic drawings of the old (a) and new (b) tool systems

While comparing the two systems, the two main differences—aside from the different probe geometry—are the reduced number of components and the more compact configuration after the redesign. The second aspect reduces the bending moment that the probe and the machine, which was indicated with T9000 in the figure, had to withstand during the process. The smaller number of components reduces the uncertainty of the eccentricity between the probe and the shoulder, reducing the possibility of contact between the two components, which would critically degrade the robustness of the SSFSW process.

In conclusion, owing to the newly developed tool system, all the welds performed in the current study could be carried on without failure of any of the components, reaching more than 100 meters of the total joined specimens.

5. Investigation of Notch-skin Single-pass Joint Configuration

In this chapter, a deep analysis of the joint configuration called the NS-SP was performed. The scope was to perform a clear understanding of how the process behaves and how different process parameters influenced the microstructure and the joint formation. Once this connection was made clear, the next step was to clarify the relationship between the microstructure and the mechanical properties achieved for the joints. In this manner, according to the author, the process could be considered completely under control and all the aspects involved were deeply understood. A similar analysis was performed for the other two joint configurations with a summary of the results shown in Appendix B.

5.1. Process Analysis

As possible to observe from Figure 5.1, the variation in the torque was mainly influenced by the changes in rotational speed and only small differences can be noticed at a fixed RPM for a change in the welding speed.

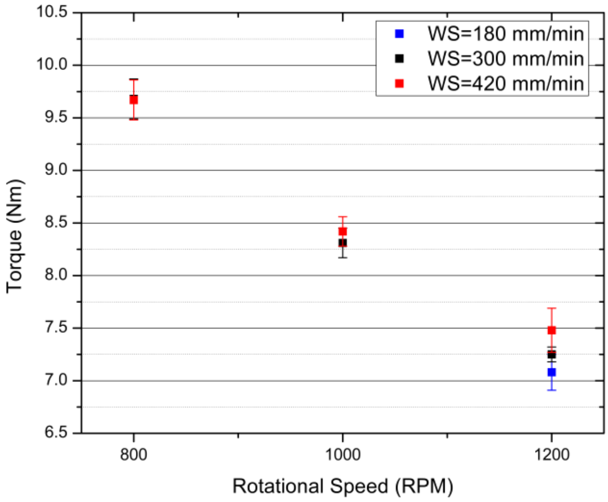

Figure 5.1. Measured torque for different welding parameters

This leads to the conclusion that the thermal field in the vicinity of the tool and, consequently, the contact condition between the probe and the surrounding material is not influenced by the welding speed but mainly by the rotational speed, within the parameter ranges investigated in this work.

The conventional equation for heat generation (5.1) shows how, in theory, by decreasing the rotational speed and/or increasing the welding speed, a reduction in the energy produced is achieved (Figure 5.2).

$$E_{in} = Q/v = M(2\pi\omega)/v + F_x \tag{5.1}$$

In this equation, E_{in} is the energy input per unit length, Q is the power produced during the welding process, M is the torque applied by the tool, ω is the angular velocity, F_x is the force in welding direction and v is the welding speed.

In this type of analysis, an inconsistency between the theoretical heat input (Figure 5.2) and the temperature measurements performed during the welds (Figure 5.3) was found. As observable from Figure 5.3, the highest peak temperature, for the range of parameters analysed, was reached for the lowest rotational speed. This contradicts the Rosenthal equation, in which the peak temperature is directly proportional to the heat input [98].

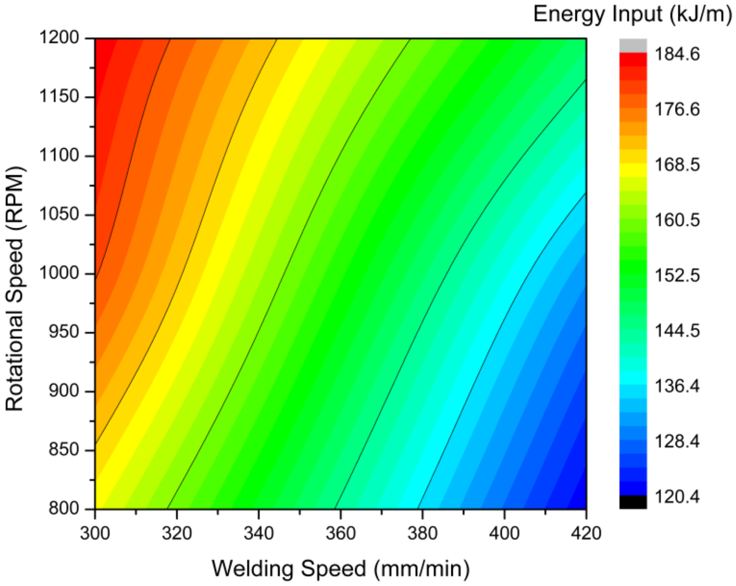

Figure 5.2. Energy Input calculated according to Eq. (5.1) for different welding parameters

In order to understand better this issue, it is better to take a closer look at the formula used by Barbini et al. [67] to characterize the torque and, consequently, the heat generated during SSFSW. Equation (5.2) derives from the analytical model developed by Schmidt et al. [56] for FSW and gives a qualitative idea of the deformation mechanisms around the tool. The last part of the equation takes the geometry of the tool used into consideration, such as the diameter and the taper angle. Since the same tool was used for all the joints analysed, this part can be considered as a constant.

$$M_p = \left(\frac{2}{3}\right)\pi\left[\varphi\left(\tau_{yield}\right) + (1-\varphi)\tau_{friction}\right] * f(geom) \tag{5.2}$$

The first part of the equation, is composed by three parameters: τ_{yield} and $\tau_{friction}$ are the shear stresses developed in case of pure sticking or pure sliding contact conditions, while φ is the parameter representing the ratio between the sticking and the sliding condition.

In general, when the temperature increases, both the terms related to the contact condition decrease, either by decreasing the yield strength or by the friction coefficient. How can the torque increase at a lower RPM when both of these two conditions are decreased? The answer is certainly not simple—a possible explanation might be found by separately considering the two different contact conditions. We already saw how the welding speed has a low influence on the area in the proximity of the tool (Figure 5.1). Moreover, at a lower RPM, no variation of the welding force could be observed by increasing the welding speed (Figure 5.4). This possibly signifies that the contribution of the $\tau_{friction}$ in this case is very small; in fact, an increase in the welding force should be expected due to the larger pressure between the probe and the surrounding material. As a consequence, the dominant value at 800 RPM is the first term of the equation, indicating a predominantly sticking condition. At 1000 RPM, we are probably in a transitional condition in which the two terms contribute almost equally. At 1200 RPM, the temperature increases again; this time, it is not supported by an increase in torque but a sharp increase in the welding force (Figure 5.4), thus representing a deviation towards a larger amount of material sliding around the probe.

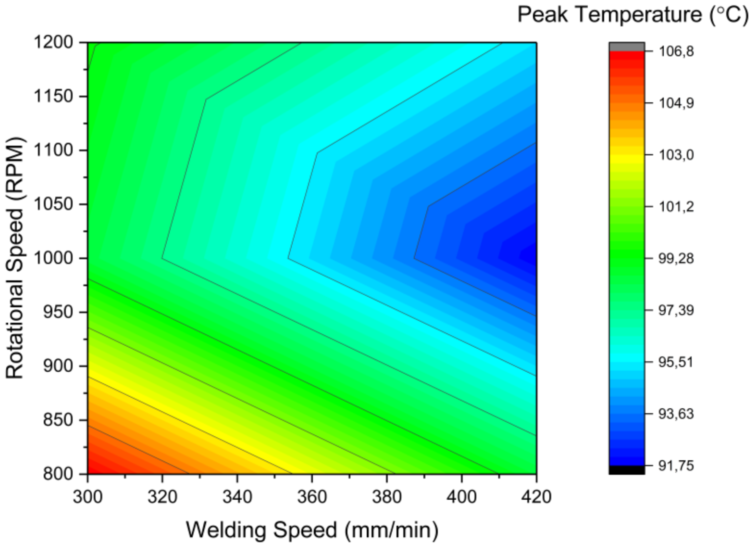

Figure 5.3. Measured peak temperature for different welding parameters

Considering Figure 5.3, it can be concluded that in the case of SSFSW, a minimum in the peak temperature at a fixed rotational speed can be reached when the contact condition is in equilibrium between sticking and sliding, and a variation towards either of these conditions leads to an increase in the temperature. It will be shown that this fact has a direct consequence on the amount of material that is stirred as well as on the size of the area directly affected by the process.

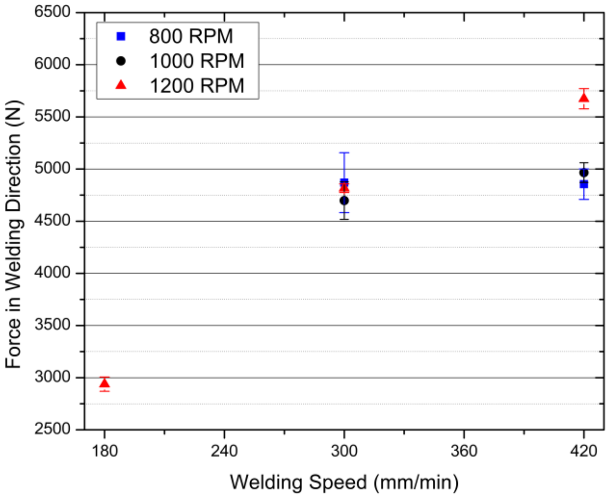

Figure 5.4. Measured force in welding direction for different welding parameters

The influence of welding speed on the force in welding direction increases with increasing rotational speed (Figure 5.4). At the lowest RPM, no difference on the welding force could be measured; at 1200 RPM, the increase in force with the welding speed was remarkable. According to the previous discussion, this could be explained by considering the state of the material in front of the tool and the way in which it changes at different rotational rates. At higher rotational speeds, a larger amount of material was sliding around the probe, changing the resistance of the material in front of the tool when the welding speed was increased. At 800 RPM, a thin layer of material was mostly attached to the probe and rotating with it. In this condition, it cannot be expected to have an influence on large scale on the force measured.

In Figure 5.5, the thermal cycles that the materials undergo during SSFSW for the full set of parameters is shown.

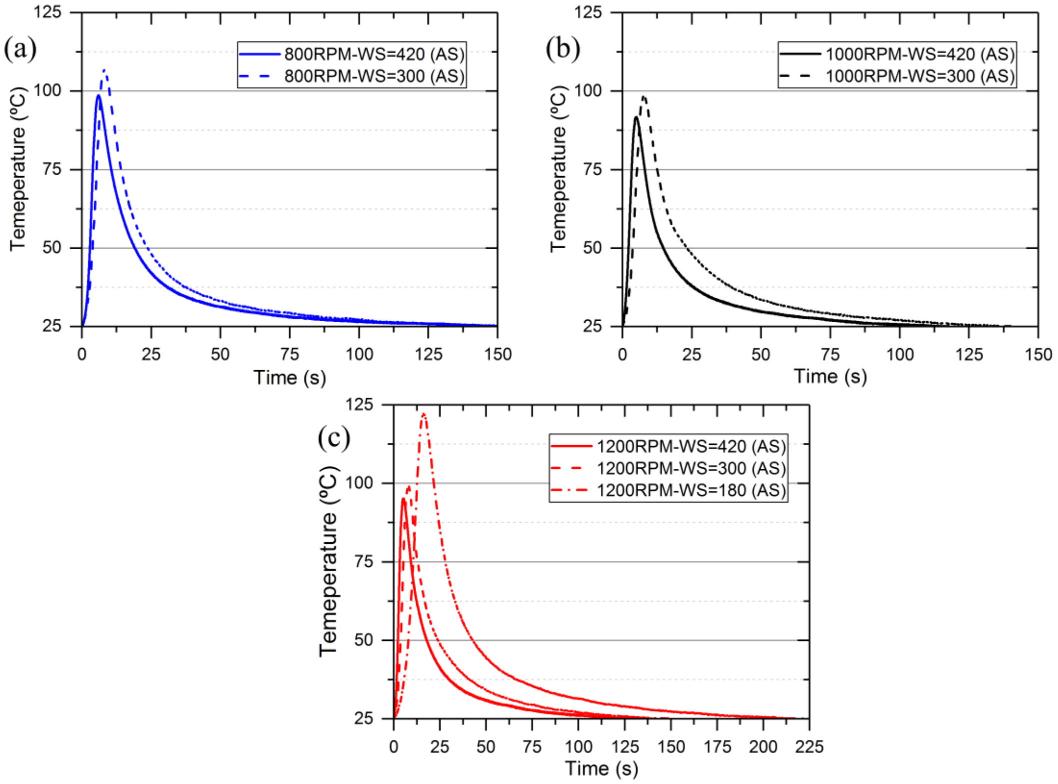

Figure 5.5. Temperature profiles for different welding speeds at (a) 800 RPM, (b) 1000 RPM, and (c) 1200 RPM.

The cooling rate after the passage of the tool was mostly influenced by the welding speed. At fixed RPM, with higher welding speeds, beside the decrease in peak temperature, it was possible to observe an increased cooling rate. The influence of the welding speed on the cooling rate was not the same for all the rotational speeds. At a lower rotational speed, the cooling rate remains almost constant and the two thermal profiles run parallel after the peak temperature is reached. For the two higher WSs, the cooling rate increased by 1ºC/s at each step in which the WS was increased. As seen previously for the welding force, when the rotational speed is kept low, the influence of the welding speed on all the properties of the material in the contact area is extremely limited.

One last consideration is to be accounted for is the validity of the equation (5.1). As shown in this discussion, the energy generation measured through this equation gives a poor idea of what is actually happening during the process. No correlation could be found between the heat input and the temperature measured and, as it will be shown in paragraph 5.2, it is not helpful to understand the microstructure developed afterwards as well. The author suggests that in case of the SSFSW, a different formula for the energy input in the weld should be developed. The importance of the rotational speed in this formula is too high and it covers other important terms, such as torque and welding force, which due to the nature of the process, i.e., the absence of the shoulder rotational contribution, cannot vary as significantly as seen in the case of conventional FSW.

5.2. Microstructural Characterization

The cross-section of the joints obtained for different welding parameters were analysed following a top-down approach. At first, a macrographic overview was performed to understand large-scale phenomena and the common characteristics of the joint. Subsequently, a more detailed analysis of the created microstructure and the most interesting features of it, influenced by different WSs and RPMs, were executed.

5.2.1. Macrostructural Behaviour & Joint formation

Owing to the relatively large parameter windows used to analyse the process, it was of particular interest to analyse the two cross-sections of joints realized with the parameter window extremes. The contour of the probe is represented with black lines in Figure 5.6 to facilitate the discussion. In Figure 5.6a, the cross-section of the so-called ‘cold’ weld (800 RPM, WS = 420 mm/min) was examined, where the rotational speed was the lowest among the selected set and the WS was the fastest.

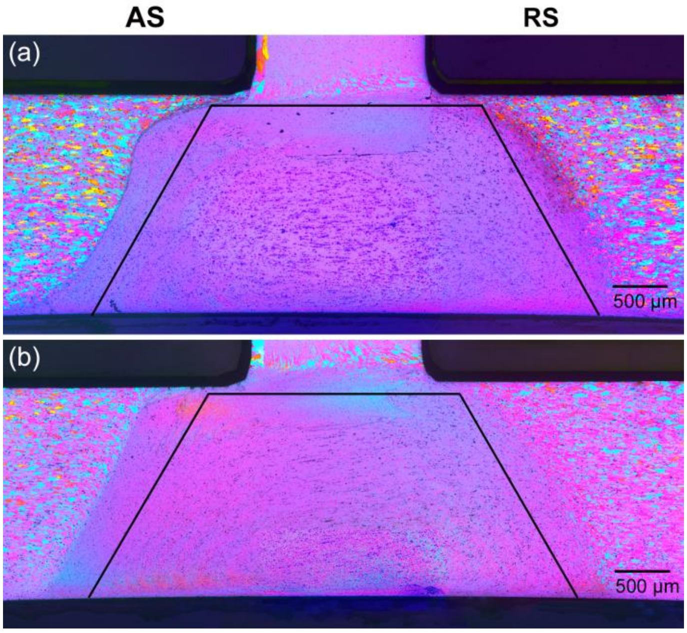

Figure 5.6 Macrographs of the welds obtained with (a) ‘cold’ parameters and (b) ‘hot’ parameters

The opposite situation, with the highest RPM = 1200 and the lowest WS = 180 mm/min, is presented in the ‘hot’ weld of Figure 5.6b. The joining mechanism is the same for all the welding parameters analysed; the defining distinction among them is the relationship between the material stirred around the probe and the one that simply extrudes and is pushed aside. For this reason, similarities can be found in all the welds, as the sharp microstructural transition in the AS of the joint and the smoother and more gradual transition in the RS. In this particular joint configuration (i.e., skin–stringer joint), another zone of microstructural transition can be found in the root of the weld while moving towards the stringer. This area, usually not seen in conventional butt joints, shows a behaviour comparable with the thermo-mechanically affected zone (TMAZ). The grains are strained and rotated, indicating a deformation induced by the probe movement—but there are no signs of dynamic recrystallization. The combination of strain energy and heat is not sufficient to initiate the dynamic recrystallization mechanism, but it is still enough to transform the original microstructure of the base material. In Figure 5.6b, owing to the low WS and the high RPM, a large amount of material is deformed and transported around the probe, both horizontally and vertically. This complex deformation mechanism leaves evidences that can be recognised as ‘onion rings’. By comparing hot welds and cold welds, it is evident how the onion rings tend to disappear in Figure 5.6a. The combination of high WS and low RPM not only leads to a reduction of transferred heat in the material but it also causes a decrease of strain energy and deformation.

In order to have a quantitative measure of the influence of the welding parameters on the material transport mechanism, the area of the stirred zone (SZ) is analysed and compared with the cross-sectional area of the probe (Figure 5.7)

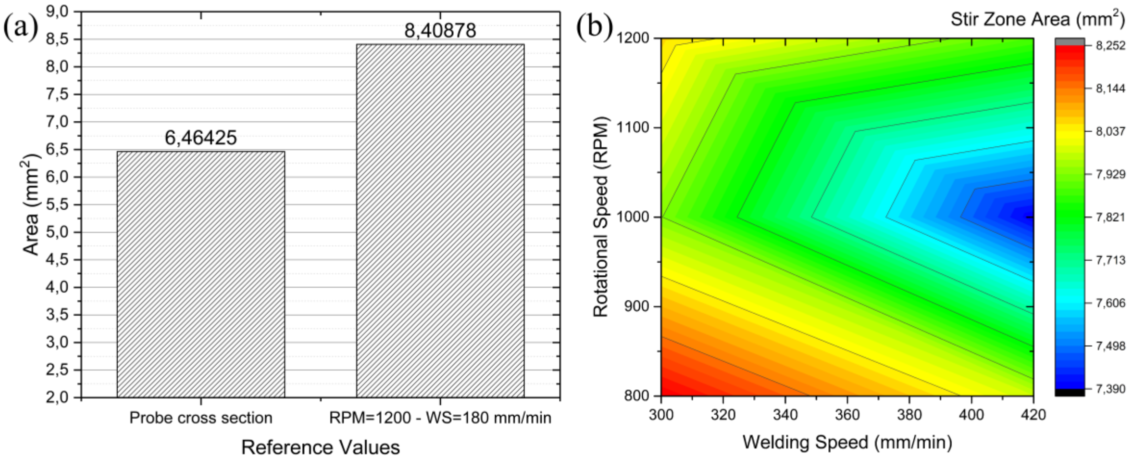

Figure 5.7 Cross section measurements of: (a) probe and SZ at 1200 RPM and WS= 180 mm/min and (b) the remaining set of welding parameters

To interpret the data obtained, it is convenient to separately consider the effect of rotational speed and welding speed.

At a fixed RPM, for the range of the parameters considered, the SZ area decreases with an increase in the WS. An increase of the WS causes different effects on the joint-formation mechanism. The most direct consequence involves the reduction of peak temperature and cooling rate, which lead to a reduction of the affected material and different contact conditions between the probe and the surrounding material. Therefore, the deformability of the surrounding material decreases with a mixed stick/slip condition, guaranteeing contact between a thinner layer of material and the tool. These conditions generate defect-free welds with less material transported around the probe, consequently, reducing the SZ area.

When the WS remains constant, the SZ area shows a parabolic trend with respect to the variations of the RPM. The minimum surface was found, for all the WSs, at an intermediate value of RPM equal to 1000. As mentioned in the previous paragraph, the change in the contact condition generates a parabolic trend in the temperature profile as well. By decreasing the RPM, the peak temperature increases without significantly influencing the cooling rate, which tends to remain constant. A contribution to this trend is provided by material extruded in the RS of the weld. From Figure 5.6a, it can be clearly seen how the SZ follows the tool shape in the AS of the weld, with even a reduction at the probe tip. No recognisable effect can be seen in the RS, however, where the SZ appears to be enlarged.

To analyse the effect of the welding parameters outside the SZ on the material not in direct contact with the probe, the width of the TMAZ in the AS and RS of the joint have been measured (Figure 5.8). In the RS at a fixed RPM, the TMAZ area increases in the case of faster welds, confirming the validity of the model in which the deformation mechanism in this part of the joint is mainly an extrusion around the probe. A higher WS leads to a decrease in the energy input and lower temperatures, which lead to larger forces in the welding direction and the involvement of a greater amount of material in the extrusion process. The amount of material involved in the process is similar for the two lower rotational speeds but it decreases drastically when the RPM is equal to 1200. At this level of rotational speed, the increase in sliding condition, as previously observed, reduces the amount of material transported and extruded in the RS (TMAZ).

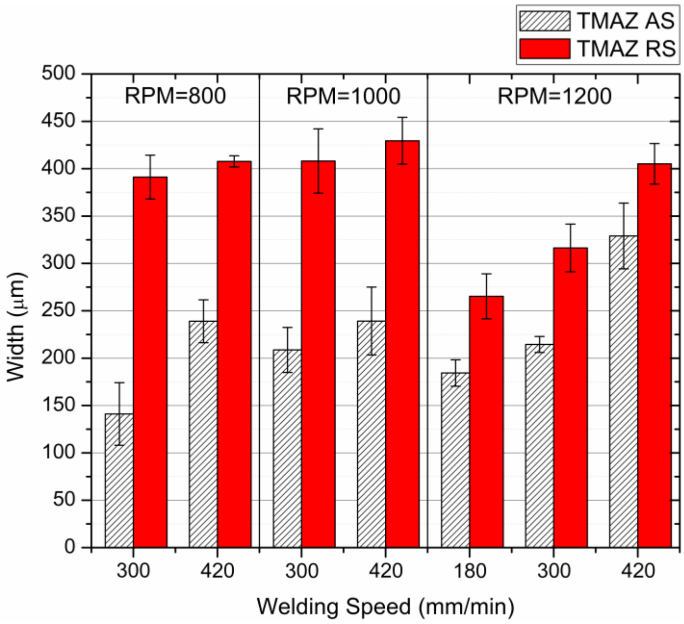

Figure 5.8. TMAZ analysis in the AS and the RS for different welding conditions

As previously observed for FSW [99], also in SSFSW the TMAZ in the AS of the weld is significantly smaller for all the parameters considered with respect to the RS. The asymmetry between the AS and the RS tends to reduce increasing the rotational speed due to the reduction of the TMAZ in the RS in combination with an increase of TMAZ in the AS, especially at 1200 RPM. The enlargement of the TMAZ increasing the WS is similar to the case that was previously discussed for the RS of the joint. A colder weld, in similar rotational conditions (i.e., the same RPM and similar torque), leads to a large amount of non-dynamically recrystallized material being pushed aside by higher forces on the horizontal plane. The AS seems to have a stronger correlation with the energy transferred on to the joint. The process of stirring is strongly correlated with the torque generated by the probe and has a strong impact in the AS. Since the torque plays a key role in energy generation, it can explain the increase of the TMAZ in the AS of the weld for all the WS when the RPM is increased.

5.2.2. Microstructural Analysis

In the joints, for all the parameters considered, four main microstructural areas were observed (Figure 5.9). The weld realised at 1200 RPM and 420 mm/min was chosen as an example to explain the characteristic of these zones. As previously seen, the changes in the welding parameters affected the morphology and the amount of material transported, but not the main characteristic of the different welding zones.

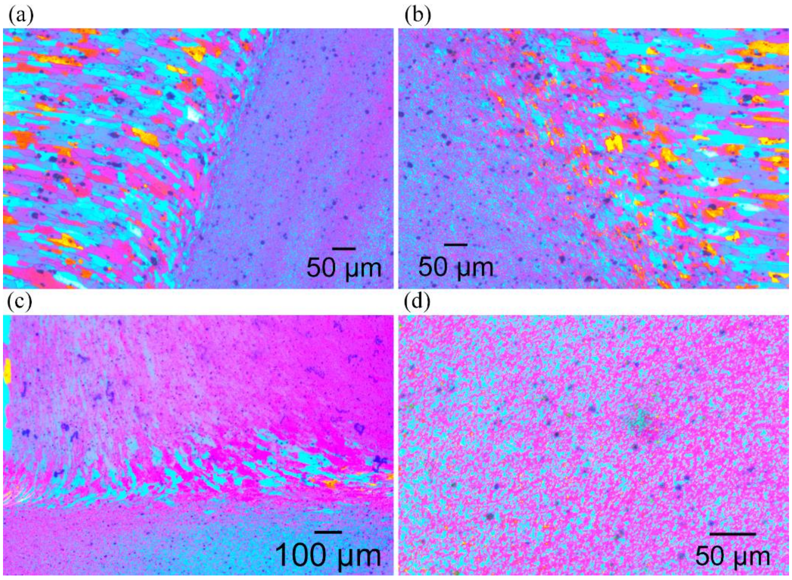

Figure 5.9 Microstructure of the joint obtain for 1200 RPM and WS = 420mm/min in (a) TMAZ-AS, (b) TMAZ-RS, (c) TMAZ-stringer, and (d) SZ

Figure 5.9a and b shows the TMAZ in the AS and the RS, respectively. The difference in the material flow between the two parts of the weld generates different microstructures, with a very narrow transitional area between the SZ and the base material in the AS, where the material was completely stirred around the probe. In this area, it was possible to observe the growth of the grain size in combination with a change in the orientation. The material close to the SZ presented grains oriented parallel to the border between the SZ and the TMAZ. Moving toward the base material, the grains were tilted upwards, until they reached the same direction of the elongated AA2024-T3 rolled grains. On the RS, where the probe extruded most of the material, the transition between the deformed grains and the base material microstructure was smoother and more gradual. In this case, the rotation of the grains was reduced and they mostly grew in size, moving further from the SZ.

In Figure 5.9c, it was possible to see an area similar to the TMAZ, where the SZ ended up at the tip of the probe. In case of conventional butt joints, this area is usually not visible when full penetration is achieved and the SZ ended directly at the root side of the plates. The grain difference in this area was dictated by the different production techniques of the stringer and skin. In the extruded stringer, the grains are oriented upwards, while in the rolled sheets, they are horizontally elongated. Another factor influencing the size of the grains in this area was the abnormal grain growth of the grains at the outer surface of the AA7050-T7651 owing to the rolling process itself, as investigated by Van Geertuyden at al. [100]. These larger grains were dynamically recrystallized when they were directly in contact with the probe, assuming the typical globular shape in the SZ. On this thin layer above the SZ, the strain rate and the temperature were not sufficient to promote dynamic recrystallization and, as a consequence, the grains were broken down and transported up to a certain point. The increase in size of the grains towards the centre of the stringer shows in which location the tangential speed and, consequently, the material transport was reduced. The influence of the process in grain orientation and size, extended from 180 µm at the edges of the probe, where the material was stirred around up to 250 µm at the centre, where the material was mostly extruded and pushed upwards. In conclusion, this area of the weld, owing to the gradient in the tangential speed, combined the characteristics of both analysed TMAZs.

The last picture (Figure 5.9d) showed the microstructure generated in the SZ. This area shares common characteristics with the one generated in conventional FSW. The main difference between conventional and SSFSW is in the volume of material that is included in the SZ. Owing to the absence of a rotating shoulder, the size of the SZ is reduced and more homogeneously distributed through the plate thickness [67]. The microstructure is represented by homogeneously distributed small globular grains. Liu et al. assessed that, in case of AA2219-T6, this is the typical structure obtained from dynamic recrystallization in this area [101]. Su et al. concluded that a continuous dynamic recrystallization is happening on the basis of dynamic recovery [46].

The grain size of the areas previously described was analysed, in order to understand the influence of the process parameters on the generated microstructure. In order to simplify the analysis and focus on the effect of one parameter at a time, the rotational speed or the welding speed were kept constant, while varying the other significant parameter. The results of this study are presented in Figure 5.10a and b for the variation of the welding speed and the rotational speed, respectively.

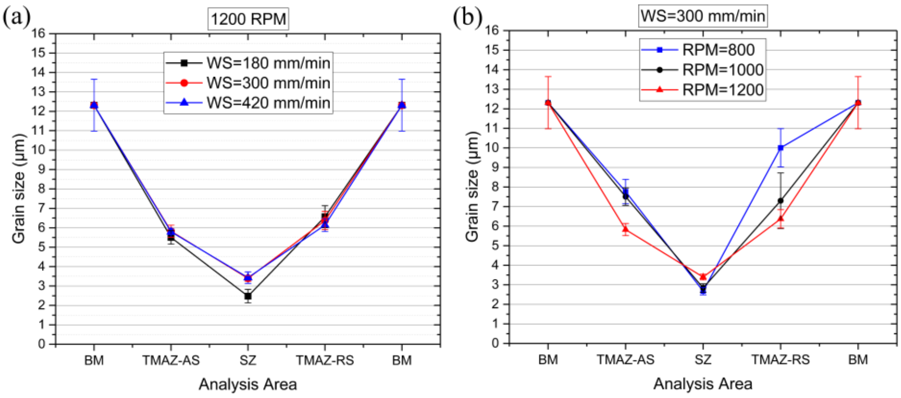

Figure 5.10 Grain-size measurements for the different WS and RPM at (a) 1200 RPM and (b) WS = 300 mm/min

At a fixed rotational speed (Figure 5.10a), the grain size did not appear to be affected by the changes in the welding speed in TMAZ for both sides of the joint, AS and RS. Theoretically, a reduction in the welding speed, with a consequent increase in the heat input, should cause an increase in the grain size owing to the grain growth phenomenon. Instead, for the two higher welding speeds, the grain size in the SZ was almost the same, with a reduction of the grain size when the WS was decreased to 180 mm/min. Contrary to what was studied in the case of conventional FSW [102], it seems that in the SSFSW for the lower WS, the probe provided more effective plastic deformation on the surrounding material.

When the welding speed was kept constant (Figure 5.10b), differences could be noticed in the grain size of the entire area analysed. In the SZ, smaller grain sizes were measured for the two lower rotational speeds. In the case of 1000 RPM, this reduction was due to the lower temperature experienced; for 800RPM, a different contact condition increased plastic deformation. Interestingly, the largest differences were observed in the two TMAZs, especially in the RS. For the two fastest RPMs, the difference between the small-recrystallized grains of the SZ to the strained grains of the TMAZ were larger, despite the size increase in the area affected by grain rotation shown in section 5.2.1. Since the measured grain size was averaged over the area analysed, the smoother transition between the SZ and the base material was driven by an enlarged TMAZ, which affected the results with higher values but also with an increase in the standard deviation. This was particularly clear while considering the RS, where the differences were much larger.

5.2.3. Interface Analysis

The interface between the two aluminium alloys had a strong influence on the joint strength and its failure mechanism. In Figure 5.11, the interfaces generated by different welding conditions are shown. For the full range of the parameters used, the interface in the AS is largely diffused and does not show a clear separation between AA2024 and AA7050. Owing to the large deformation that the materials undergo in this area of the joint, i.e., a complete rotation around the probe, they result in strongly mechanical interconnections and do not cause any deterioration in the joint strength. On the other hand, attention was focused on the part of the interface located in the RS of the weld since there the most interesting microstructural characteristic, which plays an important role in joint behaviour, could be found. In this zone, the deformation is mainly caused by material extrusion around the probe, leading to a reduced mixing of the two alloys. The shape of the interface is strongly influenced by the two investigated parameters. In Figure 5.11, the interface between the two alloys is highlighted with a red line.

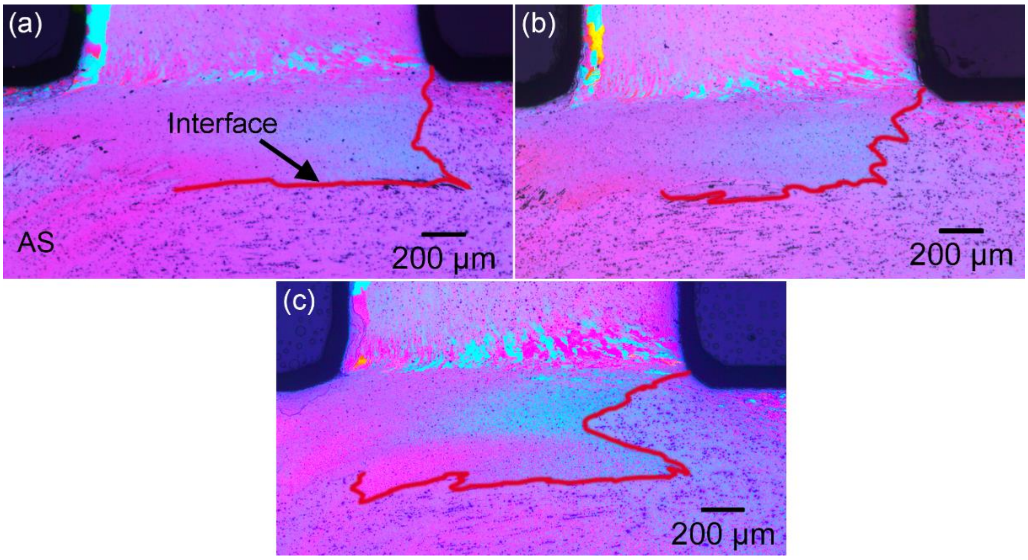

Figure 5.11 Interface evolution at fixed WS=300 mm/min for: (a) 800 RPM, (b) 1000 RPM and (c) 1200 RPM

While comparing different process parameters, it was possible to observe how the almost rectangular interface generated at 800 RPM (Figure 5.11a) becomes gradually more irregular at each increase of the rotational speed, therefore leading to an increase in the mechanical interlocking. Furthermore, the interface tended to deform towards the AS of the joint at higher rotational speeds as it can be observed at 1200 RPM, where a Z-shaped interface is formed, reaching almost the centre of the joint (Figure 5.11c).

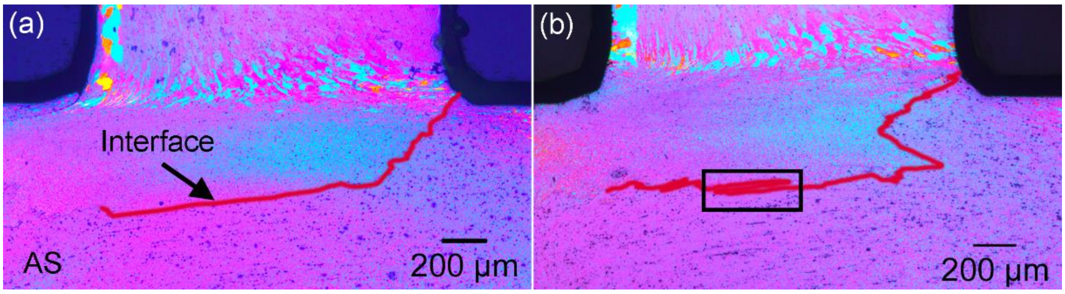

Figure 5.12 Interface evolution at 1200 RPM for: (a) WS=420 mm/min and (b) 180 mm/min

The exact opposite phenomenon was observed while analysing the effects of welding speed (Figure 5.12). The contact time between the probe and the surrounding material, at higher welding speeds, decreased, thus leading to an interface which presents very few irregularities (Figure 5.12a). Although the WS was increased, the interface is not as vertical in the RS as in case of 800 RPM, clarifying the importance of the rotational speed in moving the material towards the AS of the joint. At low WS, beside the aforementioned increase in the material interlocking in the RS, it is possible to observe an increase in the layering of the interface in the central part of the joint (black rectangle in Figure 5.12b). This gradual increase of the interface layering with the reduction of the WS leads to the extension of the interface surface, causing an increase strength of the joint under particular load conditions (as it will be shown later on).

As it is evident that the welding parameters influence the shape of the interface, it was necessary to understand its nature. From SEM analysis, it was possible to visualize a weak bonding immediately above the interface at the corner of the skin–stringer joint (Figure 5.13a).

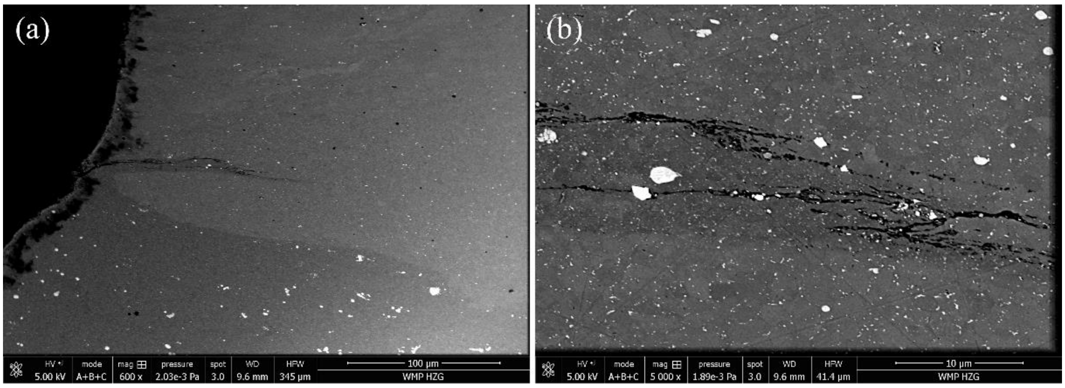

Figure 5.13. SEM image of the interface end at the skin–stringer corner in the RS: (a) overview and (b) detail

In this area, the material was pushed against the edge of the backing bar, where the contact surface was extremely small, thus causing a reduced pressure between the material and the probe, with the generation of the joint line remnant. At higher magnification (Figure 5.13b), it was possible to observe how large inclusions migrate into the bonding area. The 2024 sheets used in the current study appear to be rich in impurities leading to the formation of inclusions that remains trapped and contributes to stress localization due to inhomogeneous behaviour.

In order to quantitatively investigate the influence of the welding parameters on the interface shape, two features were analysed: the interface angle and the interface length (Figure 5.14). The interface angle, positioned at the corner of the skin–stringer joint in the RS, was defined between the lower SZ boundary and the materials interface. A small interface angle implies that the interface is approaching the TMAZ at the root of the welds. The interface length was measured from the beginning of the interface in the RS corner until the middle of the stringer thickness (0.8 mm). This approach involved avoiding considering the interface in the AS of the joint, which is more diffused (harder to visualize) and does not have a strong influence on the failure mechanism.

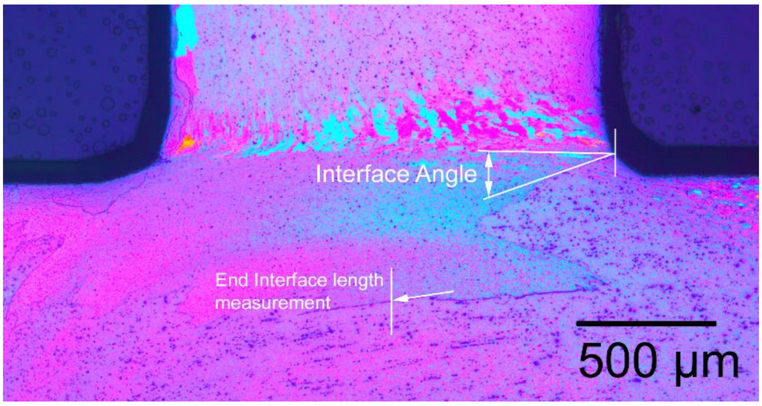

Figure 5.14 Example of interface measurements performed

The interface angle and length play a key role in the mechanical performance of the joints in hoop- and pull-out directions, respectively. For this reason, it is important to understand the influence of the welding parameters on them. The results of this study are shown in Figure 5.15.

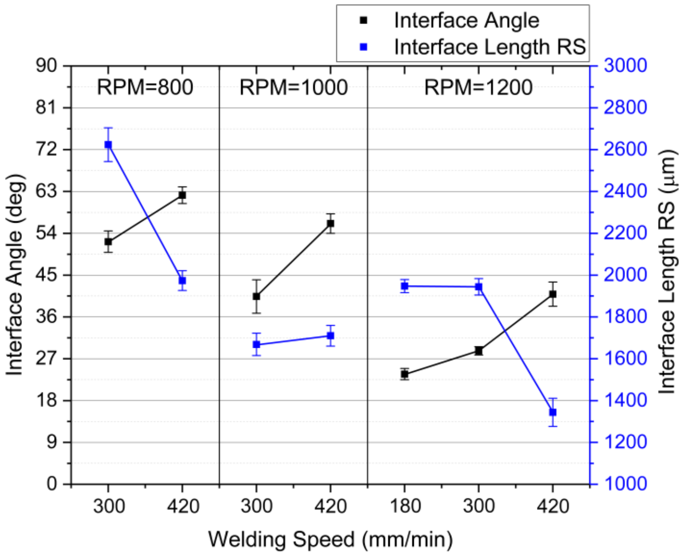

Figure 5.15 Interface angle and length in different welding conditions

The interface angle, for the three different RPMs considered in the study, tend to decrease when the welding speed decreases. A longer contact time between the probe and the surrounding material allows a greater vertical movement of the material towards the stringer, with consequently flattening of the interface and a reduction of the angle in the RS. A similar effect is also noticeable when the RPM is increased and the WS is maintained constant. This clearly proves the existence of vertical material flow, enhanced by the conical shape of the probe, which generates a pressure field around it, directed downwards.

The length of the interface can be divided into vertical and horizontal components. The material movement around the probe in the horizontal plane is mainly responsible for the vertical part of the interface. The horizontal part was instead hardly influenced by the process parameters and, in all the experiments, tended to become completely flat towards the centre of the probe. The reduction of tangential velocity at the centre of the probe clearly explained this phenomenon. At a fixed RPM, the interface length tended to decrease for higher WS, proving the beneficial effect of a longer contact time between the probe and the surrounding material on its formability. The only exception was found when the rotational speed was equal to 1000 RPM, when the interface length almost remained constant. In combination with what was previously analysed for the SZ area measurements, for this RPM, an equilibrium was reached between material stirred and extruded around the probe and the range of WSs considered in this study do not influence significantly the interface length.

5.3. Mechanical Testing

The analysis of the mechanical properties of the joints was conducted, starting from a local analysis through the micro-hardness variations for the different energy inputs, before determining the strength of the joints for different loading conditions.

5.3.1. Micro-Hardness Analysis

The hardness of the joints realized with different process parameters was measured in two directions. Firstly, the horizontal variation of the hardness in the middle thickness of the skin was analysed and afterwards, the influence on the stringer penetration in the vertical direction was considered. Similar to what was shown previously for the grain size, at the time, the rotational speed or the welding speed were fixed while varying the other parameters.

The hardness profile in the horizontal direction shows the typical shape obtained in the case of FSW for precipitation-hardened aluminium alloys, with differences in the minimum hardness or in the amount of material involved, for all the parameters analysed (Figure 5.16). For these alloys, the variation in hardness is mainly determined by the concentration and the size of the precipitates in the aluminium matrix, with little influence of the grain size [103]. At the position that was analysed in terms of thickness, there was no influence of the stringer material on the hardness of the joint, thus leading to the properties being determined by the phenomena occurring in AA2024-T3. In both graphs, three main areas, symmetrical with respect to the weld centre, could be determined aside from the base material. The HAZ, which was not visible by the optical microscope, became clear through the hardness analysis owing to the influence of the heat generated on the precipitation behaviour.

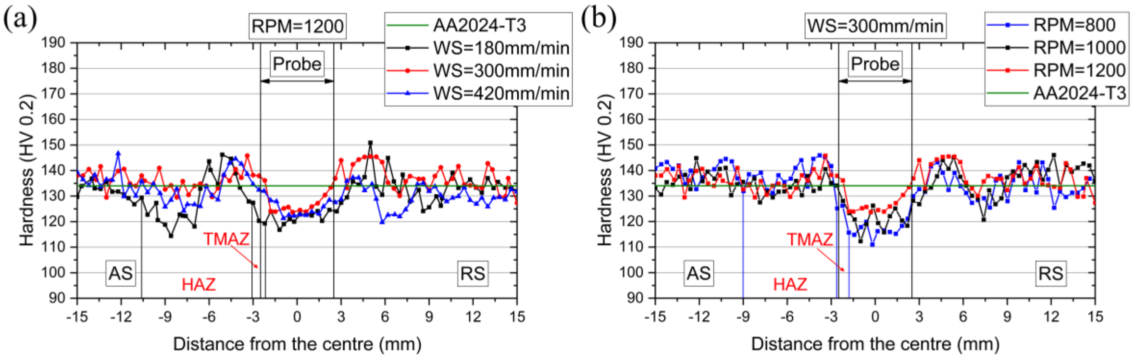

Figure 5.16. Horizontal micro-hardness profiles at different RPM and WS for (a) 1200 RPM and (b) WS = 300 mm/min

The evidence of the precipitates' transformation during the welds are clearer for the joint obtained at 1200RPM and WS =180 mm/min (Figure 5.16a), where the highest temperature was measured. The shape of the hardness profile for this condition results shows more similarity to the one obtained in conventional FSW of AA2024-T3 and already observed in numerous studies [54, 103]. Owing to the higher measured temperature peak (paragraph 5.1), a hardness drop in the TMAZ followed by a recovery in the SZ could be observed, similar to the FSW case. However, the measured temperature was not high enough to justify such large hardness drops as in case of FSW and the differences between the welding zones are smoothed down. Also the volume of material involved in the precipitate evolution is drastically reduced proving a smaller influence of the SSFSW welding process on the material deterioration in comparison with conventional FSW.

The behaviour of the precipitates distribution among the different welding areas was clearly affected by the process parameters. At a fixed rotational speed, the increase in the welding speed caused a smaller decrease of hardness in the first part of the HAZ, combined with a faster normalization of the hardness profile at the level of the base material. This showed how an increase in the WS led to a faster cooling rate both in terms of time (paragraph 5.1) and space, with lower temperatures reached at the same distance from the weld centre. The other noticeable difference can be seen in the absence of a hardness minimum and the subsequent recovery between TMAZ and SZ. For higher WS, the minimum reached in the TMAZ remains constant through all the SZ. This can be connected the observed reduction of the peak temperature in the SZ when the WS increased, which did not cause the partial dissolution of *S'(S)*, with consequent absence of free precipitates for re-precipitation.

A similar influence was also observed in the case of an increase in the rotational speed for a fixed WS (Figure 5.16b). The hardness in the SZ reached a maximum in the case of a higher rotational speed, where the temperature reached during the process was higher (see section 5.1). Outside the SZ, a variation in the rotational speed did not seem to have a particular influence on the measured hardness.

From these observations, we can assume that the rotational speed clearly affected the peak temperature reached in the SZ, as already seen by the difference in the contact condition between the probe and the surrounding material in the first paragraph, and, consequently, the amount of free solute available for the formation of the GPB zones at room temperature. The influence of the welding speed is stronger on the cooling profile between SZ and the base material, with an influence on the size of the precipitates and the distribution in the HAZ and TMAZ of the weld.

Before discussing the influence of the parameters on the vertical distribution of hardness, it is important to point out that for this joint configuration, the stringer (AA7050-T7651), in the pre-welding setup, is located at −0.5mm from the skin-stringer line represented on the graphs (Figure 5.17). For this reason, it was possible to observe a sharp increase in the hardness in all the curves before reaching the delimitation line between the skin and the stringer.

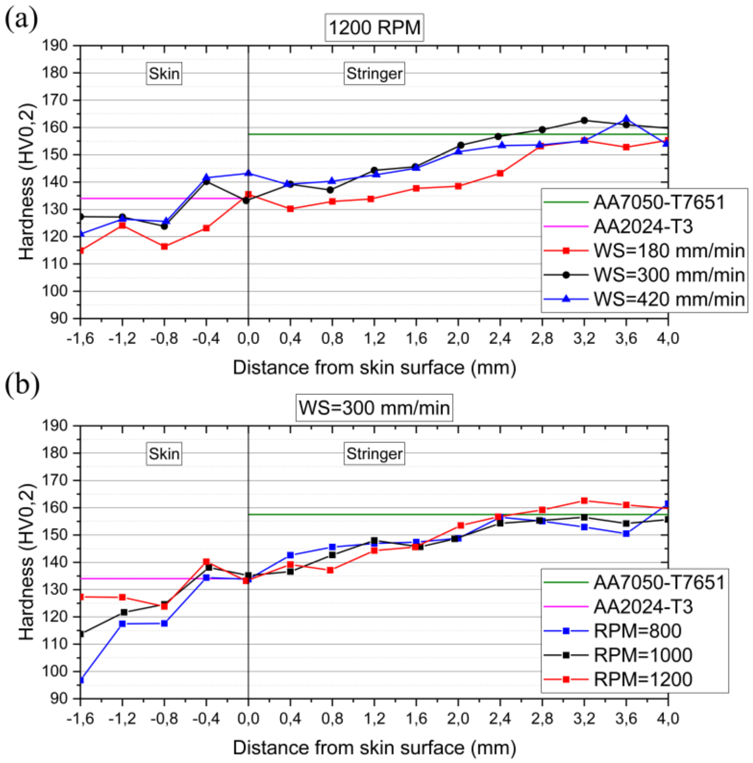

Figure 5.17. Vertical micro-hardness profiles at different RPM and WS for (a) 1200 RPM and (b) WS = 300 mm/min

The hardness variation should only be related to the presence of the AA7050 and different precipitation mechanisms but not by different microstructures through the weld thickness. Uniform microstructural distribution in the case of SSFSW was proved in many studies, as in Ahmed et al. [64] in the case of the 6-mm thick AA6082. In the SZ, where the highest temperature was reached, the precipitates changed into solution state and could re-precipitate after cooling and natural aging, as was the case for the AA2024 [47]. As a result, for all the different parameters, the hardness increased at the original skin–stringer interface, thanks to the formation of a combination of GP zones and η^{I} precipitates.

At a fixed RPM (Figure 5.17a), the main influence of the WS was on the distance required to reach the base material level, while moving into the stringer. Two causes were behind this particular behaviour. On one side, as seen in section 5.1, at lower welding speed the cooling rate was reduced and higher temperatures were experienced at larger distances from the weld centre. This was proved true in the horizontal plane and the same was to be expected in the vertical plane as well. The other cause behind this phenomenon was a result of the material transportation around the probe in the vertical direction. As observed for the interface evolution in section 5.2.3, at lower welding speeds a larger amount of material was transported upward towards the stringer. Consequently, both the TMAZ and the HAZ moved deeper in the stringer and the hardness recovery was reached at a larger distance from the skin surface.

While the welding speed was kept constant (Figure 5.17b), the variation of hardness with the rotational speed was limited to the SZ and the stringer's TMAZ and HAZ were not influenced at all, with the three hardness profiles overlapping each other. From this analysis, it became clear that rotational speeds mostly influence the peak temperature and the consequent precipitate transformation in the SZ but it just plays a minor role in vertical cooling and material transportation.

5.3.2. Hoop Strength

The case analysed here simulated a load in the hoop direction, i.e. an in-plane load perpendicular to the stringer, similar to what an aircraft fuselage experiences due to pressurization. The load was applied on the AA2024-T3 and transferred into the stringer, causing detachment with the consequent failure of the joint. The hoop stress is calculated by dividing the applied load with the cross-section of the skin. In Figure 5.18, the yield strength as a function of process parameters is shown.

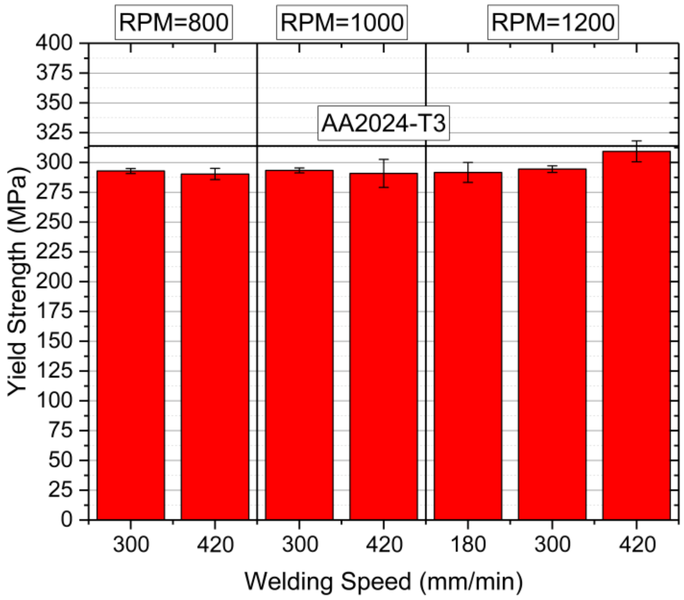

Figure 5.18. Yield strength in the hoop direction for different welding parameters and the AA 2024-T3

The results exhibited a robust trend with a small influence of the welding speed and rotational speed on the yielding of the joint. The smallest yield strength reached 92.3% of the base material in the transverse direction and went up to 98.6% for the highest welding speed and rotational speed. The stringer played an important role on the robustness and the high values measured for the yield strength. A part of the load was transferred to the stringer made of high strength AA7050-T7651, levelling up the general yielding and reducing the influence of microstructural variations. The higher yielding at high rotational and welding speeds was probably related to the short and flat interface generated at these parameters.

While analysing the stress immediately before failure, the differences between the joints, which were obtained varying process parameters, led to a clearer analysis. In Figure 5.19, the values of the tensile strength, combined with the interface angle measurement previously presented, are shown.

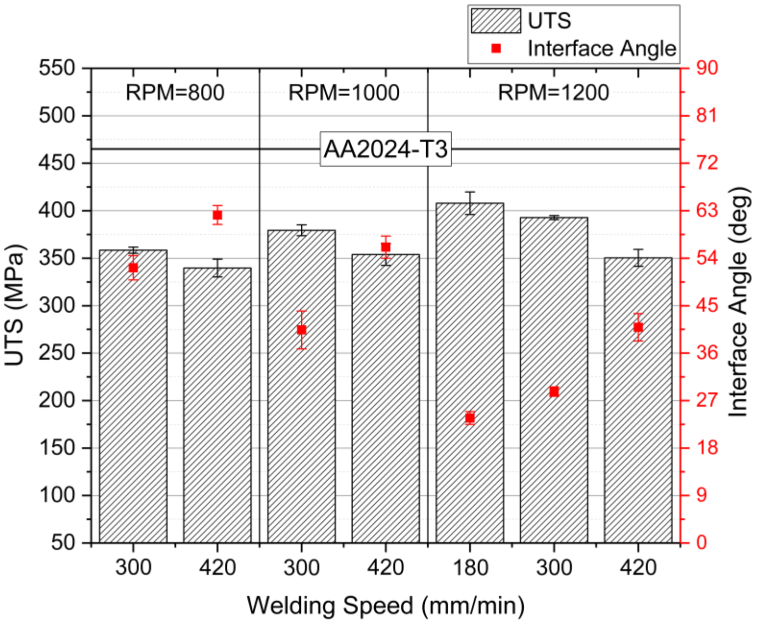

Figure 5.19. Tensile strength in the hoop direction and the interface angle for different welding parameters

For all the rotational speeds, the tensile strength decreased by increasing the welding speed. These results appeared in contrast with the temperature and the micro-hardness that was previously analysed. At higher welding speeds, the peak temperature measured during the thermal cycle was reduced and the hardness increased. This led to the conclusion that the phenomenon of precipitate coarsening and growth was diminished and simultaneously should have caused an increase in the mechanical properties of the joint. Therefore, the causes for this trend in the tensile strength of the joint should be explored elsewhere. The comparison between the yield strength behaviour, not affected by WS, and the tensile strength one, which decreases with WS, provides a strong indication of how stress intensity elements control the failure mechanism.

While comparing the trend of the interface angle for different process parameters with the tensile strength, it was possible to see an inverse proportionality between them. An increase of the interface angle led to a decrease in the joint strength and vice versa. After all the analysis previously presented, it clearly resulted in the fact that the interface played a key role in the failure mechanism and that different effects contributed to it. The first observation was that the weak bonding at the end of the interface while approaching 90° caused a reduction in the cross-section perpendicular to the load and, consequently, increased the stress concentration in the area, especially around it.

According to the linear elastic fracture mechanics, the situation that was being analysed could be simplified as shown in Figure 5.20. The crack had an Angle β, equal to the 90° minus the interface angle, with respect to the plane orthogonal to the principal stress in which the crack would be loaded in the pure Mode I.

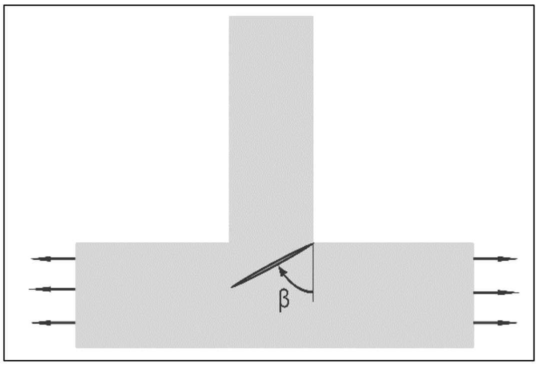

Figure 5.20. Schematic of the relationship between the crack angle and applied load

For different interface angles, the crack-opening mode changed as well. The stress intensity factor, in such a complex situation, could be expressed in the function of the stress intensity factor, $K_{I(\beta=0)}$, in the pure Mode I load, where the crack is perpendicular to the load, as shown in the equation (5.3) [81, 82].

$$K_I = K_{I(\beta=0)} cos^2\beta$$
$$K_{II} = K_{I(\beta=0)} cos\beta sin\beta \tag{5.3}$$

When β tends to 0º, high interface angles, the interface tends to be loaded in the pure Mode I, with $K_I = K_{I(\beta=0)}$. An increase in the stress-intensity factor allowed the crack to easily propagate until the fracture toughness of the material was reached and the propagation became unstable. For low-interface angles, when the interface flattened and β tended to 90º, the initial crack opening mechanism became more similar to a sliding mode (Mode II).

When the stress-intensity factors were calculated for the two extreme conditions of β (see Figure 5.19), it could be seen that K_{II} remained nearly unchanged ($K_{II} = 0.4K_{I(\beta=0)}$), while K_I was much larger for smaller values of β ($\beta = 28° \rightarrow K_I = 0.78K_{I(\beta=0)}$ and $\beta = 66.5° \rightarrow K_I = 0.16K_{I(\beta=0)}$). A propagating crack seeks the path of maximum driving force and will tend to propagate orthogonal to the applied load. Therefore, for a large value of β (small interface angle), the crack would have to rotate and dispose in a direction perpendicular to the principal stress direction until it, once again, became pure Mode I loading. This rotation phase slowed down crack propagation and reduced the stress-intensity factor before the crack became orthogonal to the applied load.

Another factor to be considered was related to the role played by the strength mismatch between the two microstructures (AA2024/AA7050) on the ductility of the region. However, this effects is not as relevant as the interface weak bonding (with the consequent fracture mechanics) and other geometrical issues such as the corner. This corner between the skin and the stringer, which naturally act as stress concentration factors for this type of joint, intensifies this entire situation.

Confirmations about the role played by the interface on the failure mechanism of the joints was obtained by analysing the fracture location and the morphology. Similar fracture profiles were obtained for all the analysed parameters, with the crack always initiated at the skin–stringer interface in the SZ towards the RS of the joint. An example of the fracture surface is shown in Figure 5.21 for the weld with the highest tensile strength. This crack location is quite unusual while considering just the microstructure of the joint; in fact, in this area, the hardness is higher and the transition between the base material and the area affected by the process is smoother.

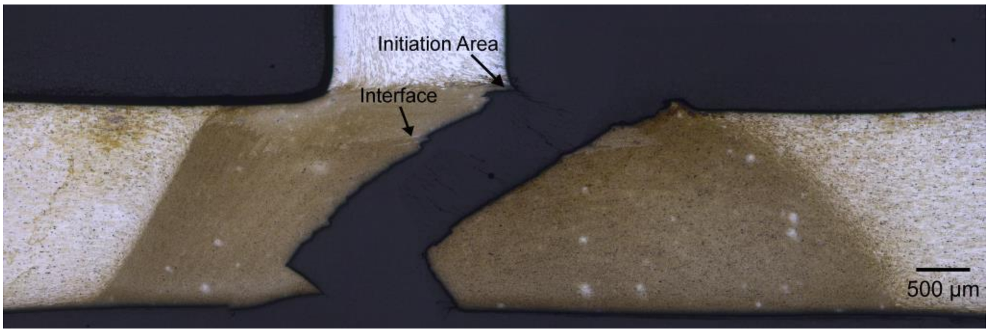

Figure 5.21. Fracture analysis in the hoop direction for the joint obtained at 1200 RPM and WS = 180 mm/min

The fracture was initiated in the defect at the end of the interface and it was propagated until it reached a critical length. At that point, the crack continued to grow along a 45º line, where the shear stresses were expected to reach a maximum.

5.3.3. Pull-out Strength

The second load case analysed involved a force applied directly to the stringer that tended to remove it from the skin. Such a situation is an uncommon load configuration for fuselage structures but it is helpful to analyse the strength of the joint between the skin and the stringer and in order to have a deeper insight of the role played by the interface in a different condition.

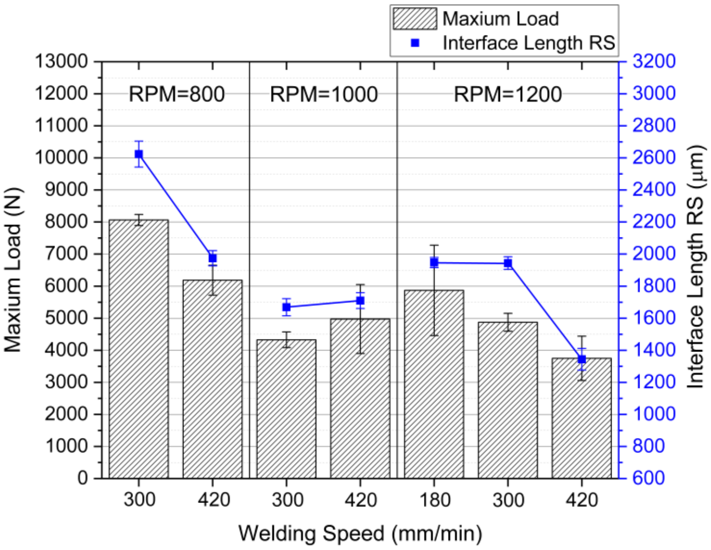

Figure 5.22. Joint strength in pull-out and interface length for different welding parameters

In this type of test, it is extremely difficult to extrapolate a value of the stress from the measured load due to the tri-dimensionality of the geometry of specimens. In the stringer, the load prevalently caused a tensile stress while the skin was subjected to bending and shearing, which made it difficult as well as meaningless to define a single value for the stress as seen in a uniaxial tensile test. Alongside the values of the maximum load reached, the measured length of the interface, as previously explained, was reported on the graph. The results of the test have been shown in Figure 5.22.

In general, both the rotational speed and the welding speed influenced the results of the tests; those with the highest values of the maximum load were obtained for the lowest rotational and welding speeds. The trend of the variation of the maximum load for different parameters closely followed the one of the interface length. The results of this study showed a beneficial effect when the interface length increased. In this load configuration, the forces acted orthogonally to the interface. The difference in length, owing to the changes in the interface flatness, caused a mechanical interlocking between the two materials, thus increasing or decreasing the resistance of the joints. In the end, despite the differences in the failure load, it was not possible to observe any plasticization of the specimens from the load-displacement curves, with an example of the load-displacement curve showed in the next chapter (6.2.3). For all the analysed parameters, the curves present an almost linear behaviour with a sudden failure once a certain load-level was reached.

The fracture analysis confirmed the brittle nature of the failure mechanism, thereby showing how the crack propagated all along the interface. An example of the fracture location and its development is shown in Figure 5.23—for the specimen obtained with 800RPM and a welding speed equal to 300 mm/min—which achieved the highest pull-out load.

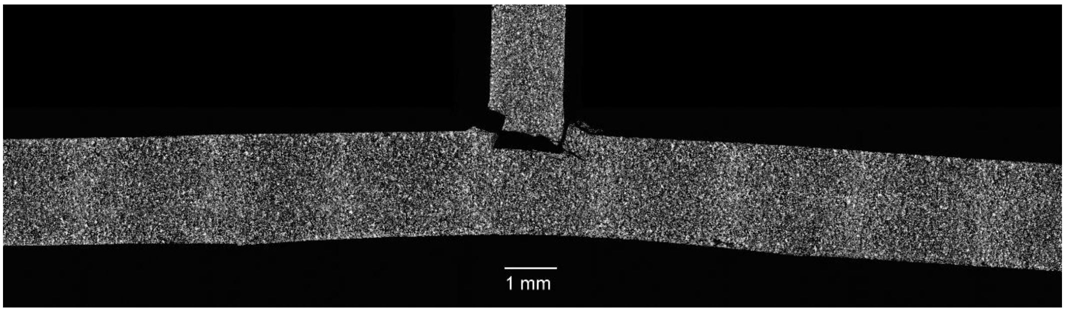

Figure 5.23. Fracture analysis in the pull-out direction for the joint obtained at 800 RPM and WS = 300 mm/min

The skin underwent a bending load that caused the maximum tensile stress to be reached in the interface area. The stringer was pulled out all along the interface, starting from the joint remnant line at the corner in the RS. The origin of the crack was confirmed by the bifurcation of it, which originated in a secondary crack propagating from the bottom edge of the interface towards the RS of the joint. At that point, the joint was kept together just by the horizontal part of the interface, which became the surface with the highest stress applied. The results clearly show that by increasing the interface length, the cross-section that was subjected to the maximum load was extended, favouring a better stress redistribution along the interface.

5.4. Summary

In this chapter, the NS-SP configuration was analysed, starting from the process influence on the joint formation and microstructure, right up to the mechanical properties of the joints as a function of the different parameters. The main conclusion of this study is summarized in the following points:

- The contact condition between the probe and the surrounding material as well as the temperature peaks in the weld area are mainly controlled by the rotational speed.
- The influence of the welding speed on the force and the cooling rate is increasing at higher rotational speeds owing to the material conditions ahead of the tool.
- A direct correlation could be found between the temperature peak and the SZ size, thus showing the importance of the contact condition on joint formation.
- Aside from the conventional areas developed in SSFSW, a new zone could be observed in the stringer at the top of the SZ, which shows features similar to a TMAZ—but with variations in the thickness and grain-size owing to the changes in the tangential speed and shear forces.
- A key microstructural feature in the joint is the interface between the two alloys and the geometry of it. It is controlled by both the welding parameters due to the changes in material flow.
- The SEM analysis showed weak bonding at the end of the interface due to the reduced pressure between the material and the backing bar at the joint corner.
- While the yield strength of the joints is similar for all the parameters analysed, the UTS is controlled by the interface angle developed and the failure at different stress levels can be explained by the variation in the SIF.
- The pull-out test showed that the fracture happened directly in the interface of the two alloys, leading to the stringer delamination and that the mechanical interlocking is responsible for strength variations.

6. Comparison between the Different Joint Configurations

In this chapter, the three different joint configurations, introduced in the paragraph 3.2.1, are analysed and compared to each other. The approach is similar to the one followed in the previous chapter, starting from the microstructural characterization and continuing with mechanical analysis. At the end of the chapter, strong emphasis is laid on the strain analysis of the joints during mechanical testing by using the Digital Image Correlation (DIC) system.

6.1. Microstructural Comparison

The comparison between the microstructures generated for the three different process variants was analysed by starting from the general characteristic of the formed joints. Afterwards, a more detailed characterization of the specific microstructural features typical to each of the process variants, which differentiate them, were performed.

The microstructural overview of the three variants is shown in Figure 6.1 for the same combination of the welding parameters (1200 RPM, WS = 180 mm/min). The general properties of the interesting areas (SZ, TMAZs and HAZs) were similar for the three variants and will not be hereby repeated in order to focus on the differences among the variants.

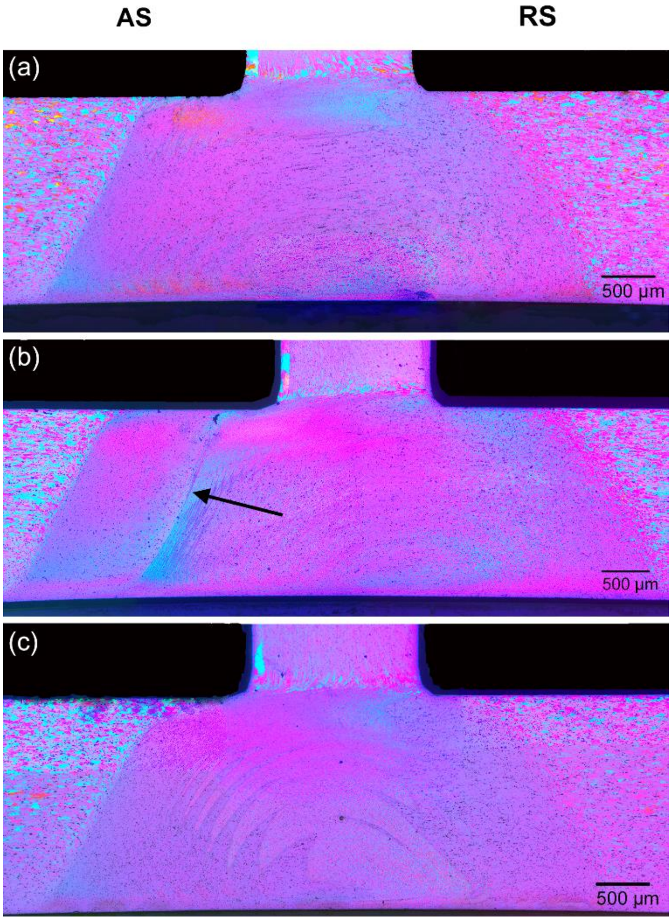

Figure 6.1. Macrographs of the welding area for the joint configuration: (a) NS-SP, (b) NS-DP, and (c) 3-Parts

The first image (Figure 6.1a) was relative to the notch–skin single pass that was previously shown and it will be used as a comparative basis for the other two variants.

In the case of notch-skin double pass joints (Figure 6.1b), it is possible to see the border of the SZ in the AS for both the welds run (indicated with the arrow), proving the double effect on the microstructure and the resultant increased recrystallized area in the SZ. This led to the formation of a new grain boundary wall within the SZ itself, with slight grain growth and rotation beyond the surface. This same behaviour could not be observed in the RS, where the second weld pass completely overrode the first pass, making it impossible to see the previous SZ boundary. The smoother transition of the microstructure in the RS caused by the extrusion mechanism around the probe could be recrystallized by the second pass, thus generating a homogeneous globular microstructure without discontinuity. A new TMAZ is formed in the RS, far ahead with similar characteristics to the one of the single pass variant.

No differences could be noticed in the general macrostructure of the weld comparing the NS-SP and the 3-Parts weld (Figure 6.1c). The shape of the SZ and the TMAZs showed similar results when analysed at such a level of magnification. The fundamental difference between the two microstructures could be seen in the centre of the SZ where the two materials were stirred together. In the 3-Parts weld, the presence of the AA7050 in the centre was clear throughout all the skin thickness, with sharp interfaces between the two materials towards the AS and RS. This full penetration of the interface provides the opportunity to visualize the different material flows between the two sides of the joint, especially around the middle of the sample thickness. In the AS, where the material was fully stirred around the probe, the interface is layered in periodic hemispheres, with strong interlocking between the two materials. On the other hand, in the RS, the interface appeared mostly flat due to the extrusion of the material outwards and reduced movement around the tool. Another effect of asymmetric rotation and the flow of the material can be seen in the movement of the AA7050 from the centre of the joint towards the AS. As previously discussed, in the NS-SP weld, this interface was limited to less than a millimetre at the topside of the joint. Therefore, the reduced tangential speed and strain energy, owing to the smaller diameter at the probe tip, did not allow the layering of the material that remained compact and moved towards the AS.

In order to fully capture the nature of the interface between the two alloys and the transition region between the skin and the stringer, higher magnification images were realized for the three variants. The focus of this analysis was on the top part of the weld, which was the most critical part from a structural point of view owing to the vicinity to the skin-stringer corner and the stress concentration effect (Figure 6.2). From a comparison between the NS-SP and NS-DP (Figure 6.2a, b), it was clear that owing to the second weld in the latter variant, the interface moved towards the AS of the joint. As a result of this effect, the interface angle, as defined in section 5.2.3, decreased drastically and the material mixing increased. The separation between the alloys appears unclear due to higher diffusion and mechanical inter-locking. Through the second pass, the grains in the TMAZ at the top of the SZ resulted in more strained conditions and the convergence of the grains from the globular to the extruded condition moved deeper into the stringer height. The purely extruded grains, which were arranged over the symmetry axis of the probe in the NS-SP, where there was zero tangential speed, are now moved towards the RS after the second passage, as well.

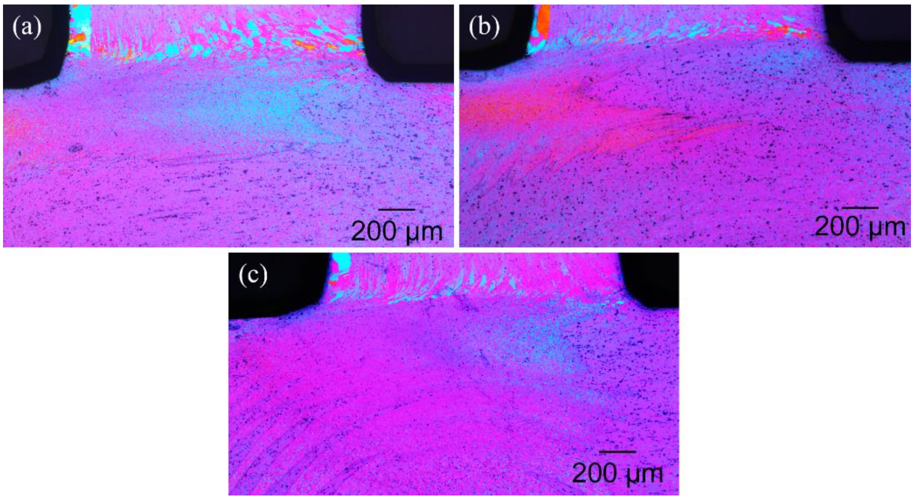

Figure 6.2. Materials interface and TMAZ at the skin–stringer border for (a) NS-SP, (b) NS-DP, and (c) 3-Parts

In the 3-Parts weld (Figure 6.2c), the materials interface in the area of the joint underneath the stringer showed similar results to the interface observed for the NS-SP. The material flow in this area was influenced by the process parameters and not by the joint configuration analysed. Naturally, the materials' interface between the two configurations diverges while moving deeper in the skin, as previously explained. The larger amount of AA7050 stirred around the probe influences the TMAZ between the skin and the stringer. The grain growth observed in the case of the NS-SP is not visible for the 3-Parts weld. In the NS-SP, the overlap between the two alloys influences the vertical heat transportation, which caused grain growth. Owing to the material continuity of the 3-Parts in the centre of the joint, this zone looked very similar to what was observed in the TMAZ at the AS of the joint.

As for the NS-SP welds, an SEM analysis of the interface endings was performed for the other two configurations in order to identify possible defects and weak bonding (Figure 6.3).

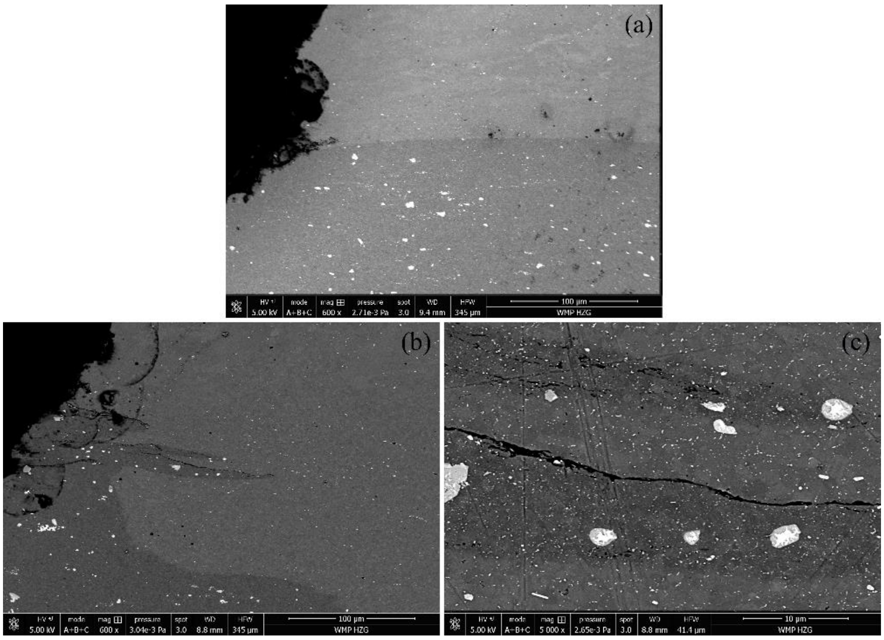

Figure 6.3. SEM analysis of the interface-end for (a) NS-DP, (b) 3-Parts overview, and (c) 3-Parts detail view

In the NS-DP (Figure 6.3a), no presence of any kind of defect was found at the end of the interface. The second run and stirring of the material solved the problem of the weak bonding as previously seen for the single pass variant. The interface between the two alloys is still very clear and it is still possible to see the larger inclusions present in the AA2024. For the 3-Parts weld, a similar feature to the one generated in the NS-SP was observed (Figure 6.3b). Once again, at the edge of the backing bar, the lack of necessary pressure leads to a line defect (weak bonding) at the corner of the joint at the RS of the weld. From the higher magnification of the SEM image (Figure 6.3c), it is possible to see that the imperfection develops at one of the interfaces between the two alloys. The interface between AA2024 (darker alloy in the image) and the AA7050 resulted in more interlocking at the microstructural level, thus increasing the overall resisting surface.

Quantitative measurements were performed on the SZ and the interface angle to determine the influence of the process variant on material transport (Figure 6.4). The interface angle drastically decreased after the second pass with the same welding parameters in the notch skin joints (Figure 6.4a). The double-stirring of the materials pushes the SZ area upwards, causing an angle reduction of around 10 degrees. A smaller interface angle was also measured in the case of the 3-Parts welds. Owing to an absence of the overlap region between the two alloys, the resistance in vertical material transport was reduced and the interface angle decreased by 3 degrees.

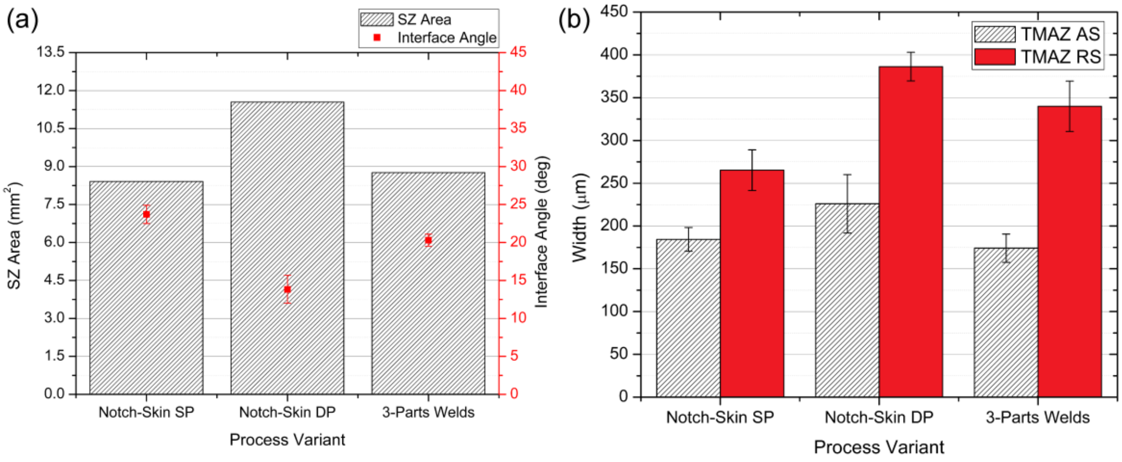

Figure 6.4. Microstructural measurements of joint configurations for (a) SZ and (b) TMAZ

The size of the SZ was measured in the case of the NS-DP and was, as expected, larger in relation to the other two variants. Nevertheless, while comparing the effective size of the SZ with the cross-sectional area of the cumulative probe (the geometry of the probe by combination during the two-weld path), the difference is exactly the same—approximately 1.9 mm^2—of what was measured in the case of the single pass variant. Consequently, it can be stated that the second pass does not influence the amount of material stirred and recrystallized by the probe during each pass. In the 3-Parts weld, a small increase in the SZ area could be measured in comparison to the NS-SP pass variant. An important role for this phenomenon is played by the through thickness interface between the two alloys that influences the amount of material extruded outward. A confirmation of the interface's influence in the extrusion process of the material could be seen in TMAZ measurements (Figure 6.4b). While the TMAZ width of the 3-Parts and the NS-SP variants are similar in the AS of the joint, where the material is stirred around the probe and the interface is layered and inter-locked, in the RS, a significant increase of the TMAZ width could be measured. In the case of the NS-DP, both the TMAZs, in the AS and RS, showed enlarged results. The influence of the double heat and deformation cycles led to a delay in the re-orientation of the grains parallel to the rolling direction.

The grain-sizes, developed after welding with the three variants, were measured for the characteristic areas of the weld: TMAZ-AS, SZ, and TMAZ-RS, and were referred to the AA2024 original grain size (Figure 6.5).

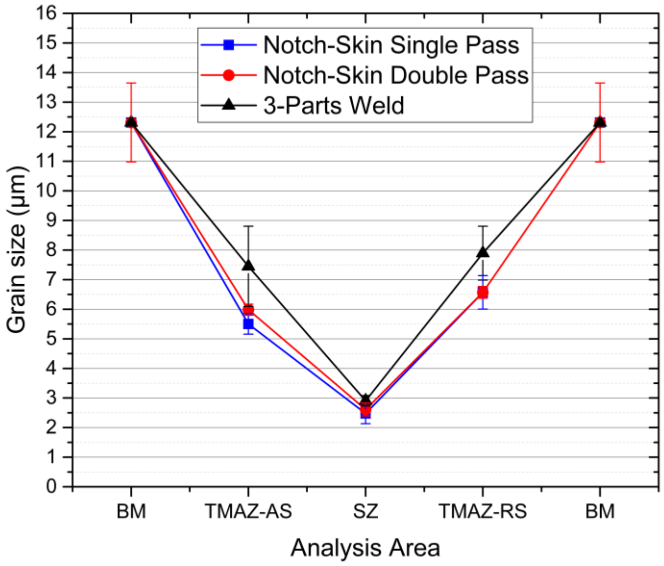

Figure 6.5. Grain size measurements for the three joint configurations

While comparing the two notch-skin joints, it was not possible to see any strong influence of the double heat cycle on the grain size of the material in the SZ and in the RS; instead, an increase of the grain size could be measured in the AS. The specific growth in the TMAZ at the AS was expected by considering that this area was formed during the first weld and it was not mechanically influenced during the second pass. The lack of mechanical stirring and material transport caused the absence of the recrystallization phenomenon, while the heat generated during the second pass could cause grain growth.

The 3-Parts weld presented a different grain size profile in comparison to the two notch skin variants. The smaller difference between the variants was seen in the SZ, where the dynamic recrystallization phenomenon controlled the grain size and the shape, and the different alloys located in the SZ centre only played a small role. In the two TMAZs, the grain size showed enlarged results with respect to the other process variants. It is assumed that the higher strength of the AA7050 influences the deformation induced by the material in direct contact with the probe on the surrounding material. Owing to this, the grains were less strained resulting in an increase in their size.

6.2. Mechanical Comparison

The comparison between the process variants was performed initially based on the hardness results and by comparing the local properties of different zones. Afterwards, the structural behaviour of the joints was analysed through load cases—same as the ones shown in the paragraph 5.3.

6.2.1. Micro-hardness Analysis

The hardness variation for the three joint configurations in the horizontal direction in the middle of the skin thickness is shown in Figure 6.6.

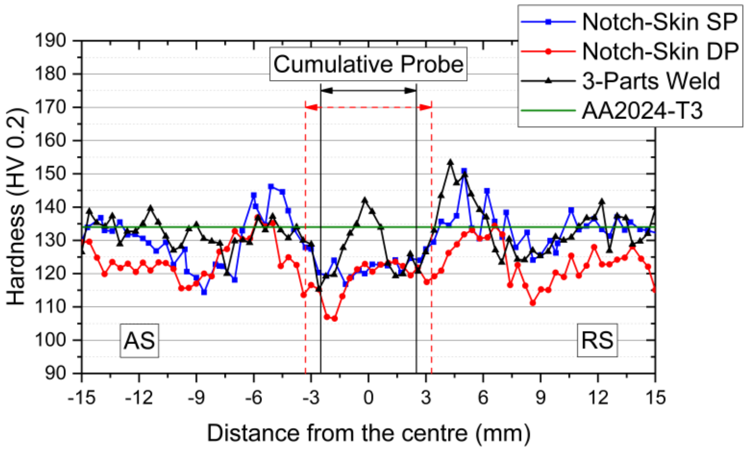

Figure 6.6. Horizontal hardness profiles for the three joint-configurations

Outside the SZ area, the hardness measurements in the case of the 3-Parts welds showed a similar behaviour to what had been seen in the case of the NS-SP. On both sides of the 3-Parts joint, the hardness decreased in the initial part of the HAZ (AS: -11 to -8 mm and RS: 12 to 8.5 mm) to increase once again in its second part (AS: -8 to -5 mm and RS: 8.5 to 4.5 mm). The hardness valley and the peak of the HAZ in the AS are smoother in respect to the other configuration. The minimum hardness values in the TMAZs are the same as for the notch skin variant, showing no influence of the AA7050 and a comparable behaviour of the precipitates. The main difference could be noticed in the SZ, where the hardness profile was influenced by the presence of the AA7050 throughout skin thickness. The change of hardness was observed in a limited area and did not create a plateau since the indentations, aside from the peak point, were in an area where both the alloys were present. The peak of hardness was moved towards the AS (-0.5 mm), as previously observed in the case of interface analysis (Figure 6.1c), followed by a flat part of the curve in the area of the SZ that was possibly dominated by AA2024 re-precipitation.

The evolution of hardness in the case of the NS-DP presented characteristics that were different with respect to the same joint configuration welded in a single pass. The area affected by the heat developed during the process was extremely enlarged and the AA2024 hardness was not reached along the 30-mm line over which it was measured. In the first part of HAZ at the RS of the joint (up to 9 mm), the hardness had a larger reduction owing to the double heat transfer and consequent precipitate coarsening. This phenomenon was more pronounced in the RS since the second weld pass was moved towards this area. A similar behaviour could be noticed in the second part of the

HAZ (±9 to ±5 mm) on both sides of the joint, where the hardness increase was reduced significantly and reached the level of the base material, without overcoming it. The resulting material properties seemed to exhibit three different TMAZs—two in the AS of the joint (-5 to -4 mm and -3 to -2.5 mm) and the conventional one in the RS (5 to 4 mm). The two outer ones (±5 to ±4 mm), where the hardness decreased from the HAZs to reach a minimum, behaved in a similar way to the other two configurations even if the minimum values were reduced for this area as well. The third valley of hardness, with a behaviour similar to TMAZ, could be seen where the edges of the SZ, which were created during the second pass, were observed. This hardness reduction was observed within the dynamically recrystallized grains of the SZ and, therefore, it was certainly not connected with grain size variation, as previously seen (Figure 6.5). The newly formed precipitates, after the dissolution caused by the first weld step, were coarsened in the second pass, thus leading to the largest hardness drop measured along the profile. Soon, it will be seen how this strongly influences the mechanical properties of the joint and the location of the final failure. The other part of the SZ did not show any difference with respect to the parent configuration and the hardness values lay on the same line. It is assumed that the precipitates in this area could dissolve once again in the second pass and generate new phases similar to the ones formed in the NS-SP.

In Figure 6.7, the hardness variation is shown while moving from the skin to inside the stringer.

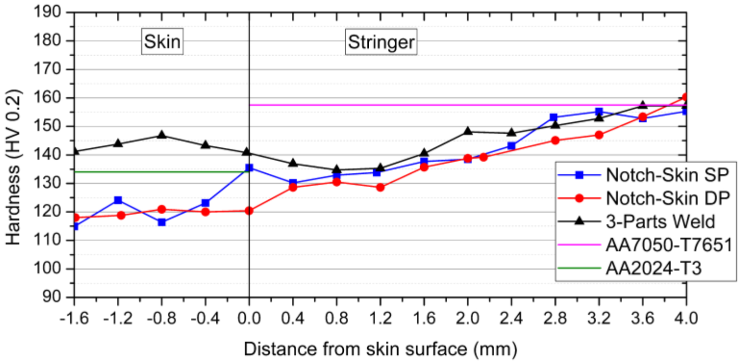

Figure 6.7. Vertical hardness profiles for the three-joint configurations

In the NS-DP variant, the retardation in the recovery of the AA7050 hardness was similar to what observed in the horizontal hardness measurement. The SZ hardness was uniform up till the skin upper surface without any influence of the stringer material, even after the original overlap between the two alloys. Owing to the upward pushing of the AA7050 in the multi-run, there was no influence of it on the SZ and the usual reduction of hardness in the TMAZ could not be seen. In that case, the area was characterised by the transformation of AA7050 precipitates, which were still higher in hardness than the newly formed precipitates of the AA2024 in the SZ. The profile increased steadily from the TMAZ up to the base material with a large HAZ that showed a gradual transformation on the precipitates.

For the 3-Parts weld, the hardness profile was similar to what it could be expected from welding just AA7050, with no influence of the other alloy. The hardness drops in the TMAZ at the top of the SZ probably owing to the coarsening of the precipitates. While moving upwards in the stringer, the hardness gradually increased in the HAZ until the base material value of hardness was reached. For all three variants, the division between the two parts of the HAZ that was previously shown in the horizontal hardness profile (Figure 6.6) could not be observed. Lower heat transfer and reduced stirring in the vertical direction influenced the hardness increase/decrease due to the transformation of the precipitates and in all variants, the transition showed smoother and almost linear results.

6.2.2. Hoop Strength

The comparison between the yield and the tensile strength achieved during the hoop-tensile test by the three joint configurations produced with the same process parameters is shown in Figure 6.8. The yielding levels were similar in all the configurations analysed and they overcame 90% of the AA2024 yield strength in the transverse direction. A high constancy of the results could be achieved for all the configurations, thus confirming the robustness of the process and the developed microstructure throughout the entire welding length, even while changing the joint configuration or after repeated welds as for the double pass configuration. For both the notch skin variants, single and double pass, a slight increase of the yield strength could be observed. The more homogeneous SZ material, without the influence of the AA7050, except for a few microns after the skin–stringer interface, led to a reduced concentration of stress/strain in the area of the joint, where the minimal limit of the hardness values were measured, thus improving the yielding performance of the joints.

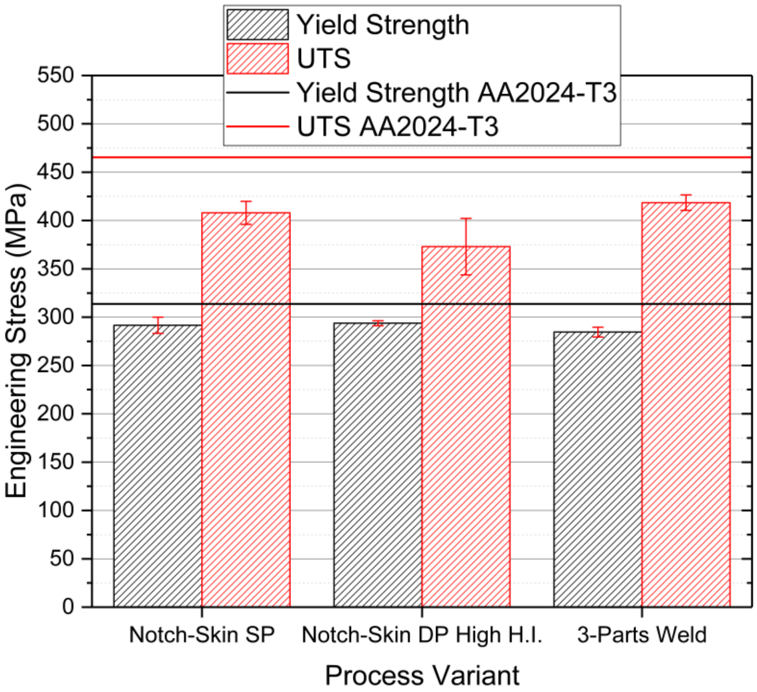

Figure 6.8. Yield strength and UTS for the three joint configurations and the AA 2024-T3

While considering the final strength, the differences between the three configurations became evident. The NS-DP joints reached lower hoop strength, with an increase in standard deviation. This increase in standard deviation was probably caused by the variability in the distribution of precipitates along the joint and the reduction of microstructural repeatability while double heat generation was applied. The higher hoop strength was reached in the 3-Parts welds, where 90% of the base material tensile strength was achieved with an increase with respect to the NS-SP process.

For a more detailed overview of the results, the full stress–strain curves for the three processes are shown in Figure 6.9. In addition to the results analysed, the curves for the NS-DP joint obtained under the coldest welding condition (800 RPM and 420 mm/min welding speed) and for a riveted joint were plotted. This curve was obtained from Kashaev et. al. [104], relative to the static strength of the riveted joints between AA 2024 skin and AA 7075 stringer.

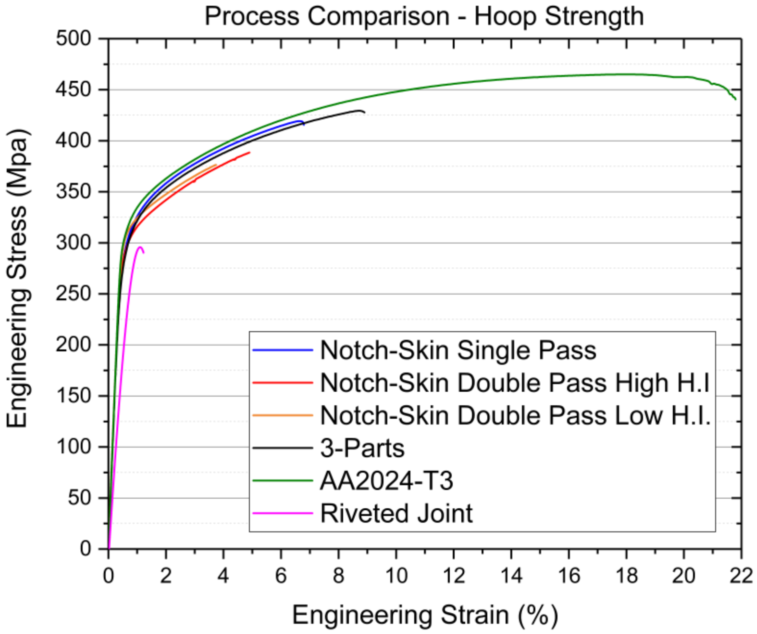

Figure 6.9. Engineering stress–strain curves for SSFSW, riveted T-joints, and AA 2024-T3

The NS-DP pass joint, obtained with low-heat input, showed an increase in the yielding point but a slight reduction of the stress and strain corresponding to the final failure. The lower energy transferred into the weld possibly caused a reduction in the coarsening of the precipitates and in the total surface affected by the welding process that led to the higher yield strength. In order to understand the reason for the lower joint strength, it is interesting to analyse the fracture mechanism shown in Figure 6.10b and c. In the joint obtained with the higher heat input (Figure 6.10b), the fracture was located exactly at the TMAZ formed by the second weld pass in the AS, where the minimum hardness was also measured. The failure, in this case, was dominated by the post-process formed microstructure and its influence on strengthening precipitates. The crack at the end, near the top surface, was turned by 90° due to the presence of the AA7050 in the upper layer of the SZ, which characterized a higher strength path for the crack to propagate. In the low-heat input joint, the fracture was completely dominated by the interface between the two alloys in the skin-stringer corner and, as previously shown, it was influenced by the angle that was formed with the top surface (interface angle). The higher angle measured for ‘cold-weld’ parameter set, around 33^{o}, led to a failure similar to what observed for the NS-SP variant. The earlier crack initiation, after the yielding, causes the reduction of strength with respect to the joint obtained with the high heat input. The double pass variant shows an important limitation in the possibility of further improvement of joint properties since increasing energy input leads to a deterioration of the microstructure and decreasing it causes a high interface angle that determines the early failure.

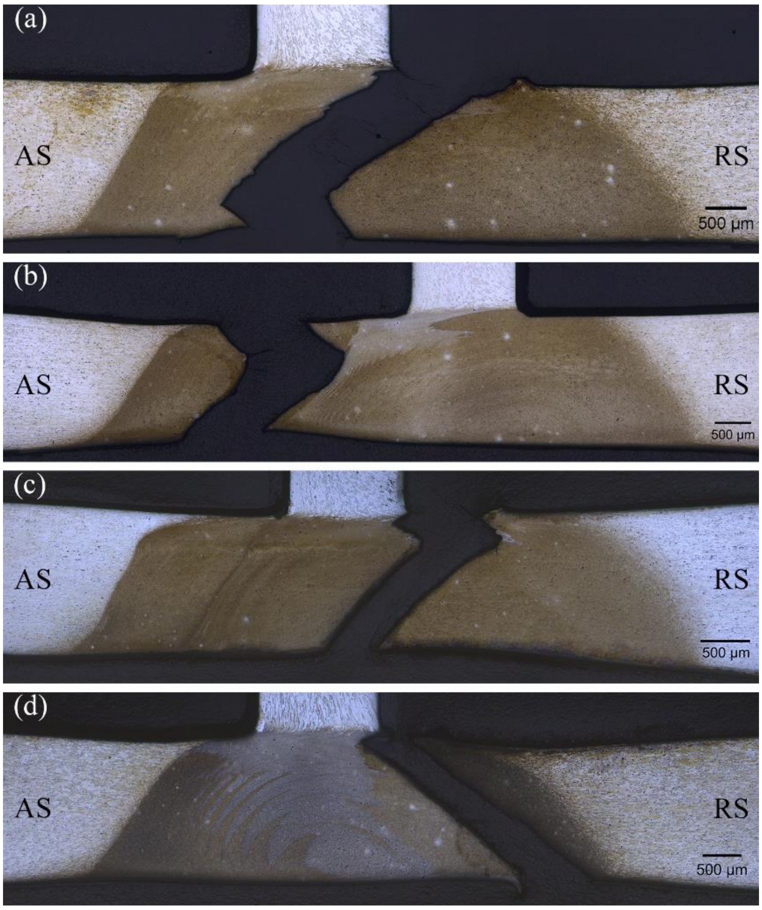

Figure 6.10. Fracture analysis in hoop direction for the joint configurations in (a) NS-SP, (b) 'hot' NS-DP, (c) 'cold' NS-DP, and (d) 3-Parts

The 3-Parts and NS-SP curves experience similar development until the final failure, where the influence of the AA7050 on the first joint configuration leads to higher strength and deformability (Figure 6.9). The differences between these two joints' strengths can be explained through the analysis of the fracture mechanism (Figure 6.10a and d). For both the configurations, the fracture was initiated at the interface between the two alloys and was, once again, influenced by the interface angle. In the 3-Parts weld, the fracture propagates along the interface before turning and running on the maximum shear stress path with a 45° angle outside the centre of the SZ. The smaller interface angle, which was previously measured (Figure 6.4a), causes a retardation in the failure initiation in comparison to the NS-SP. This factor, combined with crack-turning driven by the presence of the AA7050, contributes to an improvement in the joint strength.

While comparing all the process variants with the curve obtained for the riveted joint, it can be seen an improvement on both the failure strength and the ductility of the joint (Figure 6.9). The stiffness in the elastic area of the curve for all the welded configurations is similar to the stiffness of the AA 2024 and higher than the stiffness of the riveted joint. The hoop strength improvement varies between 26% in the case of the NS-DP joints up to the 41.5% for the 3-Parts welds (+38% for the NS-SP joint). The advantage with respect to the riveted joint is not only in its higher strength but also in a more damage-tolerant design due to the higher ductility of the joint, which allows for a certain degree of safety after the yielding is reached. In contrast, in the riveted joint, the failure mode is brittle with no measured plasticity.

In this loading condition, by using the 3-Parts weld configuration, it would be possible to reduce the skin thickness to 1.5 mm and reaching a force higher than the one of the riveted joints at failure. With this thickness, a stress level equal to 394 MPa was reached, warranting a safety margin of the 6% over the hoop strength. Without considering the absence of the stringer foot with respect to the riveted joint, this thickness reduction would lead to a weight saving in a 1 m^2 panel of 25%.

6.2.3. Pull-out Strength

The load–displacement curves of the three joint configurations, obtained with the combination of process parameters that guaranteed the highest failure load, are shown in Figure 6.11.

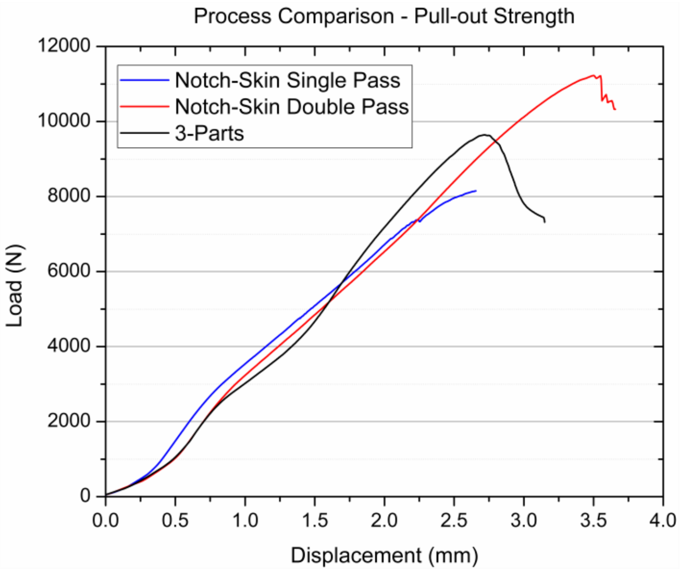

Figure 6.11. Pull-out strength of the three joint configurations

For the 3-Parts and the NS-DP, the same set of process parameters (1200RPM, 180 mm/min) led to the highest strength both in the pull-out and the hoop direction. On the other hand, for the NS-SP, the highest strength was obtained in the case of 'cold' welding conditions (800 RPM, WS = 300 mm/min), as observed in the section 5.3.3. Even by using different process parameters, the lowest failure load was reached in the NS-SP variant alongside an increase in joint stiffness in the initial phase of the test. Aside from the higher loads achieved for the other two joint configurations, it is of special interest the behaviour of the curves before the failure. While in the NS-SP joint, the failure suddenly happened, without showing any signs of plastic deformation; in the 3-Parts welds, the joint kept a certain load-bearing capability after the peak of the curve was reached. The failure behaviour for the double pass variant was showing a small level of load bearing capability after the maximum load was reached during the test. However, the damage propagation was not as large as the one seen for the 3-Parts joint.

The analysis of the fracture mechanisms, as shown in Figure 6.12, clearly explains the reason behind the different behaviours noticed at the end of the tests. As seen in the section 5.3.3 and reported in Figure 6.12a, the fracture behaviour in the case of NS-SP was completely defined by the length of the interface between AA2024 and AA7050, and the failure was located alongside it.

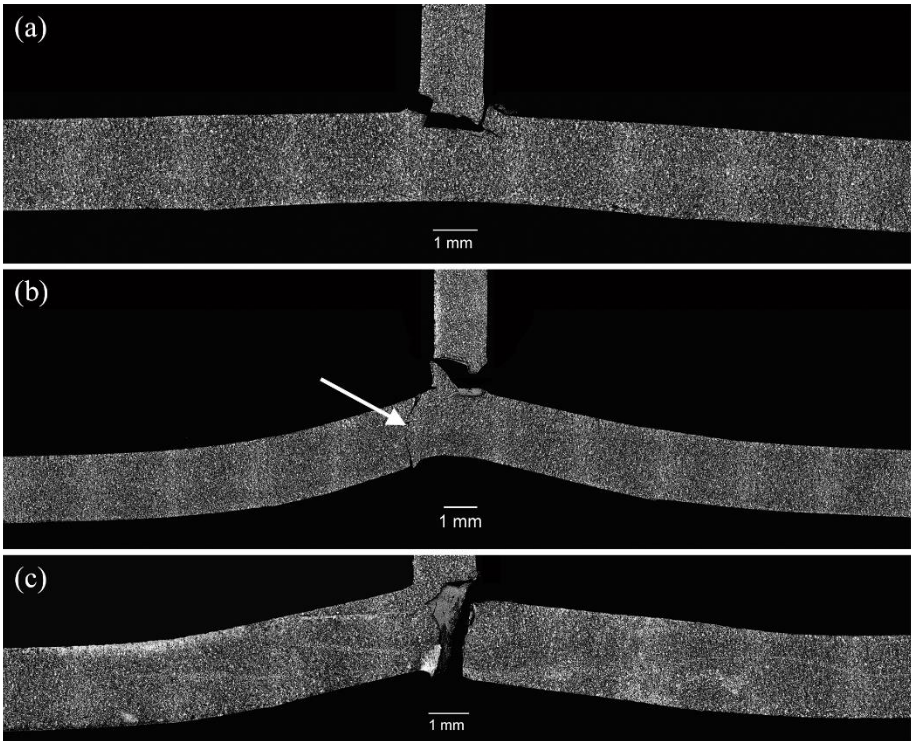

Figure 6.12. Fracture analysis in the pull-out direction for the joint configurations (a) NS-SP, (b) NS-DP, and (c) 3-Parts

For the 3-Parts weld (Figure 6.12c), the fracture starts at the interface angle, alike the hoop strength and propagates along the two alloys' interface throughout the skin thickness. At the end of the test, the stringer does not detach from the skin and the crack is driven by bending and shear stresses along the interface, where the strength is minimum. The interface length, measured, in this case, in the vertical direction, plays a major role in the strength of the joint and it was observed that the longest interface length and the increase in the mechanical interlocking between the two alloys determined the highest load achieved for the set of parameters investigated. The propagation of the crack along the interface explains the load-bearing capability of the joint after the peak load was reached. The fracture mechanism showed similar results for all the welding conditions analysed and, although differences were measured in the maximum load, the stringer was never detached from the skin.

The final failure (Figure 6.12b), in the NS-DP variant, for the chosen welding condition was located above the interface of the two alloys in the TMAZ at the top of the SZ. The stress concentration at the skin-stringer corner initiates the crack that found an easier propagation's path in the area where the double heat input affects the transformation as well as the coarsening of the precipitates the most, as observed in the vertical hardness profile (Figure 6.7). The high loads caused significant bending and shearing stresses in the skin and, as a result, it was possible to observe a secondary crack propagating in the skin indicated with an arrow in the picture. This crack was developing in the same area, at the edge of the second welding pass, where the failure, in case of the hoop strength, was observed and the minimum hardness of the joint was measured. In contrast with the 3-

Parts weld, in the NS-DP configuration, a large variability of results was obtained for the different process parameters. With a lower heat input, reduced RPM, and increased WS, the fracture mechanism showed identical results in comparison to what was observed for the single pass-variant with a strong influence of interface geometry and the drastic drop in the maximum load reached during the test.

6.3. Local Strain Analysis with the DIC

The strain analysis performed through the ARAMIS system provides important information with regard to strain partitioning in samples containing different microstructural characteristics. The structural influence of the stringer on the strain behaviour during the hoop- and pull-out tests can also be analysed.

6.3.1. Load Condition: Hoop-strength

In the first part, the analysis for the hoop-strength of the joints will be focused on the 3-Parts weld, showing the strain profiles in different sections of the joint and the local stress–strain curves for specific areas of interest. In the second part, the focus of the study will be on the differences in the strain mechanism between the three variants.

In Figure 6.13a, the strain map over the lower skin surface before the final failure is shown, with the RS of the weld in the upper part of the image. A detail of the already formed and propagating crack through the sample's thickness is presented in Figure 6.13b with the arrow indicating the position of the crack. The strain map shows a certain degree of symmetry of the sample during the test, both in the horizontal and the vertical direction.

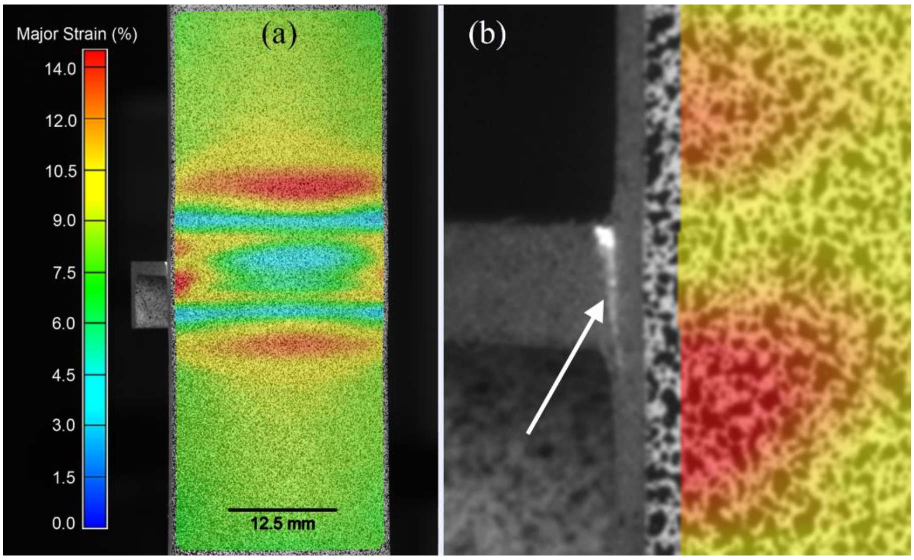

Figure 6.13. Strain map in hoop tests before the failure for the 3-Parts configuration—(a) complete map and (b) detail of the crack

The strain varies in the horizontal direction differently to what was expected during a conventional tensile test. The lateral contraction of the sample happened outside the SZ, where the lower hardness of the first HAZ part was previously determined, contributing to the strain peaks that are to be analysed. Owing to the high-strength stringer in the centre of the joint, the lateral contraction driven by the Poisson’s ratio is impeded, thus leading to stress concentration at the edges of the specimen. As observable from the detailed Figure 6.13b, this strain concentration was particularly high at the edges of the stringer and caused the initiation of the crack where the interface angle was located. The image showed a considerable amount of crack propagation already through the thickness before reaching the maximum load, thus proving the good fracture toughness of the material in the SZ.

A quantitative strain analysis was performed along the horizontal section placed exactly in the area where the strain peaks were measured and the crack was propagating (Figure 6.14). While the strain was still distributed homogeneously at the yielding moment (σ = 292 MPa), within the 0.2%, high variations could be observed prior to the final failure. At such load level, the strain profile along the section was distributed in a parabolic shape, with a minimum value of around 5% reached at the centre of the sample. The strain, at the edges of the specimen, was approximately twice as high, with a peak value higher than 11%. According to the data, the crack was not only propagating through the thickness but was formed at the edges of the specimen and it ran in a perpendicular direction to the applied load in the direction of the width.

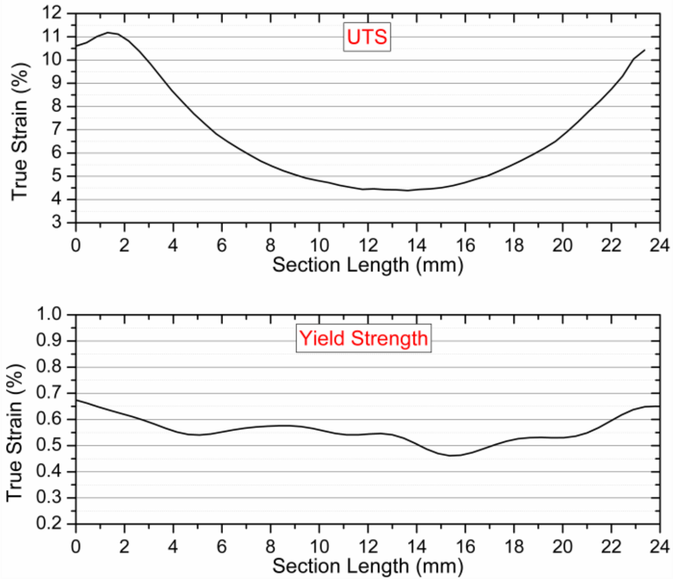

Figure 6.14. Horizontal strain profile for the 3-Parts welds at UTS and yielding

The specimens’ size, therefore, influences the strain and stress distribution. In a wider sample, the strain would be more homogeneously distributed in the horizontal direction with a larger area in which the crack could propagate. Since the failure was driven by the crack propagation and the SIF, it was expected that in the case of specimens’ upscaling, the weld would be able to withstand higher stresses, thus increasing the global strength of the skin–stringer connection in the hoop direction.

If in Figure 6.13 the attention is focused on the strain variation in vertical direction, the part of the joint underneath the stringer showed the lowest strain owing to the combined effect of the local thickness increase and the higher strength of AA 7050. The strain increased both under the stringer edges and in the area outside the SZ, where the second part of the two HAZs were located. The first two strain peaks were caused by the combined effect of the stress concentration due to the skin–

stringer corner and the transition between the area of the SZ dominated by the AA 7050 and the one characterised mainly by the AA 2024. The outer strain peaks were located at the first part of HAZ where the microstructure has been weakened by the effects of the weld thermal cycle.

The true strain profile, alongside a vertical section in the moment of global yielding and before the final failure, is shown in Figure 6.15.

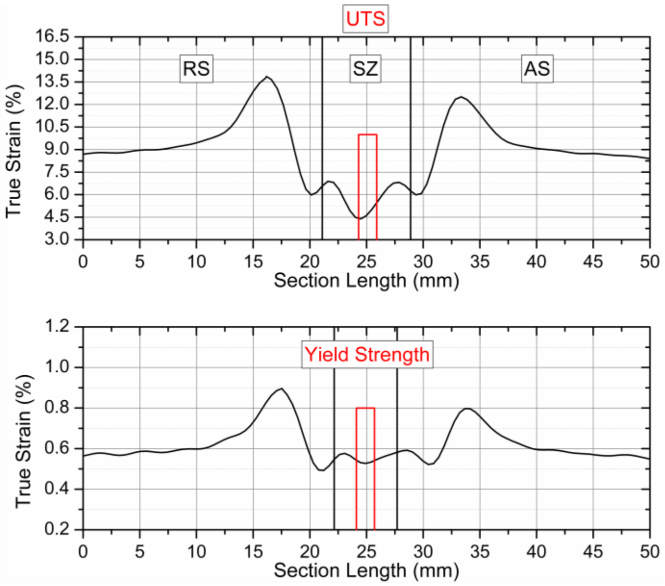

Figure 6.15. Vertical strain profile for the 3-Parts welds at UTS and yielding

When yielding was reached, all the material in the SZ had a lower level of strain in comparison to the AA 2024. A slight strain increase could be observed in the areas beside the stringer, which was equal to 0.6%. In all the SZ as well as in the base material, the strain level was still entirely in the elastic field with the possibility of reversing the deformation. A significant increase of the strain could be measured in the first part of the HAZ, especially in the RS of the joint, where the material was already fully plasticized.

The differences highlighted for the strain profile at yielding became more evident before the final failure. The combined analysis of the hardness profile, shown in Figure 6.6, and the strain profile helped to separate the influences due to microstructural features, such as precipitate evolution and grain size, from the structural influences. The minimum strain (4.5%) at the centre of the SZ increased up to 7% in the small area at the side of the stringer. The two strain peaks in the SZ did not find correspondence in the hardness profile and this was a consequence of the stress concentration at the skin–stringer corner and the material discontinuity at the interface of the two alloys. This last feature plays a role in the displacement of the peaks toward the RS, similar to what was observed for the interface at the bottom surface of the specimen (Figure 6.1). In the area where the minimum hardness was measured, the edge between the SZ and the TMAZ, the strain decreased, showing a difference with respect to what was expected from the microstructural analysis. This is a clear example of the structural influence of the stringer and the mutual influence of each welding area. On one side, the TMAZ has an area where the effect of the skin-stringer corner, with its stress concentration, creates the peak; on the other side, it has the second part of the HAZ, where it had previously shown an increase in hardness, correlated with the transformation of the precipitates. Therefore, in spite of the better material properties of the SZ, the level of strain in the TMAZ decreased. As already observed, the minimum strain outside the SZ was reached in the second part of the HAZ. The strain here was below the AA2024-T3 base material strain (9%) and around 6%. Finally, the last two peaks of strain were in agreement with the hardness profile, corresponding to the first part of the HAZ where microstructural weakening took place, leading to a strain peak over 13.5%.

The slight strain asymmetry in these two peaks was the same as previously seen in the hardness profile, where a larger decrease was measured in the RS.

Through DIC analysis, it was possible to calculate the true stress of the joint's areas previously described and plotted in stress-strain curves in each case. The model used to calculate the true stress, once the true strain was known, was based on the following set of equations (6.1):

$$\begin{cases} \boldsymbol{\sigma_T = \sigma(1+\varepsilon)} \\ \boldsymbol{\varepsilon_T = \ln(1+\varepsilon)} \end{cases} \rightarrow \begin{cases} \boldsymbol{\sigma_T = \sigma e^{\varepsilon_T}} \\ \boldsymbol{1+\varepsilon = e^{\varepsilon_T}} \end{cases} \tag{6.1}$$

where, σ and ε are the engineering stress and strain, respectively, while ε_T and σ_T are the true ones. The calculated true stress could be used with high confidence owing to the direct acquisition of the true strain from the surface of the specimens. Consequently, the engineering stress could be related directly to the true stress by the accurate measurement of the true strain over a small area. This approach avoided the use of more complex analytical relations that required a large number of parameters to simulate material behaviour.

Owing to the general symmetry and fracture location, the stress–strain analysis was performed from the RS until the centre of the joint at the vertical section at the centre of the specimen. In Table 6.1, the location of the points used for the analysis and the respective joint area have been shown:

Table 6.1. Locations for the stress–strain analysis

Point Position (PP)	Section Length (mm)	Joint Area
15	3.97	AA2024-T3
40	16.17	HAZ1
48	20.12	HAZ2
51	21.58	SZ/Stringer
57	24.49	SZ-Centre

The true stress–true strain curve of the AA 2024 (PP15), shown in black in Figure 6.16, was used to confirm the validity of the method used to calculate the stress as well as a term of comparison for the analyzed area. This curve was in agreement with the curve obtained from base material testing, both in terms of yield stress and the stress reached for the final level of deformation, when the influence of necking on the base material's tests was included. The only curve that shows a deterioration of the strength with respect to the base material was the one relative to the first part of the HAZ (PP40). In this case, the yield stress decreased to around 260 MPa, thereby explaining the large difference in the strain previously measured at both global-yielding and failure. The curvature of the plastic part proceeded parallel to the base material's part and the strength difference at the failure between the two parts was expected to be similar to the difference measured for the yield stress. There is a high probability that this area is where the failure of the joint would occur if the crack did not initiate at the skin–stringer corner.

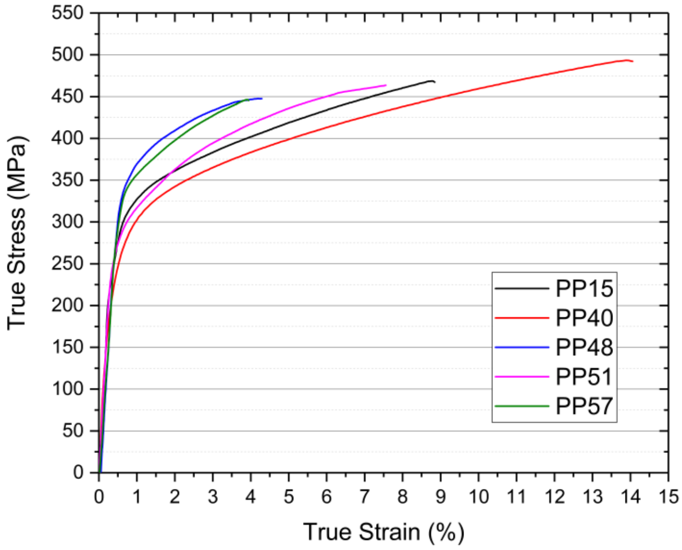

Figure 6.16. Local true stress-strain curves of the 3-Parts welds

The curve relative to the area underneath the stringer edge (PP51) shows a behaviour similar to the base material (PP15). The yield strength is slightly reduced (290 MPa), but a similar level of ultimate stress was measured due to the flattening of the base material curve after the initial state of plasticization. The two curves relative to the centre of the SZ (PP57) and the second part of the HAZ (PP48) presented a higher yield stress than the AA 2024 (333 and 342 MPa), and they could be differentiated from each other in the curvature of the plastic region. The AA 7050 in the SZ centre had a curve with a higher slope due to the better load capability at fixed strain values and lower ductility.

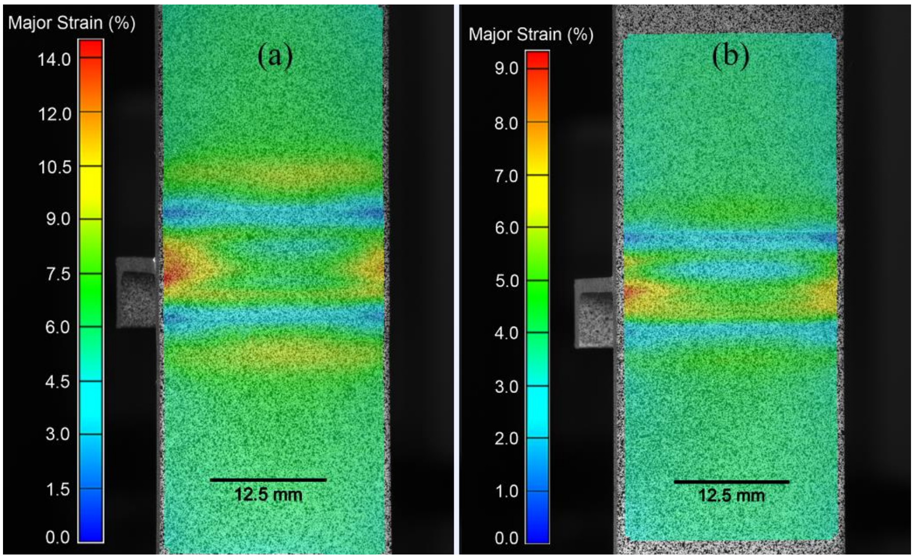

Figure 6.17. Strain maps in hoop tests before failure for (a) NS-SP and (b) NS-DP

A qualitative comparison of the deformation behaviour of the other two joint variants on the strain map before failure is presented in Figure 6.17. The RS of the joints is, once again, located in the upper part of both the pictures. The strain map relative to the notch-skin double pass process (Figure 6.17b) has a different scale bar in order to facilitate the visualization of different strain areas for a lower load level.

The strain maps of the two variants show qualitatively similar results to each other, with the main difference observable at the side of the specimens under the stringer. In the NS-SP, all the lateral area underneath the stringer showed strain intensification, while in the double pass, it was more localized to the skin–stringer corner in the AS. In contrast with the 3-Parts joint (Figure 6.13a), both variants did not show the strain reduction at the centre of the specimens, while a slight strain decrease could still be seen in the SZ towards the RS.

In order to quantify the different deformation mechanisms derived from the joint configurations, the strain had been analysed on a vertical section at the centre of the specimens. As an example, the different zones formed during welding are indicated directly on the graphic in Figure 6.18a. At global specimen yielding (Figure 6.18a), the differences between the three variants were already clear. While the same level of strain was reached for the base material and similarities could also be found at the first part of the HAZ (HAZ1), the largest differences appeared between the TMAZ and SZ. The strain level in the SZ for the two notch skin processes were higher, on average, than for the 3-Parts weld and the strain peaks could be seen in the AS of the SZ, especially for the double pass variant. This was the area where the minimum hardness was previously measured after the second run, when the sharp discontinuity in the SZ formed. These two factors led to weakening on one side and to a stress concentration on the other, owing to microstructural inhomogeneity, causing the abnormal strain peak.

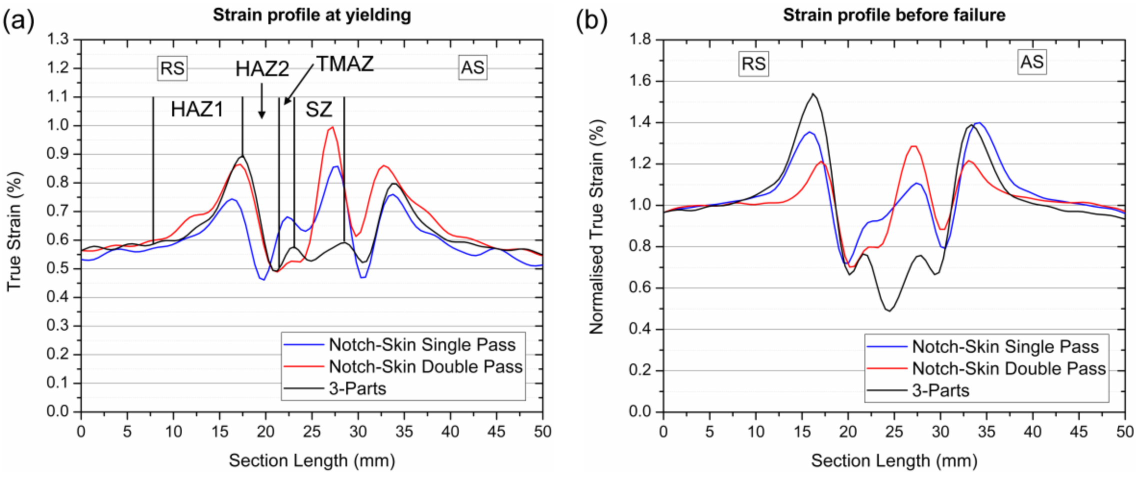

Figure 6.18. Vertical strain profile for the different joint configurations at (a) yielding and (b) UTS

The strain profile for the NS-SP was similar in terms of shape to the double pass variant but lower levels were reached at the peak (0.25% reduction). In the HAZ2, the lowest level of strain is reached both in the AS and RS while comparing the two other variants. The reason for this lower deformation, with respect to the double pass variant, was due to the lower heat input that caused different precipitates' evolution. In the 3-Parts variant, the larger dissimilarity of the microstructure and the strength between SZ and HAZ, generates a strain concentration with a peak in the HAZ, thus leading to the observed difference between the two configurations in the area.

In order to have a clear comparison between the three variants, the strain levels before the failure were divided by the level reached in the AA 2024-T3, leading to what is called a ‘Normalised True Strain’ (Figure 6.18b). In the NS-SP joint, the failure did not happen where the highest strain was measured and, as for the 3-Parts, the strength of the joint depended on the crack-resistance of the area where the initial defect was located. The strain peaks were in the first part of the HAZ due to the deteriorated microstructure and at the edges of the stringer caused by the stress concentration. In the SZ, the higher strain was in the AS as the crack propagated transversally in the area crossing the centre of the joint (Figure 6.17a). This behaviour was different from the behaviour observed in the case of the 3-Parts joints where the crack propagates outwards.

In the NS-DP variant, the strain profile and the fracture mechanism were in total agreement, with the highest strain measured at the interface generated by the second weld. The stress was higher in the area due to the combination of the stress concentration caused by the skin–stringer corner and the sharp microstructural change; it was located exactly in the zone where the minimum strength of the joint was expected, according to the hardness previously measured (Figure 6.6).

The strain profiles differ between the process variants when measured on the same horizontal section in the AS of the SZ previously analysed for the 3-Parts weld (Figure 6.19).

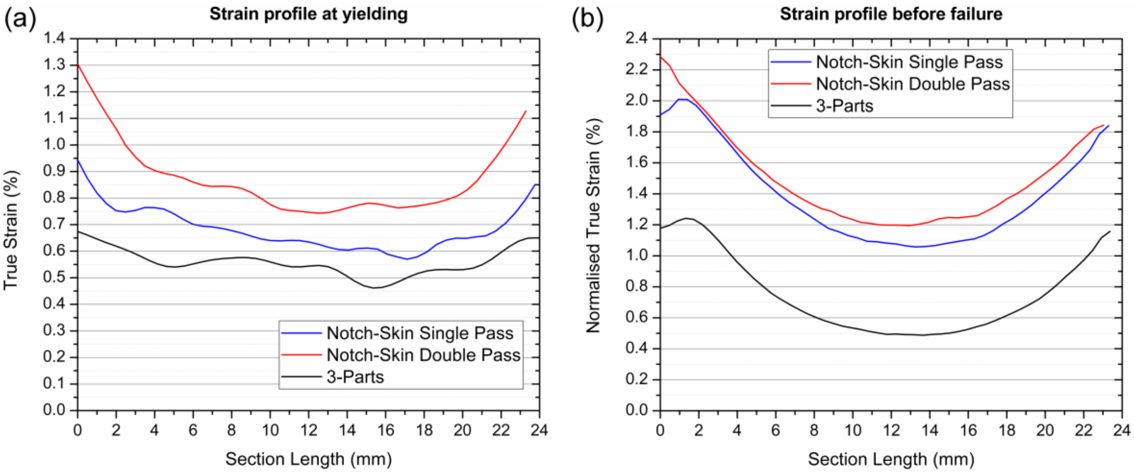

Figure 6.19. Horizontal strain profile for the different joint configurations at (a) yielding and (b) UTS

In spite of similar yield stress for all the three variants (Figure 6.8), large differences can be noticed along the strain profiles. In Figure 6.19a, the strain increases progressively passing from the 3-Parts weld to the NS-DP due to the lower strength of the material in the SZ. These differences are more pronounced at the side of the specimens where the stress is intensified.

While considering the strain profiles before failure (Figure 6.19b), the two notch skin variants have a similar deformation trend and the values of the strain at the centre of the specimens are more than double in comparison to the 3-Parts weld. The strain for both the variants was above the AA 2024 level at all the points of the curves, thus showing a decrease in the material properties in the SZ in agreement with hardness measurements. The strain difference between the edges and the centre of the specimens was similar for the three variants, showing the same influence of the stringer on the constrained edges. In the NS-DP, the level of strain at the edge was much higher than the measurement in the fracture location. This observation shows that, even if higher stress levels were present in the area, the material strength was improved in the SZ due to the re-precipitation mechanism. In the NS-SP, the maximum strain was not right at the edge but further inside the specimen; as for the 3-Parts variant, the maximum strain due to the crack propagation appeared in the direction of the width where the crack tip is located before failure. For the NS-SP, in comparison with the double pass variant, lower levels of normalized strain were reached in the SZ, despite the identical configuration of the joints. This difference was also observed during hardness analysis and was caused by the transformation of the precipitates in the second weld, which reduced the resistance of the material in the area.

6.3.2. Load Condition: Pull-out Strength

The strain maps for the three different variants obtained at the maximum load are shown in Figure 6.20. For the NS-SP joint, the maximum load was measured immediately before failure; for the other two cases, it was measured before crack propagation and load drop.

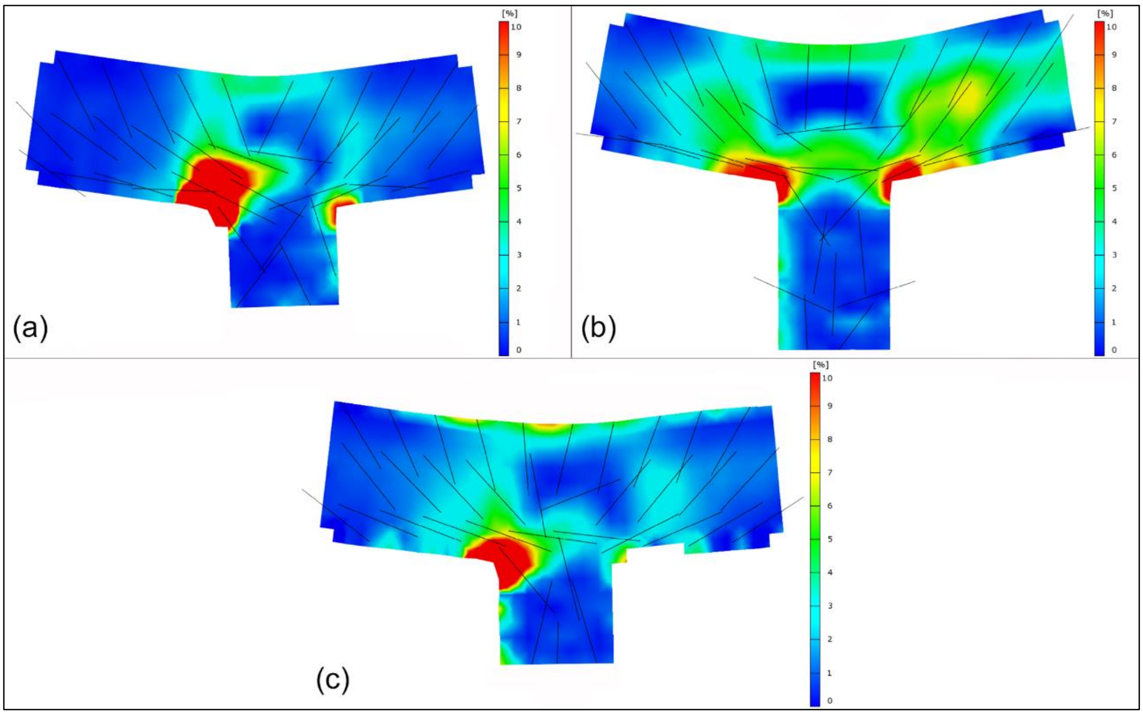

Figure 6.20. Strain maps in the pull-out tests before failure for (a) NS-SP, (b) NS-DP, and (c) 3-Parts

In all the strain maps, the RS of the joints were to the left side of the images and the black lines represented the local major strain directions. The variations in direction justified the use of the load instead of stress in the analysis of the joints' pull-out strength. Owing to the continuous change in the major strain orientation through the skin thickness and width, a simple stress condition (i.e., pure tensile or shear) could not be identified. Only in the stringer, at a certain distance from the corners, was it possible to recognize a state of uniaxial tensile stress with the direction of the major strain oriented parallel to the applied load. Although different load levels were reached during the test, the NS-SP (Figure 6.20a) and 3-Parts (Figure 6.20c) joints presented a similar straining mechanism. The strain maps showed asymmetric behaviour, with a larger strain concentration at the skin-stringer corner in the RS rather than in the AS. The stress concentration in the area caused an increase in the strain at both corners but, as previously observed, the material in the RS showed lower strength due to the weak-bonding at the interface end. These maps clearly explained why the crack began in that specific location and the type of propagation that was undergone. In the double pass variant (Figure 6.20b), the absence of the interface influence in the strength of the joint led to a more symmetrical strain map in the skin upper surface. Higher levels of strain were reached in the stringer, which caused the failure that was previously analysed.

For the three configurations, the strain profiles measured on a vertical section in the stringer's centre (Figure 6.21) showed how the levels of the major strain had low dependency on the microstructure of the joints. In spite of the different properties of the SZ for the three variants, the strain profiles showed similar results in all the cases. The skin was subjected to a bending load that caused compressive strain/stress on the crown surface of the joint (major strain between 4–5 %) and tensile strain at the skin–stringer separation.

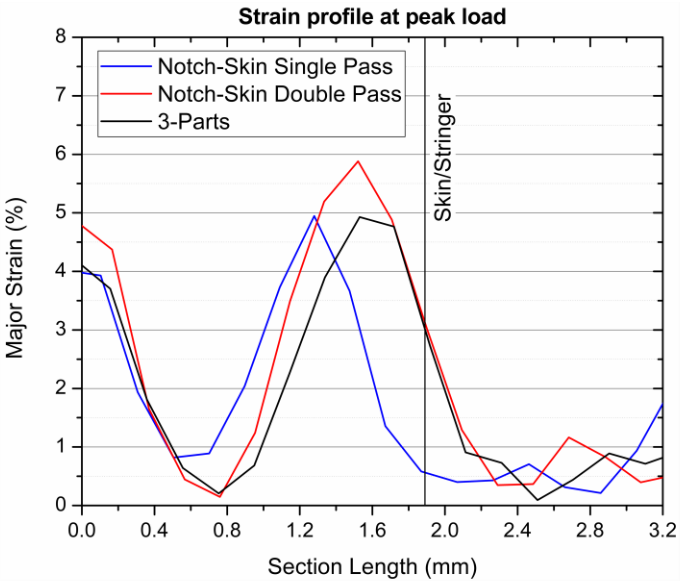

Figure 6.21. Vertical strain profile at the maximum load for different joint configurations

Along this section, the area around the middle of the skin thickness showed a level of strain that was very low with no plasticity owing to the typical butterfly stress profile developed under the bending condition. The low level of strain was also reached in the stringer at a certain distance from the skin, where the stress was predominantly uniaxial and the material was high-strength AA7050. The higher load that the joint could withstand, with consequent plastic deformation, caused a larger strain peak for the NS-DP joint with respect to the other variants. The main influence of the SZ properties could be seen for the 3-Parts joint, in which the same strain as the NS-SP was measured for a higher load level. This confirmed the higher material strength in the area. Owing to the non-uniform stress distribution, it was not possible to find a correlation between the strain and the hardness profiles previously measured.

The analysis of the strain profile along the mid-thickness section in the skin is shown in Figure 6.22. Owing to the limitation with regard to section length for the NS-DP joint, the strain characterization was performed only in the SZ, while in the other variants, the two TMAZs and part of the two HAZs could also be analysed.

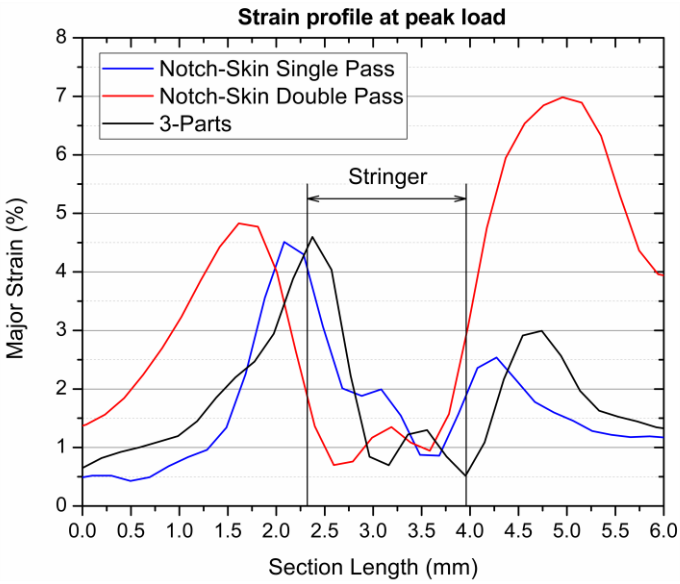

Figure 6.22. Horizontal strain profile at the maximum load for different joint configurations

On a horizontal section, the level of stress should be uniform and the differences in strain are caused either by changes in the strength of the different microstructural areas or by structural influences. The peaks of strain at the sides of the stringer locations are clear examples of how the stress concentration at the corner raises the strain throughout all the thickness of specimens. On the other hand, the microstructural influences lead to an asymmetry in the strain profiles between RS and AS in each of the process variants. In the NS-DP, an increase of major strain from 5 to 7 % can be seen in the AS. As previously observed, this was the location where the AS of the second weld was located and where the secondary crack was developing at the end of the pull-out test. The opposite situation could be seen for the other two variants, with a higher strain in the RS. The two materials' interface at the corner caused a local increase in the stress that brought about the failure of the joints. In both variants, the crack initiated for the same level of strain and the difference in the maximum loads were determined by a higher local yield strength of the 3-Parts joints. In this case, after the crack was formed, the joint required a longer time for failure to take place due to the vertical development of the weak interface that conveyed the crack front in the area where the stress was reduced, as seen in Figure 6.21.

6.4. Summary

In this chapter, the three joint configurations, obtained with the same set of welding parameters, were analysed and compared. The main results of this study are as follows:

- The NS-DP configuration led to a movement of the interface of the two alloys towards the AS of the joint. The interface resulted in more diffused and interlocking, with no presence of defects observed at the skin–stringer corner. The second weld pass generated a border between the first and the second recrystallization process, with larger and rotated grains. This was also the zone where the minimum hardness was measured due to the strong thermo-mechanical effect on the precipitates. The double material stirring pushed both the interface and the TMAZ at the SZ top upward, leading to a reduction in the interface angle and the larger affected area in the stringer. While the grain size in the SZ and the TMAZ at the RS were similar to what was measured for the NS-SP, the double heat input led to an increase in grain size in the TMAZ of the AS.

- In the 3-Parts configuration, the two alloys interface is visible throughout the entire skin thickness, with a strong mechanical interlock in the AS owing to the material layering. The material continuity in the weld centre led to a reduction in the interface angle and to smaller grains in the TMAZ on top of the SZ. Similar to the NS-SP, a weak bonding could be observed at interface-end but without the entrapment of inclusions in the small crack. The higher strength of the AA 7050 in the weld centre caused both an increase in the grain size and in the amount of material extruded toward the RS in comparison to NS-SP. However, this also caused a drastic increase of hardness in the centre of the SZ.
- The three configurations showed similar results with regarding the yield strength in the hoop-direction. When the UTS results were considered, the 3-Parts configuration reached the highest value, equivalent to 90% of the AA 2024-T3. In the NS-DP, a similar level of UTS was reached for two opposite welding condition with two distinguished fracture mechanisms. In the case of ‘hot’ welds, the fracture was driven by the transformation of the precipitates and happened at the border between the two passes, where the minimum hardness was measured. For ‘cold’ welds, the fracture was driven by the interface angle in a similar way as for the NS-SP and the 3-Parts configurations.
- The three configurations showed higher strength and stiffness in the hoop-direction when compared to conventional riveted skin–stringer joints.
- In the pull-out direction, the best mechanical performance was achieved for the NS-DP because of higher mechanical interlocking and diffusion in the interface between the two alloys. The fracture mechanism changed with the configuration. For the NS-DP, the failure, on the other hand, was located in the TMAZ in the stringer; for the 3-Parts joint, the fracture vertically developed along the interface and no stringer delamination could be observed.
- Through DIC analysis it was possible to distinguish the influence of the modified microstructure from the structural influence of the joint configuration itself for both the testing conditions.
- The strain analysis in hoop-direction showed an impeded lateral contraction under the stringer that led to a combination of stress concentrations caused by this and the skin–stringer corner.
- In the 3-Parts configuration, the only area that showed reduced strength with respect to the AA 2024-T3 was the first part of the HAZ, with a significant reduction of the yield strength. If the failure was not dominated by the crack propagation at the skin–stringer corner, the area where the fracture would occur was caused by microstructural deterioration.
- The strain maps of the three configurations differ in the central area of the joints. In spite of this, the same failure mechanism could be observed for the NS-SP and the 3-Parts joints, with the fracture location away from the area with the highest strain. In the NS-DP, the strain profile completely explained the causes behind the final failure, with a peak of strain in the SZ, where a combination of material deterioration and stress concentration could be observed.

- During the pull-out tests, the cracking phenomenon began at the same level of major strain for both the NS-SP and the 3-Parts joints. The higher load in this last case was attributed to the stronger material in the SZ centre of the weld.

7. Fatigue Behaviour of Skin–stringer Elements Realised with Different Joint Configurations

In the current chapter, the fatigue analysis of large specimens at the sub-component scale, was performed for the NS-SP and the 3-Parts variants. The NS-DP variant was excluded from the current study due to the lower mechanical performance in the hoop direction caused by the microstructural deterioration of the joints. Furthermore, the longer realization times of the joints was penalizing a possible industrial applications. The welding parameters used to produce the sub-components were the ones that lead to the best mechanical properties for the two variants: 1200 RPM and a welding speed of 180 mm/min. The fatigue behaviour of the joints was measured with the two variants investigated in two different load directions. The first load case was the one already statically analysed in the hoop-direction to simulate the circumferential load of the fuselage. The other load condition was the most important, considering the structural function of the stringers in an aircraft and it corresponded to a load directed longitudinally in the fuselage. Before starting the fatigue analysis of the joints, the explanation with regard to the type of statistical analysis performed on the results was presented.

7.1. Statistical Analysis of the Fatigue Life Data

In the current study, among the many probabilistic approaches available, the two-parameter Weibull distribution was used to statistically analyse the results obtained from the fatigue tests [105-107]. For this distribution, the probability density function (PDF) was expressed as follows:

$$f(x) = \frac{\beta}{\alpha}\left(\frac{x}{\alpha}\right)^{\beta-1} e^{-\left(\frac{x}{\alpha}\right)^{\beta}} \qquad \alpha \geq 0, \beta \geq 0 \tag{7.1}$$

where, α and β are the scale and the shape parameters, respectively.

The cumulative density function (CDF), necessary to understand the probability that a variable has a value less than or equal to the target data is obtained by integrating the PDF.

In the case of Weibull distribution, the CDF can be expressed as shown in Equation (7.2).

$$F(x) = 1 - R(x) = 1 - e^{-\left(\frac{x}{\alpha}\right)^{\beta}} \tag{7.2}$$

where, $R(x)$ is the so-called reliability function, which in the case of fatigue experiments is the probability of the survival of the specimens. Therefore, by subtracting this function from one, the probability of failure, expressed by the CDF, was obtained.

By applying the natural logarithm to the CDF, we obtained a form of the equation that could subsequently be linearized in the Weibull probability plot by using a log–log scale. In this case, the Equation (7.2) becomes

$$\log \ln\left(\frac{1}{1-F(x)}\right) = \beta \log x - \beta \log \alpha \tag{7.3}$$

When this equation is plotted, the results show that β represents the slope and α is the intercept with the X-axis. At this point, in order to obtain the shape and the scale parameters, it is necessary to know the values of the CDF. Since it is not possible to extrapolate these values directly from Equation (7.2), it is necessary to use Bernard's Median Rank (MR) empirical estimator. For each number of cycles ($N_{f(i)}$) at the i-th failure the CDF or, in our case, the Weibull percentiles could be obtained through the MR by using the Equation (7.4):

$$MR = 100\left(\frac{i - 0.3}{n + 0.4}\right) \tag{7.4}$$

where, i is the failure serial number and n is the total number of specimens. The numbers of cycles for each stress amplitude have to be arranged from the smallest to the largest when the serial number is assigned.

Once the Weibull parameters α and β are computed, it is possible to calculate the Weibull mean life, which is also called the mean time to failure (MTTF), which defines the expected number of cycles until the failure of a certain stress level takes place. Hence,

$$MTTF = \alpha\Gamma(1 + 1/\beta) \tag{7.5}$$

where, Γ(x) is the gamma function [108].

Another interesting statistic that was calculated through the Weibull distribution was the coefficient of variation (CV) that was necessary to analyse the dispersion between the sets of the observed data and consequently the quality of the results. The CV was defined as the ratio between the standard deviation (SD) and the MTTF and could be expressed through the Equations (7.6) and (7.7).

$$SD = \alpha\sqrt{\Gamma(1 + 2/\beta) - (\Gamma(1 + 1/\beta))^2} \tag{7.6}$$

$$CV = \frac{SD}{MTTF} = \sqrt{\frac{\Gamma(1 + 2/\beta)}{(\Gamma(1 + 1/\beta))^2} - 1} \tag{7.7}$$

In the last step of the fatigue analysis, at each stress level, the value of the number of cycles that corresponds to the required level of reliability was calculated. In order to obtain the desired level of reliability, called the Weibull reliable life, it is necessary to apply the natural logarithm to the reliability function and solve it for the variable x, which, in this case, was the number of cycles (Eq. (7.8)).

$$N_R = \alpha\{-\ln(R)\}^{1/\beta} \tag{7.8}$$

where, R is the level of reliability chosen and N_R is the fatigue life for the reliability selected.

In the current study, the S-N curves are plotted on the MTTF and at R_{99}, which correspond to a probability of survival of the sub-components equal to or higher than 99%.

7.2. Fatigue Analysis in the Hoop Direction

In the current study, the load ratio (R) was equal to 0.1 for all the variants and cases analysed. Owing to similar tensile strength (UTS) measured for the NS-SP and the 3-Parts variants in the static tests (Figure 6.8), the same load levels were used, allowing a direct comparison between the two configurations. The main properties resulting from the static analysis of the two joint configurations are reported in Table 7.1.

Table 7.1. Static test results for the NS-SP and 3-Parts joints in hoop direction

	Yield Strength (MPa)	Tensile Strength (MPa)
NS-SP	291.6±8.4	408±11.9
3-Parts	284.6±5.1	418.4±8.0

The fatigue life of the sub-components were evaluated for six different levels of maximum stress, expressed as a percentage of the tensile strength, for simplicity set equal to 420MPa. The cycles to failure for the two variants with the relative levels of stress are presented in Table 7.2.

Table 7.2. Results of fatigue tests in hoop direction for the two joint configurations with R=0.1. S_{min}, S_{max} and S_m are respectively the minimum, maximum and mean stress of the cyclic load, while ΔS is the stress amplitude.

Load (%)	S_{max} (MPa)	S_{min} (MPa)	S_m (MPa)	ΔS (MPa)	Notch-Skin SP	3-Parts
					Cycles (N_f)	Cycles (N_f)
80	336	33.6	184.8	302.4	1430	16448
					6926	19178
					13337	19511
70	294	29.4	161.7	264.6	13317	19784
					14532	20907
					50394	22529
60	252	25.2	138.6	226.8	19486	34998
					70099	37881
					146116	56781
50	210	21.0	115.5	189	86744	156489
					225105	207832
					244614	288898
40	168	16.8	92.4	151.2	271165	255018
					402293	352670
					678121	568748
30	126	12.6	69.3	113.4	423155	> 2E6
					> 2E6	> 2E6
					> 1E7	> 1E7

At first observation of the results, it appears that at high load levels, the number of cycles reached in the case of the 3-Parts configuration was higher than for the other case, while an inversion in the tendency was observed at lower load levels. For both the joint configurations, 30% of the failure load could be considered as the fatigue limit, with just one broken specimen for the NS-SP.

The Weibull probability plots at the different load levels are shown for the NS-SP and 3-Parts joints in Figure 7.1(a) and (b), respectively. In the graphs, the load levels corresponding to 30% of the failure loads are not reported since an insufficient number of sub-components failed and consequently these cannot be used for further statistical analysis.

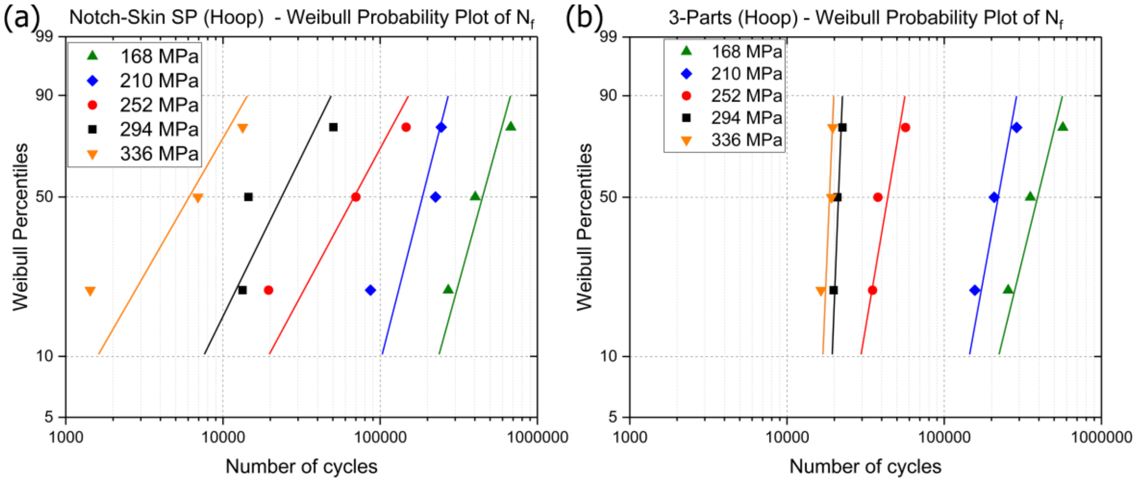

Figure 7.1 Weibull plots for the tested maximum stresses in the hoop-direction for (a) NS-SP and (b) 3-Parts welds

For each load level, the Weibull percentiles were approximated by using Equation (7.4) and, as a result, they were equal for all cases since the same number of components were tested. From these graphs, it was possible to obtain the values for the Weibull characteristic life (α) and slope (β) by the linear regression shown in Equation (7.3). Once the Weibull parameters were known, the Weibull mean life could be calculated (Equation (7.5)) and all the results of this analysis are summarized in Table 7.3.

Table 7.3. Weibull parameters and MTTF for each stress amplitude and joint configuration

S_{max} (MPa)	Notch-Skin SP			3-Parts		
	α (cycles)	β	MTTF (cycles)	α (cycles)	β	MTTF (cycles)
336	7.911E^3	1.401	7.209E^3	1.897E^4	19.238	1.845E^4
294	2.947E^4	1.644	2.636E^4	2.162E^4	20.543	2.106E^4
252	8.707E^4	1.497	7.862E^4	4.721E^4	4.760	4.322E^4
210	2.084E^5	3.162	1.865E^5	1.816E^5	6.482	1.692E^5
168	5.075E^5	2.921	4.526E^5	4.389E^5	3.288	3.936E^5

At this point, all the data necessary in order to plot the S-N curves of the two variants has been obtained, despite having no information regarding the quality of the statistical analysis performed. Before investigating the cyclic behaviour of the sub-components, it is important to consider the variation of the coefficient of variation, CV (Eq. (7.7)) for the two variants at the different stresses. The results of this analysis are plotted in the graph shown in Figure 7.2. At all the load levels, the relative dispersion of data in the case of NS-SP is higher, showing a decrease while entering in the field of high-fatigue life. This behaviour is problematic in terms of accuracy and repeatability for design purpose, especially when the fatigue life values are between the 10^3 and 10^5 cycles. In this range, the standard deviation, SD is higher than 50% of the mean life. A part of this scatter can be explained by the differences in surface finishing and by considering the complex geometry of the sub-components. More detailed discussion on crack initiation issues is given in section 7.2.1 – Fracture Surface Analysis.

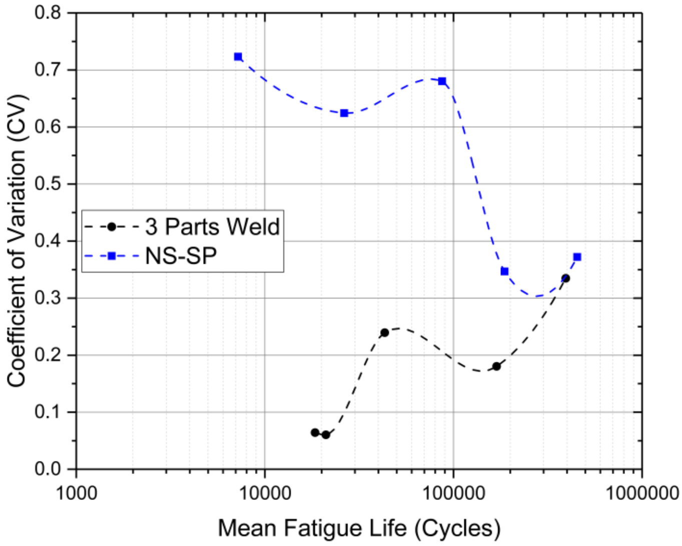

Figure 7.2. Evolution of CV as function of the mean fatigue life n for the load in the hoop-direction

Flat butt-joints that would undergo a post-process milling of the crown surface of the weld would undoubtedly lead to lower CV for the same welding conditions. However, the reproducibility and robustness of the 3-Parts joints' tests is high with a CV that remains below the 30% at all the load levels. In the left part of the graph, relative to low-fatigue life, the constancy of the results is particularly excellent (around the 5%). This analysis, at first, provides an element that differentiate the fatigue behaviour of the sub-components obtained with two-joint configurations, with a higher deviation in the results of the NS-SP variant.

The influence of the CV on the S-N curves is shown in Figure 7.3.

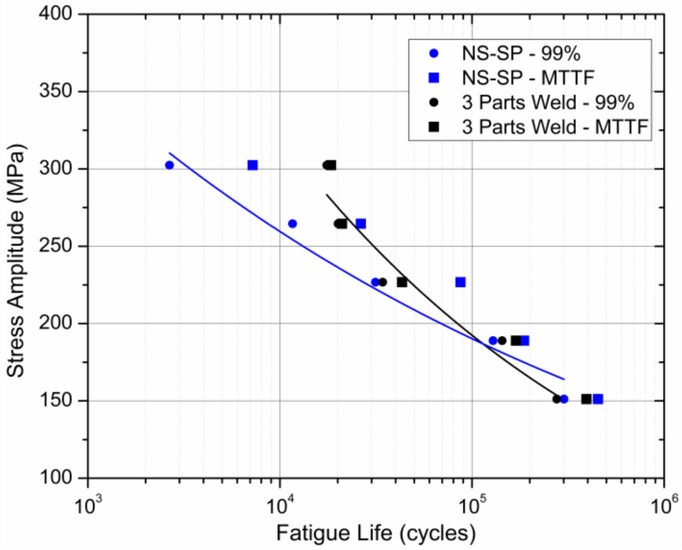

Figure 7.3. S-N curves in the hoop-direction for different reliability levels

In this graph, the fatigue results are reported in terms of the Weibull mean fatigue life (MTTF) and at a reliability level of the 99% that was calculated from Equation (7.8). The points on the graph relative to the 3-Parts variant resulted in a smaller horizontal displacement when the reliability level was increased from the MTTF to 99%. At high load amplitudes, the difference in the robustness of results between the two variants was important, leading to a drastic reduction of the fatigue life in the NS-SP components. The choice of plotting the Y-axis in terms of the stress amplitude was made in order to apply Basquin's power function (Eq. (7.9)) to correlate the stress amplitude (ΔS) with the number of cycles (N).

$$\Delta S = a(N)^b \tag{7.9}$$

In Eq. (7.9) a and b are constants that can be drawn by regression from Figure 7.3. This equation proved valid for a wide range of heterogeneous materials and could be used to approximate the fatigue behaviour in the range of $10^3 - 5 \times 10^8$ cycles [109, 110].

The two curves initially diverge at high stress amplitudes, indicating a better resistance to fatigue initiation in the sub-components realized with the 3-Parts variant. Considering that most of the cycles are necessary for initiating the crack in this kind of test, the 3-Parts sub-component has a higher resistance to crack initiation in the case of possible overloading cycles in the fuselage. On the other hand, while approaching the area of the graph relative to high cycles, the two variants show similar behaviour. Consequently, the curve relative to the 3-Parts presents a higher slope with a larger absolute value of *b* (3-Parts: *b*= -0.22 and NS-SP: *b*= -0.13). Since the fatigue limit showed the same results for both the configurations, it is expected that by adding data in the range between 40 and 30% of the failure load, the *b* value in the 3-Parts would decrease, and the two curves would proceed asymptotically towards the same stress level.

The results obtained for the two variants together with the one relative to the AA 2024-T3 for different levels of the stress concentration (K_t) are shown in Figure 7.4. In the same graph, it has been reported the S-N curve for riveted AA2024/AA7075 skin–stringer joints with a cross-section of 400 mm^2 and a line of 10 rivets [104].

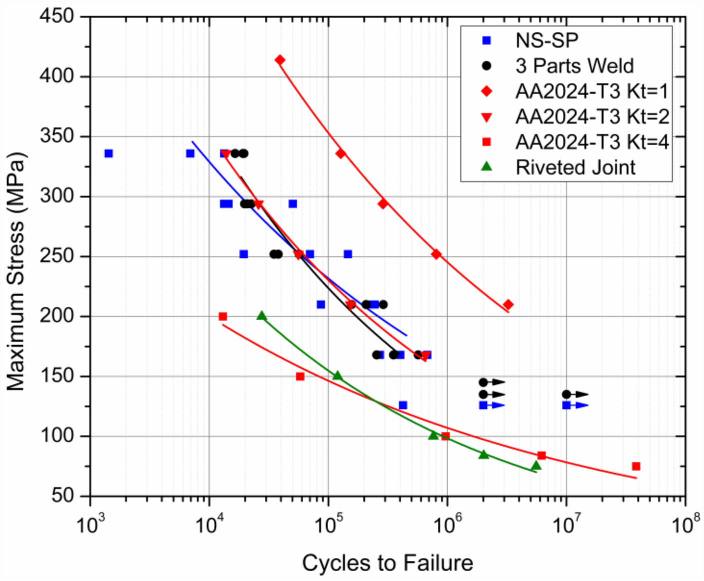

Figure 7.4. Comparison of fatigue behaviour in the hoop-direction for different technologies

The curves relative to the base material are obtained from the ‘Metallic Materials Properties Development and Standardization (MMPDS)’ book, which is commonly used in the aerospace industry to compare new materials and technology [111]. By using this, it is possible to identify a level of theoretical stress concentration introduced by the joining technology, which can be used as a simple tool for a comparison between different processes.

From the MMPDS, the curves were calculated using the Equivalent Stress Equation (7.10), which was expressed in the following form:

$$\log N = a - b \log(S_{eq} - c) \qquad \textbf{(7.10)}$$

where, a, b, and c are three parameters that are obtained by regression from the experimental curves at different stress concentrations;

$$S_{eq} = S_{max}(1 - R)^{d} \qquad \textbf{(7.11)}$$

with, d as the last parameters necessary to plot the curves and R as the stress ratio. The values of the four parameters for each stress concentration level with the respective coefficient of determination (R-squared) are reported in Table 7.4.

Table 7.4. Coefficients of the Equivalent Stress Equation for rolled AA2024-T3 (0.09 inches) at different K_t [111]

	AA2024-T3 Unnotched (K_t = 1)	**AA2024-T3 Notched (K_t = 2)**	**AA2024-T3 Notched (K_t = 4)**
a	11.1	9.2	8.3
b	3.97	3.33	3.30
c	15.8	12.3	8.5
d	0.56	0.68	0.66
R-squared	82 %	91 %	90 %

From Figure 7.4, it is possible to see how the curve relative to the AA 2024 at K_t = 2 approximates the fatigue behaviour of the two studied joint configurations very well. It is important to observe that this stress concentration factor it is not caused entirely by the welding process but is a combination of the corner between the skin and the stringer (geometrical stress concentration), the joining technology and the notch effect originating from the dissimilar materials.

In both the joint configurations, no failure could be observed up to 10^7 cycles for a maximum stress equal to 126 MPa. Therefore, this could be defined as the experimentally evaluated fatigue limit. At the same load level, the curve relative to the riveted joint shows a fatigue life between two and three hundred thousand cycles, proving a great improvement in the fatigue behaviour of the two welded joints. In order to have a quantitative evaluation at different stress levels, the curve relative to the AA 2024 at a K_t = 4 can be used as an approximation of the riveted joint. The approximation in this case is not as good as the previous one but it leads to conservative results in the high stress area up to ~125 MPa. Considering that in the riveted joint, the geometry of the stringer is already optimized to reduce the stress concentration at the stringer foot, the technological stress concentration introduced is more than double of one of the SSFS-welded sub-components. The fatigue limit in the riveted joint was equal to 65 MPa, which is 49% lower in respect to the newly investigated technology.

7.2.1. Fracture Surface Analysis

The fracture analysis focused on the ranges of low and high cycles of fatigue life due to the changes in fracture mechanism. The general fracture location for all the sub-components tested was recorded and the results are shown in the Table 7.5.

Table 7.5. Fracture location of the two joint configurations at different load levels

	Fracture Location														
S_{max} (MPa)	168			210			252			294			336		
Notch-skin SP	AS	RS	RS	RS	RS	RS	RS	AS	AS	RS	RS	RS	AS	AS	RS
3-parts	AS	AS	AS	RS	AS	AS	AS	RS	RS	AS	AS	AS	AS	AS	AS

In the 3-Parts configuration, 80% of the specimens failed in the AS of the joints, showing an important difference with what was observed for the static analysis. The interface between the two alloys, which had a critical impact on the static performance of the welds, lost its significance while considering the failure locations in cyclic testing. The main drive for the initiation of the fatigue crack was the stress concentration at the skin–stringer corner and not the weak bonding at the interface, which was previously observed. The predominance of failure at the corner of the AS could be related to the position of the stringer head. This is always directed towards the AS of the joint, causing a shift in the centre of mass and an asymmetry in the stiffness between the two sides of the stringer. For the NS-SP variant, the influence of the interface of the two materials was still predominant in the failure mechanism with over 70% of the specimens failing in the RS of the joint. This failure mechanism was predominant at all the load levels with the only exception being when the sub-components were tested at the 80% of the tensile strength.

7.2.1.1. High-cycles Loading Conditions

In Table 7.5, the fracture locations for the 3-Parts joints in the high fatigue cycle area are highlighted in red due to completely different fracture behaviour. At this load level, the fracture initiation becomes independent from the stress concentration induced by the corner and is localized in the TMAZ of the AS (Figure 7.5).

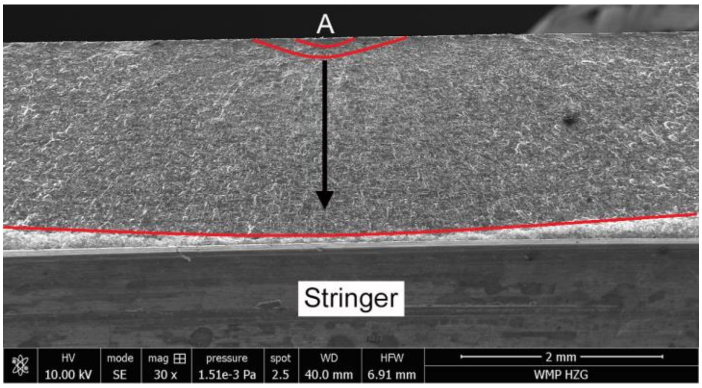

Figure 7.5. SEM image of the fatigue initiation and propagation for the 3-Parts joint under the high-cycles loading condition in the hoop-direction

The failure is initiated in the mark left by the edge of the shoulder (A) and then propagates in the direction of the arrow until it completely penetrates the skin. Since the area of fatigue initiation is determined by the shoulder mark on the top surface of the weld, this explains the increase in the CV (Figure 7.2), which was observed at this load level owing to the variations in the surface finishing between the different welds.

In the NS-SP configuration, the failure was located, as in all the other cases, at the corner between the skin and the stringer. At this load level, the damage predominantly progressed from the RS of the joint; both the initiation and the propagation of the crack were strongly influenced by the interface of the two materials. In the analysed sample, the two main fatigue-initiation points were observed, both at the skin–stringer corner in two different positions along the joint (1 and 2 in Figure 7.6).

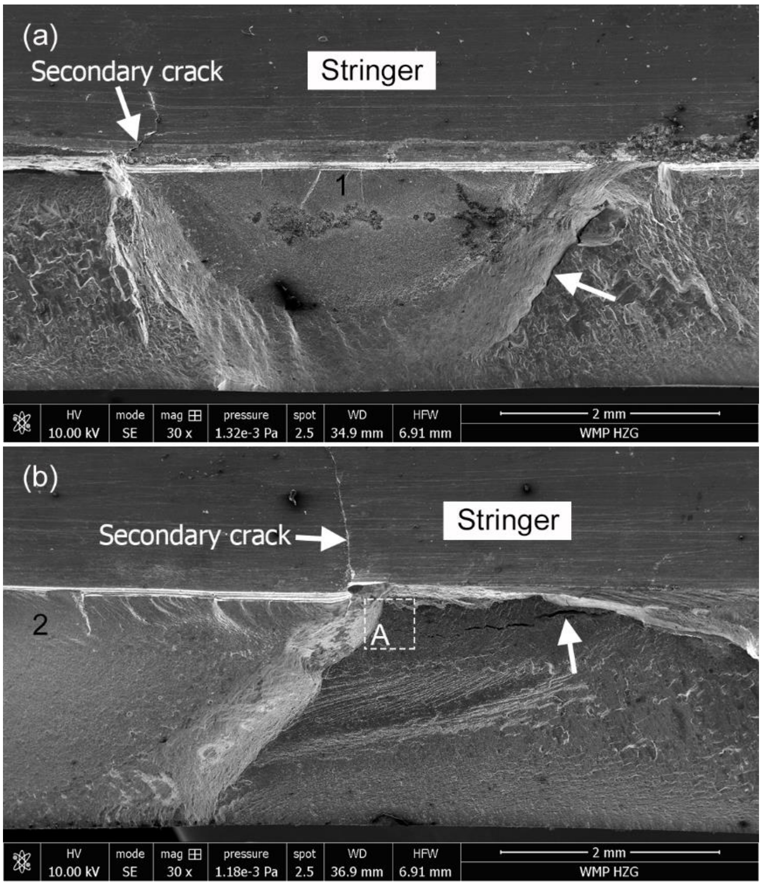

Figure 7.6. SEM images of the fatigue fracture surface for the NS-SP joint under high-cycles loading condition in the hoop-direction—(a) Fracture Surface 1 and (b) Fracture Surface 2

Both the initial cracks, while propagating through the skin thickness, rotate; the lateral edges penetrate under the stringer. At the end of the fatigue propagation in the direction perpendicular to the stringer, i.e., parallel to the load direction, it is possible to observe the secondary cracks in both the skin and, more importantly upward, in the stringer. The transfer of a fatigue crack in the stringer is highly undesirable in terms of damage-tolerance, especially considering that in this case, the stringer should theoretically withstand very small levels of stress. The main problem was the tendency of the crack to turn and delaminate the stringer; this can be seen in more detail in Figure

7.7a. This image was taken from the box marked with A in Figure 7.6b. In the picture, multiple secondary cracks could be seen originating from the fatigue planes. From the higher magnification image, Figure 7.7b, the vertical striations, originated by the propagation parallel to the load direction appear clearly and the secondary crack that separates the two planes with different fatigue propagation directions can be seen.

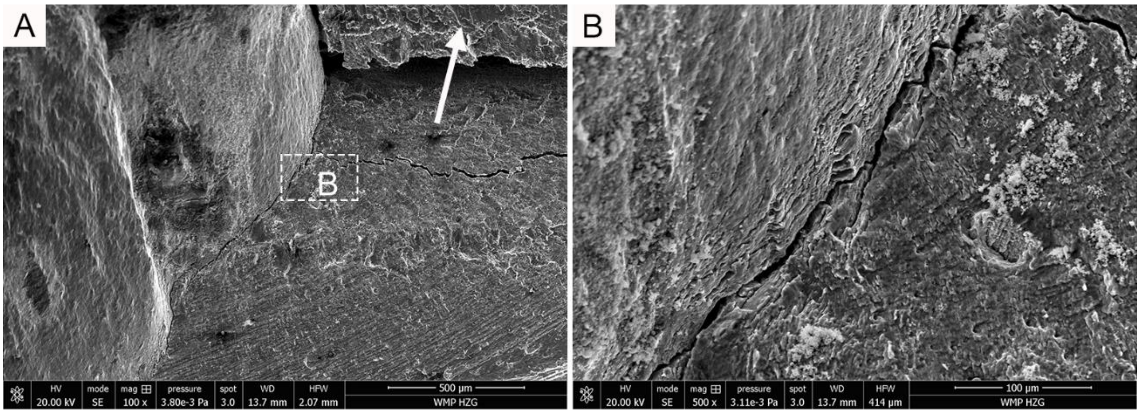

Figure 7.7. SEM images of the fatigue fracture surface for the NS-SP joint under high-cycle loading condition in the hoop-direction—(a) different planes of fracture propagation and (b) high magnification image showing striations and secondary cracking

In Figure 7.7a, the lower surface of the stringer, which is completely separated from the skin, is indicated with a white arrow. In order to understand the nature of this crack, an image of the lower stringer surface was considered (Figure 7.8). The traces of the rotating probe can be seen in the highlighted areas. These are characterized by rounded profiles at a constant distance which is bridged by a less-strongly connected interface.

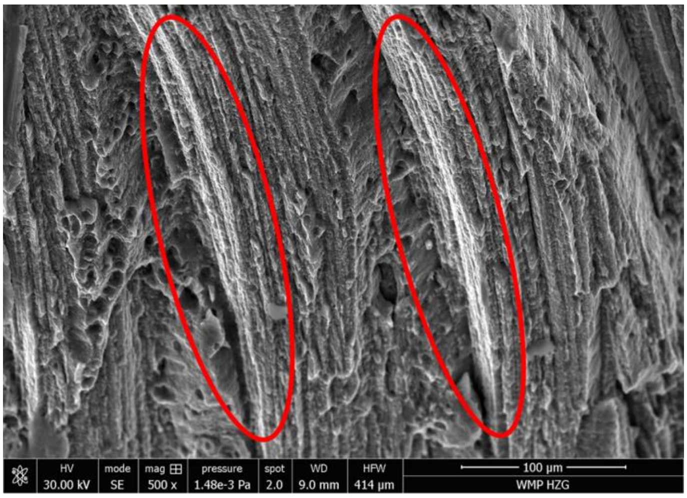

Figure 7.8. SEM images of fatigue striations at the interface under the stringer for the NS-SP joint under the high-cycles loading condition in the hoop-direction

The fatigue crack propagated not only in the skin along the two different planes but also at the bottom of the stringer, where the interface between the two alloys was originally present. The striations due to the cyclic crack propagation are visible in between the marks left by the rotating probe, despite the contact between the two cracks surfaces that caused a smoothing of the peaks. It also appears that the fatigue crack is interrupted in certain area by unstable ductile cracking, with the presence of dimples.

7.2.1.2. Low-cycles Loading Condition

When the maximum force increases up to 80% of the tensile strength the failure tends to be located in the AS of the joint for both configurations, as reported in Table 7.5. In spite of the same initiation area, determined by the stress concentration at the skin–stringer corner, the fracture mechanism of the two configurations is radically different.

In the 3-Parts configurations, multiple zones of fatigue initiation, and propagation can be observed all along the stringer edge (Figure 7.9a).

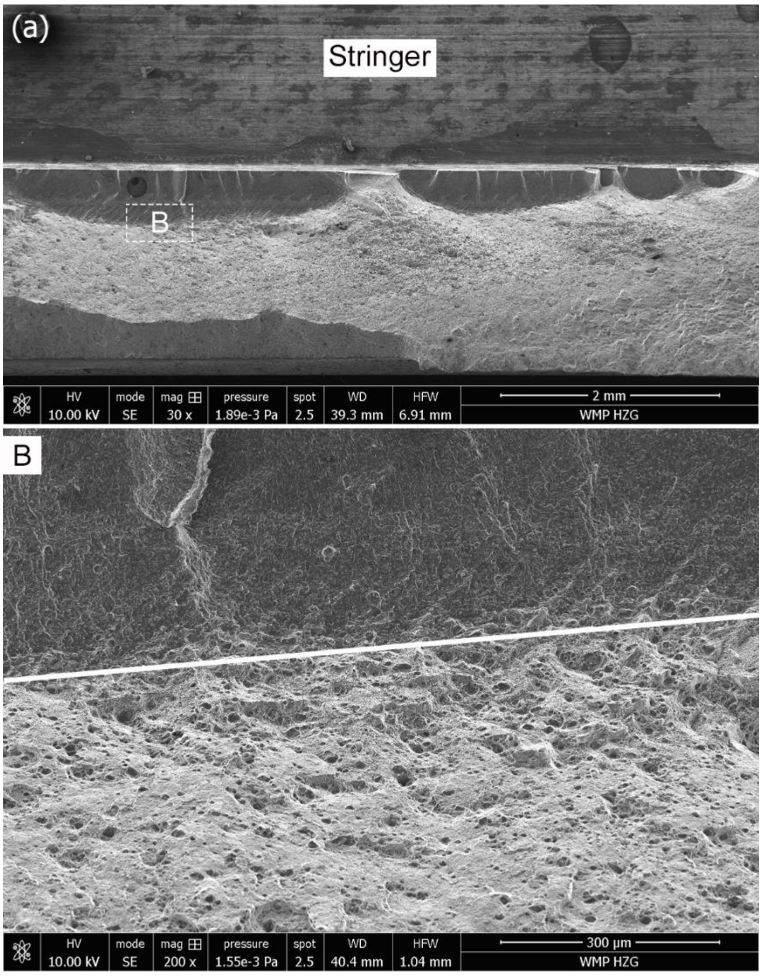

Figure 7.9. SEM images of the fatigue initiation and propagation for the 3-Parts joint under low-cycles loading condition in the hoop-direction—(a) overview of the fracture initiation and propagation and (b) the transition between the fatigue fracture and ductile failure

The fatigue cracks propagated for less than half of the skin thickness before the specimen failed due to the high stresses in the remaining section. This phenomenon can be clearly observed in Figure 7.9b, where a close-up of the transition area is shown and the boundary between the two fracture morphologies is marked. The presence of an irregular surface, with a large number of dimples, in the lower part of the image indicates that the specimen in this area underwent a large plastic deformation in contrast to the flat surface characteristic of fatigue propagation (upper part of the image). It is important to notice that due to the higher strength of the centre of the SZ, the plastic part of the fracture surface is inclined outwards with respect to the stringer edge, leaving this part untouched.

The failure behaviour in the NS-SP variant is radically different, with one single area of fatigue initiation, which propagates deeply into the skin (Figure 7.10a).

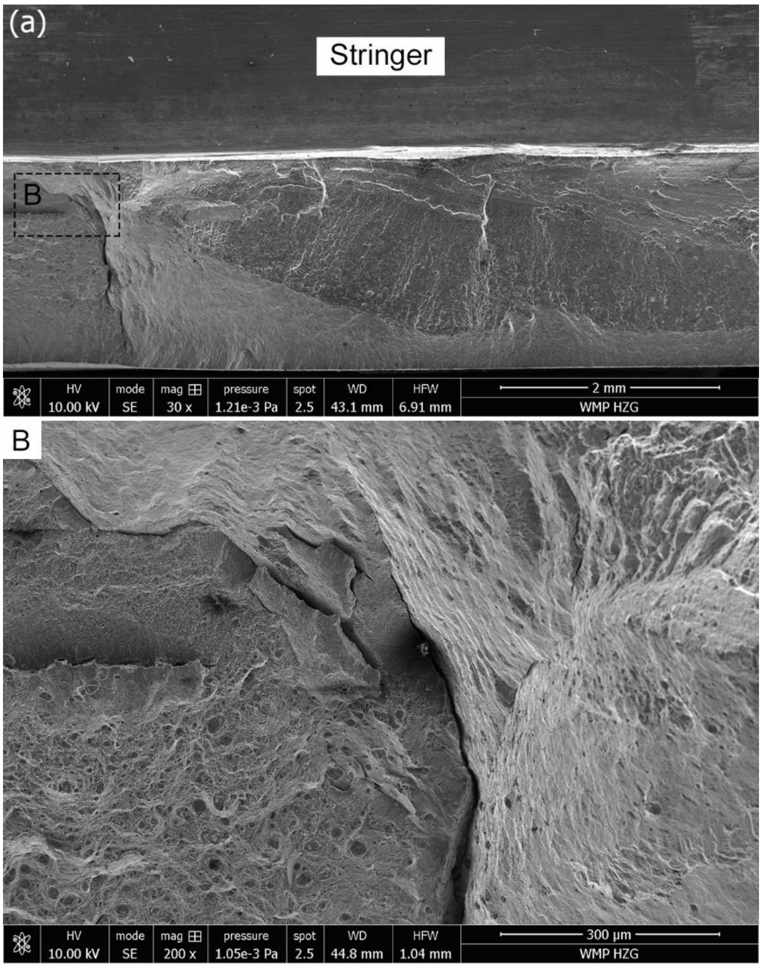

Figure 7.10. SEM images of the fatigue initiation and propagation for the NS-SP joint under low-cycles loading condition in the hoop-direction—(a) overview of the fracture initiation and propagation, and (b) fatigue crack rotation and secondary cracking and the interface with ductile failure

The crack initiates at the skin–stringer corner and presents the main direction of propagation along the plane normal to the load direction. The most interesting area of crack propagation was highlighted in the box marked with B. From the high magnification image (Figure 7.10b), it is possible to see how the fatigue crack turns parallel to the load and finds a propagation path underneath the stringer that tends to delaminate it. The striation marks indicate that in the light grey area of the image, the fatigue loads cause crack propagation and that these are interrupted by multiple secondary cracks, where there are sharp changes in the fracture plane. Beyond these cracks, normal to the observed plane, the failure is induced once again by the high stresses in the remaining ligament, with the presence of dimples that indicate the plastic nature of the fracture. The horizontal secondary cracks, which separate the fatigue delamination of the stringer from the plastic failure of the skin, are located in the interface area of the two alloys. The horizontal interface, caused by the joint configuration in the NS-SP, appears to be critical in a cyclic loading condition. While the crack initiation is caused by stress concentration, this area of the joint shows weaker behaviour, facilitating the progression of failure and leading to the undesirable event of stringer delamination.

7.3. Fatigue Analysis in the Longitudinal Direction

The first step of the analysis, before proceeding with fatigue investigation, was to determine the strength of the joints in the longitudinal direction. The main properties resulting from the static analysis of the joints obtained with the 3-Parts configuration are reported in Table 7.6.

Yield Strength (MPa)	Tensile Strength (MPa)	Elongation (%)
381.5±3.3	492.7±6.9	4.6±0.9

Table 7.6. Static test results for 3-Parts joints in longitudinal direction

The mechanical properties of the joints were higher in respect to the values measured in hoop-direction as well in respect to the AA 2024-T3 base material. The higher strength stringer supports a large part of the load, leading to an increase in the strength of the joint. This observation became evident from the strain analysis performed by DIC. The strain on the outer surface of the skin remained homogeneous throughout the entirety of the test until the moment before the failure of the component, as shown in Figure 7.11. From the strain map, it is possible to notice the homogeneous distribution of the strain in the entire specimen, except for the area in the centre where the stringer is starting to fail. From this point, the strain peaks distribute in the form of a cross with 45° of inclination with respect to the applied load, where maximum shear stresses are expected. Once the stringer failed, the skin alone was incapable of withstanding the full load, leading to the sudden catastrophic failure of the component.

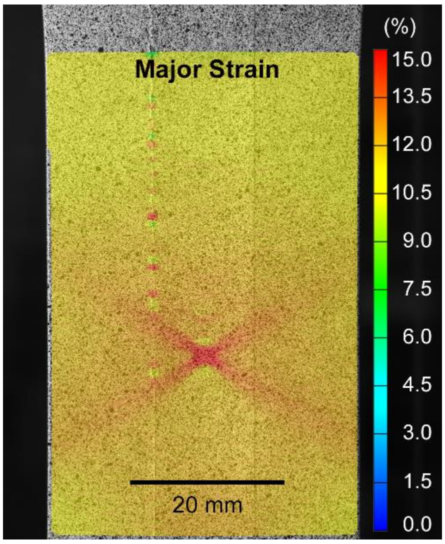

Figure 7.11. Strain map before the failure in the longitudinal direction for the 3-Parts joint configuration

From the deformation behaviour, it was clear that in the case of a monotonic longitudinal load, joint configuration played a smaller role than in the case of the hoop-direction since the stringer absorbs most of the stress until its failure. Based on this result and on the already minimum strength difference between the two configurations in the hoop-direction, it was decided not to perform static tests for the NS-SP in the longitudinal direction. The results obtained for the 3-Parts joints were used to define different load levels for the fatigue testing.

The analysis in longitudinal direction was performed following the same procedure previously shown for the hoop-direction. The maximum loads were defined as a fraction of the failure load and three sub-components were tested for each load level. The stress ratio was kept constant throughout the tests at a value of 0.1. The results of the tests, with the parameters necessary for the fatigue analysis, are reported in Table 7.7.

Table 7.7. Results of fatigue tests in longitudinal direction for the two joint configurations with R=0.1. S_{min}, S_{max} and S_m are respectively the minimum, maximum and mean stress of the cyclic load, while ΔS is the stress amplitude.

Load (%)	S_{max} (MPa)	S_{min} (MPa)	S_m (MPa)	ΔS (MPa)	Notch-Skin SP	3-Parts
					Cycles (N_f)	Cycles (N_f)
80	392	39.2	215.6	352.8	13013	7649
					13128	9839
					14417	13820
70	343	34.3	161.7	308.7	18324	15164
					24229	23972
					30746	26675
60	294	29.4	188.65	264.6	38702	49173
					44460	82965
					60758	91265
50	245	24.5	134.75	220.5	54396	104937
					93071	116136
					112625	116847
40	196	19.6	107.8	176.4	213623	178743
					233389	251036
					279262	266583
30	147	14.7	80.85	132.3	407372	1,92039E6
					581383	X
					985146	X

In the case of the 3-Parts joints, just one sample failed in the area of interest at the lowest load level. For the other two sub-components, failure took place in the grip region, starting from the stringer due to the high sensitivity of the AA 7050 to stress concentrations. This shows that the stress concentration in the joints was lower than the stress introduced by mechanical clamping. Moreover, the fact that the same behaviour was not observed in the case of the NS-SP configuration showed a significant difference between the two processes. Differently from the 3-Parts joints, the stress concentration induced by the NS-SP process is higher than the one caused by the grips allowing the specimens to fail in the correct location.

By applying the same procedure that was previously explained and using the Equations (7.3)-(7.5), it was possible to calculate the main factors needed for two-parameter Weibull probability. This analysis was possible for all the load levels, except for the 3-Parts configurations where, as previously explained, not enough specimens failed in the correct location. The main results of the analysis are highlighted in Table 7.8.

Table 7.8. Weibull parameters and MTTF for each stress amplitude and joint configuration in the longitudinal direction

S_{max} (MPa)	Notch-Skin SP			3-Parts		
	α (cycles)	β	MTTF (cycles)	α (cycles)	β	MTTF (cycles)
392	$1.384E^4$	21.579	$1.350E^4$	$1.145E^4$	4.514	$1.045E^4$
343	$2.652E^4$	5.518	$2.449E^4$	$2.386E^4$	5.763	$2.209E^4$
294	$5.194E^4$	5.530	$4.797E^4$	$8.145E^4$	5.301	$7.503E^4$
245	$9.574E^4$	4.360	$8.721E^4$	$1.150E^5$	30.346	$1.130E^5$
196	$2.548E^5$	9.430	$2.418E^5$	$2.478E^5$	8.205	$2.337E^5$
147	$7.403E^5$	2.984	$6.609E^5$	X	X	X

Once the Weibull's parameters, α and β, are known, it is possible to verify the dispersion of the data for the load in the longitudinal direction through the Equations (7.6) and (7.7). The results of this study are plotted in Figure 7.12 as the CV in the function of the mean fatigue life.

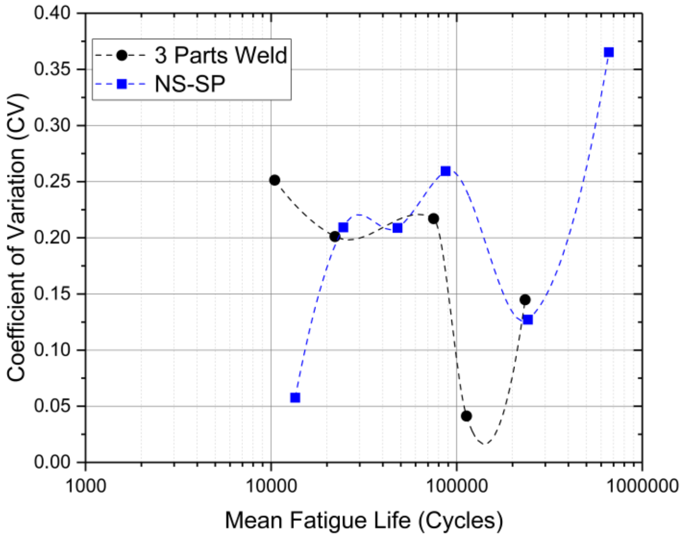

Figure 7.12. Evolution of CV as function of the mean fatigue life n for the load in the longitudinal direction

In general, the deviation of the results in the longitudinal direction was lower at all the load levels and for both the configuration in respect to the one observed for the hoop-direction. All the data were below 30% of variation, with the only exception for the NS-SP variant at the high-fatigue life. The reason for this reduction in the CV was connected with the load-bearing capability that had been previously demonstrated by the stringer that decreased the stress levels in the critical part of the joint (i.e., the corner of the skin–stringer connection), thus normalizing the results of the tests. Moreover, the geometrical stress concentration in case of a load parallel to the stringer was lower than for a perpendicular stress, thereby avoiding the peaks of stress in the skin side of the components.

The lower CV leads to, as previously explained, a smaller reduction in the fatigue cycles when the reliability level of the curves is increased. This phenomenon can be observed in Figure 7.13 for both the notch-skin SP and the 3-Parts variants.

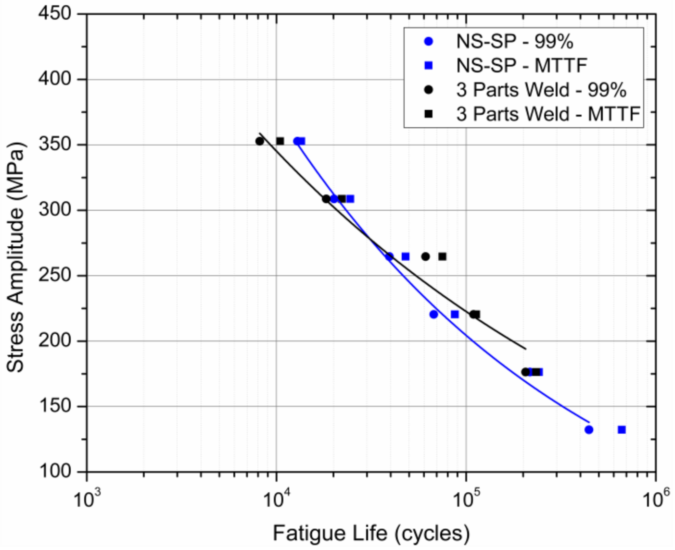

Figure 7.13. S-N curves in the longitudinal direction for different reliability levels

The behaviour of the fatigue curves for each joint configuration is the opposite of what was observed in the hoop-direction. The coefficient *b*, representing the slope of the curves obtained from equation (7.9), was higher in absolute value for the NS-SP (*b*=-0.26) than for the 3-Parts variant (*b*=-0.19), leading to a reduction of the fatigue life in the range of low stresses. This confirms the trend observed for the results at the 30% of the tensile strength, where the NS-SP components failed in the region of interest, without problems deriving from the clamping system. The reduction of fatigue strength approaching the fatigue limit was partially compensated by an improvement of the performances at high loads with respect to the 3-Parts variant. The difference in this zone of the graph, where the maximum stress overcomes the yielding strength of the AA 2024-T3, might have been related to the lower strength measured in the SZ in the case of the NS-SP joints. While in the case of the 3-Parts joints, the centre of the SZ remains elastic due to the presence of the higher strength AA 7050; in the notch-skin SP, all the SZ was plasticized leading to the hardening of the area and a reduction in the effective maximum stress necessary to open the crack.

In Figure 7.14, the results of the fatigue analysis at the MTTF for the two configurations and the curves relative to the extruded AA 7050-T7651 are shown. Owing to the mechanical behaviour of the joint, comparing the results obtained from the two configurations with the fatigue behaviour of extruded AA 7050-T7651 obtained from the MMPDS was found appropriate [111].

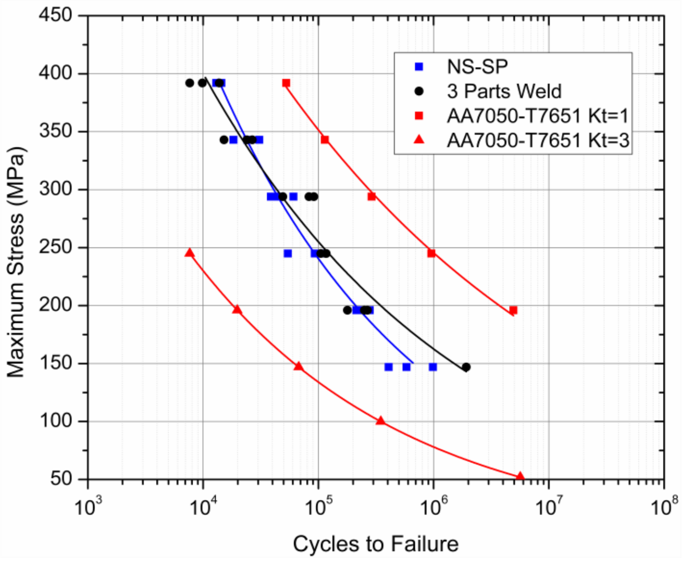

Figure 7.14. Comparison of fatigue behaviour in the longitudinal direction for different joint configurations and AA7050-T7651

The equation used to approximate the S-N curves of the base material are expressed in the same form as shown previously (Eq. (7.10)–(7.11)) and the parameters for the un-notched and notched specimens are reported in Table 7.9.

Table 7.9. Coefficients of the Equivalent Stress Equation for extruded AA7050-T7651 (0.5 to 5.0 inches) at different K_t [111]

	AA7050-T7651 Unnotched (K_t = 1)	**AA7050-T7651 Notched (K_t = 3)**
a	11.8	10.38
b	4.38	4.26
c	12	0
d	0.61	0.563
R-squared	76 %	74 %

The notch sensitivity of the AA 7050 is higher than the one previously observed in case of the AA 2024, explaining the problem observed for the 3-Parts variant close to the fatigue limit. Owing to this high sensitivity of the base material, the stress concentration induced by the welding technology in both the joint configurations is lower than what was observed in the hoop direction with respect to AA 2024. The low-stress concentration level leads to fatigue initiation in the stringer near the corner while approaching the fatigue limit.

7.3.1. Fracture Surface Analysis

The analysis of the fracture mechanism in the longitudinal direction was performed in a similar way as the analysis in hoop-direction, distinguishing between the range of high and low-cycles loading. According to the fatigue life analysis performed, these were the two areas of the S-N curves where the difference between the two joint configurations was more accentuated, requiring a deeper investigation to understand the reasons behind it.

7.3.1.1. High-cycles Loading Condition

Two main fracture initiation areas, independent from each other, could be identified in the 3-Parts joint as they are shown in Figure 7.15. The location of the fatigue crack and the point of initiation, shown in Figure 7.15a, was the same previously observed for the cyclic load in the hoop direction. The mark left by the shoulder passage becomes a critical point of fatigue initiation for both the load directions while approaching the fatigue limit with large damage propagation. The fact that this mark is in correspondence with the TMAZ of the joint, where minimum hardness and strength of the joint were measured, gives an additional explanation for its criticality.

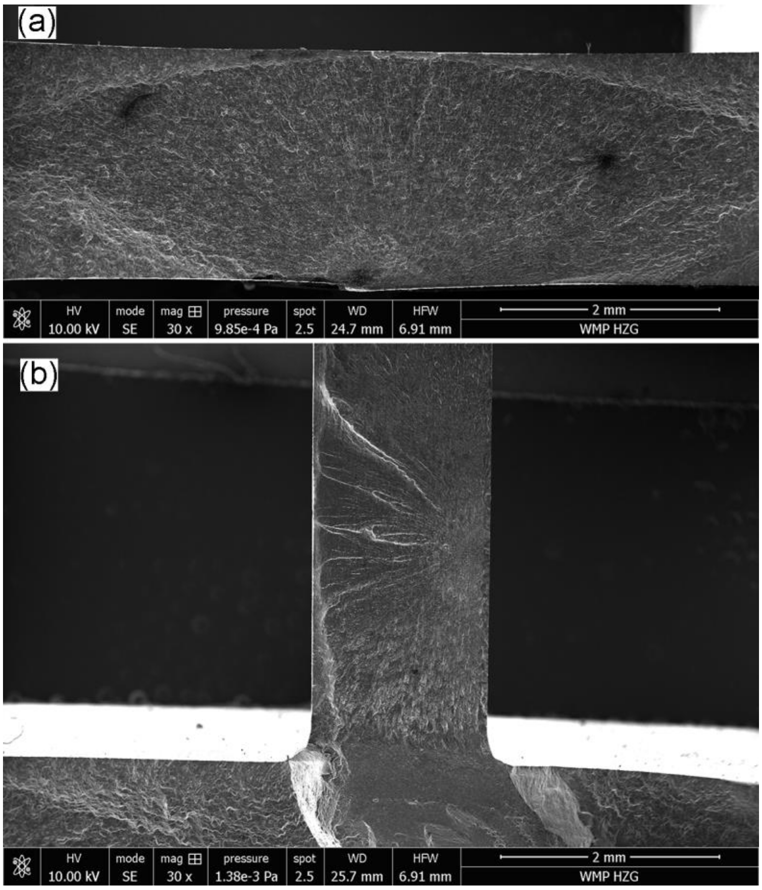

Figure 7.15. SEM images of the fatigue initiation and propagation for the 3-Parts joint under the high-cycle loading condition in the longitudinal direction—(a) skin crack initiation and (b) stringer crack initiation

The second point of fatigue initiation is located in the stringer at around 1.5 mm from the corner that it forms with the skin (Figure 7.15b). The crack propagates through the entire stringer and penetrates into the SZ, where interesting features could be observed, with three different planes of propagation (Figure 7.16a). The first propagation path (1), where the crack grows by fatigue for more than 1 mm, is normal to the applied load parallel to the stringer crack initiation. The other two planes (2 and 3) are parallel to the load direction and the crack turns by 90º with respect to the original propagation. As observed for the NS-SP fatigue crack in the hoop direction, secondary cracks are visible in the boundary between the end of the fatigue crack and the final ductile fracture of the specimen (indicated with an arrow).

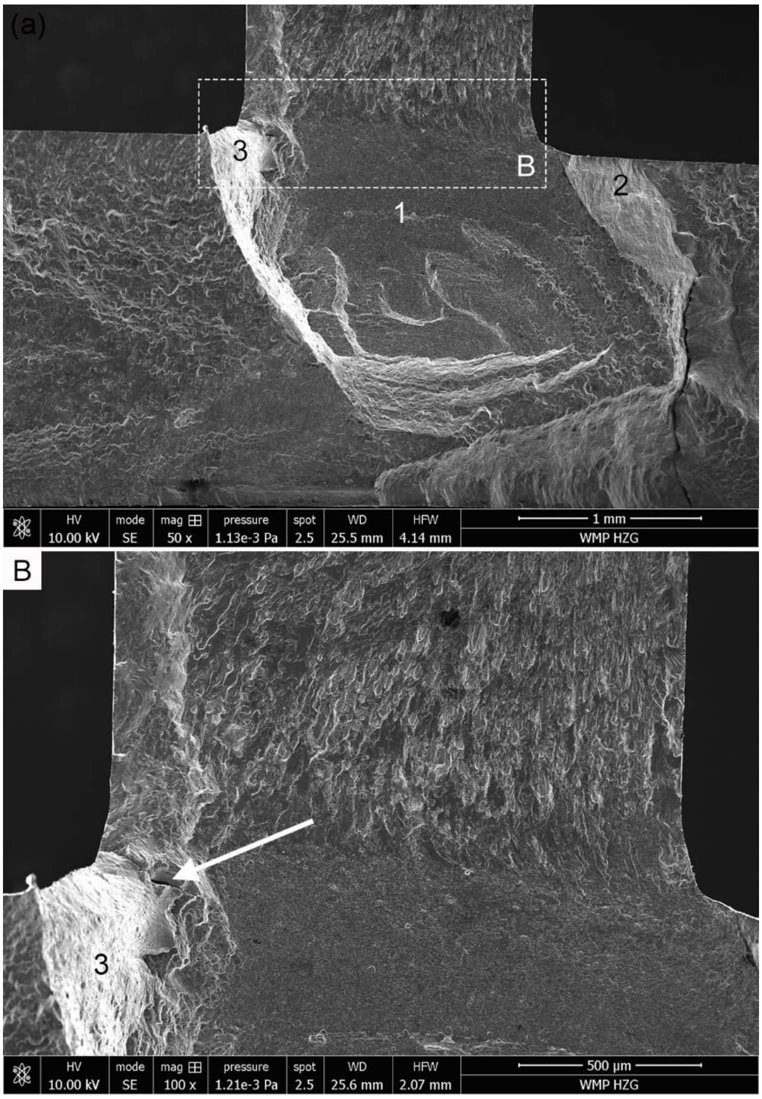

Figure 7.16. SEM images of the fatigue propagation from the stringer to the SZ for the 3-Parts joint under the high-cycles loading condition in the longitudinal direction—(a) fracture overview in the SZ with the three planes of propagation and (b) high magnification of the different fracture surfaces and corner crack

By having a closer look at the area highlighted with the letter B (Figure 7.16b), different fracture surfaces can be observed. A sharp transition can be seen when the crack passes from the stringer to the SZ in the skin. The large elongated grains of the extruded stringer determine a more irregular surface due to the inter-granular nature of crack propagation [112]. On the other hand, due to the refined globular grains of the SZ, it becomes impossible to see the fatigue striation at such a level of magnification. On the left side of the image (3), the striations are determined by the fatigue crack in the out of plane direction, which are clearly visible, and it is possible to observe a small crack located in the RS corner and marked by the arrow. This position corresponds with the one of the interface between the two alloys that clearly remains a critical area for micro-cracking when cyclic loads are applied as well.

In the NS-SP joints, the fracture behaviour has drastically different results since no fatigue initiation can be observed in the stringer due to the lower number of cycles. An overview of the fatigue crack can be observed in Figure 7.17a.

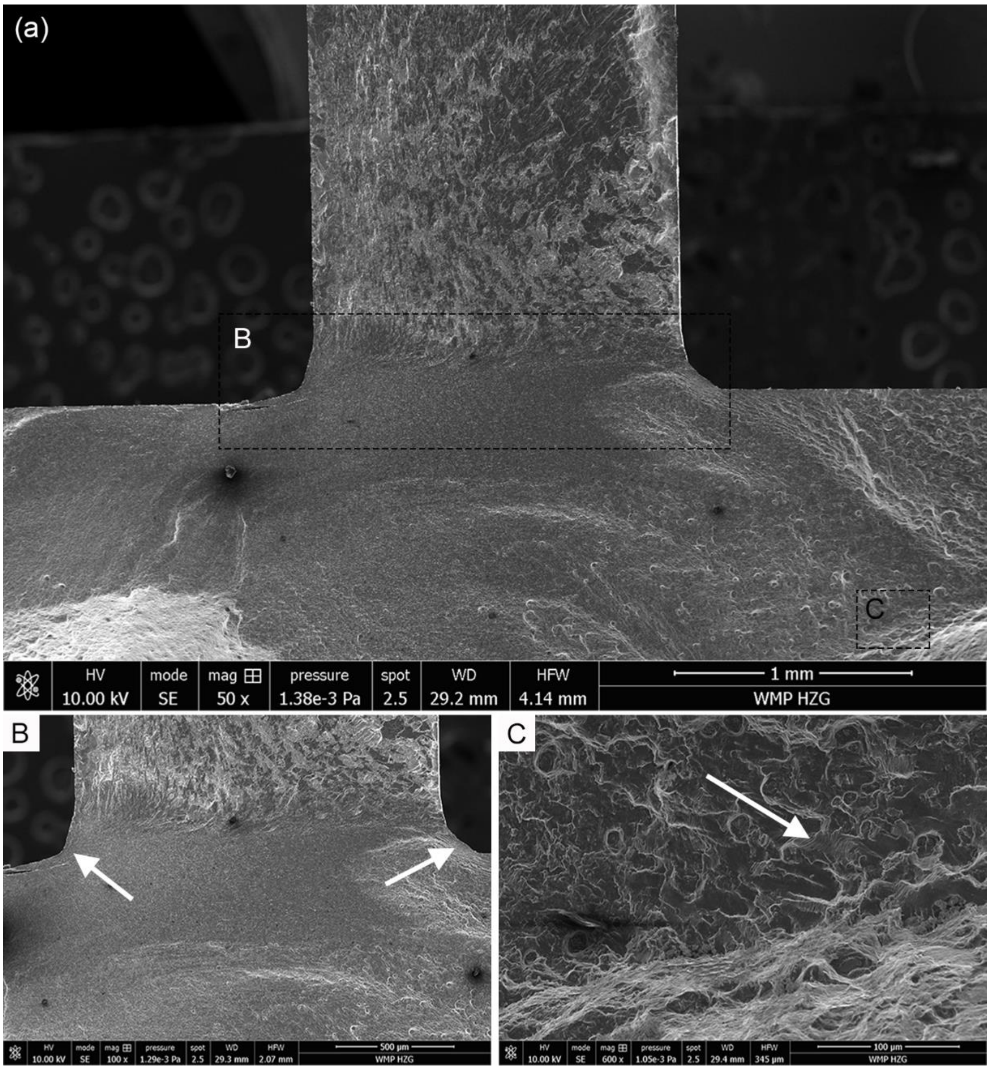

Figure 7.17. SEM images of fatigue initiation and propagation for the NS-SP joint under the high-cycles loading condition in the longitudinal direction—(a) fracture overview in the SZ, (b) high magnification image of the skin-stringer corners with fatigue-crack initiation, and (c) high magnification image, showing fatigue striations and ductile failure

Owing to the refined grain structures of the SZ, it was hard to see the signs of the fatigue crack in the small magnification image. However, while focusing on the border between the skin and the stringer (Figure 7.17b), it was possible to notice two areas of crack initiation at both the corners of the joint indicated with the two arrows. At this location, two major cracks were present perpendicular to the image plane in both the AS and RS at the interface of the two alloys, which tended to delaminate the stringer. Owing to the two-cracks propagation, the outline of the general crack did not have a typical penny-shape like the one previously observed for the 3-Parts configuration. Multiple cracks initiated in different locations. Each crack propagated in its own direction before converging together and leading to the final ductile tearing. The confirmation that we were in the presence of fatigue propagation could be seen in Figure 7.17c, where a high-magnification image was taken at the edge between the fatigue crack and ductile failure (marked with C in Figure 7.17a). Striations marks could be seen at the top-left corner of the image showing the crack propagating parallel to the arrow direction until it reached the lighter grey area, where the surface became more irregular with the presence of dimples. In the area where the fatigue crack propagated, it was possible to see some valleys, where large precipitates that were formed in the TMAZ during the process, were located.

7.3.1.2. Low-cycles Loading Condition

When the maximum stress of the fatigue cycle reached the 80% of the tensile strength for both joint configurations, the main initiation area of the fatigue cracks was located entirely on the stringer, as seen in Figure 7.18 in the case of the 3-Parts joint.

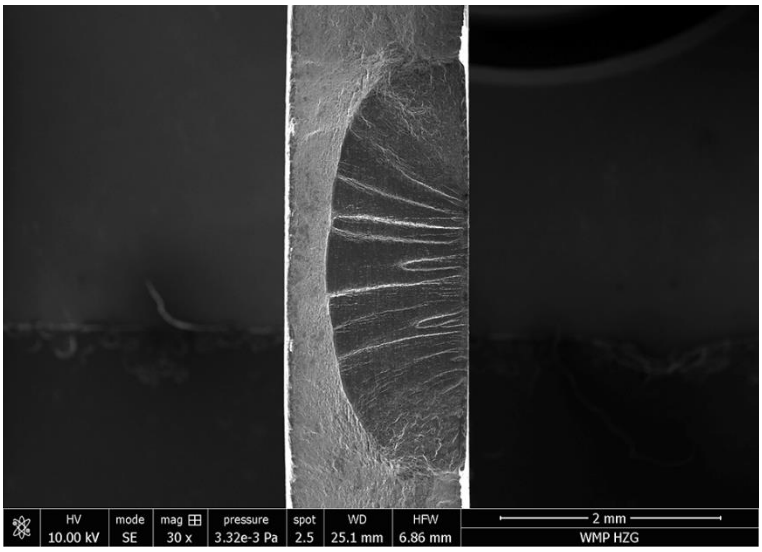

Figure 7.18. SEM image of the fatigue initiation and propagation in the stringer for the 3-Parts joint under the low-cycles loading condition in the longitudinal direction

The location of the fatigue initiation is important since it shows that when the maximum load approaches the failure strength, the stringer, which carries most of the stress, is the critical part of the joint. The welded joint has no influence on the fatigue crack initiation. This also proves that the microstructure generated by the SSFSW can withstand fatigue overloads without deteriorating the residual strength of the joint. This observation was confirmed by the fracture analysis of the SZ and the transition area between skin and stringer shown in Figure 7.19.

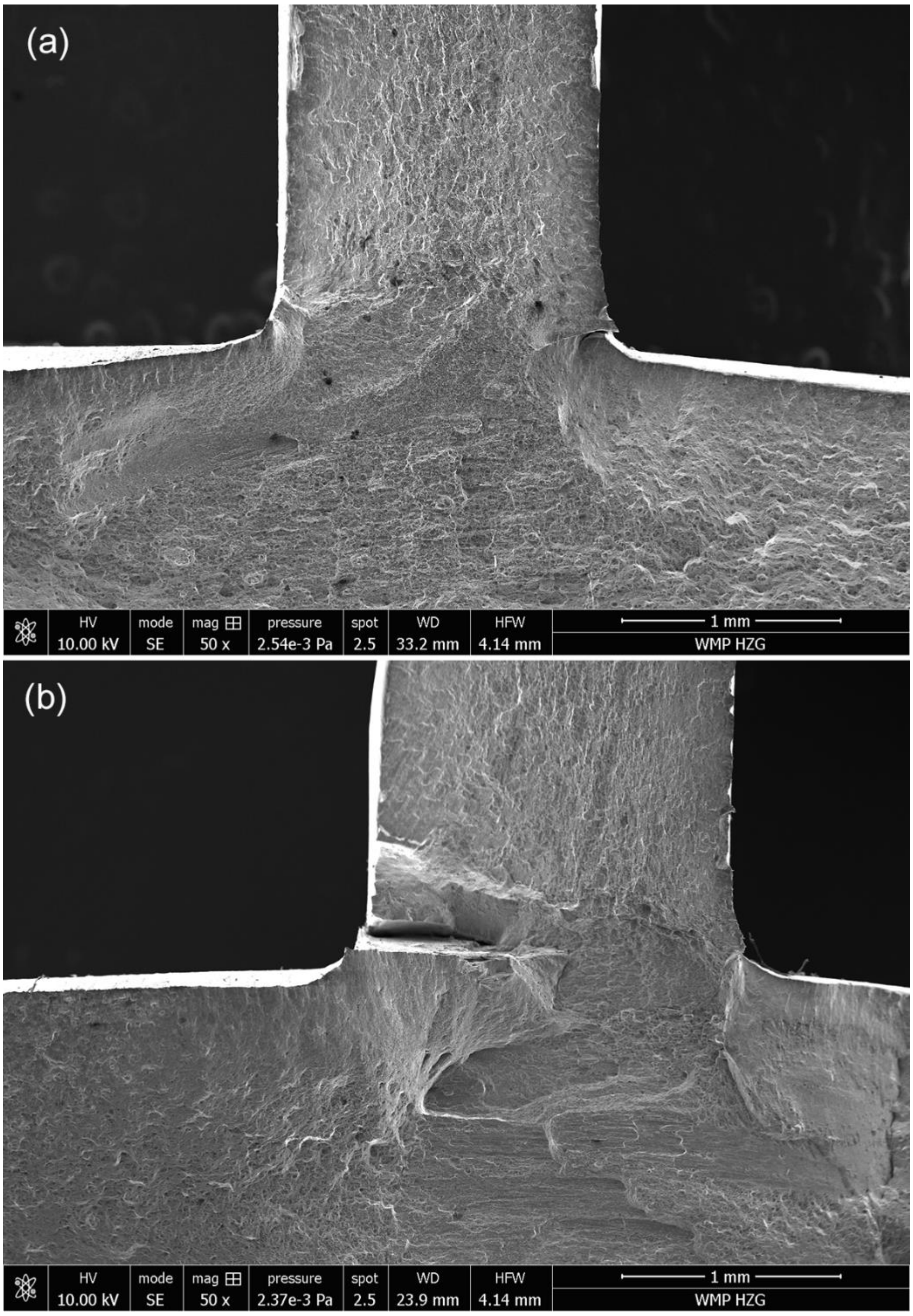

Figure 7.19. SEM images of the ductile fracture surface in the SZ under the low-cycles loading condition in the longitudinal direction (a) for the 3-Parts joint and (b) for the NS-SP configuration

For both joint configurations, the fracture in the centre of the SZ is completely ductile, even if the appearance of the cracks differ. In the NS-SP joint (Figure 7.19a), the area of the SZ close to the stringer shows a reduced number of dimples. This area is very similar to the fracture surface observed in the 3-Parts joint throughout the entire skin thickness in the centre of the SZ (Figure 7.19b). Owing to this observation, it can be concluded that the higher strength AA7050, located exactly in the areas described in the two configurations, still shows a reduction in plasticization of the crack front with respect to the AA2024, even after being welded and after undergoing massive microstructural transformation. In the two corners formed by the skin and the stringer, both configurations show similar behaviour, with small fatigue cracks propagating parallel to the load direction. In this area, it is also possible to observe secondary cracks, similar to the cracks seen in the case of the high-cycling condition that are caused by the reduced strength of the two alloys' interface, which was thoroughly analysed in the previous chapters.

7.4. Summary

The main conclusion of the fatigue investigation performed in this chapter for the two-joint configurations are summarised as follows:

- During the fatigue tests in the hoop-direction, the 3-Parts joints showed the higher robustness of the results with respect to the Notch Skin-Single Pass, with a lower coefficient of variation for all the stress levels analysed. The 3-Parts configuration is beneficial for the fatigue life at high stress levels; however, the two variants have the same fatigue limit at 30% of the UTS.
- The T-joints realized by the SSFSW have a stress concentration of two with respect to the AA 2024-T3. The stress concentration is not only technological, caused by the welding technology, but a major contribution is geometrical, own to the absence of the skin–stringer radius. In respect to the riveted T-Joints with optimized geometry, the SSFSW technology leads to half the stress concentration and more than a 50% increase in the fatigue limit.
- In the 3-Parts joints, the fatigue crack initiates at the shoulder mark in the TMAZ of the welds at high-cycles. For the NS-SP variant, the skin–stringer corner and the material interface cause crack initiation and the unwanted delamination of the stringer. Similar initiation areas could be observed for both the configurations in the low-fatigue cycle range. For the NS-SP variant, crack turning towards the stringer was seen in the low cycle area as well as in the high cycle one.
- In the longitudinal load direction, the 3-Parts joints present a higher fatigue life while entering in the high-cycles area with respect to the NS-SP variant. The fatigue initiation is caused by the shoulder mark and the stress concentration in the stringer for the 3-Parts variant. In the low-cycles fatigue, the two joint configurations show similar fatigue initiation behaviour, with the largest part of fatigue propagation happening in the stringer.

8. Damage Tolerance Analysis of 5-stringer Fuselage Panels

In this part of the study, skin–stringer panels were realized by SSFSW with the 3-Parts configuration. The welding parameters used were the same as already investigated for the fatigue initiation analysis, 1200 RPM, and WS = 180 mm/min, which showed the best mechanical response in the static tests. The specimens were cut from two-meters-long welded panels, down to a dimension of 1200 x 896 mm, with the most important dimensions of the cross-section for the following analysis shown in Figure 8.1. In all the specimens, the central stringer was severed and an initial crack length ($2a$) of 12 mm was placed in the skin underneath it. The first 2 mm of crack propagation was not considered in this study since they were a pre-cracking necessity in order to have a conventional stress-state at the crack-tip.

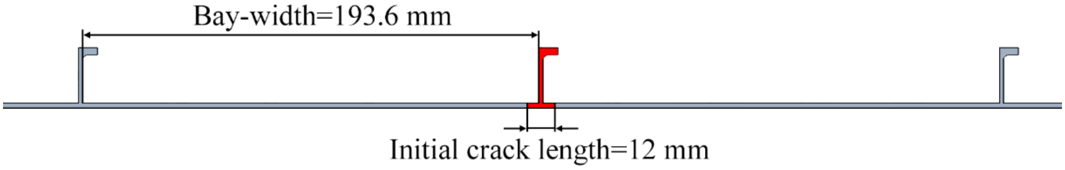

Figure 8.1. Schematic view of the panels' cross-section with the dimensions of interest, only the inner three stringers are shown

As explained in the introduction, the damage-tolerance analysis was based on the investigation of the fatigue-crack propagation behaviour and the residual strength of the structures and these investigations are performed in this chapter. For the five welded specimens, FCG tests were carried up to half-crack length (a) equal to the one bay-width (b). The FCG test was continued in three of the panels until final failure; the remaining panels were monotonically loaded in order to measure the residual strength.

In the first section, the experimental results of the FCG tests for the new technology were analysed and compared to the model developed by Professor Zhang's group at Cranfield University [113] and with the current joining technologies. A part of this study was also dedicated to the application of the DIC system to the FCG experiments, and the possibility of using this technique for calculating the changes in the SIF for the growing crack under cyclic loading. The second part was dedicated to the residual strength of the panels and their applicability to real aerospace structures.

8.1. Fatigue Crack Growth

8.1.1. Experimental Investigation

The tested specimens were loaded in tension to provide a remote stress of S_{max} = 90 MPa at a frequency of 1 Hz. The crack growth was recorded by the periodic observations of the locations of the two crack-tips by using a travelling optical microscope with a magnification factor of 40. A clip-gage was applied to the head of the severed central stringer and the crack-opening displacement (COD) was measured. The COD was set to zero at the mean stress level and all the measurements during the test were performed at the maximum stress level. Some of the main results of the experiments are reported in Table 8.1. The specimens 5-S-2 and 5-S-3 do not show the cycles at failure and the final crack length since they were the one used for the residual strength analysis.

Table 8.1. Main results of the FCG analysis for the five measured panels – the crack length are given for the left and right half-crack

Specimen number	Cycles (2-bays crack)	Crack length (mm) (failure)		Cycles (failure)
5-S-1	33300	343.8	209.79	38000
5-S-2	41700	-		-
5-S-3	39000	-		-
5-S-4	40300	280.6	292.2	44000
5-S-5	33700	297.15	324.5	34500

It was possible to see a large difference in the number of cycles necessary in order to reach both the two-bays crack and the final failure between the specimens 5-S-1, 5-S-5, and the 5-S-4. The difference between the three specimens was in the type of anti-buckling devices used to avoid the out-of-plane displacement of the panels during the test. The specimens 5-S-1 and 5-S-5 were tested with an anti-buckling device with a reduced cross-section necessary to leave an empty area on the stringer side of the specimens, to perform the DIC measurements. The test data show both a larger initial COD and a higher slope of the COD-2a curves when a 'lighter' anti-buckling device is used (Figure 8.2). The initial value of the COD does not particularly influence the FCG for the small values of the half-crack length, with the three a-N curves that show the same behaviour up to an a between 25 and 30 mm. In this small crack length regime, despite differences can be measured in the slope of the COD-2a curves, it seems that the stiffening of the stringer is sufficient to limit the buckling and the crack propagation rates are similar.

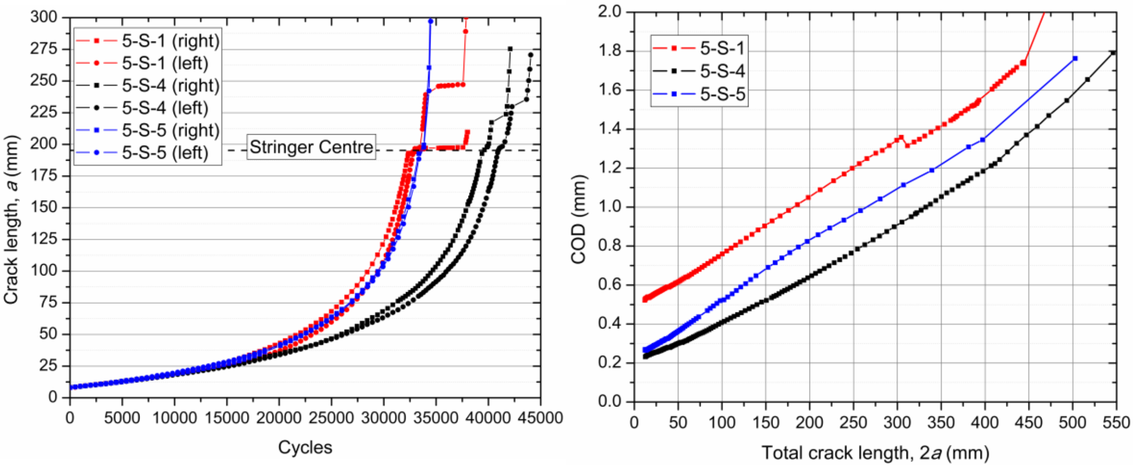

Figure 8.2. Comparison of the FCG behaviour and the COD for different specimens and anti-buckling systems

The influence of the out-of-plane displacement becomes more consistent when the crack moves away from the stringer. The change in the COD curve's slope for the specimens with light anti-buckling devices took place at smaller values of crack length than for the 5-S-4 specimen. The buckling influence, which causes a different stress-state at the crack-tip and SIF, is maximum at the centre of the bay. The confirmation of this phenomenon can be seen in the area of the graphs corresponding to this region of the panels, where the maximum difference in the slope of the COD-2a curves is measured. Approaching the other stringers, their stiffening reduces the skin-buckling again and the slopes of the three curves become similar to each other. A difference in behaviour between the three specimens is observed once the crack reaches the stringer centre and propagates until the final failure. In the specimen 5-S-5, the two cracks propagate directly from the skin to the stringer and, as shown in Figure 8.2, just a small retardation could be observed at a crack length of 192 mm. In the other two specimens, the curves relative to the left and the right cracks differ since while one crack shows a similar behaviour, the other turns 90º and runs parallel to the stringer (Figure 8.3). Consequently, one stringer failure is caused by crack propagation into it and the other shows a ductile failure due to the high stresses in the remaining section.

Figure 8.3. Different crack propagation behaviour between the right and the left crack at the skin-stringer weld for the specimen 5-S-4

The extra retardation in the specimen 5-S-1 for the right crack is caused by the presence of small defects on the weld surface, shown in Figure 8.4.

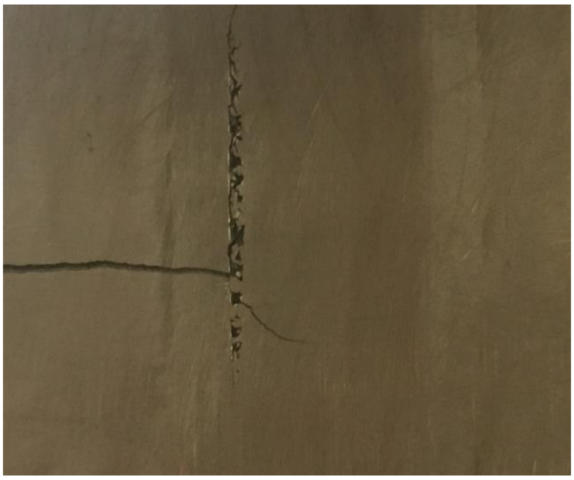

Figure 8.4. Interaction between the propagating crack and surface defects of the weld

This defect was found just in this specimen and only for one stringer. The surface defect was caused by the poor tolerance of the stringer that caused a reduced pressure between the stirred material and the shoulder. On one hand, the crack turns in the direction parallel to the load where the defects create a lower resistance path and on the other hand, the shape of the defects causes a redistribution of the stress at the crack-tip, reducing the SIF. Once the crack-tip reaches the defect, these two combined effects lead to the retardation of crack propagation.

The FCGR (da/dN) as a function of the half-crack length, is shown in Figure 8.5 for the specimen 5-S-4. The FCGR in the graph is presented for two different data reduction techniques defined according to the ASTM E647-11. The blue data points present a larger variation in the trend due to the secant method used as the interpolation technique. In this case, the FCGR is determined by the slope between the two measured crack lengths plotted as a function of the number of cycles. The other two curves are obtained by using the 7-points incremental polynomial technique that requires a more complex computational method but shows a significant improvement in result stability and more importantly a higher reliability. This method consists of fitting a parabola to sets of seven consecutive data points.

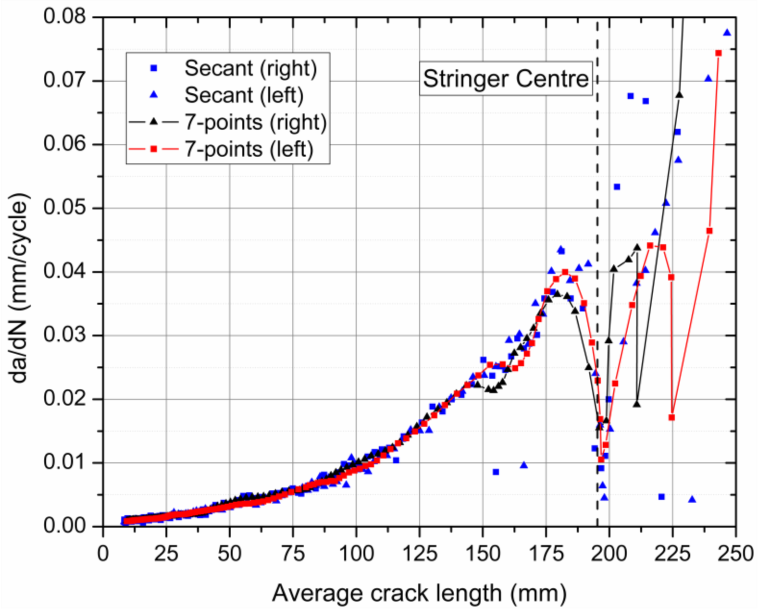

Figure 8.5. FCGR measurements of the specimen 5-S-4 calculated with different reduction techniques

In order to understand the variation of FCGR with the increasing half-crack length, it is important to correlate this with the changes in SIF. One of the simplest models to correlate these two parameters was developed by Paris and Erdogan and it quite accurately approximates the trend in the stable crack growth zone (Eq. (8.1)) [114].

$$\frac{da}{dN} = C\Delta K^n$$
$$\Delta K = \beta\left(\frac{a}{b}\right)\Delta\sigma\sqrt{\pi a} \qquad \textbf{(8.1)}$$

Since the stress variation is constant in this study, the FCGR depends on the half-crack length (a), the geometry factor $\beta(\frac{a}{b}) = f(a/b)$ with b as bay-width, and the two parameters C and n. These last two parameters are mainly determined by the material in which the crack is propagating, according to the similarity principle [79]. In fact, this states that specimens with different crack lengths and cyclic stresses but similar ΔK cycles should have the same crack extension Δa per cycle. This principle is particularly important in the design of aircraft structures as once C and n are known from the coupon level tests for which the ΔK has known analytical solutions; the same two parameters can be used in the prediction of the FCGR for large structures realized with the same material. Therefore, while considering structures such as the one in this study, the variation of the geometry factor as a function of the distance between the crack-tip and the stringer plays a key-role.

The FCGR increases, following a progressive trend, until the half-crack reaches a length of ~150 mm. At this point, a decrease in the FCGR could be observed for around 10 mm before the FCGR increases steeply until â=180 mm. Once the crack approaches the stringer, the load is redistributed between this and the skin, causing a reduction in the SIF at the crack-tip. According to Eq. (8.1), the lower SIF leads to a drop in the FCGR that could be observed from the graph up to a crack-length of 196.6 mm, around 1 mm after the stringer. In this area, both the left and right half-cracks turn after penetrating the SZ (Figure 8.6). This phenomenon was already observed in the case of FSW of aluminium alloys and contributes to the crack-growth retardation already observed [115]. The interface between the layers of deposited material behind the probe are an area of easier crack propagation. Despite the smaller size of the SZ in case of SSFSW, this layering phenomenon is still present in the centre of the weld where the probe rotates.

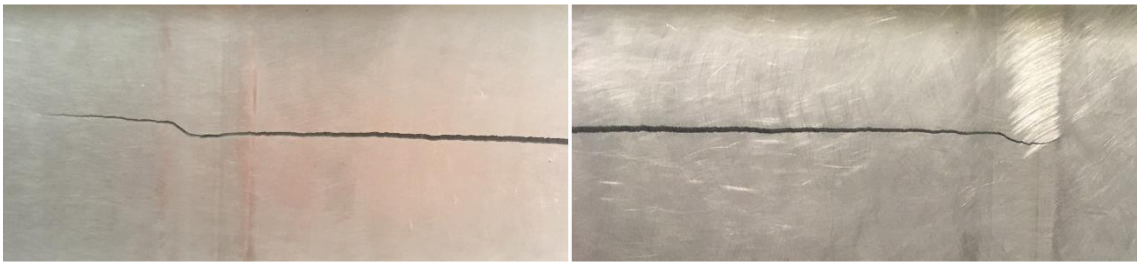

Figure 8.6. Crack-turning in the SZ for both right and left crack

After such a crack-length was reached, a difference could be observed in the FCGR between the left and the right crack. As shown in Figure 8.3, the left crack keeps propagating in the skin, while the right crack bifurcates and propagates into both skin and stringer. The lower crack propagation resistance of the AA7050 with respect to the AA2024 leads to a steeper increase of the FCGR in the right crack. The successive reduction in the FCGR is caused by the stringer crack reaching the head of the stringer. The increase of cross-section in this area leads to a reduction of stress at the crack-tip that slows down the crack propagation and the drop in the FCGR. With the growing crack, the K_{max} at the crack-tip in the stringer finally reaches the fracture toughness of the material, leading to the failure of the stringer. When this happens, the stress in the skin increases drastically, causing the final acceleration in the crack growth and the failure of the panel.

8.1.2. Application of DIC to FCG

The use of DIC during FCG experiments allows obtaining measurements during the tests which are otherwise impossible to determine experimentally.

At first, it is interesting to quantify the amount of buckling that the surface of the specimen undergoes during crack-extension. In order to do that, the out of plane displacement (z-displacement) is measured along a section coincident with the crack profile and the results of this study are shown in Figure 8.7. The beginning of the section is 43.5 mm from the centre of the severed stringer and no closer measurements could be performed due to obstacle in front of the cameras.

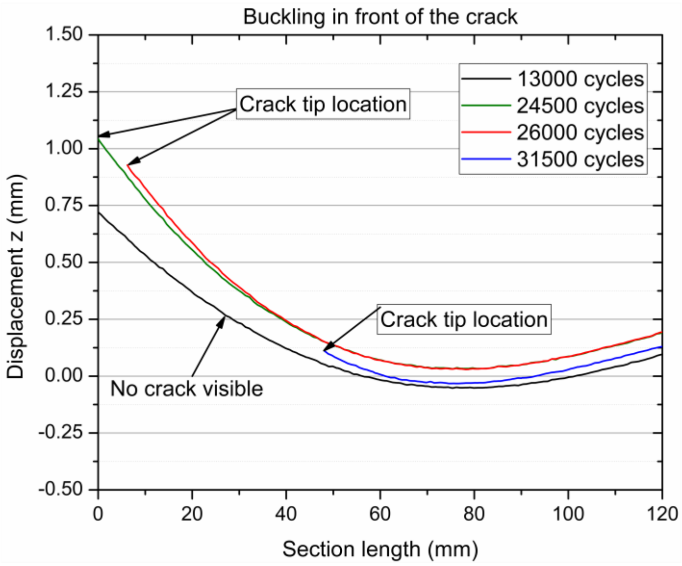

Figure 8.7. Out-of-plane displacement for different numbers of cycles along the crack profile

At the maximum load, the centre stringer moves towards the cameras, generating a positive z-displacement, which increases with the growing crack. At 31500 cycles, the fact that the displacement is close to zero does not mean that there is no buckling but simply that the crack-tip horizontal plane is close to the original one. The buckling phenomenon is the difference between maximum and minimum displacement, which is more than 1 mm in just 70 mm of section length; this is important to quantify. In general, the parabolic shape of the z-displacement shows that the stringers move outward, leading to the maximum buckling around the centre of each bay. This analysis gives a quantitative confirmation of what was hypothesized before from the analysis of the COD at the central stringer.

The outward movement of the stringers indicates that the load is not homogeneously distributed between these and the skin. To understand the amount of stress in the skin at the maximum load, the strain measurement was performed at 18000 cycles, which could be used as an example. After the number of cycles, the measured total crack length was equal to 52.3 mm, leaving an intact cross-section of 1920 mm^2. If the load was homogeneously distributed between the skin and the stringers, the average stress over the cross-section should have been 94 MPa. Since the strain map was reasonably homogeneous in all the analysed area, it was possible to average the strain and obtain a value of 0.001 mm/mm; completely in the elastic field. Consequently, the average stress in the bay, away from the crack-tip, is around 70 MPa, proving that the welded stringers have efficiently unloaded the skin, slowing the FCG not only when the crack is nearby them but also for short cracks.

In order to characterize the crack-driving force, a common parameter used in fracture mechanics is the crack-tip opening displacement (CTOD). The CTOD, initially developed by Wells [116] for small-scale yielding, allows the correlation of the transverse displacement in front of the crack-tip with the SIF. The correlation between these two parameters in the plane stress state, such as the one in the experiments, is as follows:

$$CTOD\ (\delta) = \frac{K_I^2}{\sigma_y E} \tag{8.2}$$

where, σ_y is the yield stress and E is the Young's modulus.

A similar parameter, δ_5, developed by Schwalbe [117], allowed the extension for the use of the CTOD also in the case of large plasticity at the crack-tip and, therefore, could be related with the typical concepts of EPFM, such as the J-integral. This parameter was shown to have a larger independence from the size of the specimens and its geometry with respect to the classical CTOD. In conventional experiments, the δ_5 is measured directly on the surface of the specimen at the side of the original crack-tip and the gauge has a length of 2.5 mm at either side of the crack.

In spite of being a useful chracterization tool in case of small specimens, the problem with the conventional use of the δ_5 is that when the crack grows, the distance between the crack-tip and the clip gauge increases, causing the loss of significance of the measured value of CTOD. In this study, the use of a DIC system allowed to overcome the main problem related to the δ_5 measurements. As shown in Figure 8.8, as the crack grows, it is possible to reposition a new 'digital' extensometer directly at the crack-tip every time.

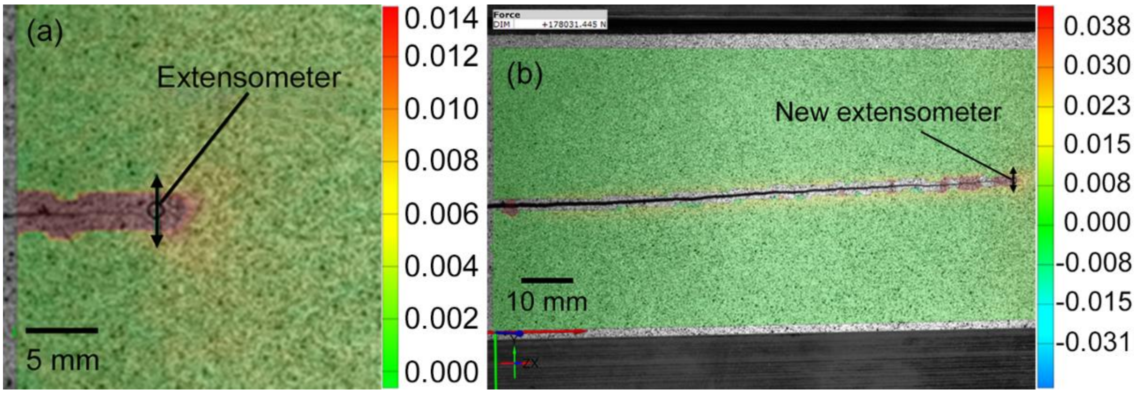

Figure 8.8. Major strain map (mm/mm) and the use of the 'digital' extensometer to measure the CTOD for (a) 27000 cycles and (b) 36500 cycles.

The initial extensometer, used for a crack-length of 53.06 mm (Figure 8.8a), would lose any physical meaning if it were used to chracterize the CTOD for a crack of 150.49 mm (Figure 8.8b).

As an example of the use of this technique, three measurements of the CTOD from three different extensometers, re-positioned at new crack-tip locations, as a function of the number of cycles are shown in Figure 8.9. The red curve is relative to the extensometer placed at the crack-tip position after 26500 cycles and the black arrow indicates the CTOD measurement relative to the same number of cycles. The other two curves show the same type of analysis but for different crack lengths and, consequently, different positions of the extensometer.

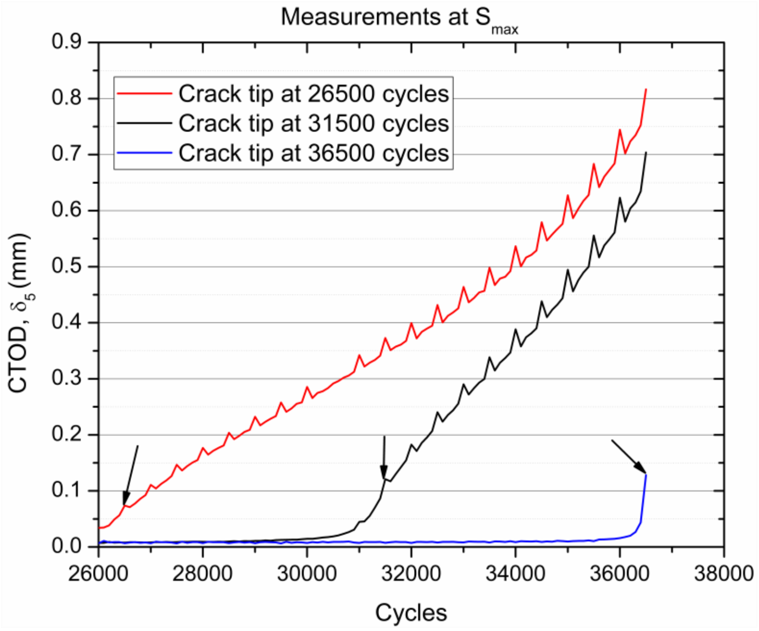

Figure 8.9. CTOD variations as a function of the number of cycles for the different positions of the 'digital' extensometer and crack-tips

If the conventional method had been used to measure the δ_5, after 36500 cycles, the gauge placed at the tip of a 51.12 mm crack (26500 cycle) would show a value of CTOD above 0.8 mm. In reality, the correct measurement obtained from the extensometer placed at the correct crack length (150.49 mm) is equal to 0.13, thus avoiding incurring an error of over 600%. In a structure with such a complex geometry, large errors can also occur for smaller crack-length variations and they can be easily avoided using a DIC system.

Following the procedure just explained, the δ_5 was analysed at the crack-tip every 500 cycles (Figure 8.10).

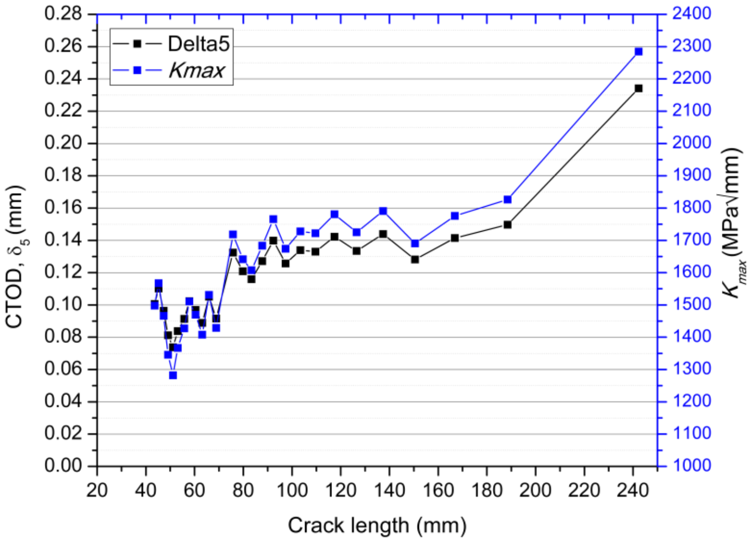

Figure 8.10. CTOD and K_{max} variations as functions of the measured crack-length

In spite of the measurements that were performed over each 100 seconds (i.e., 100 cycles), using a larger interval in order to correlate the CTOD with the exact crack-length obtained by optical microscopy was chosen. It was possible to observe from the graph that the δ_5 increased in steps after a sharp drop, for a crack length of 51.12 mm (26% of the bay width). After reaching a value around 0.14 mm for a crack-length of 117.41 mm, the CTOD remains constant while approaching the stringer. In the last three measurements before the one-bay crack length, the δ_5 increased at a low constant slope; after the crack overcame the stringer, the curve steeply rose.

Since the plastic zone at the crack-tip was very small in comparison to the crack length, the Equation (8.2), valid in the case of an LEFM analysis, could be used to correlate the measured values of the δ_5 with the SIF at the maximum load. For this analysis, the yield stress obtained from the tensile tests of the AA2024-T3 (see Chapter 3) and the Young's modulus equal to 71 GPa were used. As expected, similar trends were observed for K_{max} and the measured δ_5. It was interesting to see how, for long cracks between 100 and 150 mm, the SIF did not change significantly, thus showing the influence of the welded stringer that limited the SIF variations for the increasing crack-length. After the stable phase of the CTOD, both this and the SIF increased in the last three measurements before reaching the stringer. Once the crack tip overcame the stringer, the SIF sharply increased and reached a value of around 2280 MPa$\sqrt{mm}$. This value was quite close to the critical SIF (K_c) of the material (equal to 2380 MPa$\sqrt{mm}$ [90]) and justified unstable crack propagation, which happens a few cycles later after the both stringers fail.

In order to quantify the influence of the welded stringers on the evolution of the crack and the FCG behaviour, it was possible to obtain the geometry factor from the maximum SIF (Equation (8.3)) as follows:

$$\beta = \frac{K_{max}}{\sigma_{max}\sqrt{\pi a}} \qquad \textbf{(8.3)}$$

Since the δ_5 was measured at the maximum load, the SIF corresponded to a remote stress (σ_{max}) of 90 MPa. From this equation, it was possible to obtain the variation of β as a function of the normalized crack length (a/b), where b was the distance between the two stringers.

In spite of being named the geometry factor, the β determined from the experiments was not simply influenced by the distance from the stringers, i.e., specimen geometry. Other effects, such as the residual stresses generated after SSFSW and the crack closure caused by the plastic zone around the crack-tip, as the one seen in Figure 8.8a, determined the variations in the β and, consequently, in the FCGR. The results of this analysis are shown in Figure 8.11. The development of the β can be divided into three main phases. For a crack length up to 25% of the bay width, the β decreases sharply, probably caused by the larger influence of the plastic zone and the crack-closure for shorter cracks. In the second phase, up to the crack-length equal to 75% of the bay width, β decreased steadily with the increasing crack length. A larger part of the load was gradually transferred from the skin to the stringer, causing the reduction of the β and, as previously observed, a constant SIF at the crack-tip.

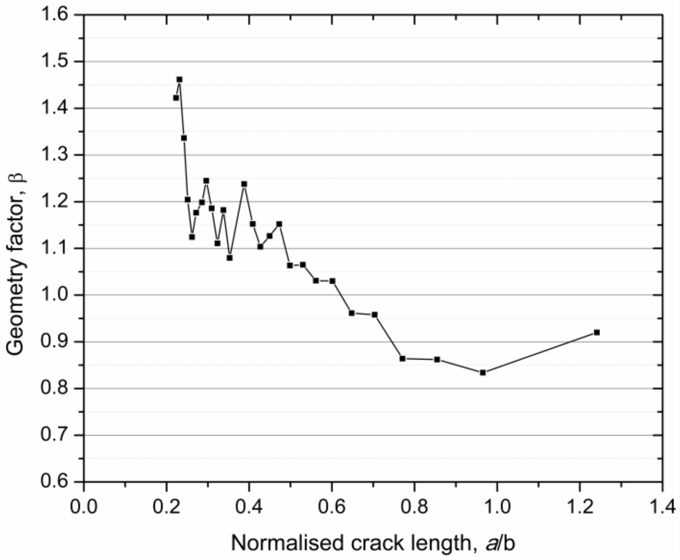

Figure 8.11. Variation of the geometry factor in the function of the normalized crack length

The third phase, until the crack reaches the stringer, shows an almost constant β. In this area, the decrease of the β, caused by the load transfer was probably compensated by the changes in microstructure induced during the welding process. Another contribution to the increase in the SIF is given by the tensile residual stresses introduced [72, 73]. In LEFM, the influence of the residual stress can be superimposed with the stress range applied during the test, causing an increase in the effective K_{max} [118].

By using the DIC technique, it is possible to analyse the evolution of the strain profile at the crack-tip, with an increase in the crack length (Figure 8.12).

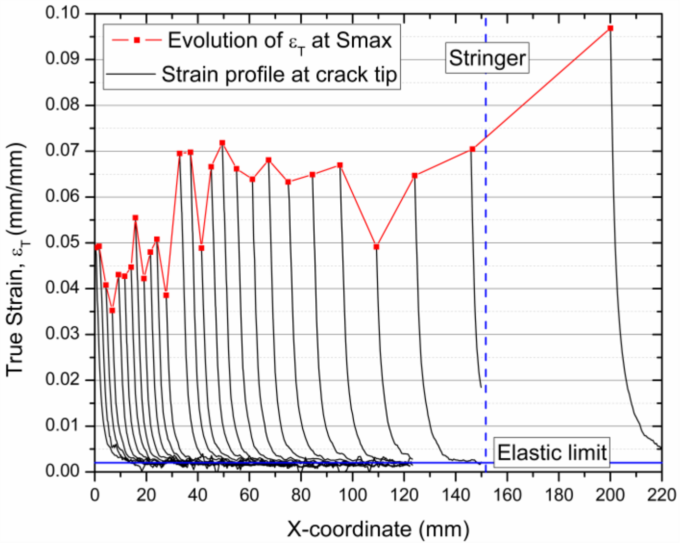

Figure 8.12. True strain profile for different crack lengths along a section in front of the crack-tip

The major true strain was measured on a section in front of the crack-tip, each 500 cycles and for different crack lengths. Since the crack-path is not linear, as it can be seen in Figure 8.8b, multiple sections have to be defined in order to track the vertical movement (Y-direction) of the crack-tip.

The true strain measured in front of the crack-tip decreased linearly, with similar slope, for different crack lengths, until a strain level of 0.01 was reached. The behaviour shows that up to that level of strain, the plastic area in front of the crack was almost the same for different crack-lengths. Since this strain difference corresponded to the flat part of the stress–strain curve, large strain variations caused small stress changes. By increasing the crack-length, the larger changes between the strain profiles were in the curvature at the elbow of the curves that showed three different behaviours, as previously observed for the β. The beginning of the curvature was moved towards the upper levels of strain, since the asymptotical true strain in the last part of the section was raised as well. In particular, for crack lengths above 150 mm, the asymptotic strain remains still above 0.2% due to the small cross section remaining between the skin and the stringer and the residual stresses introduced during welding. This is particularly clear when observing the last profile before the stringer (a = 188.5 mm) where the strain remains above the 2% (Figure 8.13).

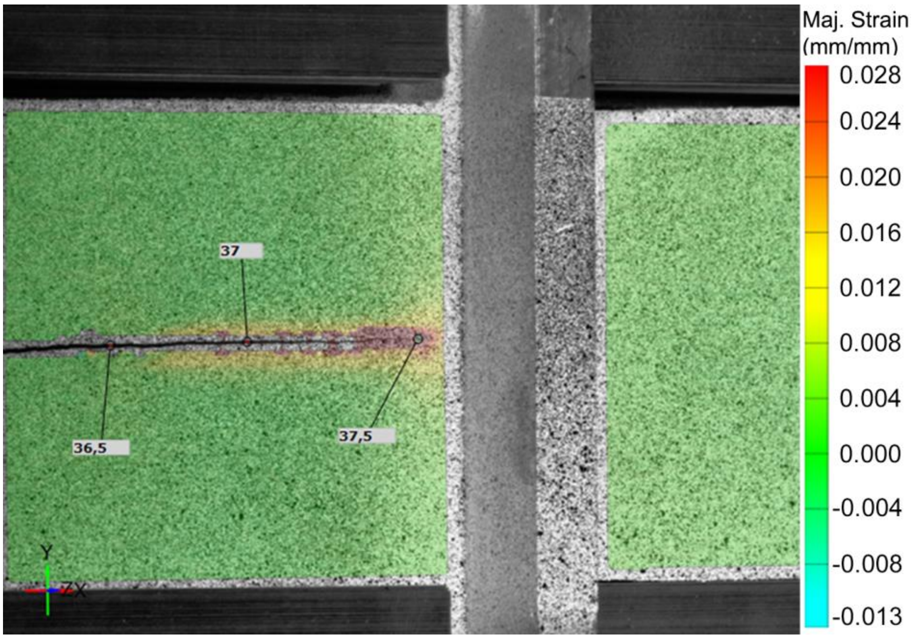

Figure 8.13. Strain map for a crack length of 188.5 mm at 37500 cycles.

While considering just the peak of the strain profile in front of the crack-tip, this showed a similar behaviour as the K_{max} and δ_5 up to 36500 cycles. The strain-peak at the crack-tip could be a useful measurement to characterize the crack-driving force instead of the classic definition of the SIF. Different to the LEFM definition of the SIF, which was assumed to have a singularity at the crack-tip where the stress tended to infinity, the measured strain already included the influence of crack-tip plasticity and could be correlated as well with the energy necessary to extend the crack.

Unfortunately, it was not possible to measure the strain at the crack-tip for 38000 cycles since this was hidden behind the stringer. However, once the crack-tip overcame the stringer, the strain levels increased abruptly both at the peak and in the asymptotic area, even if the stringer was not fully fractured, as observable in Figure 8.14.

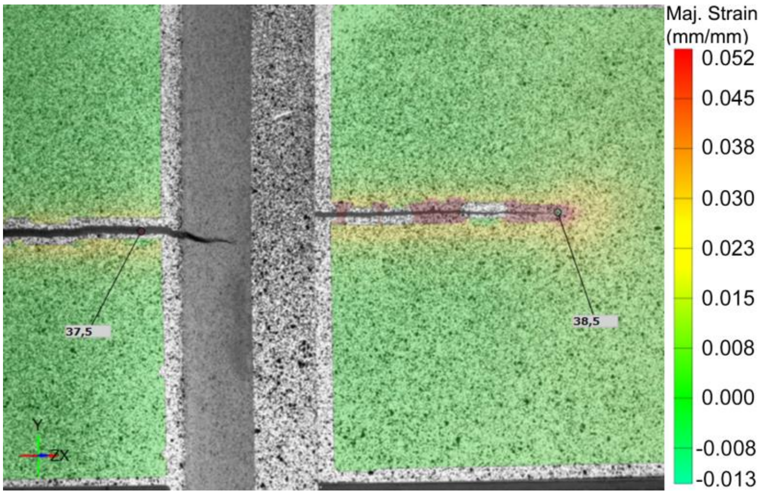

Figure 8.14. Strain map for a crack length of 242.3 mm at 38500 cycles.

The strain map confirms what was already observed from the strain profile that although the stringer has not failed, the cross-section of the specimen was largely plasticized. In this contest, the assumption of operation in a state of low plasticity at the crack-tip, on which LEFM was based, was no longer realistic. The use of a strain-based analysis of the crack-tip condition allowed the incorporation of the influence of the plastic zone ahead of the crack that was not included in the standard definition of the SIF.

8.1.3. Comparison with a Simulation Model

The model used to simulate the experimental results was developed at Cranfield University in the MSc final work of Bansal [113] under the academic supervision of Professor Zhang. The simulated structure was an 11-stringer integral panel made by an aluminium alloy with the Young's modulus (E) equal to 71 GPa and a Poisson's ratio (ν) of 0.3, similar to the ratio investigated in this study. The bay-width of the panel was 140 mm, while all the other main dimensions were shown in Figure 8.15.

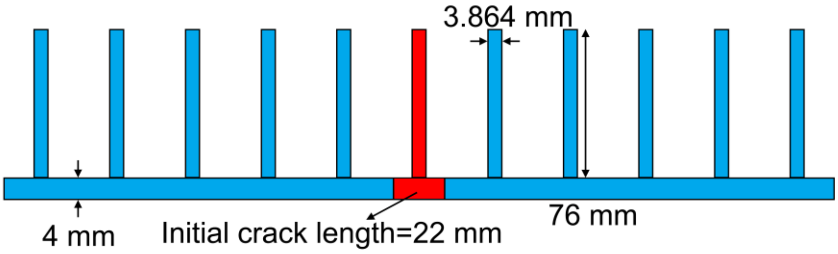

Figure 8.15. Cross-section of the panels used for the modelling study

In spite of the differences in the geometry between the model and the experimental panel, the main parameter for the comparison was the ratio between the stringer cross-sectional surface and the half-bay area (s). In the simulation, the smaller investigated s-parameter was 0.5 and it could be considered a good approximation of the one resulting from the panels realized by SSFSW (0.32). In this way it was possible to compare the solution obtained from the simulation with the one from the experiments.

In case of the stiffened panels, the SIF varied continuously with the growing crack through the changes in the geometry factor, as seen in Eq. (8.1). The simulation of the panel allowed computation in the variation of the β as a function of the normalized crack-length, with the results of the study shown in Figure 8.16. The graph shows how the geometry factor decreases continuously while approaching the stringer. The dissimilarity in the behaviour between the two simulated curves after the crack overcomes each stringer was caused by the different assumption regarding the FCGR of the stringer. For a velocity ratio, i.e., crack-growth profile pattern equal to one, the crack-growth speed in the skin and the stringer are assumed to be the same, while in the other case, the FCGR of the stringer is half of that of the skin. Therefore, in the first case, the crack retardation effect of the stringer was reduced and the β increased faster after the crack in the skin overcame each stringer. Since the two components were made of dissimilar aluminium alloys and the crack growth resistance of the AA7050 was lower than the one of the AA2024 in this study, the curve relative to a velocity ratio of one was used for further analysis.

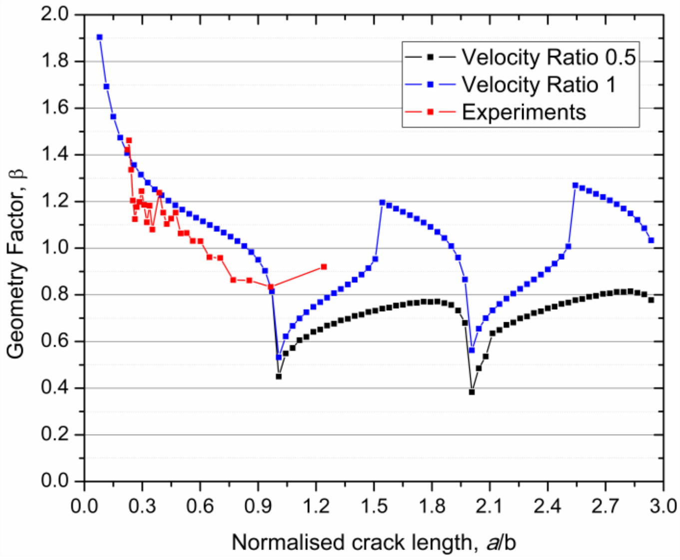

Figure 8.16. Predicted behaviour of the geometry factor for multi-stringer panels

The β-curve obtained from the simulation showed a similar trend to the one experimentally determined with the DIC system. Despite this similarity of the global behaviour, differences could be observed in the measured values. When the crack is in the central part of the bay, a/b is between 0.3 and 0.7, the results of the simulation tend to overestimate the β. The source of this difference is in the larger initial drop of β in the experiments, which is probably caused by the residual stresses introduced during welding. The fact that the two curves run parallel once away from the stringer and the welding area seems to support this hypothesis. The larger difference between the curves was in the area around the stringer. The influence of the stringer in the variation of β was more marked in the simulation, where an abrupt drop of the geometry factor could be seen right in correspondence with the stringer. In the experiments, the changes of the β seem smoother both before and after the stringer, although no data could be recorded by DIC when the crack was in proximity of the stringer due to the interference of this. From the available data, the simulated curve exhibits an underestimation of the β as well as the ΔK, which can be problematic in a conservative approach.

The ΔK for different crack length could be calculated by replacing the correct value of the geometry factor for each value of a. In order to calculate the FCGR with Paris' equation (8.1), the only missing data are the C and n parameters measured for the same material, and the stress ratio. In this study, the two parameters relative to the AA2024-T3 at R = 0.1 were set to 1.64x10^{-09} and 3.99, respectively [119]. The results of the FCGR were calculated from the model and the experimental one is shown in Figure 8.17a. For small crack lengths, the computed FCGR was above the experimental result and showed a higher slope. With the growing crack, the slope of the simulated curve remained almost constant until it reached the maximum around 25 mm in front of the stringer. The modelled behaviour presented a discrepancy from the experiments, where the FCGR increased at different rates with a crack acceleration in the middle of the bay. The differences between the two curves could be related with the buckling phenomenon in the experiments that was maximum in the area and was not considered in the model. In contrast with the experiments, the FCGR constantly dropped until the stringer centre was reached. In that area, the tensile residual stresses might have affected the FCGR in the experiments. Their effect over the crack propagation behaviour was not included in the model, causing the difference between the two curves. The residual stress' influence probably contributed to higher acceleration of the crack after overcoming the stringer in the experiments with respect to the simulation. The absence of the stringer head in the model also explained why no second drop could be observed in the simulated curve. The stringer head' effect was clearly explicable from the experiments, considering the basic concepts of fracture mechanics and it was already observed in the previous simulated model when the geometrical feature was included [90]. After stringer failure, the experimental curve showed immediately a steep increase in the FCGR, which was not observed in the simulated curve. This difference was explicable, considering the difference in the panel's width and number of stringers between the specimen and the model. A larger number of stringers led to a stress redistribution between the intact stringer and a consequent reduction of the SIF at the crack-tip, as represented in the simulation. In the experiment, once the two stringers beside the central one failed, the stress in the remaining section was extremely high and, as seen from the DIC analysis, the K_{max} reached the fracture-toughness of the material leading to unstable crack-growth and static failure of the outer stringers.

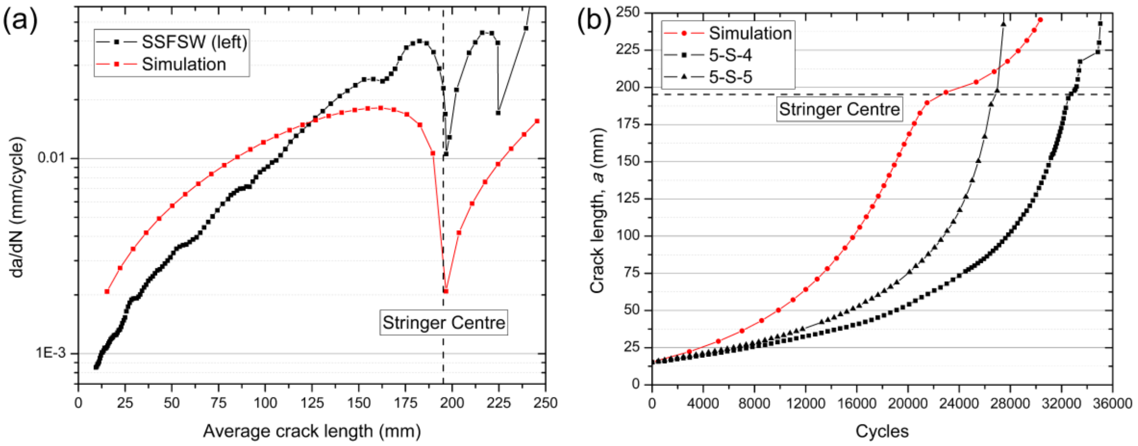

Figure 8.17. Comparison between the predicted and experimental curves of (a) FCGR and (b) FCG behaviour

By numerical integration, it is possible to obtain the a-N curve for the modelled panel and compare it with the experimental results (Figure 8.17b). The curve obtained from the simulation resulted in more conservative values with respect to the experimental case. The higher FCGR in the initial phase of the crack propagation led to a lower number of cycles for a fixed crack length, even when the worst results of the experiments (i.e., ‘light’ anti-buckling device) were considered. As previously explained, this model was a first approximation of this type of structural problem and some additional aspects had to be included in order to increase its precision. The interest around the simulation was related to the possibility of the model to mimic the tendency of the curve. The trend of the model and the experiments were similar in terms of crack-retardation while approaching the stringer caused by the sharp decrease in the β in the area and the consequent reduction of the SIF. In spite of the scope of the work, the improvement in the model could have been achieved by considering the influence of the residual stresses and the presence of the crack closure phenomenon, which would lead to the generation of an effective ΔK different from the one used.

8.1.4. Comparison with other Joining Technologies

The results necessary to compare the fatigue crack propagation behaviour of panels realised by SSFSW with the conventional joining technologies used in the aerospace industry were provided by EMBRAER [120]. The panels from EMBRAER were produced by using the same stringer geometry, skin thickness and bay width as the one realised in this study.

In order to better visualize the differences in the FCGR between the panels realised by SSFSW, riveting and adhesive bonding, the initial focus was on a crack length below 50% of the bay width (Figure 8.18a).

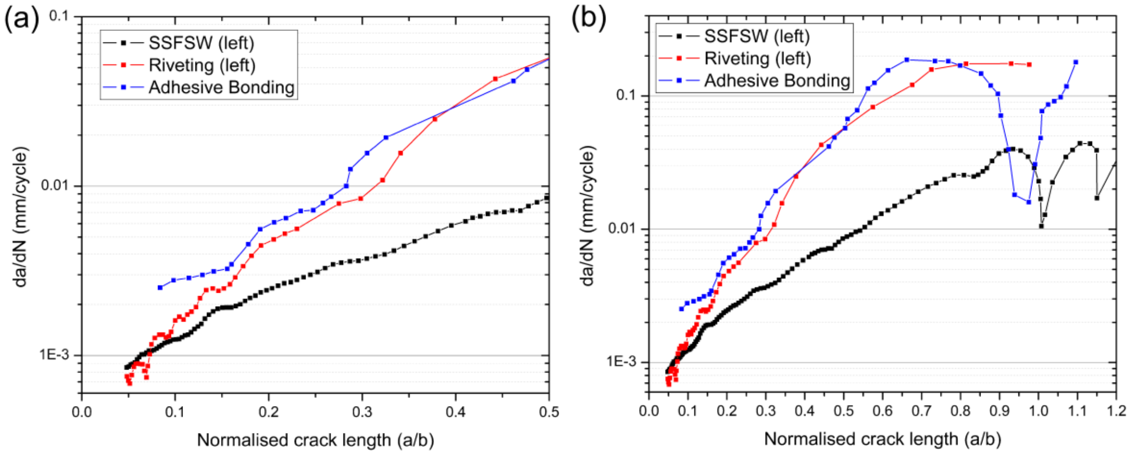

Figure 8.18. Comparison of the FCGR between panels obtained by SSFSW and conventional joining techniques for: (a) crack length up to 50 % of the bay-width and (b) complete bay failure.

For the adhesive bonded stringers, the FCGR was higher from the beginning of the crack propagation; in the case of the riveted stringer, the behaviour was similar to the SSFSW stringers up to a value of a/b, equal to 0.15. In the riveted stringer after the initial phase, a first acceleration in the FCG could be seen, followed by another sharp increase in the FCGR after 30% of the bay-width. In the SSFSW panels, the increase in the FCGR remained stable, leading to a difference of 0.048 mm/cycle (almost 5 mm less each 100 cycles) at 50% of the bay width in comparison to both the riveted and adhesive-bonded panels. The reduction in the FCGR, in case of SSFSW, can be attributed to the improved load transfer between the skin and the remaining stringers, which allows to reduce the stress in front of the crack, also when this is small in comparison to the bay-width.

When the curves for the full bay were analysed (Figure 8.18b), it was possible to see how the crack retardation effect of the stinger was anticipated in the case of adhesive bonding as well as for riveted stringers. The different failure mechanisms between a build-up structure with the possibility of crack bridging of the intact stringer and an integral structure explained the enlarged crack retardation area when the crack approached and overcame the stringer. In spite of the smaller reduction in the FCGR for the SSFSW panels, the valued remained well below the one of the adhesive bonded structures. Unfortunately, the data are available for the riveted connections until the crack reached the bay width and it was not possible to analyse and compare their behaviour with the SSFSW panels after this point.

The observed differences in the FCGR between the three technologies, ultimately lead to the FCG curves shown in Figure 8.19. The improved load transferability and redistribution between skin and stringer for the SSFSW panels led to an increase of 62% in the number of cycles at the two-bay crack-length in comparison to conventional riveted joints. This life improvement was achieved with a weight reduction of around 10%, just by removing the stringer foot necessary for the installation of the rivets or as a bonding surface.

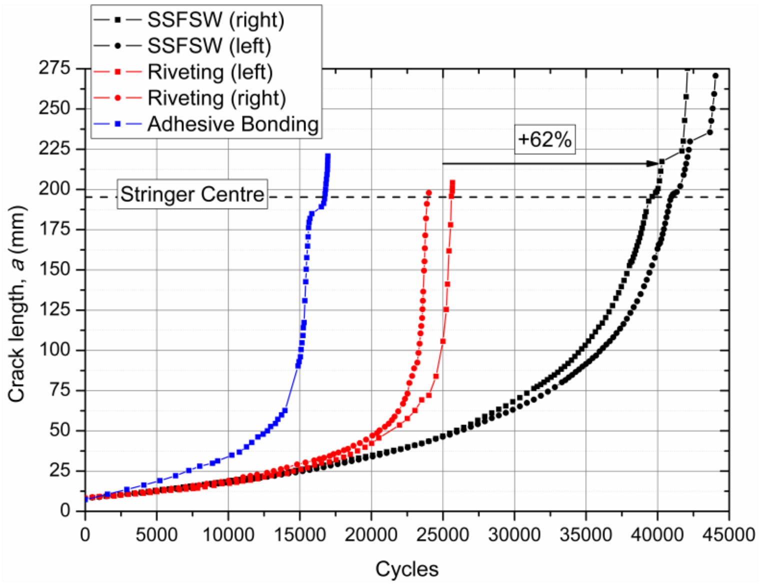

Figure 8.19. Comparison of the FCG behaviour between the panels obtained by SSFSW and conventional joining techniques

Undoubtedly, the different failure mechanisms of the stringer have to be considered in order to implement this technology in an aircraft. In a riveted-stiffened panel, more than two-bay crack length leave the stringer intact until it fails due to ultimate load, allowing the replacement of the broken skin. For a stiffened panel realised by SSFSW, this study showed that the crack could propagate by fatigue in at least one of the two lateral stringers, with its failure being controlled by fracture mechanics laws. This means that in order to guarantee the safety of the aircraft, it would be ideal to repair the cracked skin before the crack reached the two-bay length and damaged the stringer. The positive aspect is that with SSFSW stringers, the crack-growth is reduced since the beginning of propagation and an increase of the maintenance interval could be achieved, even when shorter cracks are considered as critical.

8.2. Residual Strength Analysis

Probably the main cause that lead to a delay in the application of integral structures, such as welded skin-stringer panels, to primary aircraft components is the reduction of the residual strength in comparison to traditional built-up (differential) riveted structures [121].

Ideally, in order to estimate the residual strength of an integral structural component that operates mostly under plane stress, such as the component investigated in this study, an R-curve approach is needed. While in a riveted structure, the residual strength can be determined by the R-curve properties of the skin material and the tensile strength of the stringer, in a welded structure, the properties also depend on the crack-strength of the welded area and the stringer. By analysing the full R-curve of the structure, it would be possible to obtain the critical crack-length for different crack driving forces, K or J, depending on the type of study performed, and, ultimately, to plot the residual strength as a function of the crack-length. Unfortunately, this procedure would require an extremely large number of panels (more than 10) to be tested and it is common practice in the industry to limit the study to the case of an established critical crack-length.

In this work, the two panels, 5-S-2 and 5-S-3, from Table 8.1, used for the residual strength analysis, were pre-cracked by fatigue up to a half-crack length of approximately 190 mm, 3 mm before the stringer edge. The different FCG behaviour between the left and the right crack, for the specimen 5-S-3, lead to a variance between the initial crack lengths of the two specimens (Table 8.2).

Table 8.2. Fatigue crack-lengths at the beginning of the residual strength tests

Specimen number	Crack length left (mm)	Crack length right (mm)	Crack length total (mm)
5-S-2	186.18	187.41	373.59
5-S-3	177.65	189.93	367.58

The curves showing the force as a function of the COD for the two tested panels are shown in Figure 8.20. Both specimens showed a drop in force (pop-in), usually connected with the initiation and the arrest of a brittle crack [122] for a similar value of the COD, equal to ~3.8 mm. This behaviour of the curves probably corresponded to the moment in which the crack started to propagate and reached the stringer edge. After this moment, the two specimens showed different behaviours due to the different initial left crack-length for the panel 5-S-3. While in one panel both stringers failed at the same time on reaching the maximum stress, in the other two, the distinguished stringer’s failures could be observed. The first stringer of the panel 5-S-3, corresponding to the right crack, failed a few moments after the pop-in, as it could be seen from the graph in correspondence with the second drop in force. In spite of this event, the panel was still capable of withstanding increases in force and the maximum was reached immediately before the failure of the stringer in front of the left crack. The two panels, after the two stringers failed, showed a phase in which the force slowly decreased in correspondence with the stable growth of the crack. Once a certain value of the COD was reached the abrupt fracture happened. The fact that both specimens failed for almost an identical value of the COD (around 7 mm) proved that the K_c was not reached until the crack-length was well beyond the two bays, independent from the maximum force reached at the moment of the stringers' failure.

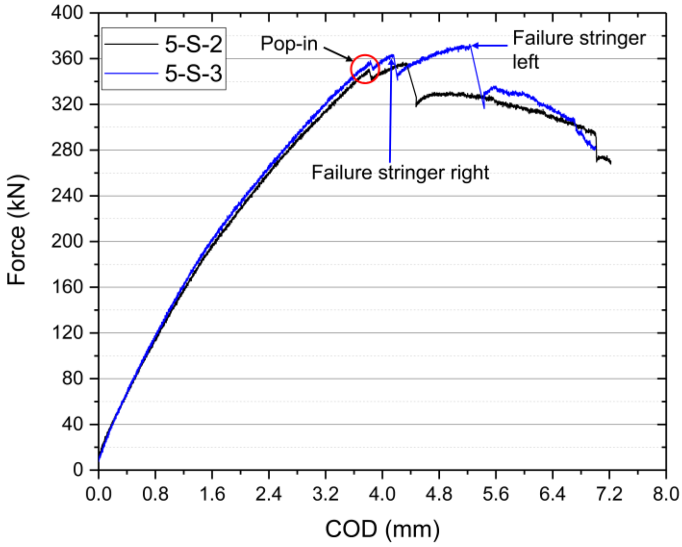

Figure 8.20. Force-COD curves of the two panels tested in terms of residual strength

At last, the value of the residual strength obtained from the two panels could be compared with the results obtained for the riveted structures from the literature [123]. The residual strength of the skin–stringer panels joined by SSFSW were obtained simply by dividing the maximum force reached during the test by the area of the cross-section after fatigue cracking.

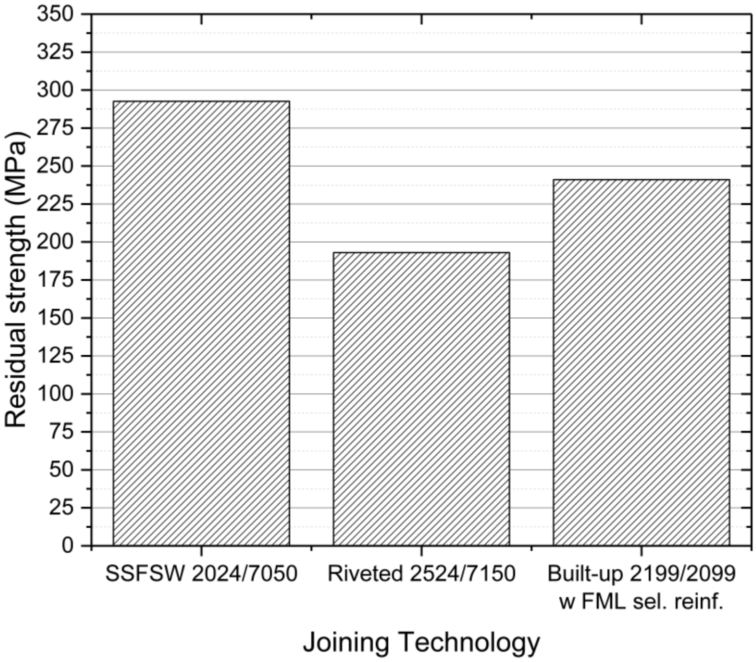

Figure 8.21. Comparison of the residual strength of the SSFSW panels and conventional joining technologies

The residual strength of the panels were higher not only in comparison to a riveted skin–stringer panel but even in the case of the one realized with the addition of reinforcement in fibre-metal laminates (FML). This proves that the application of SSFSW to join the stiffened panels in primary aircraft structures is a serious possibility that would not lead to deteriorations of the structural safety.

8.3. Summary

The analysis performed in this chapter in terms of FCG and residual strength, necessary in order to quantify the damage-tolerability of an integral skin-stringer structure obtained by SSFSW, showed that:

- The buckling of the bay in between the two stringers influences the FCG behaviour.
- The stringers joined by SSFSW are very effective in redistributing the load and reducing the stress within the bay. The load redistribution causes a decrease in the SIF at the crack-tip that is proved by the low FCGR for short cracks as well.
- The use of a DIC system during the FCG tests allows obtaining information with regard to the SIF and the strain profile at the crack-tip, which are fundamental in order to understand the changes of the crack-driving force in such a structural component.
- The model realized by Professor Zhang’ group provides the first good approximation of FCG behaviour in integral panels. The combination of this simulation work and the experimental DIC analysis can be used to extend the analysis to even larger components and a full-scale analysis.
- Both the FCG behaviour and the residual strength showed an improvement in the SSFSW panel with respect to a conventional riveted panel. From a damage-tolerance point of view, this work shows that SSFSW is a serious alternative to riveting in order to reduce weight without deteriorating the safety of primary aircraft structures.

9. Conclusions

In this study, SSFSW was successfully developed in order to join primary aircraft skin–stringer structures. The investigation was initially aimed at the basic understanding of the influence of the process parameters on heat generation, joint formation, microstructure, and the mechanical properties of the coupon-size specimens. Three different joint configurations were analysed and compared by showing each of their advantages and disadvantages. Once the influence of the welding process was understood, the fatigue behaviour of the sub-components was determined with regard to both the critical areas for fatigue initiation and the development of the design curves. At last, 5-stringer panels were investigated and their structural performance in a damage-tolerant environment was clarified. Throughout the entire study, a comparison with the existing joining technologies was performed at different scale levels and under different loading conditions. In accordance with the objectives of this work, the main conclusions and observation were as follows:

A new robust tool system was successfully designed through FEM analysis. This not only produced hundreds of meters of welds without any failure, but also allowed extension of the parameters of the investigation beyond the limits of the window initially expected.

For the three joint configurations, it was shown how, for SSFSW of T-joints, the rotational speed is the key parameter to control the contact condition between probe and surrounding material as well as the temperature peak in the weld area for the SSFSW of T-joints was shown. Consequently, the microstructure and the size of the SZ can be directly affected by varying this parameter. A key microstructural feature, the interface between the skin and stringer’s alloys, controls the mechanical performances of the joints. The geometry of this feature is determined by both the welding speed and the rotational speed due to their influence on the vertical material flow. The angle that the interface forms with the top of the SZ affects the strength of the joint in the hoop-direction by controlling the SIF after the formation of micro-cracks. The length of the interface influences the pull-out strength by varying mechanical interlocking.

The NS-DP configuration proved to have limitations in terms of process development. Lower mechanical performances were obtained with respect to the other two variants both for ‘cold’ and ‘hot’ welds. In the first case, the failure of the joints was caused by the high interface angle, while in the second case the deterioration of the precipitates after the second weld led to a premature failure in the minimum hardness area. In spite of a different microstructure at the centre of the SZ, the 3-Parts and the NS-SP configuration achieved a similar level of UTS with a similar failure mechanism. However, all the three configurations showed higher strength and stiffness in the direction of the hoop in comparison to conventionally riveted skin–stringer joints.

Through DIC analysis it was possible to distinguish the influence of the modified microstructure from the one caused by the joint structure itself. The strain analysis in the hoop-direction shows an impeded lateral contraction under the stringer that leads to a combination of the stress concentrations caused by this and the skin-stringer corner. The strain maps of the three joint configurations differ in the central area of the joints. In spite of this, the same failure mechanism can be observed for the NS-SP and the 3-Parts joints, with the fracture location away from the area with the highest strain.

During the fatigue tests in the hoop-direction, the 3-Parts joints showed the higher robustness of results with respect to the NS-SP. This configuration also shows a higher fatigue life at high stress levels; however, the two variants have the same fatigue limit at 30% of the UTS. The T-joints realized by SSFSW have a stress concentration of two with respect to the AA 2024-T3. In spite of a stress concentration (K_t) being partially influenced by the non-optimized radius at the skin-stringer corner, SSFSW technology leads to half of the stress concentration in comparison to a riveted T-joint and an increase of 50% in the fatigue limit. In the high-fatigue range, the fracture analysis of the NS-SP joints showed the unwanted delamination of the stringer after the crack has been initiated at the interface of the materials. In the longitudinal load direction, the 3-Parts joints present a higher fatigue life while entering into the high-cycles area with respect to the NS-SP variant. In low-cycles fatigue, the two joint configurations show a similar fatigue initiation behaviour, with the largest part of the fatigue propagation happening in the stringer.

The FCG and the residual strength experiment proved the advantages of structures realized by the SSFSW in a damage-tolerant environment. The optimum load-redistribution between the skin and the stringers joined by SSFSW leads to a reduction of the FCGR since the beginning of the crack propagation. Thanks to this, the crack growth behaviour with respect to riveted and adhesive bonded structures has improved over 62% for a crack length that reaches the two-bay width. However, it is important to consider the different failure mechanisms between the welded and riveted stringers. No crack bridging happens in the welded structure and the stringer failure is caused by the propagation of the crack into it. Two new methods to evaluate the variation of crack-driving force for a growing crack in a stiffened structure were developed by using a DIC system. The use of these methods allowed the computation of the SIF at the crack tip that could be compared with the model developed at Cranfield University. The combination of DIC and the simulation provided a deep understanding of the factors influencing the FCGR and an explanation of the reasons for the improved FCG behaviour of the SSFSW panels. A higher residual strength of the SSFSW panels was measured for a two-bay crack with respect to conventional joining methods. This last evidence necessary proves the appropriate design of the stringer and when the different failure mechanisms are considered, SSFSW is a concrete possibility for joining primary aircraft structures.

References

[1] AIRBUS, Growing Horizons 2017 / 2036, 2017.

[2] MIL-HDBK-17-1F, Composite Materials Handbook: Volume 1. Polymer Matrix Composites Guidelines for Characterization of Structural Materials, U.S Department of Defense, U.S.A, 2002.

[3] R. Wanhill, Chapter 2: Fatigue Requirements for Aircraft Structures, in: Aircraft sustainment and repair, Butterworth-Heinemann, Cambridge, MA, USA, 2017 pp. 17-40.

[4] G. Çam, S. Mistikoglu, Recent Developments in Friction Stir Welding of Al-alloys, *Journal of Materials Engineering and Performance* 23(6) (2014) 1936-1953.

[5] E.D.N. W.M. Thomas, J.C. Needham, M.G. Murch, P. Temple-Smith, C.J. Dawes, Improvements to Friction Welding, in: TWI (Ed.) GB Patent, UK, 1991.

[6] J.T. M. Pacchione, Challenges of the metallic fuselage, ICAS 2006, Hamburg, 2006.

[7] D.G. Hattingh, C. Blignault, T.I. van Niekerk, M.N. James, Characterization of the influences of FSW tool geometry on welding forces and weld tensile strength using an instrumented tool, *Journal of Materials Processing Technology* 203(1–3) (2008) 46-57.

[8] R. Nandan, T. DebRoy, H.K.D.H. Bhadeshia, Recent advances in friction-stir welding – Process, weldment structure and properties, *Progress in Materials Science* 53(6) (2008) 980-1023.

[9] A.J. Leonard, Lockyer S. A., Flaws in Friction Stir Welds, 4th International Symposium on Friction Stir Welding, Park City, Utah, USA, 2003.

[10] T.L. Dickerson, J. Przydatek, Fatigue of friction stir welds in aluminium alloys that contain root flaws, *International Journal of Fatigue* 25(12) (2003) 1399-1409.

[11] C. Zhou, X. Yang, G. Luan, Effect of root flaws on the fatigue property of friction stir welds in 2024-T3 aluminum alloys, *Materials Science and Engineering: A* 418(1–2) (2006) 155-160.

[12] S. Cui, Z.W. Chen, J.D. Robson, A model relating tool torque and its associated power and specific energy to rotation and forward speeds during friction stir welding/processing, *International Journal of Machine Tools and Manufacture* 50(12) (2010) 1023-1030.

[13] K.J. Colligan, R.S. Mishra, A conceptual model for the process variables related to heat generation in friction stir welding of aluminum, *Scripta Materialia* 58(5) (2008) 327-331.

[14] P.A. Colegrove, H.R. Shercliff, R. Zettler, Model for predicting heat generation and temperature in friction stir welding from the material properties, *Science and Technology of Welding and Joining* 12(4) (2007) 284-297.

[15] M. Maeda, H. Liu, H. Fujii, T. Shibayanagi, Temperature Field in the Vicinity of FSW-Tool During Friction Stir Welding of Aluminium Alloys, *Welding in the World* 49(3-4) (2005) 69-75.

[16] J.H. Yan, M.A. Sutton, A.P. Reynolds, Processing and banding in AA2524 and AA2024 friction stir welding, *Science and Technology of Welding and Joining* 12(5) (2007) 390-401.

[17] P.A. Colegrove, H.R. Shercliff, Two-dimensional CFD modelling of flow round profiled FSW tooling, *Science and Technology of Welding and Joining* 9(6) (2004) 483-492.

[18] H.N.B. Schmidt, T.L. Dickerson, J.H. Hattel, Material flow in butt friction stir welds in AA2024-T3, *Acta Materialia* 54(4) (2006) 1199-1209.

[19] A.P. Reynolds, Flow visualization and simulation in FSW, *Scripta Materialia* 58(5) (2008) 338-342.

[20] J. Schneider, R. Beshears, A.C. Nunes Jr, Interfacial sticking and slipping in the friction stir welding process, *Materials Science and Engineering: A* 435–436(0) (2006) 297-304.

[21] A. Tongne, C. Desrayaud, M. Jahazi, E. Feulvarch, On material flow in Friction Stir Welded Al alloys, *Journal of Materials Processing Technology* 239(Supplement C) (2017) 284-296.

[22] X. He, F. Gu, A. Ball, A review of numerical analysis of friction stir welding, Progress in *Materials Science* 65 (2014) 1-66.

[23] J.-Q. Su, T.W. Nelson, C.J. Sterling, Microstructure evolution during FSW/FSP of high strength aluminum alloys, *Materials Science and Engineering: A* 405(1) (2005) 277-286.

[24] Z.W. Chen, T. Pasang, Y. Qi, Shear flow and formation of Nugget zone during friction stir welding of aluminium alloy 5083-O, *Materials Science and Engineering: A* 474(1–2) (2008) 312-316.

[25] R.D. Doherty, D.A. Hughes, F.J. Humphreys, J.J. Jonas, D.J. Jensen, M.E. Kassner, W.E. King, T.R. McNelley, H.J. McQueen, A.D. Rollett, Current issues in recrystallization: a review, *Materials Science and Engineering: A* 238(2) (1997) 219-274.

[26] R.W. Fonda, J.F. Bingert, K.J. Colligan, Development of grain structure during friction stir welding, *Scripta Materialia* 51(3) (2004) 243-248.

[27] P.B. Prangnell, C.P. Heason, Grain structure formation during friction stir welding observed by the 'stop action technique', *Acta Materialia* 53(11) (2005) 3179-3192.

[28] M.A. Sutton, B. Yang, A.P. Reynolds, R. Taylor, Microstructural studies of friction stir welds in 2024-T3 aluminum, *Materials Science and Engineering: A* 323(1) (2002) 160-166.

[29] R.S.M. M. Mahoney, T. Nelson, J. Flintoff, R. Islamgaliev, Y. Hovansky, in: K.V. Jata, M.W. Mahoney, R.S., S.L.S. Mishra, in: *TMS (Ed.) Friction Stir Welding and Processing*, Warrendale, PA, USA, 2001, p. 183.

[30] Z.H. Zhang, W.Y. Li, Y. Feng, J.L. Li, Y.J. Chao, Global anisotropic response of friction stir welded 2024 aluminum sheets, *Acta Materialia 92* (2015) 117-125.

[31] P.B. Srinivasan, K.S. Arora, W. Dietzel, S. Pandey, M.K. Schaper, Characterisation of microstructure, mechanical properties and corrosion behaviour of an AA2219 friction stir weldment, *Journal of Alloys and Compounds* 492(1–2) (2010) 631-637.

[32] K. Deplus, A. Simar, W. Haver, B. Meester, Residual stresses in aluminium alloy friction stir welds, *The International Journal of Advanced Manufacturing Technology* 56(5-8) (2011) 493-504.

[33] R.K. Shukla, P.K. Shah, Comparative Study of Friction Stir Welding and Tungsten Inert Gas Welding Process, *Indian Jurnal of Science and Technology* 3(6) (2010) 667-671.

[34] S.T. Amancio-Filho, S. Sheikhi, J.F. dos Santos, C. Bolfarini, Preliminary study on the microstructure and mechanical properties of dissimilar friction stir welds in aircraft aluminium alloys 2024-T351 and 6056-T4, *Journal of Materials Processing Technology* 206(1–3) (2008) 132-142.

[35] A.A.M. da Silva, E. Arruti, G. Janeiro, E. Aldanondo, P. Alvarez, A. Echeverria, Material flow and mechanical behaviour of dissimilar AA2024-T3 and AA7075-T6 aluminium alloys friction stir welds, *Materials & Design* 32(4) (2011) 2021-2027.

[36] A. Barbini, J. Carstensen, J. dos Santos, Influence of Alloys Position, Rolling and Welding Directions on Properties of AA2024/AA7050 Dissimilar Butt Weld Obtained by Friction Stir Welding, *Metals* 8(4) (2018) 202.

[37] J.F. Guo, H.C. Chen, C.N. Sun, G. Bi, Z. Sun, J. Wei, Friction stir welding of dissimilar materials between AA6061 and AA7075 Al alloys effects of process parameters, *Materials & Design* 56(0) (2014) 185-192.

[38] M.J. Peel, A. Steuwer, P.J. Withers, T. Dickerson, Q. Shi, H. Shercliff, Dissimilar friction stir welds in AA5083-AA6082. Part I: Process parameter effects on thermal history and weld properties, *Metallurgical and Materials Transactions A* 37(7) (2006) 2183-2193.

[39] S. Lomolino, R. Tovo, J. dos Santos, On the fatigue behaviour and design curves of friction stir butt-welded Al alloys, *International Journal of Fatigue* 27(3) (2005) 305-316.

[40] L. Fratini, S. Pasta, A.P. Reynolds, Fatigue crack growth in 2024-T351 friction stir welded joints: Longitudinal residual stress and microstructural effects, *International Journal of Fatigue 31*(3) (2009) 495-500.

[41] C. Dalle Donne, G. Biallas, SM98-048/324 Fatigue and Fracture Performance of Friction Stir Welded 2024-T3 Joints, in: B. Kaldeich-Schürmann (Ed.) Spacecraft Structures, *Materials and Mechanical Testing*, 1999, p. 309.

[42] K.A.A. Hassan, P.B. Prangnell, A.F. Norman, D.A. Price, S.W. Williams, Effect of welding parameters on nugget zone microstructure and properties in high strength aluminium alloy friction stir welds, *Science and Technology of Welding and Joining* 8(4) (2003) 257-268.

[43] D. Richard, P.N. Adler, Calorimetric studies of 7000 series aluminum alloys: I. Matrix precipitate characterization of 7075, *Metallurgical Transactions A* 8(7) (1977) 1177-1183.

[44] X. Fan, D. Jiang, Q. Meng, Z. Lai, X. Zhang, Characterization of precipitation microstructure and properties of 7150 aluminium alloy, *Materials Science and Engineering: A* 427(1) (2006) 130-135.

[45] H. Löffler, I. Kovács, J. Lendvai, Decomposition processes in Al-Zn-Mg alloys, *Journal of Materials Science* 18(8) (1983) 2215-2240.

[46] J.Q. Su, T.W. Nelson, R. Mishra, M. Mahoney, Microstructural investigation of friction stir welded 7050-T651 aluminium, *Acta Materialia* 51(3) (2003) 713-729.

[47] C.B. Fuller, M.W. Mahoney, M. Calabrese, L. Micona, Evolution of microstructure and mechanical properties in naturally aged 7050 and 7075 Al friction stir welds, *Materials Science and Engineering: A* 527(9) (2010) 2233-2240.

[48] L. Zhou, T. Wang, W.L. Zhou, Z.Y. Li, Y.X. Huang, J.C. Feng, Microstructural Characteristics and Mechanical Properties of 7050-T7451 Aluminum Alloy Friction Stir-Welded Joints, *Journal of Materials Engineering and Performance* 25(6) (2016) 2542-2550.

[49] R.S. Mishra, Z.Y. Ma, Friction stir welding and processing, *Materials Science and Engineering: R: Reports* 50(1–2) (2005) 1-78.

[50] G. Sha, R.K.W. Marceau, X. Gao, B.C. Muddle, S.P. Ringer, Nanostructure of aluminium alloy 2024: Segregation, clustering and precipitation processes, *Acta Materialia* 59(4) (2011) 1659-1670.

[51] S.C. Wang, M.J. Starink, Two types of S phase precipitates in Al–Cu–Mg alloys, *Acta Materialia* 55(3) (2007) 933-941.

[52] C. Genevois, A. Deschamps, A. Denquin, B. Doisneau-cottignies, Quantitative investigation of precipitation and mechanical behaviour for AA2024 friction stir welds, *Acta Materialia* 53(8) (2005) 2447-2458.

[53] C. Genevois, D. Fabrègue, A. Deschamps, W.J. Poole, On the coupling between precipitation and plastic deformation in relation with friction stir welding of AA2024 T3 aluminium alloy, *Materials Science and Engineering: A* 441(1) (2006) 39-48.

[54] E. Bousquet, A. Poulon-Quintin, M. Puiggali, O. Devos, M. Touzet, Relationship between microstructure, microhardness and corrosion sensitivity of an AA 2024-T3 friction stir welded joint, *Corrosion Science* 53(9) (2011) 3026-3034.

[55] M.Z.H. Khandkar, J.A. Khan, A.P. Reynolds, Prediction of temperature distribution and thermal history during friction stir welding: input torque based model, *Science and Technology of Welding and Joining* 8(3) (2003) 165-174.

[56] H. Schmidt, J. Hattel, J. Wert, An analytical model for the heat generation in friction stir welding, *Modelling and Simulation in Materials Science and Engineering* 12(1) (2004) 143.

[57] M.J. Russell, P L Threadgill,P. L., Thomas, M. J., Wynne, B. P., Static shoulder friction stir welding of Ti-6Al-4V; process and evaluation, 11th World Conference on titanium, Kyoto, Japan, 2007.

[58] M.J. Russell, C. Blignault, N.L. Horrex, C.S. Wiesner, Recent Developments in the Friction Stir Welding of Titanium Alloys, *Welding in the World* 52(9-10) (2008) 12-15.

[59] P.S. Davies, B.P. Wynne, W.M. Rainforth, M.J. Thomas, P.L. Threadgill, Development of Microstructure and Crystallographic Texture during Stationary Shoulder Friction Stir Welding of Ti-6Al-4V, *Metallurgical and Materials Transactions A* 42(8) (2011) 2278-2289.

[60] X. Jiang, B.P. Wynne, J. Martin, Variant selection in stationary shoulder friction stir welded Ti-6Al-4V alloy, *Journal of Materials Science & Technology* 34(1) (2018) 198-208.

[61] S. Eslami, P.J. Tavares, P.M.G.P. Moreira, Friction stir welding tooling for polymers: review and prospects, *The International Journal of Advanced Manufacturing Technology* 89(5) (2017) 1677-1690.

[62] A. Bagheri, T. Azdast, A. Doniavi, An experimental study on mechanical properties of friction stir welded ABS sheets, *Materials & Design* 43 (2013) 402-409.

[63] N. Mendes, A. Loureiro, C. Martins, P. Neto, J.N. Pires, Effect of friction stir welding parameters on morphology and strength of acrylonitrile butadiene styrene plate welds, *Materials & Design* 58 (2014) 457-464.

[64] M.M.Z. Ahmed, B.P. Wynne, W.M. Rainforth, P.L. Threadgill, Through-thickness crystallographic texture of stationary shoulder friction stir welded aluminium, *Scripta Materialia* 64(1) (2011) 45-48.

[65] H.J. Liu, J.Q. Li, W.J. Duan, Friction stir welding characteristics of 2219-T6 aluminum alloy assisted by external non-rotational shoulder, *The International Journal of Advanced Manufacturing Technology* 64(9-12) (2013) 1685-1694.

[66] Z. Li, Y. Yue, S. Ji, P. Chai, Z. Zhou, Joint features and mechanical properties of friction stir lap welded alclad 2024 aluminum alloy assisted by external stationary shoulder, *Materials & Design* 90 (2016) 238-247.

[67] A. Barbini, J. Carstensen, J.F. dos Santos, Influence of a non-rotating shoulder on heat generation, microstructure and mechanical properties of dissimilar AA2024/AA7050 FSW joints, *Journal of Materials Science & Technology* 34(1) (2017) 119-127.

[68] D. Li, X. Yang, L. Cui, F. He, X. Zhang, Investigation of stationary shoulder friction stir welding of aluminum alloy 7075-T651, *Journal of Materials Processing Technology* 222 (2015) 391-398.

[69] D. Li, X. Yang, L. Cui, F. He, H. Shen, Effect of welding parameters on microstructure and mechanical properties of AA6061-T6 butt welded joints by stationary shoulder friction stir welding, Materials & Design 64 (2014) 251-260.

[70] S.D. Ji, X.C. Meng, J.G. Liu, L.G. Zhang, S.S. Gao, Formation and mechanical properties of stationary shoulder friction stir welded 6005A-T6 aluminum alloy, *Materials & Design* 62(0) (2014) 113-117.

[71] H. Wu, Y.-C. Chen, D. Strong, P. Prangnell, Stationary shoulder FSW for joining high strength aluminum alloys, *Journal of Materials Processing Technology* 221 (2015) 187-196.

[72] T. Sun, A.P. Reynolds, M.J. Roy, P.J. Withers, P.B. Prangnell, The Effect of Shoulder Coupling on the Residual Stress and Hardness Distribution in AA7050 Friction Stir Butt Welds, *Materials Science and Engineering: A* 735 (2017) 218-227.

[73] T. Sun, M.J. Roy, D. Strong, P.J. Withers, P.B. Prangnell, Comparison of residual stress distributions in conventional and stationary shoulder high-strength aluminum alloy friction stir welds, *Journal of Materials Processing Technology* 242 (2017) 92-100.

[74] FAA, Advisory Circular 25.1529-1A - Instructions for Continued airworthiness of Structural Repairs on Transport Airplanes, in: U.S. Department of Transportation, 2007.

[75] M.C.Y. Niu, Airframe Structural Design: Practical Design Information and Data on Aircraft Structures (Second Edition), Adaso Adastra Engineering Center, Granada Hills, CA, USA, 1999.

[76] M.C.Y. Niu, Airframe Stress Analysis and Sizing (Second Edition), Adaso Adastra Engineering Center, Granada Hills, CA, USA, 1999.

[77] T.H.G. Megson, Chapter 22 - Fuselages, in: T.H.G. Megson (Ed.), Aircraft Structures for Engineering Students (Fifth Edition), Butterworth-Heinemann, Cambridge, MA, USA, 2013, pp. 643-651.

[78] A. Skorupa, M. Skorupa, Riveted Lap Joints in a Pressurized Aircraft Fuselage, Riveted Lap Joints in Aircraft Fuselage: Design, Analysis and Properties, Springer Netherlands, Dordrecht, 2012, pp. 1-9.

[79] J. Schijve, Fatigue of Structures and Materials (Second Edition), Springer Netherlands, Dordrecht, 2008.

[80] A.P.B. Peggy C. Miedlar, Allan Gunderson, J.P. Gallagher, USAF Damage Tolerant Design Handbook: Guidelines for the Analysis and Design of Damage Tolerant Aircraft Structures, Wrigth-Patterson Air Force Base, OH, USA, 2002.

[81] T.L. Anderson, Fracture Mechanics: Fundamentals and Applications (Third Edition), Taylor & Francis, Boca Raton, FL, USA, 2005.

[82] D. Broek, Elementary engineering fracture mechanics (Third Edition), Springer Netherlands, Dordrecht, 1982.

[83] J.W. Hutchinson, Singular behaviour at the end of a tensile crack in a hardening material, *Journal of the Mechanics and Physics of Solids* 16(1) (1968) 13-31.

[84] J.R. Rice, A Path Independent Integral and the Approximate Analysis of Strain Concentration by Notches and Cracks, *Journal of Applied Mechanics* 35(2) (1968) 379-386.

[85] G.R. Irwin, Analysis of Stresses and Strains Near the End of a Crack Traversing a Plate, *Journal of Applied Mechanics-Transactions of the ASME* E24 (1957) 351-369.

[86] H.M. Westergaard, Bearing pressures and cracks in: Selected papers on Foundations of Linear Elastic Fracture Mechanics, SPIE Mechtronic Series, Bellingham, WA, USA, 1997, 18-22.

[87] D. Rozumek, E. Macha, A survey of failure criteria and parameters in mixed-mode fatigue crack growth, *Materials Science* 45(2) (2009) 190.

[88] G.R. Irwin, The Crack-extension-force for a Crack at a Free Surface Boundary, Naval Research Laboratory, Washington D.C., USA, 1958.

[89] A.A. Griffith, The phenomena of rupture and flow in solids, Philosophical Transactions of the Royal Society of London A: Mathematical, *Physical and Engineering Sciences* 221(582-593) (1921) 163-198.

[90] X. Zhang, Y. Li, Damage Tolerance and Fail Safety of Welded Aircraft Wing Panels, *AIAA Journal* 43(7) (2005) 1613-1623.

[91] R.J. Allen, G.S. Booth, T. Jutla, A review of fatigue crack growth characterisation by linear elastic fracture mechanics (LEFM). Part I—Principles and methods of data generation, *Fatigue & Fracture of Engineering Materials & Structures* 11(1) (1988) 45-69.

[92] W. Elber, The Significance of Fatigue Crack Closure, in: Damage Tolerance in Aircraft Structures (M. Rosenfeld Edition), ASTM International, West Conshohocken, PA, USA 1971, 230-242.

[93] T. Dursun, C. Soutis, Recent developments in advanced aircraft aluminium alloys, *Materials & Design* 56(0) (2014) 862-871.

[94] Z. Zhang, B.L. Xiao, Z.Y. Ma, Hardness recovery mechanism in the heat-affected zone during long-term natural aging and its influence on the mechanical properties and fracture behavior of friction stir welded 2024Al–T351 joints, *Acta Materialia* 73 (2014) 227-239.

[95] J.-H. Schmidt, B. Schmidth, Design Principles and Examples for Metal Structures in Aerospace, AeroStruc, Stade, Germany, 2014.

[96] J. Hilgert, Knowledge Based Process Development of Bobbin Tool Friction Stir Welding, Solid State Joining (Doctoral dissertation), Hamburg Technical University (TUHH), Hamburg, Germany, 2012.

[97] K.E. B. E. Goldberg, R. Stevens, N. Babbitt III, P. Clemens, L. Stout, System engineering toolbox for design-oriented engineers, in: NASA (Ed.) NASA Technical Reports, NASA, Washington, United States, 1994.

[98] D. Rosenthal, Mathematical theory of heat distribution during welding and cutting, *Welding Journal* 20 (1941) 220s-234s.

[99] X. Li, J.L. Li, Z.X. Liao, F. Jin, F.S. Zhang, J.T. Xiong, Asymmetric microstructure and fracture behaviour of friction stir welded joints of 2024 aluminium alloy under cyclical load, *Science and Technology of Welding and Joining* 21(7) (2016) 515-522.

[100] W.H. Van Geertruyden, H.M. Browne, W.Z. Misiolek, P.T. Wang, Evolution of surface recrystallization during indirect extrusion of 6xxx aluminum alloys, *Metallurgical and Materials Transactions A* 36(4) (2005) 1049-1056.

[101] J.Q. Li, H.J. Liu, Effects of tool rotation speed on microstructures and mechanical properties of AA2219-T6 welded by the external non-rotational shoulder assisted friction stir welding, *Materials & Design* 43(0) (2013) 299-306.

[102] P. Carlone, G.S. Palazzo, Influence of Process Parameters on Microstructure and Mechanical Properties in AA2024-T3 Friction Stir Welding, *Metallography, Microstructure, and Analysis* 2(4) (2013) 213-222.

[103] S.A. Khodir, T. Shibayanagi, M. Naka, Microstructure and Mechanical Properties of Friction Stir Welded AA2024-T3 Aluminum Alloy, *Materials Transactions* 47(1) (2006) 185-193.

[104] [104] S.R. Nikolai Kashaev, Rielson Falck, Josephin Enz, Yingtao Tian, Joseph Douglas Robson, Alexandra Karanika, Development of laser beam welding concepts for fuselage panels, 5th CEAS AIR & SPACE CONFERENCE, Delft, The Netherlands, 2015.

[105] A.J. Hallinan, A Review of the Weibull Distribution, *Journal of Quality Technology* 25(2) (1993) 85-93.

[106] NIST/SEMATECH Engineering Statistics Handbook, National Institute of Standards and Technology, U.S Department of Commerce, 1999.

[107] W. Weibull, A Statistical Distribution Function of Wide Applicability, *Journal of Applied Mechanics* (1951) 293-297.

[108] P.J. Davis, Leonhard Euler's Integral: A Historical Profile of the Gamma Function: In Memoriam: Milton Abramowitz, *The American Mathematical Monthly* 66(10) (1959) 849-869.

[109] F. Kun, H.A. Carmona, J.S. Andrade, H.J. Herrmann, Universality behind Basquin's Law of Fatigue, *Physical Review Letters* 100(9) (2008) 094301.

[110] C. Vidal, V. Infante, P. Vilaça, Assessment of improvement techniques effect on fatigue behaviour of friction stir welded aerospace aluminium alloys, *Procedia Engineering* 2(1) (2010) 1605-1616.

[111] MMPDS-06: Metallic materials properties development and standardization (MMPDS), Federal Aviation Administration, Washington, D.C., USA, 2011.

[112] S. Konstantinos, P. Dimitrios, P. George, P. Spyros, Failure analysis of an aluminum extrusion aircraft wing component, *International Journal of Structural Integrity* 7(6) (2016) 748-761.

[113] S. Bansal, Finite Element Analysis of Stress Intensity Factor of Integrally Stiffened Panels (Master thesis), School of Engineering, Cranfield University, Cranfield, UK, 2008.

[114] P. Paris, F. Erdogan, A Critical Analysis of Crack Propagation Laws, *Journal of Basic Engineering* 85(4) (1963) 528-533.

[115] [115] H.J.K. Lemmen, Fatigue and Damage Tolerance of Friction Stir Welded Joints for Aerospace Applications (Doctoral dissertation), Structural Integrity, TU Delft, Delft, Netherlands, 2010.

[116] A.A. Wells, Unstable Crack Propagation in Metals: Clevage and Fast Fracture, Proceeding of Crack Propagation Symposium, Cranfield, UK, 1961.

[117] K.H. Schwalbe, Introduction of D5 [delta 5] as an Operational Definition of the CTOD and Its Practical Use, GKSS, Geesthacht, Germany, 1997.

[118] D. Schnubel, Laser heating as approach to retard fatigue crack growth in aircraft aluminium structures (Doctoral dissertation), Hamburg Technical University (TUHH), Hamburg, Germany, 2012.

[119] P.M.G.P. Moreira, P.M.S.T. de Castro, Fatigue Crack Growth on FSW AA2024-T3 Aluminum Joints, Key *Engineering Materials* 498 (2012) 126-138.

[120] C.E. Chaves, A Review of Aeronautical Fatigue Investigations in Brazil, International Committee on Aeronautical Fatigue and Structural Integrity (ICAF), Nagoya, Japan, 2017.

[121] F. Palm, Can welded fuselage structures fulfil future A/C damage tolerance requirements? - Lessons learned and new concepts derived from 10 years of research in fatigues crackgrowth and residual strength, First International Conference on Damage Tolerance of Aircraft Structures, Delft, The Netherlands, 2007.

[122] C.S.P. Wiesner, H.G., The significance of pop-ins during initiation fracture toughness tests, *Drei R International* 35 (1996) 638-643.

[123] R.J.K. Bucci, M. Heinimann, M. B. James, M. A. Grassel, W. H. Brazill, R. L. Hooijmeijer, P. A. , Large Panel Validation of Advanced Metallic and Hybrid Structural Concepts for Next Generation Transport Aircraft, AEROMAT 2007, Baltimore, MD, USA, 2007.

Appendix A

Technical drawings of the specimens used in this study

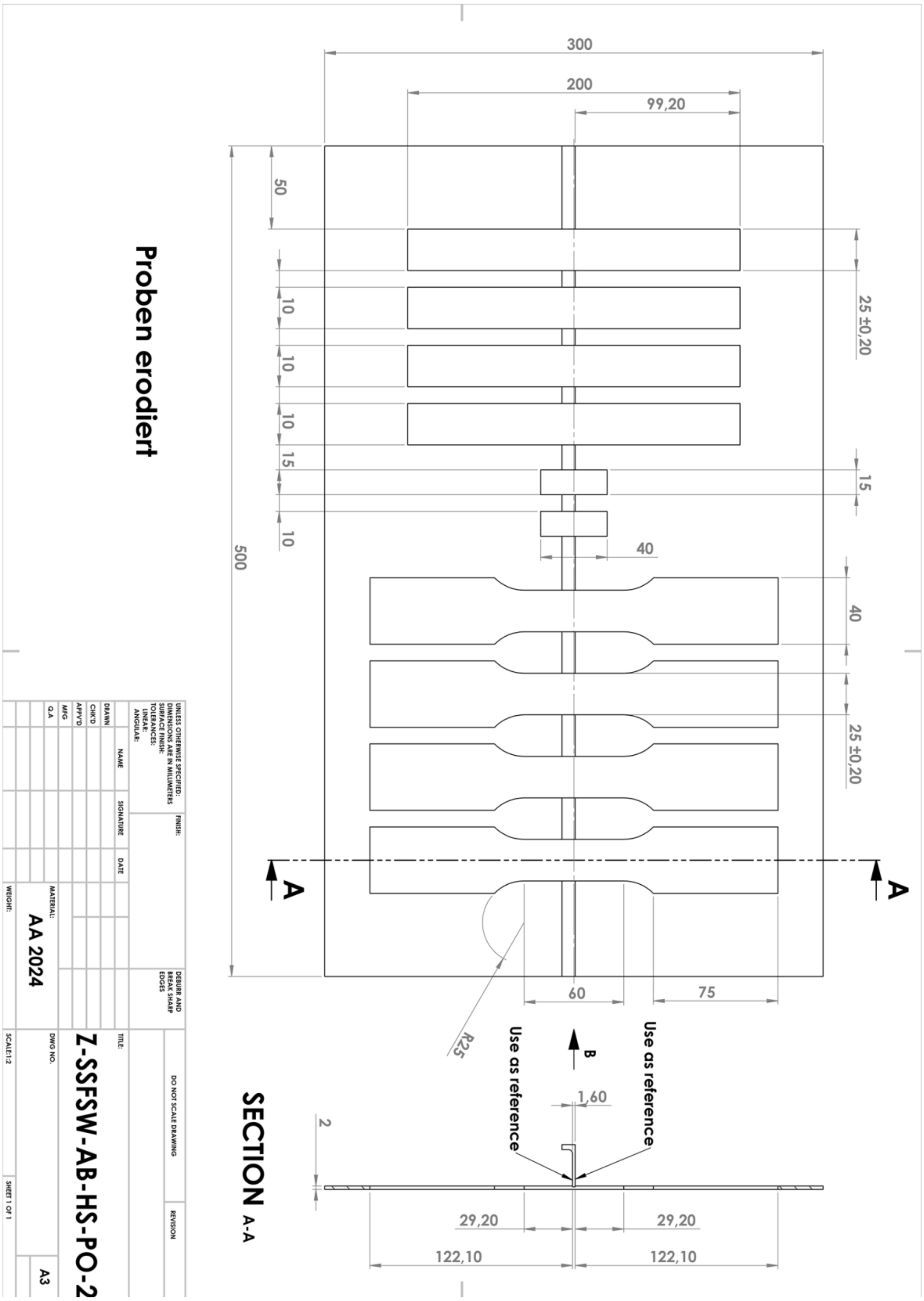

Figure 0.1. Technical drawings of the Hoop, Pull-out and micrographic specimens

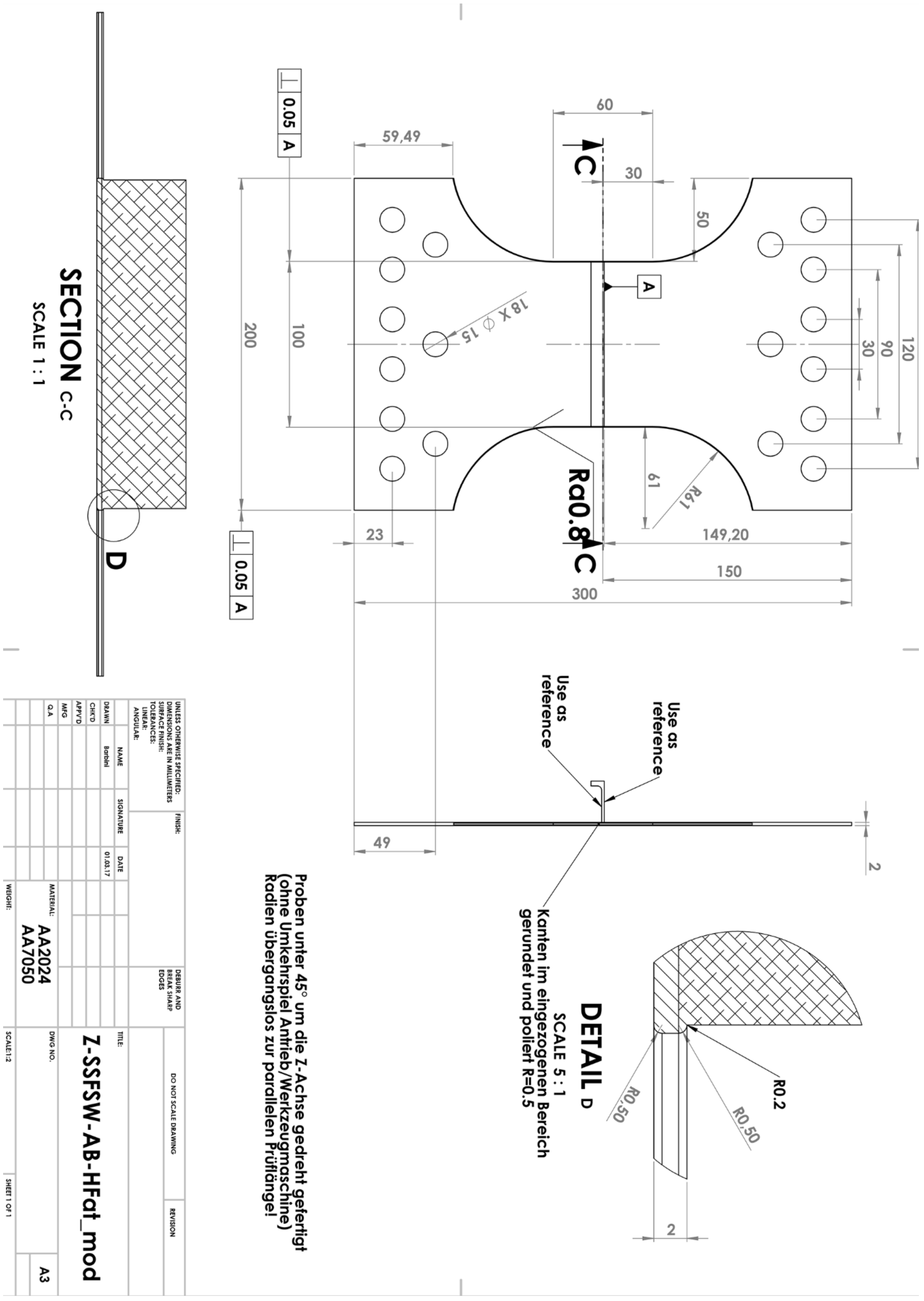

Figure 0.2. Technical drawings of the fatigue specimens in hoop direction

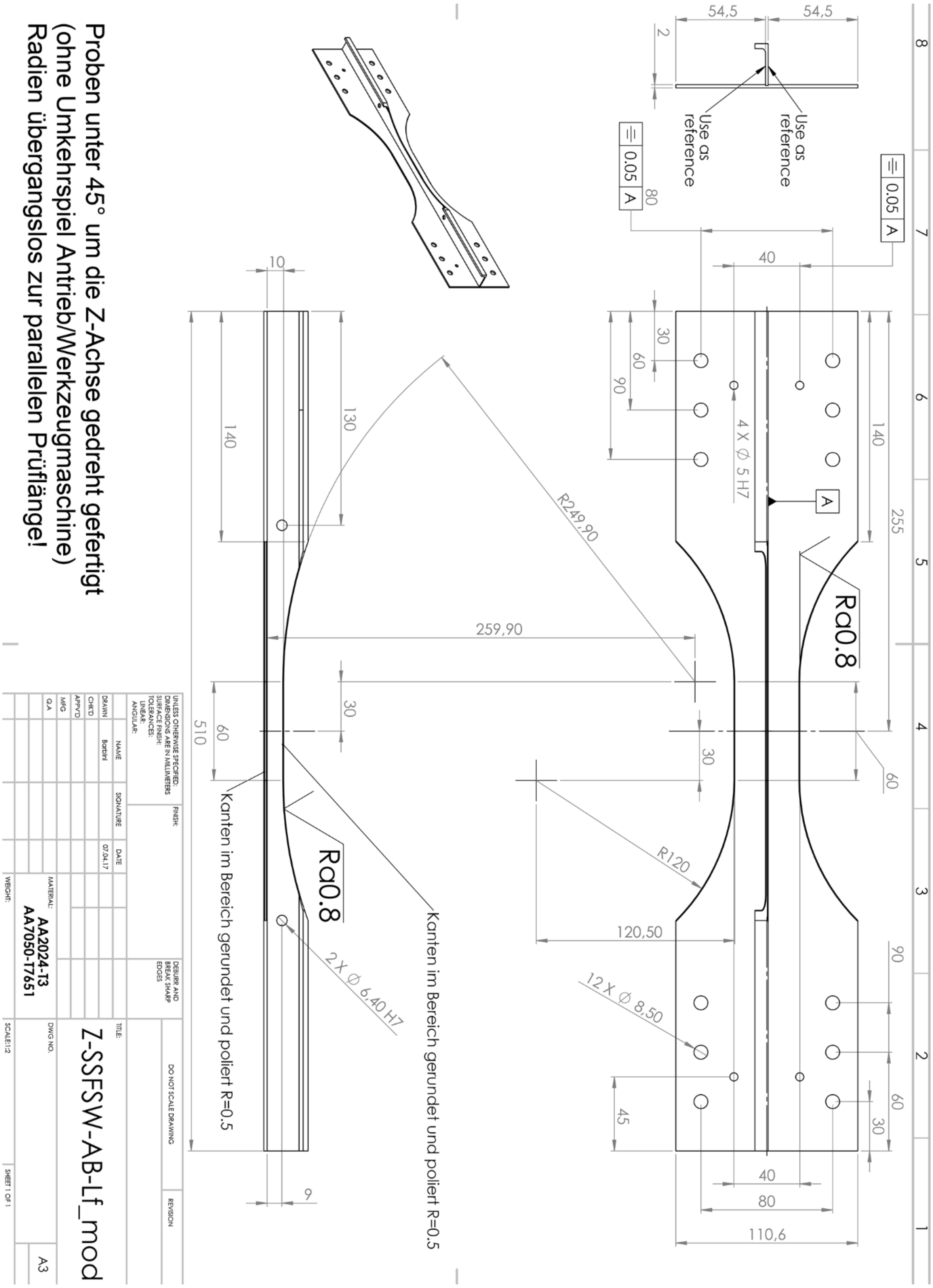

Figure 0.3. Technical drawings of the fatigue specimens in longitudinal direction

Appendix B

Parameter Study of Notch-Skin Double Pass

The graphs and images highlighting the influence of the different set of welding parameters on the joint performances are presented in the following paragraph. The structure is mostly in agreement to the one of the Chapter 5 regarding the NS-SP.

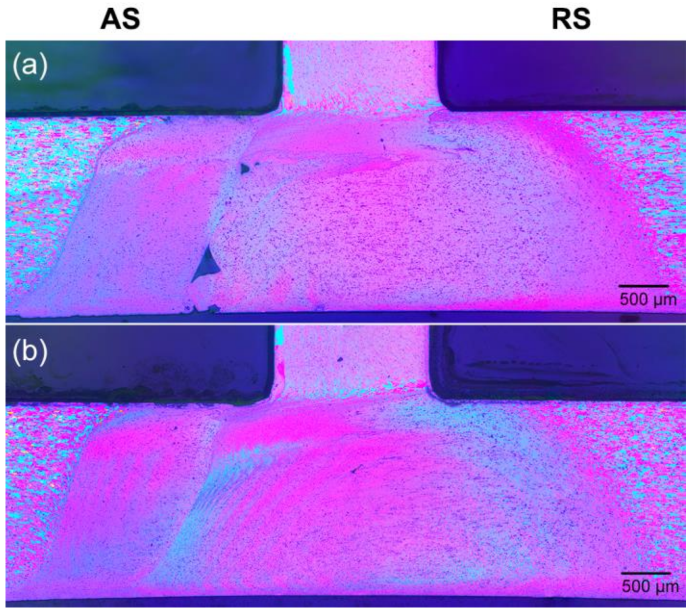

Figure 0.1. Macrographs of the welds obtained by NS-DP with (a) 'cold' parameters (800RPM and WS= 420 mm/min) and (b) 'hot' parameters (1200RPM and WS=300 mm/min)

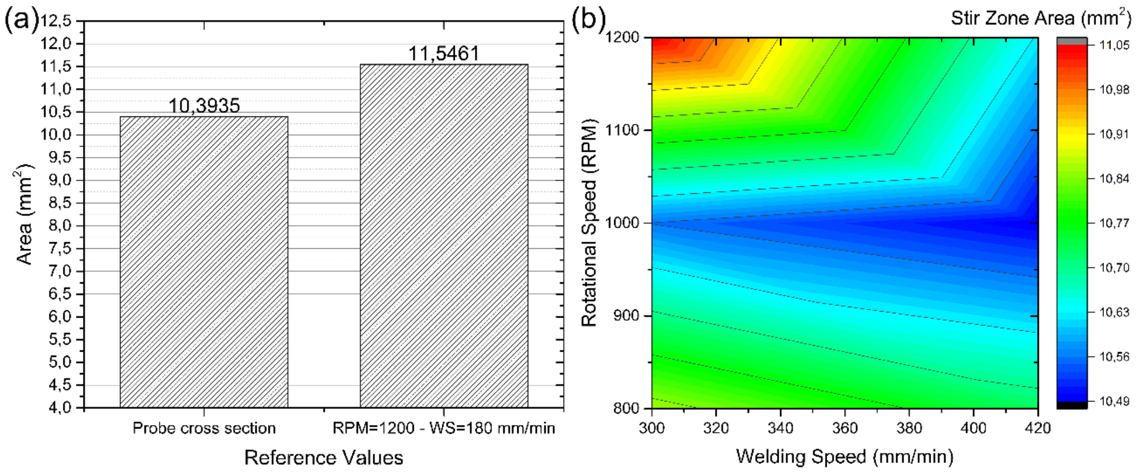

Figure 0.2. NS-DP cross section measurements of (a) probe and SZ at 1200 RPM and WS= 180 mm/min and (b) the remaining set of welding parameters

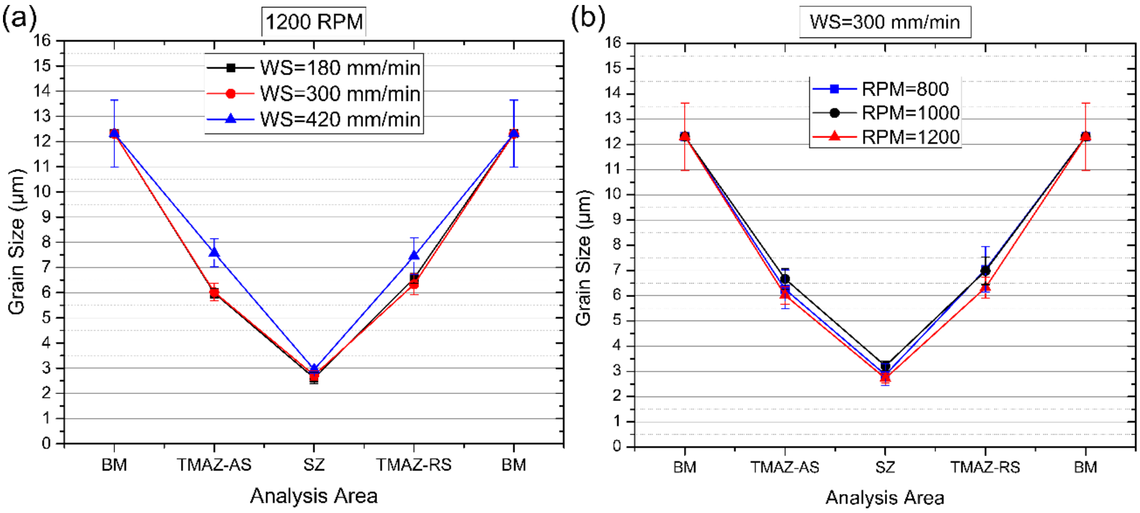

Figure 0.3. NS-DP joint: grain-size measurements for the different WS and RPM at (a) 1200 RPM and (b) WS = 300 mm/min

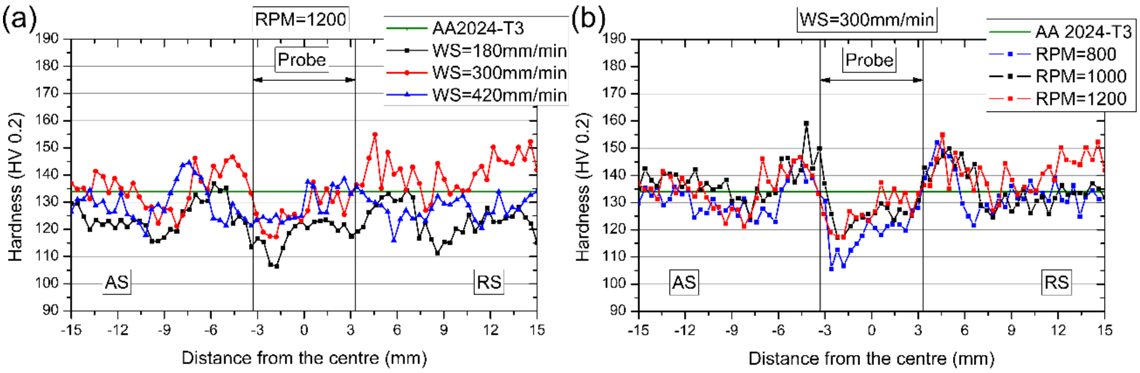

Figure 0.4. NS-DP joints: horizontal micro-hardness profiles at different RPM and WS for (a) 1200 RPM and (b) WS = 300 mm/min

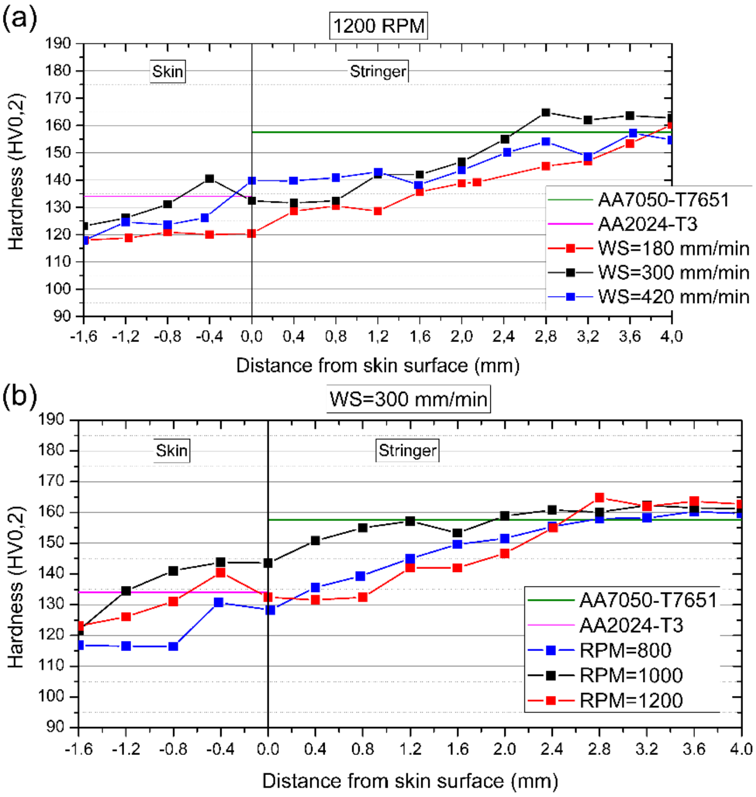

Figure 0.5. NS-DP joints: vertical micro-hardness profiles at different RPM and WS for (a) 1200 RPM and (b) WS = 300 mm/min

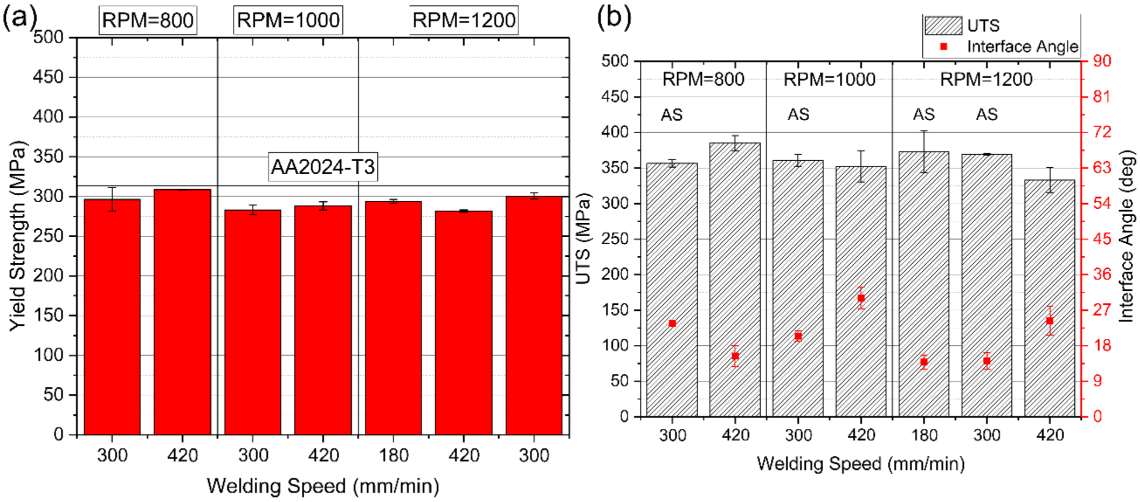

Figure 0.6. NS-DP: Mechanical performances of the NS-DP welds in hoop direction for different welding parameters at (a) yielding and (b) failure together with interface angle evolution

In Figure 0.6b, it is indicated with the AS when the fracture was located in the advancing side of the joint and it is caused not by the interface. The failure in this case is caused by the double thermal cycle experienced by the material and the consequence deterioration of it.

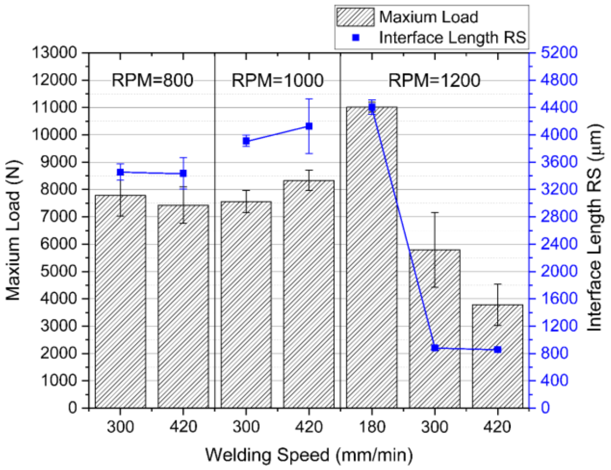

Figure 0.7. NS-DP: Joint strength in pull-out and interface length for different welding parameters

Parameter Study of 3-Parts Welds

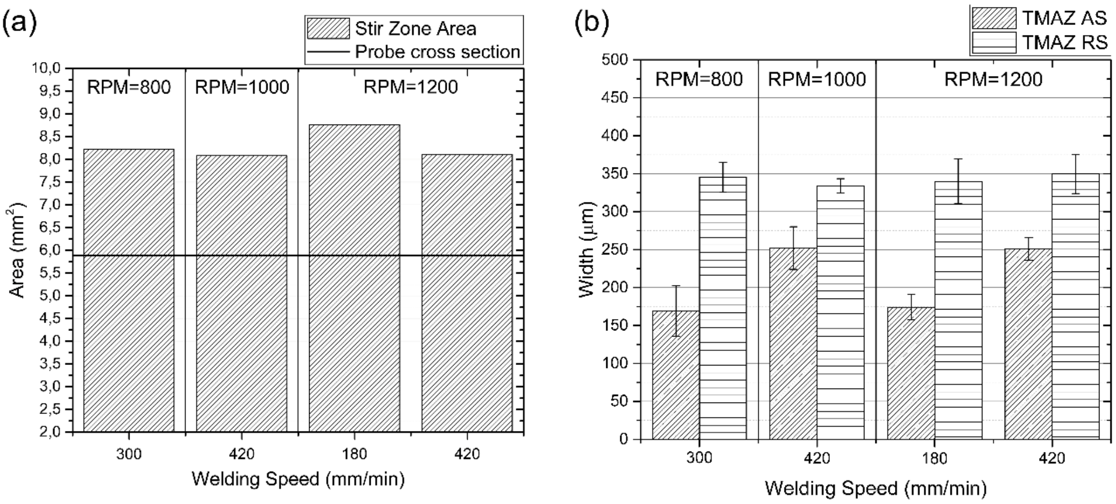

Figure 0.8. 3-Parts welds cross sectional measurements at different WS for (a) SZ area and (b) TMAZ width

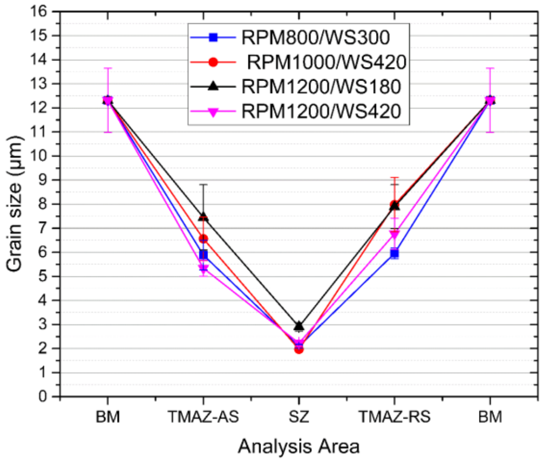

Figure 0.9. 3-Parts welds: Grain-size measurements for the different WS and RPM

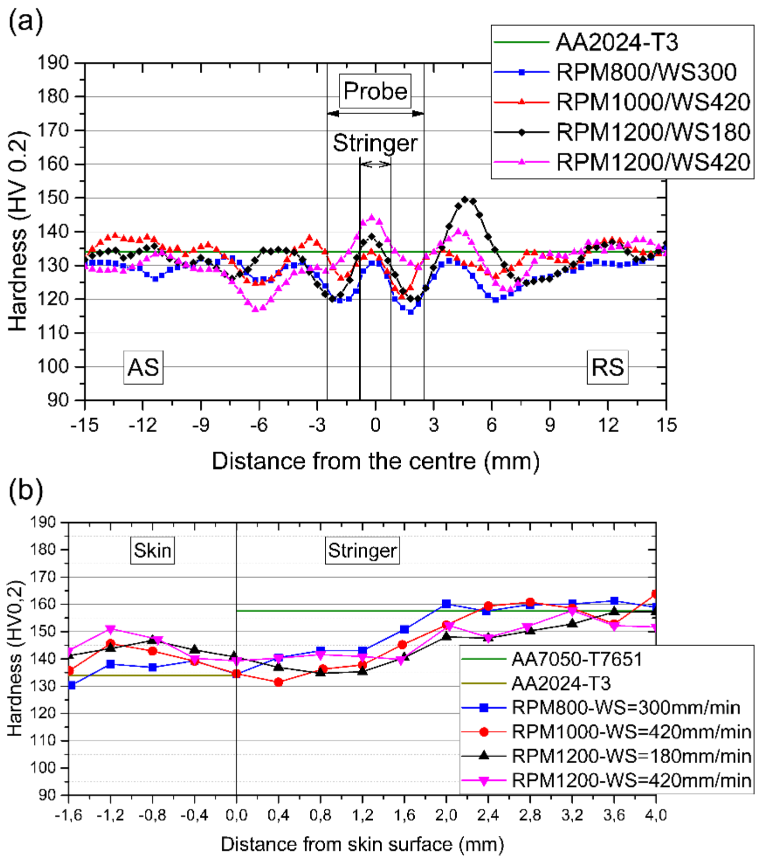

Figure 0.10. 3-Parts welds micro-hardness distributions at different RPM and WS for (a) horizontal profile and (b) vertical profile

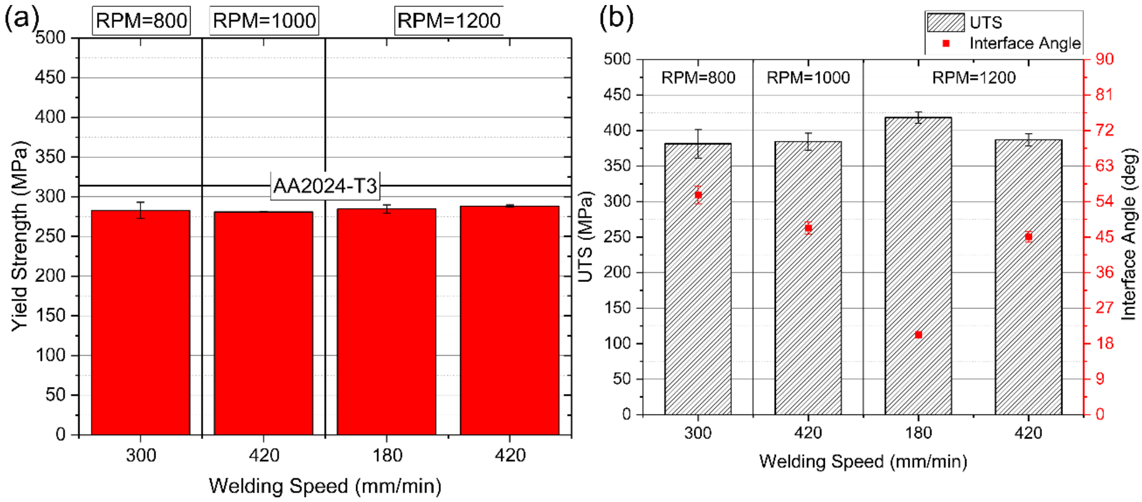

Figure 0.11. Mechanical performances of the 3-Parts welds in hoop direction for different welding parameters at (a) yielding and (b) failure together with interface angle evolution

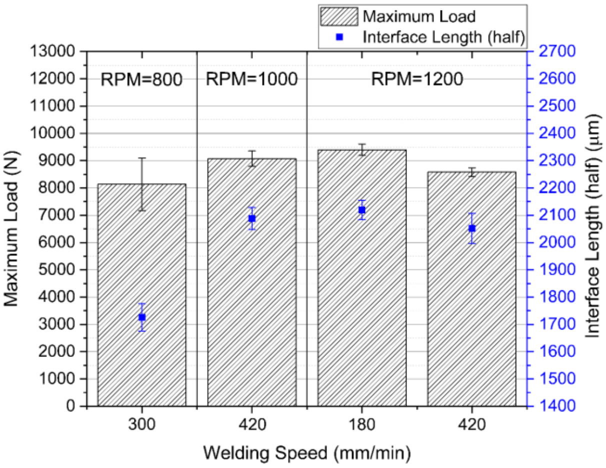

Figure 0.12. 3-Parts joints strength in pull-out and interface length for different welding parameters

List of Figures

List of Tables